# Towards Real-Time Antibody-Based Vital Optical Imaging of Early Oesophageal Neoplasia




Edyta Magdalena Augustyniak

Trinity College

University of Oxford

Supervisors: Professor Katherine Vallis and Professor Boris Vojnovic

A thesis submitted to the University of Oxford in partial fulfilment of the requirement for the degree of

*Doctor of Philosophy*

Michaelmas Term 2019

**Declaration**

I declare that this thesis has been written solely by myself, and that it has not been submitted, in whole or in part, in any previous application for a degree. Except where stated otherwise by reference or acknowledgment, the work presented is a true and honest account of my own research, which was conducted ethically, and the results obtained are genuine.

Edyta Magdalena Augustyniak

**Edyta Magdalena Augustyniak**
Trinity College
Michaelmas Term 2019

# Towards Real-Time Antibody-Based Vital Optical Imaging of Early Oesophageal Neoplasia.

**Background**: The incidence of oesophageal cancer is rising worldwide, yet the surveillance of patients at risk is very ineffective when using white-light reflectance endoscopy. Overexpression of proteins such as the intracellular enzyme Cyclooxygenase-2 (COX-2) and the tyrosine kinase receptor c-Met has been reported in oesophageal premalignant lesions and adenocarcinomas. The goal of this study is to develop optical imaging probes that target diagnostic biomarkers for the detection of early oesophageal neoplasia *in vivo*.

**Materials and Methods**: Probes based on anti-COX-2 [AS66], anti-c-Met [EP1454Y] and (Met13) monoclonal IgG antibodies were synthesised by addition of Cy5 fluorescent dye. For anti-COX-2 probes, and the cell-penetrating peptide TAT was also added to allow intracellular access. Cy5-labelled GE-137 (Edinburgh Molecular Imaging), a peptide-based probe which binds c-Met, was also evaluated. Binding and competition assays were used to determine $K_d$ values. The binding efficiency of each probe was investigated in two oesophageal adenocarcinoma-derived cell lines with high (OE33) and low (FLO-1) COX-2 and c-Met expression. The specificity of each probe was investigated using siRNA knockdown assays. The ability to detect oesophageal cancer *in vivo* was tested in mice bearing OE33 or FLO-1 xenografts using an in-house fluorescence imaging device, following intravenous administration of the probes at a well-tolerated dose of 0.5 mg/kg.

**Results**: Low $K_d$ values in the same order of magnitude as the native antibodies were obtained for the conjugated probes, representing high binding affinity. All probes demonstrated significantly higher binding and retention in OE33 as compared to FLO-1 cells ($P < 0.001$). However, the fluorescence signal from the Cy5-COX-2-TAT probe in OE33 cells was comparable to its control, Cy5-COX-2 without TAT, suggesting high off-target binding of the anti-COX-2 antibody. Imaging of OE33 cells in which either COX-2 or c-Met was selectively knocked down supported earlier data, demonstrating high specificity of anti-c-Met antibodies and low specificity of anti-COX-2 [AS66]. *In vivo* studies showed tumour uptake and retention of the Cy5-Met13 in OE33 but not FlO-1 tumour xenografts ($P < 0.0001$) as well as high c-Met specificity when compared to a Cy5-IgG control ($P < 0.001$). However, Cy5-COX-2-TAT showed both poor uptake and lack of COX-2 specificity *in vivo* when compared to controls: non-specific Cy5-IgG-TAT and Cy5-COX-2 without TAT. Finally, high tumour- but low c-Met specificity was observed for GE-137, with high TBR ratios recorded in both OE33 and FLO-1 xenografts.

**Conclusions:** We have presented a feasible new approach to optical imaging of c-Met and COX-2. Successful conjugate synthesis and TAT-facilitated internalisation *in vitro* serve as a proof of concept for the future development of an anti-COX-2 fluorescent probe, on the condition of selecting an antibody with better specificity. Furthermore, a non-invasive means of optical imaging of c-Met *in vivo*, presented in this thesis, can have important diagnostic implications for various types of gastrointestinal cancer.

**Acknowledgements**

Dedykuję tę rozprawę doktorską mojej babci Czesławie i dziadkowi Henrykowi. Bardzo Was kocham.

I dedicate this thesis to my grandmother Czesława and grandfather Henryk. I love you both very much.

First and foremost, I would like to thank Professor Katherine Vallis and Professor Boris Vojnovic for giving me the opportunity to be a part of this project. Without their trust, encouragement and constant support the completion of this thesis would not have been possible. Thank you for all the help, patience, and guidance not only through my adventure into scientific research but also for teaching me many valuable lessons in life; thank you for believing in me (Boris, I promise I will improve my maths).

A big thanks goes to Cancer Research UK and Oxford Cancer Imaging Centre for funding this project.

I want to thank all the fantastic people of the Vallis and Vojnovic groups. A huge thanks goes to Sarah, for teaching me everything, including how to behead a biscuit; Martin, for all the guidance and sharing (sometimes involuntarily) all of his buffers; Javian, Irini, Elliott, Bas, Abirami, Ramon and Jyothi for your friendship and laughter. I will miss you all dearly. Davide, Paul and Iain for helping me understand (a little bit of) physics and electronics, something I never knew would be possible; John, Jerry and Kyle for fixing and making things for me, including hand-crafted Christmas gifts. Thanks to Rob for fixing the microscope, especially when something exploded, and lending me all sort of wonderful things.

I would also like to thank all the members of the Cornelissen group, especially Bart, James and Sofia (your help was invaluable); and of the Carr group, particularly Hayley, Joana and Tonia, I am really thankful for your support and understanding; a huge thanks to the biscuit team, especially Sally, Magda and Karla, whose help was priceless.

A big thanks to my best friends Hannah and Jaclyn, for your constant encouragement and your love, you bring out the best in me. Thanks to Olivia, Lien, Catherine and Charlotte for the good times we spent together.

A very special thanks must go to my sister Sandra and my parents, Lucyna and Jacek. Your support and encouragement were worth more than I could express on paper. Thank you for being there for me in every moment of this journey.

Last, but certainly not least, my sincerest thanks goes to my partner Yan. Thank you for all the love and support, I could not have done it without you. Words are not enough. Thank you!

**Table of Contents**

**List of Tables** ..... **xv**

**Chapter 1 Introduction** ..... **20**

1.1 Cancer – Overview ..... 21

1.2 Anatomy and Physiology of the Oesophagus ..... 22

1.3 Oesophageal Cancer ..... 24
1.3.1 Symptoms ..... 24
1.3.2 Epidemiology ..... 25
1.3.3 Risk Factors ..... 26

1.4 Barrett's Oesophagus, and the Pathogenesis of Oesophageal Adenocarcinoma ..... 26
1.4.1 Gastro-oesophageal Reflux Disease (GORD) ..... 26
1.4.2 Barrett's Oesophagus ..... 27

1.5 Pathogenesis of Oesophageal Adenocarcinoma in Patients with Barrett's Oesophagus, Molecular Background, and Main Biomarkers of Progression ..... 29
1.5.1 DNA Content Abnormalities and Epigenetic Changes Biomarkers ..... 30
1.5.2 Proliferation Biomarkers ..... 32
1.5.3 Cell Cycle Biomarkers ..... 32
1.5.4 Prognostic Biomarkers in Oesophageal Adenocarcinoma ..... 33

1.6 Gastro-oesophageal Reflux Disease, Cyclooxygenase-2 (COX-2) and Inflammation ..... 35
1.6.1 COX Enzymes ..... 37

1.7 c-Met and Oesophageal Cancer ..... 38
1.7.1 c-Met Signalling ..... 39

1.8 Current Surveillance, Diagnosis and Management of Barrett's Oesophagus ..... 43
1.8.1 Diagnosis of Oesophageal Adenocarcinoma ..... 45
1.8.2 Limitations of Current Screening ..... 47
1.8.3 Limitations of Current Surveillance ..... 48

1.9 Oesophageal cancer: T, N, M staging system ..... 49

1.10 Current Treatment ..... 51

1.11 Optical and Molecular Imaging ..... 54
1.11.1 Optical Imaging ..... 56

1.12 Antibodies as Imaging Agents ..... 58

1.13 Cell-Penetrating Peptides ..... 60
1.13.1 The TAT Peptide ..... 62

1.14 Thesis Aims ..... 63

**Chapter 2 Materials and Methods ..... 65**

2.1 Cell Lines ..... 66
2.1.1 CP (hTert) Cell Lines ..... 66

2.1.2 FLO-1 Cell Line ..... 66

2.1.3 OE33 Cell Line ..... 67

2.1.4 Cell Maintenance ..... 67

2.1.5 Cryopreservation and Storage of Cells ..... 68

2.1.6 Cell Culture Plastic Ware ..... 68

2.2 Western Blot (WB) Analysis ..... 69

2.3 Antibodies ..... 75
2.3.1 Main Antibodies Used ..... 75

2.3.2 Non-Specific Control Antibodies ..... 76

2.3.3 Antibody Labelling with the Cy5-NHS Dye – Anti-c-Met Antibodies ..... 76

2.3.4 Conjugation of TAT Penetrating Peptide – Anti-COX-2 [AS66] ..... 76

2.3.5 TAT Radiolabelling ..... 77

2.4 Enzyme-Linked Immunosorbent Assay (ELISA) ..... 78
2.4.1 Indirect ELISA – Anti-COX-2 and Anti-c-Met ..... 78

2.4.2 Direct ELISA – Anti-COX-2 and Anti-c-Met ..... 79

2.4.3 Competition Binding ELISA – Anti-COX-2 and Anti-c-Met ..... 80

2.5 Immunohistochemistry ..... 80
2.5.1 Ligand Binding Assays ..... 80

2.5.2 Competition Binding Assay ..... 81

2.5.3 Blocking Assay – Anti-c-Met (Met13) ..... 81

2.6 Fluorescent Imaging ..... 82
2.6.1 Live Cell Imaging ..... 82

2.6.2 Image Acquisition ..... 82

2.7 Small-Interfering RNA (siRNA)-Mediated Gene Silencing ..... 83

2.8 In Vivo Imaging ..... 84
2.8.1 Cell Preparation for Inoculation ..... 85

2.8.3 Growth Rate of OE33 and FLO-1 Xenografts ..... 85

2.8.4 In Vivo Experimental Design ..... 86

2.8.5 Ex Vivo Biodistribution Studies....86
2.8.6 Image Acquisition....87
2.8.7 Image Processing and Analysis....87
2.9 Statistical Analysis....89
**Chapter 3 In Vitro Imaging of Oesophageal Cancer by Targeting c-Met Receptors....91**
3.1 Introduction....92
3.1.1 Selective Optical Imaging of c-Met....92
3.1.2 GE-137 Peptide....95
3.1.3 Cy5, a Far-Red Fluorescent Dye....95
3.1.4 Overall Aim....97
3.2 Experimental Set Up....98
3.3 Results....101
3.3.1 Validation of the Anti c-Met [EP1454Y] and (Met13) Antibodies....101
3.3.1.1 Specificity of the Anti-c-Met [EP1454Y] and (Met13) Antibodies Tested in a Panel of Cancer Cell Lines....101
3.3.1.2 Determination of Anti-c-Met [EP1454Y] and (Met13) Affinity by ELISA....102
3.3.2 Fluor-Labelling with Cy5 Fluorophore and In Vitro Validation of Cy5-EP1454Y and Cy5-Met13 Probes....105
3.3.2.1 Cy5 Labelling....105
3.3.2.2 Determination of Cy5-EP1454Y and Cy5-Met13 Affinity by Immunocytochemistry (ICC)....106
3.3.3 Cy5-EP1454Y and Cy5-Met13 Antibodies Bind OE33 but Not FLO-1 Cells....110
3.3.3.1 Cy5-EP1454Y and Cy5-Met13 Demonstrate Uptake in OE33 but Not FLO-1 Cells....110
3.3.3.2 Investigation of the Specificity of the Cy5-EP1454Y and Cy5-Met13 Probes in OE33 Cells....115
3.4 Discussion....120
3.4.1 Specificity of the Anti-c-Met [EP1454Y] and (Met13) Antibodies Tested in a Panel of Cancer Cell Lines....120
3.4.2 Determination of the Anti-c-Met [EP1454Y] and (Met13) Affinity by ELISA....121

3.4.3 Fluor-Labelling with Cy5 Fluorophore and In Vitro Validation of Cy5-EP1454Y and Cy5-Met13 Probes ..... 122
3.4.5 Cy5-EP1454Y and Cy5-Met13 Antibodies Bind OE33 but Not FLO-1 Cells ..... 123
3.4.6 Further Investigation of the Specificity of the Cy5-EP1454Y and Cy5-Met13 Probes ..... 124
3.4.7 Conclusions ..... 125

**Chapter 4 In vivo Evaluation of the Cy5-EP1454Y, Cy5-Met13 and GE-137 in the Oesophageal Adenocarcinoma Xenograft Models ..... 126**

4.1 Introduction ..... 127
4.1.1 Current Treatment ..... 128
4.1.2 'Early' Oesophageal Cancer and c-Met ..... 129
4.1.3 Advanced Endoscopic Imaging in Gastrointestinal Neoplasia and Preneoplasia ..... 130
4.1.4 Overall Aim ..... 133

4.2 Experimental Set Up ..... 134

4.3 Results ..... 136
4.3.1 Growth Rate of Subcutaneous Oesophageal Adenocarcinoma Derived Xenografts ..... 136
4.3.2 Ex Vivo Biodistribution Analysis and Dose Study ..... 138
4.3.2.1 Cy5-Met13 ..... 138
4.3.2.2 Cy5-EP1454Y ..... 142
4.3.3 Investigation of the Specificity of the Cy5-Met13 Probe in OE33 Xenografts ..... 146
4.3.4 Investigation of the Specificity of the Cy5-Met13 Probe in OE33 and FLO-1 Xenografts ..... 151
4.3.5 Optical Imaging of GE-137 ..... 155

4.4 Discussion ..... 158
4.4.1 Establishing a Model of Subcutaneous OAC-Derived Xenografts ..... 158
4.4.2 Ex Vivo Biodistribution Analysis and Dose Study ..... 160
4.4.3 Investigation of the Specificity of the Cy5-Met13 Probe in OE33 and FLO-1 Xenografts ..... 163
4.4.4 Optical Imaging of GE-137 ..... 166
4.4.5 Conclusions ..... 167

**Chapter 5 In Vitro and In Vivo Imaging of Oesophageal Cancer by Targeting Cyclooxygenase 2 (COX-2) ..... 168**

5.1 Introduction ..... 169
5.1.1 Cyclooxygenase 2 ..... 170
5.1.2 Diagnostic Potential of Intracellular Targets ..... 171
5.1.3 TAT Cell-Penetrating Peptide ..... 172
5.1.4 Overall Aim ..... 173

5.2 Experimental Set Up ..... 174

5.3 Results ..... 175
5.3.1 Validation of the Anti-COX-2 [AS66] Antibody ..... 175
5.3.2 TAT-Antibody Conjugation ..... 179
5.3.3 Labelling with Cy5 Fluorophore and In Vitro Validation of Cy5-COX-2-TAT Probe ..... 182
5.3.4 Evaluating the COX-2 Binding and Internalising Properties of Cy5-COX-2-TAT Antibody Constructs in OE33 and FLO-1 Cells ..... 187
5.3.4.2 Specificity and Internalisation of Cy5-COX-2-TAT in OE33 ..... 190
5.3.5 Investigation of Specificity of COX-2 [AS66] Antibody ..... 193
5.3.6 In Vivo Evaluation of the Cy5-COX-2-TAT in an OE33 Xenograft Model ..... 196

5.4 Discussion ..... 200
5.4.1 Specificity of Anti-COX-2 [AS66] Antibody Tested in a Panel of Cancer Cell Lines ..... 200
5.4.2 Determination of Anti-COX-2 [AS66] Affinity by ELISA ..... 201
5.4.3 Evaluation of TAT-Anti-COX-2 [AS66] Antibody Conjugation Using $^{123}$I-TAT ..... 201
5.4.5 Cy5 Labelling and Determination of Cy5-COX-2-TAT Affinity by ELISA ..... 202
5.4.6 Evaluating the COX-2 Binding and Internalising Properties of Cy5-COX-2-TAT Antibody Constructs in OE33 and FLO-1 Cells ..... 203
5.4.7 Further Investigation of the Specificity of the Cy5-COX-2-TAT Probe ..... 206
5.4.8 In Vivo Evaluation of the Cy5-COX-2-TAT in the OE33 Xenograft Models ..... 206
5.4.9 Conclusions ..... 208

**Chapter 6 Conclusions and Future Work ..... 209**

6.2 Evaluating the COX-2 Binding and TAT Internalising Properties of Cy5-COX-2-TAT .....211
6.3 Investigation of the Specificity of the Cy5-EP1454Y, Cy5-Met13 and Cy5-COX-2-TAT probes .....212
6.4 Investigating Specificity of the Cy5-COX-2-TAT Probe In Vivo .....214
6.5 Investigating Specificity of the anti-c-Met Probes In Vitro .....216
6.6 Future Work.....220
Bibliography **.....224**

**List of Figures**

**Figure 1.1** Oesophagus .....23
**Figure 1.2** Barrett's. Metaplasia – Dysplasia – Cancer Sequence .....29
**Figure 1.3** c-Met Signalling.....42
**Figure 2.1** Gamma Correction.....88
**Figure 2.2** Region of Interest (ROI) Analysis. .....90
**Figure 3.1** The Open Microscope 'Abbe'.....99
**Figure 3.2** Maintaining Live Cells Using Live Cell Imaging Chamber .....100
**Figure 3.3** [EP1454Y] Antibody Validation and c-Met Protein Expression Levels for Neoplastic Cell Lines, Detected by Western Blot.....102
**Figure 3.4** Evaluation of Binding Affinity by ELISA.....104
**Figure 3.5** Fluorescence Intensity of Anti-c-Met Cy5-Labelled Constructs. .....106
**Figure 3.6** Evaluation of Binding Affinity by ICC.....108
**Figure 3.7** Competition Binding Assay.....109
**Figure 3.8** Binding Properties of the Cy5-EP1454Y and Cy5-Met13 in OE33 Cells.111
**Figure 3.9** Binding Properties of the Cy5-EP1454Y and Cy5-Met13 in FLO-1 Cells112
**Figure 3.10** The c-Met Binding Properties of the Antibody Constructs Were Evaluated in OE33 and FLO-1 Cells.....114
**Figure 3.11** Validation of siRNA-Mediated c-Met Knockdown in OE33 Cell Line ..116
**Figure 3.12** Validation of the Off-Target Binding of Cy5-EP1454Y and Cy5-Met13, Immunofluorescence Microscopy .....117
**Figure 3.13** Validation of the Off-Target Binding of Cy5-EP1454Y and Cy5-Met13, siRNA Knockdown .....118
**Figure 3.14** Validation of the Off-Target Binding of Cy5-EP1454Y and Cy5-Met13, Blocking Experiment.....119
**Figure 4.1** Imaging Device, Final Design.....135
**Figure 4.2** Tumour Growth Curves for the OE33 and FLO-1 Xenografts. .....137
**Figure 4.3** Biodistribution Study, Cy5-Met13.....139
**Figure 4.4** Ex Vivo Tissue Biodistribution, Cy5-Met13 .....140
**Figure 4.5** Optical Images Showing Tumour Uptake of Cy5-Met13 .....141
**Figure 4.6** Biodistribution Study, Cy5-EP1454Y.....143
**Figure 4.7** Ex vivo Tissue Biodistribution, Cy5-EP1454Y .....144
**Figure 4.8** Optical Imaging Showing Tumour Uptake of Cy5-EP1454Y .....145

**Figure 4.9** Specificity of the Cy5-Met13 Probe in OE33 Xenografts .....147
**Figure 4.10** Specificity of the Cy5-Met13 Probe in OE33 Xenografts, Skin Removed .....148
**Figure 4.11** Optical Images Showing Tumour Uptake of Cy5-Met13 and Cy5-IgG ..150
**Figure 4.12** Uptake of the Cy5-Met13 Probe in OE33 and FLO-1 Xenografts, Skin Removed.....152
**Figure 4.13** Optical Images Showing *Ex Vivo* Biodistribution .....153
**Figure 4.14** Optical Imaging Showing Tumour Uptake of Cy5-Met13 and Cy5-IgG in OE33 and FLO-1 Xenografts .....154
**Figure 4.15** *Ex Vivo* Biodistribution Analysis, GE-137 .....156
**Figure 4.16** Optical Images Showing Uptake of GE-137 in OE33 and FLO-1 Xenografts .....157
**Figure 5.1** [AS66] Antibody Validation and COX-2 Protein Expression Levels in Oesophageal Cancer Cell Lines, Detected by Western Blot Analysis .....176
**Figure 5.2** Evaluation of Binding Affinity of Anti-COX-2 [AS66] Antibody by ELISA .....178
**Figure 5.3** Evaluation of TAT-Anti-COX-2 [AS66] Antibody Conjugation Using $^{123}$I-TAT .....181
**Figure 5.4** Fluorescence Intensity of Cy5-COX-2-TAT Constructs .....183
**Figure 5.5** Evaluation of Binding Affinity by ELISA .....185
**Figure 5.6** Competitive Binding Study.....186
**Figure 5.7** Internalisation of Cy5-COX-2-TAT in OE33 and FLO-1 Cells .....188
**Figure 5.8** Uptake of Cy5-COX-2-TAT in OE33 and FLO-1 Cells.....189
**Figure 5.9** COX-2 Binding and Internalisation Properties of the Cy5-COX-2-TAT Antibody Constructs in OE33 and FLO-1 Cells.....191
**Figure 5.10** Internalisation of Cy5-COX-2-TAT in OE33 Cells.....192
**Figure 5.11** Validation of siRNA-Mediated COX-2 Knockdown in the OE33 Cell Line .....193
**Figure 5.12** Demonstration of the Off-Target Binding of Cy5-COX-2-TAT, siRNA Knockdown.....195
**Figure 5.13** *In Vivo* Biodistribution of Cy5-COX-2-TAT.....197
**Figure 5.14** *Ex Vivo* Biodistribution of Cy5-COX-2-TAT.....198
**Figure 5.15** Optical Images Showing Tumour Uptake of Cy5-COX-2-TAT, Cy5-IgG-TAT and Cy5-COX-2 in OE33 Xenografts.....199

**List of Tables**

**Table 1** Summary of the Biomarkers with a Prognostic Potential in OAC. .....35
**Table 2** Recommendation Statements for Diagnosis of Barrett's Oesophagus. .....44
**Table 3** Recommendation Statements for Surveillance and Management of Barrett's Oesophagus.....45
**Table 4** Cytological and Architectural Features of NDS, IDS, LGD and HGD in Barrett's Oesophagus. .....46
**Table 5** TNM and Histologic Grade Definitions for OAC. .....50
**Table 6** OAC Stage Groupings Based on the TNM Status. .....50
**Table 7** Antibody Dilutions Used for COX-2 and c-Met Western Blotting. .....74
**Table 8** Anti-COX-2 [AS66], Anti-c-Met (Met13) and Anti-c-Met [EP1454Y] Product Information. .....75
**Table 9** Representative Molecular Imaging Agents Developed for c-Met Imaging in Cancer. .....94

**List of Abbreviations**

AGA – American Gastroenterology Association
AGC – American College of Gastroenterologists
AJCC – American Joint Committee on Cancer
BALB – Bagg Albino
BCA – Bicinchoninic Acid
bFGF – Basic Fibroblast Growth Factor
BO – Barrett's Oesophagus
BSA – Body Surface Area
BSG – British Society of Gastroenterology
BSGI – Breast-Specific Gamma Imaging
cAMP – Cyclic Adenosine Monophosphate
CDK – Cyclin-Dependent Kinase
CDKN2A – Cyclin Dependent Kinase Inhibitor 2A
COX-2 – Cyclooxygenase-2
CPM – Counts per Minute
CPP – Cell-Penetrating Peptide
CRK – V-crk Sarcoma Virus CT10 Oncogene Homolog
CRKL – CRK-Like
Cy5 – Cyanine 5
DMEM – Dulbecco's Modified Eagle Medium
DMSO – Dimethyl Sulfoxide
ECL – Enhanced Luminescence
EDC – 1-Ethyl-3-(3-dimethylaminopropyl)carbodiimide
EDTA – Ethylenediaminetetraacetic Acid
EGF – Epidermal Growth Factor
EGFR – Epidermal Growth Factor Receptor
ELISA – Enzyme-Linked Immunosorbent Assay
EMR – Endoscopic Mucosal Resection
ER – Endoplasmic Reticulum
ERK – Extracellular Signal-Related Kinase
EU – European Union
FBS – Foetal Bovine Serum

FI – Fluorescence Intensity

FIGS – Fluorescence Image-Guided Surgery

FITC – Fluorescein Isothiocyanate

GAB1 – GRB2-Associated Binding Protein 1

GOJ – Gastroesophageal Junction

GORD – Gastro-Oesophageal Reflux Disease

GRB2 – Growth Factor Receptor-Bound Protein 2

HED – Human Equivalent Dose

HER2 – Human Epidermal Growth Factor Receptor 2

HGD – High-Grade Dysplasia

HGF – Hepatocyte Growth Factor

IHC – Immunohistochemistry

IM – Intestinal Metaplasia

Iv – Intravenously

LGD – Low-Grade Dysplasia

LOH – Loss of Heterozygosity

LOS – Lower Oesophageal Sphincter

mAbs – Monoclonal Antibodies

MAPK – p38 Mitogen-Activated Protein Kinase

MCM-2 – Minichromosome Maintenance Complex Component 2

MEK – MAPK Effector Kinase

MES – 2-(N-morpholino)ethanesulfonic Acid

MMP-2 – Matrix Metalloproteinase-2

MRI – Magnetic Resonance Imaging

Ms – Mouse

NBI – Narrow Band Imaging

ND – Non-Dysplasia

NDBO – Non-Dysplastic BO

NDS – Negative for Dysplasia

NIR – Near Infra-Red

NK – Natural Killer

NLS – Nuclear Localisation Signal

NOD – Non-Obese Diabetic

NSAIDs – Nonsteroidal Anti-Inflammatory Drugs

NT – Non-Transfected

OAC – Oesophageal Adenocarcinoma

OSCC – Oesophageal Squamous Cell Carcinoma

PBS – Phosphate Buffer Saline

PD – Pharmacodynamics

PET – Positron Emission Tomography

PGE2 – Prostaglandin E2

PGs – Prostoglandins

PI3K – Phosphatidylinositol 3-Kinase

PK – Pharmacokinetics

PKC – Protein Kinase C

PLCγ – Phospholipase Cγ

PPIs – Proton Pump Inhibitors

PTD – Protein Transduction Domain

PTGS – Prostaglandin-Endoperoxide Synthase

PVDF – Polyvinylidene Difluoride

RAS – Rat Sarcoma Viral Oncogene Homolog

Rb – Rabbit

RB – Retinoblastoma

RCF – Relative Centrifugal Force

ROS – Reactive Oxygen Species

RPMI – Roswell Park Memorial Institute

RT – Room Temperature

RTK – Receptor Tyrosine Kinase

scFv – Single Chain Variable Fragment

SCID – Severe Combined Immunodeficiency

SDS – Sodium Dodecyl Sulfate

SHC – Scr Homology 2 Domain-Containing

SHC – Src Homology 2 Domain-Containing

SHIP-2 – Src Homology 2 Domain-Containing 5' Inositol Phosphatase

siRNA – Small-Interfering RNA

SMAD4 – SMAD Family Member 4

SNVs – Single Nucleotide Variations

SOS – Son of Sevenless

SPECT – Single-Photon Emission Computer Tomography

STAT3 – Signal Transducer and Activator of Transcription

TAT – Transcriptional Trans-Activator

TBR – Tumour to Background Ratio

TLOSR – Transient Lower Oesophageal Sphincter Relaxation

TNM – Tumour, Node, Metastasis

Tris-HCl – 2-Amino-2-(hydroxymethyl)-1,3-propanedio Hydrochloride

uPA – Urokinase-Type Plasminogen Activator

US – United States

UV – Ultraviolet

VEGF – Vascular Endothelial Growth Factor

WB – Western blot

WGS – Whole-Genome Sequencing

WHR – Waist–Hip Ratio

WL – White Light

# Chapter 1 Introduction

## 1.1 Cancer – Overview

The incidence of cancer and its associated mortality are growing rapidly worldwide. The underlying reasons are complex, but include an ageing population as well as changes in the prevalence and distribution of the main risk factors for cancer, several of which are associated with socioeconomic development (WHO, 2018). In 2018, it is estimated that there was 18.1 million new cancer cases and 9.6 million cancer deaths, highlighting the demand for novel and efficacious therapeutic and diagnostic strategies (Bray et al., 2018).

Cancer, representing a heterogeneous array of diseases, was eloquently defined using a series of hallmark characteristics (Hanahan and Weinberg, 2000; 2011). These essential characteristics – including management of genome-integrity, sufficiency in proliferative and resistance to anti-proliferative signalling, altered metabolism, induction of angiogenesis, invasion and metastasis, and acquisition of the capacity for unlimited replication – underpin the development of novel therapeutic interventions, as disruption of such characteristics is expected to reduce cancer progression. Moreover, characterisation of these changes at a cellular and molecular level has led to the development of new diagnostic and prognostic tools.

For patients with cancer, the available therapy can be broadly divided into four strategies: surgical resection, radiotherapy, chemotherapy, and biological therapies such as immunotherapy and small molecules (Farkona et al., 2016). Indeed, a combination of these modalities is often associated with improved outcomes and so forms the basis of most treatment guidelines currently in clinical use (Sharma et al., 2016). However, there is a growing focus on the early detection of cancer, as delayed diagnosis is a major

contributor to poor survival, lower rate of response to treatment and higher cost of care, resulting in avoidable deaths and disability from cancer (Car et al., 2016). Early diagnosis improves cancer outcomes by delivering care at the earliest possible stage and is consequently an imperative public health strategy in all settings.

### 1.2 Anatomy and Physiology of the Oesophagus

The oesophagus is defined as a muscular tube, measuring on average 18 – 25 cm in length (Long and Orlando, 2002), commencing as a continuation of the pharynx and leading to the stomach. Histologically, the body of the oesophagus is made up of four layers: adventitia, muscle, submucosa and mucosa. The oesophagus serves primarily as a passage for swallowed food and fluid, but its role extends to preventing the reflux of gastric contents whilst allowing regurgitation, eructation and vomiting to occur (Willner et al., 1956). To aid these functions, the oesophageal tube is protected at its proximal and distal ends by the upper and lower oesophageal sphincters (Gavaghan, 1999). Any deficiency in oesophageal function can lead to debilitating symptoms, including dysphagia, gastro-oesophageal reflux disease (GORD) and pain. There is evidence that transient relaxation of the lower oesophageal sphincter (LOS) is responsible for most episodes of the reflux of gastric contents, both in normal controls and patients with GORD (Holloway et al., 1985). The reflux of a small amount of gastric fluid and air into the oesophagus, specifically after meals, is considered an ordinary physiological event and is regulated by a number of factors, including the anti-reflux barrier at the gastro-oesophageal junction (GOJ), and the response of the oesophageal body to clear the refluxate. A failure of these mechanisms results in the clinical spectrum of GORD, and

an association between gastro-oesophageal reflux disease and oesophageal cancer is well established (Shaheen and Ransohoff, 2002).

The simple structure of the oesophagus understates both its physiological importance and the potential complications associated with surgical intervention. The oesophagus is located deep within the thoracic and abdominal cavities, and is in anatomical proximity to vital structures such as the heart and the great vessels (Figure 1.1). The oesophagus receives a segmental blood supply, with extensive collaterals along its course (Yazaki and Sifrim, 2012). Taken together, these factors provide a significant challenge to successful surgical resection and reconstruction of the oesophagus, a procedure with high complication rate and ninety-day overall mortality of 8.9% (In et al., 2016).

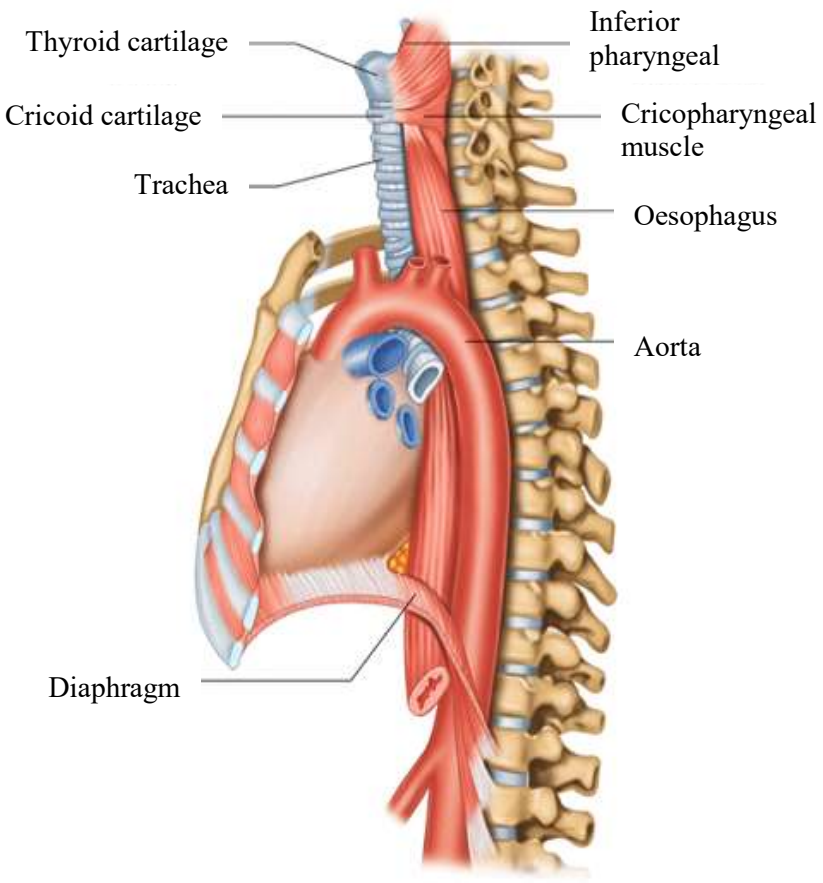



**Figure 1.1 Oesophagus.** The oesophagus is located deep within the thoracic and abdominal cavities, and is in anatomical proximity to vital structures such as the heart and the great vessels. Adapted from Di Leo et al., 2017.

The oesophagus is divided into cervical, thoracic and abdominal segments, each lying within a separate cavity, and while it is considered essentially a midline structure, it deviates to the left in the neck, to the right in the posterior mediastinum (the central compartment of the thorax which contains the heart, great vessels and other vital structures), before finally running leftward and anteriorly towards the diaphragmatic hiatus, through which it runs into the abdominal cavity (Chaudhry and Bordoni, 2019).

### 1.3 Oesophageal Cancer

Oesophageal cancer is a condition whereby neoplastic cells arise from the inner lining of the oesophagus. Its incidence is rising worldwide, and this condition exhibits a particularly poor prognosis and high mortality rate. The most recent compiled statistics show that oesophageal cancer accounts for more than 8,000 annual deaths in the UK and over 400,000 deaths globally, making it the sixth most common cause of cancer-related death worldwide and thus a major global health challenge (Wong et al., 2018). While many cancers, such as breast cancer, have decreased in incidence in recent times (DeSantis et al., 2014), the prevalence of oesophageal cancer is continuously rising (Lambert and Hainaut, 2007). Moreover, despite many advances in treatment and diagnosis, the 5-year survival rate ranges from 12–20% (Rasouli et al., 2011).

#### 1.3.1 Symptoms

Affected individuals may experience difficulty and pain when swallowing, initially for solid foods and then for fluids as the tumour expands into an obstructive mass within the

oesophagus. Other signs and symptoms include progressive weight loss, nausea, vomiting, loss of appetite, chest pain and hoarseness (Harris et al., 2017).

### 1.3.2 Epidemiology

There are two major subtypes of oesophageal cancer, oesophageal squamous cell carcinoma (OSCC) and oesophageal adenocarcinoma (OAC). Both their epidemiology and biological features are distinct. Invasive OSCC develops from intraepithelial neoplasia, such as dysplasia and carcinoma in situ, that reaches the lamina propria and extends beyond the submucosa (Wang et al., 2005). Adenocarcinoma of the oesophagus, which occurs in the distal oesophagus in approximately 75% of cases (Zhang, 2013), has a distinct link to gastro-oesophageal reflux, which if left untreated, can progress to Barrett's oesophagus (BO), a condition where the stratified squamous epithelium that normally lines the oesophagus is replaced by a columnar epithelium (Mansour et al., 2017, Napier et al., 2014).

OSCC accounts for 90% of cases of oesophageal cancer worldwide, and is most prevalent in East Asia, East Africa and South America (Abnet et al., 2018). OAC is the predominant type in developed countries. This represents a major epidemiological shift that has occurred over the last four decades. Historically, OSCC was the commonest form of oesophageal cancer in both developing and developed countries, accounting for almost 80% of cases in the United States, Australia and Western Europe in the 1980s (Xie and Lagergren, 2018). Today, however, OAC represents 90% of the cases in the West; in the United States alone OAC has increased from 4 cases per million in 1975 to 23 cases per million in 2001, making it the country's fastest growing cancer (Napier et al., 2014). The

decrease in OSCC incidence in developed countries is probably due to a reduction in alcohol and tobacco abuse, while the increase in OAC is linked to rising obesity and GORD (Jain and Dhingra, 2017).

### 1.3.3 Risk Factors

Whereas, squamous cell carcinoma more commonly arises in the upper and middle parts of the oesophagus and is particularly associated with smoking and chronic alcohol consumption (Zhang, 2013, Wheeler and Reed, 2012), adenocarcinoma often arises from the lower part of the oesophagus near its junction with the stomach (Harris et al., 2017). Important risk factors for OAC include male sex, Caucasian race (Wheeler and Reed, 2012), obesity, GORD and a condition known as Barrett's oesophagus (Domper Arnal et al., 2015), where chronic gastric reflux irritates the lower oesophagus and leads to normal cells acquiring cancerous potential (Farrow et al., 2000, Lagergren et al., 1999). The considerable differences in worldwide incidence of oesophageal cancer are thought to result from geographical differences in exposure to risk factors, as well as race (Napier et al., 2014).

## 1.4 Barrett's Oesophagus, and the Pathogenesis of Oesophageal Adenocarcinoma

### 1.4.1 Gastro-oesophageal Reflux Disease (GORD)

GORD is defined clinically by symptoms or pathologically by mucosal damage produced by the abnormal reflux of gastric contents into the oesophagus and beyond – e.g. the oral cavity including larynx, and lung (DeVault and Castell, 2005). Typical symptoms include

heartburn and acid regurgitation (Klauser et al., 1990). Uncommon symptoms can include epigastric pain, dyspepsia, nausea, bloating, and belching (Hom and Vaezi, 2013). GORD is one of the most commonly encountered conditions by both primary care physicians and gastroenterologists (Badillo and Francis, 2014, Dent et al., 2005). Previously regarded as a 'nuisance problem' and a cause of 'mild discomfort' (Shaheen and Ransohoff, 2002), GORD is now recognised to have potentially serious complications, including inflammatory strictures, erosive esophagitis (Dodds et al., 1982), and the development of Barrett's oesophagus (Wang, 2015, Thrift et al., 2013, Csendes et al., 2000). Barrett's oesophagus is an acquired oesophageal condition characterised by the presence of metaplastic columnar epithelium in the distal oesophagus, which replaces the normal stratified squamous mucosa (Nelsen et al., 2012). Its association with an increased risk of OAC has been extensively described in the literature (Reid et al., 2010, Wani et al., 2009, Drewitz et al., 1997, Cameron et al., 1985).

### 1.4.2 Barrett's Oesophagus

BO is characterised by metaplastic transformation of the squamous epithelium of the oesophagus to a columnar type often including non-native goblet cells (Sampliner et al., 2002). BO is the strongest risk factor for OAC, with its presence conferring a 30- to 50-fold increased risk of developing adenocarcinoma. (Sharma et al., 2004).

Progression of BO to invasive OAC is reflected histologically by the metaplasia-dysplasia-carcinoma sequence (Figure 1.2). The main predictor of malignant potential in BO has been the histological classification of dysplasia on endoscopic biopsy. The degree of dysplasia has been shown to correlate with the risk of developing cancer; high-grade

dysplasia (HGD) is associated with the greatest risk (Buttar et al., 2001). Indeed, data from surgical series show concurrent cancer in the resection specimen in up to 50% of patients undergoing resection of HGD (Yantiss, 2010, Falk et al., 1999, Heitmiller et al., 1996). The progression through grades of dysplasia is neither orderly nor inexorable. Patients may progress directly from nondysplastic BO to HGD or cancer without a detectable low-grade dysplasia (LGD) phase (Schnell et al., 2001). Alternatively, subjects with HGD may undergo apparent regression of the disease and spend months or even years with no detectable dysplasia (Shaheen, 2005). However, the data on disease progression may be compromised by the current diagnostic and surveillance routines (Visrodia et al., 2016, Shaheen, 2005). Subsequently, current gold standard diagnostic strategy of white light endoscopy with multiple biopsies (Sharma et al., 2016) could potentially achieve greater results if combined with detection of biomarkers of disease progression alongside the existing standard routine.

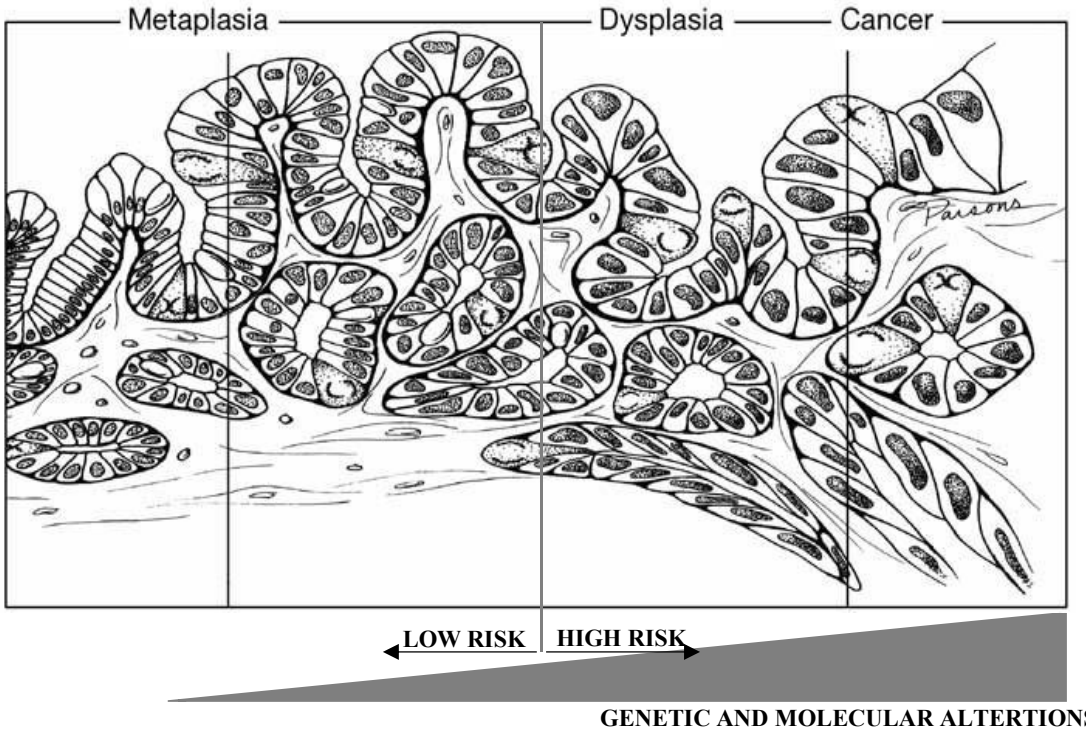



**Figure 1.2 Barrett's. Metaplasia – Dysplasia – Cancer Sequence.** A number of molecular changes have been reported in Barrett oesophagus, and these molecular alterations are implicated in the pathogenesis of OAC. Accumulation of these molecular alterations with the metaplasia–dysplasia–cancer sequence progression. Histologically, metaplasia and low-grade dysplasia are at low risk for malignant progression. However, accumulation of genetic and molecular alterations in higher grades confers an increased risk for progression to invasive oesophageal adenocarcinoma. Adapted from Williams et al., 2006.

## 1.5 Pathogenesis of Oesophageal Adenocarcinoma in Patients with Barrett's Oesophagus, Molecular Background, and Main Biomarkers of Progression

The pathogenesis of OAC in patients with BO is complex. Carcinogenesis of the oesophagus is a multistep process recognised phenotypically as the histological metaplasia-dysplasia-cancer sequence. In the past three decades, significant insight has been gained into the pathophysiology and molecular pathways associated with oesophageal carcinogenesis (Quante et al., 2018; Clemons et al., 2013; Vaezi and Richter, 1996).

### 1.5.1 DNA Content Abnormalities and Epigenetic Changes Biomarkers

To aid the understanding of progression from BO to OAC at the molecular level, it is helpful to study the genomic landscape of invasive OAC. The relationship between adenocarcinoma of the oesophagus and its precursor lesion, BO, is rather poorly understood (Reid et al., 2010). However, a recent study using whole-genome sequencing (WGS) on paired samples of BO and OAC demonstrated that OAC is one of the most highly mutated cancers, with a mutation burden of approx. 10 single nucleotide variations (SNVs) per mega base (Ross-Innes et al., 2015). The study further shows that BO itself is highly mutated even in the absence of dysplasia (Ross-Innes et al., 2015). The overall mutation rate in BO without dysplasia is around 5.4 – 6.8 SNVs per mega base, being higher than that reported for some invasive cancers – such as breast cancer and multiple myeloma (Stachler et al., 2015). The rate of mutation in OAC approaches that of cancers associated with well-defined carcinogens such as melanoma (ultraviolet, UV light, Koh et al., 1996) or lung cancer (tobacco smoke, Hecht, 1999). OAC is thought to be a very heterogenous disease (Katz-Summercorn et al., 2016) with a small number of genes that are found to be recurrently mutated across cases, and are considered driver mutations (Dulak et al., 2013). A longitudinal WGS study published in 2014 showed differences across 26 genes in patients whose BO remained stable and non-dysplastic versus those who progressed to HGD and OAC (Ross-Innes et al., 2015). A significant difference in gene mutation frequency was observed in tumour suppressor genes TP53 and SMAD Family Member 4 (SMAD4, Ross-Innes et al., 2015). Furthermore, TP53 was mutated in approx. 70% of progressive BO but in only 2% of non-dysplastic patients with stable disease (Underwood et al., 2015). SMAD4, although mutated at a lower rate (13%), was

found mainly in samples of invasive disease (Weaver et al., 2014). TP53 is a gene located at chromosome 17p13, and is considered the most important tumour suppressor in many types of cancer due to its widespread regulatory functions (Sigal and Rotter, 2000). These include arrest of cell cycle progression when the genome is damaged, permitting DNA repair, initiating apoptosis in cases of repair failure, and a key role in the cellular stress response (Joerger and Fersht, 2010). Its function in cancer is altered through TP53 somatic mutations (Oliver et al., 2010). Other studies have implicated loss of heterozygosity (LOH) as well as point mutations in Cyclin Dependent Kinase Inhibitor 2A (CDKN2A, p16) and TP53 as strongly predictive of neoplastic progression in BO (Maley et al., 2006).

CDKN2A, the second most frequently altered gene is located on chromosome 9p21. The CDKN2A gene encodes a number of proteins, including the tumour suppressors sp16(INK4A) and p14(ARF). These function as cell cycle regulatory proteins in the p53 and retinoblastoma (RB) pathways (Brown et al., 2004), involved in regulation of cell cycle progression (Shaw, 1996), cell division, senescence and apoptosis (Sherr and McCormick, 2002).

Epigenetic changes in the form of DNA hyper-, hypomethylation and alteration of histone complexes have also been implicated in the development of BO and OAC (Eads et al., 2000). Jin and colleagues reported a methylation biomarker-based panel, validating 8 methylation biomarkers, including p16, for their accuracy in predicting neoplastic progression in BO in a retrospective, multicentre study (Jin et al., 2009). These findings were corroborated by a similar study, which demonstrated that hypermethylation of p16 is a good predictor of progression to HGD or OAC (Wang et al., 2009). However, the

array of techniques that have been utilised for detection of epigenetic changes are far too technically demanding and time consuming for routine clinical use.

### 1.5.2 Proliferation Biomarkers

Dysplasia is often associated with abnormal cellular proliferation, and many reports show aberrant expression of markers of proliferation such as Minichromosome Maintenance Complex Component 2 (MCM-2, Sirieix et al., 2003) and Ki67 (Hong et al., 1995). MCM-2 in particular has been shown to be more sensitive and specific than other markers such as Ki67 in indicating oesophageal dysplasia (Huang et al., 2011). Expression of MCM-2 and Ki67, markers which can be easily used in immunohistochemistry (IHC) analyses, can be valuable adjuncts to the histopathological diagnosis of dysplasia and may have predictive value for cancer risk. Correlative histopathology of proliferative and cell cycle biomarkers, the latter described above, could potentially be utilised with multi-modality imaging.

### 1.5.3 Cell Cycle Biomarkers

Positive staining for Cyclins A and D can potentially serve as a useful biomarker in identifying BO patients at high risk of OAC (Ong et al., 2010). The cyclin D1 proto-oncogene is an important regulator of G1 to S phase progression in many different cell types (Alao, 2007), and Cyclin D1 positivity was previously demonstrated to confer a statistically significantly increased risk of progression of OAC in a case–control analysis of biopsy specimens in patients with BO (Bani-Hani et al., 2000). However, while promising, these findings were not replicated in a larger study (Murray et al., 2006).

Cyclin A is particularly interesting among the cyclin family because it can activate two different cyclin-dependent kinases (CDKs) and functions in both S phase and mitosis (Yam et al., 2002). Its expression has been reported to correlate with the degree of dysplasia and likelihood of progression to OAC in a cohort of patients with BO (Lao-Sirieix et al., 2007).

### 1.5.4 Prognostic Biomarkers in Oesophageal Adenocarcinoma

Prognostic biomarkers are useful to decide which patients can benefit from aggressive therapies, for whom the risk-benefit profile of aggressive treatment becomes more favourable (Shah et al., 2013). Moreover, it is expected that, in the near future, biomarkers can be used to identify intra-tumoural heterogeneity, leading to the use of a combination of targeted therapies to more efficiently inhibit tumour growth and overcome the intrinsic resistance that heterogeneity confers to nonselective therapy (Bianco et al., 2007). This in turn may lead to both abilities to predict the therapeutic response and determine the mechanism of patient's resistance to treatment, resulting in more personalised cancer therapy (Rybinski and Yun, 2016). Several prognostic biomarkers in OAC have been studied to determine the association between the change in their expression (as compared to healthy oesophageal mucosa) and the following outcomes: survival, invasion and metastasis, and response to treatment – currently including chemo – and/or radiation therapy (Ong et al., 2010).

Table 1 shows a summary of the biomarkers with a prognostic impact on OAC. These have been considered in terms of the hallmarks of cancer, comprising six biological characteristics acquired during the multistep development of neoplastic disease:

sustaining proliferative signalling, evading growth suppressors, resisting apoptosis, enabling replicative immortality, inducing angiogenesis, and activating tissue invasion and metastasis (Hanahan and Weinberg, 2011). It is well-known that many of these changes can occur early on during the progression of BO to OAC, potentially serving as predictors of neoplastic progression. However, as of today, most of the biomarkers which have successfully completed preclinical exploratory studies have stalled at the clinical assay development and validation stage (Shah et al., 2013). This stage aims to develop clinical assays and non-invasive *in vivo* diagnostic methods for the identification and monitoring of patients with asymptomatic BO/OAC. At the end of this phase, one should expect a test with high specificity and sensitivity, as well as feasibility for clinical use. To date, there have been few investigations into prognostic biomarkers in patients. One such study evaluated aberrant p53 expression as a predictor of progression to HGD, where the overexpression of p53 was shown to be associated with an increased risk of neoplastic progression in patients with BO, after adjusting for additional risk factors such as age, gender, the length of Barrett's mucosa and oesophagitis (Davelaar et al., 2015). However, these biomarkers are not employed in routine medical practice (Konda and Souza, 2018). Prognostic biomarkers may add some insight to the course of the disease and risk of developing OAC, however they are still subject to the limitations that accompany random-site biopsy sampling of BO. Thus, it is unsurprising that they are not routinely employed in clinical practice.

| Category of Cell Alteration | Biomarker | Study |
|---|---|---|
| **Sustaining Proliferative Signalling** | Cyclin D | (Schulmann et al., 2005) |
| | EGFR | (Cronin et al., 2011) |
| | Ki-67 | (Shi et al., 2008) |
| | HER2 | (Fritcher et al., 2008) |
| | TGF-α | (D'Errico et al., 2000) |
| | c-Met | (Herrera et al., 2005) |
| **Evading Growth Suppressors** | TGF-β1 | (von Rahden et al., 2006) |
| | APC | (Kawakami et al., 2000) |
| | P21 | (Nakashima et al., 2000) |
| **Resisting Apoptosis** | P53 | (Weston et al., 2001) |
| | Bcl-2 | (Hormi-Carver et al., 2009) |
| | COX-2 | (Buskens et al., 2002) |
| | NF-κB | (Abdel-Latif et al., 2004) |
| **Enabling Replicative Immortality** | Telomerase | (Gertler et al., 2008) |
| **Inducing Angiogenesis** | CD105 | (Saad et al., 2005) |
| | VEGF | (Saad et al., 2005) |
| **Activating Tissue Invasion and Metastasis** | Cadherin | (Falkenback et al., 2008) |
| | uPA | (Nekarda et al., 1998) |
| | TIMP | (Darnton et al., 2005) |
| | c-Met | (Watson et al., 2006) |

**Table 1 Summary of the Biomarkers with a Prognostic Potential in OAC.** Adapted from Ong et al, 2010.

### 1.6 Gastro-oesophageal Reflux Disease, Cyclooxygenase-2 (COX-2) and Inflammation

Pathological reflux of gastroduodenal[1] contents into the oesophagus can cause chronic mucosal injury resulting in inflammation (i.e. oesophagitis), which is known to promote carcinogenesis (Quante et al., 2018, Hashimoto, 2012). The mechanisms involved in the pathogenesis of GORD include motor abnormalities – such as impaired LOS resting tone, increased transient LOS relaxations (TLOSR), impaired oesophageal acid clearance and delayed gastric emptying (De Giorgi et al., 2006). Gastro-oesophageal reflux occurs

[1] Gastro-oesophageal refluxate contains a variety of noxious agents, including hydrochloric acid, pepsin, bile salts and pancreatic enzymes (Tack et al., 2005).

when LOS pressure is lower than intragastric pressure. In healthy individuals, a small amount of reflux occurs when LOS pressure is low, such as during swallowing and in normal TLOSRs, and when increases in intra-abdominal pressure or intragastric pressure overcome the resting LOS pressure (Mittal et al., 1996). The changes in LOS function that underpin abnormal gastro-oesophageal reflux are well described and in large part determine the patterns, timing, and degree of reflux (Hauser et al., 1979). Further, anatomical factors predispose to reflux, including hiatal hernia, as well as cellular abnormalities such as impaired mucosal resistance and visceral hypersensitivity (De Giorgi et al., 2006). In an experimental model of GORD, some of the mediators considered to be critical in the pathology of esophagitis were shown to be classic inflammatory products, such as prostanoids and reactive oxygen species (ROS) (Jimenez et al., 2005). Patients with complicated BO (dysplasia and cancer) reflux significantly more gastric acid and bile into their oesophagus than patients with nondysplastic BO and GORD patients without BO (Vaezi and Richter, 1996). The arachidonic acid pathway, which controls inflammation, can be activated by gastric acid or bile salts and may contribute to carcinogenesis in BO (Tatsugami et al., 2012). Low pH, as well as bile salts, have been shown to induce expression of Cyclooxygenase-2 (COX-2) – a key enzyme of the arachidonic acid pathway – in *ex vivo* culture models of human BO and OAC cell lines (Song et al., 2007, Abdalla et al., 2005). Prolonged injury related to acid and bile salts can also stimulate the production of ROS, known to promote many aspects of tumour development and progression (Liou and Storz, 2010). Despite these findings, at present, the clinical evidence for the exact role of acid and bile reflux in the progression of BO to neoplasia remains unclear (Quante et al., 2018, Souza, 2010).

### 1.6.1 COX Enzymes

COX enzymes are key mediators in the production of prostaglandins (PGs). Two isoforms of COX have been identified, COX-1 and COX-2 (Smith et al., 2000). COX-1 is expressed constitutively in most tissues, regulating important physiological processes including gastric cytoprotection – i.e. maintaining an effective mucus-bicarbonate barrier, submucosal blood flow, faster and more efficient mucosal adaptation to initial tissue damage, and subsequently quicker recovery when such damage ensues. It is also involved in maintenance of renal blood supply and platelet aggregation. These are considered important 'housekeeping' functions (DeWitt et al., 1993). In contrast, COX-2 mRNA and protein are almost undetectable in most tissues, but can be induced by a number of agents including cytokines (Laporte et al., 2000), growth factors (Fong et al., 2000), and tumour promoters (de Ledinghen et al., 2002).

COX-2 expression increases with neoplastic progression in BO (Lewis et al., 2011), supporting the association between the arachidonic acid pathway and OAC development (Shirvani et al., 2000). It has been reported that protein kinase C (PKC), extracellular signal-related kinase (ERK), and p38 mitogen-activated protein kinase (MAPK) mediate bile and acid-induced COX-2 expression (Hashimoto, 2014, Looby et al., 2009, Song et al., 2007). Analysis of the COX-2 gene, however, reveals several transcriptional regulatory sequences in the promoter including a site for CCAAT/enhancer-binding protein and cyclic adenosine monophosphate (cAMP) response element motifs, three SP1 sites, two NF-κB sites, two activator protein-2 sites, and an Ets-1 site (Appleby et al., 1994). This suggests that multiple signalling pathways participate in the induction of COX-2 expression. COX-2 and Prostaglandin E2 (PGE2) play an important role in all

stages of OAC tumorigenesis, from development to invasion and metastasis, through numerous mechanisms. COX-2 expression promotes cell proliferation by the activation of the epidermal growth factor receptor (EGFR, Pai et al., 2002), and a concurrent increase in the expression of COX-2 and EGFR during progression from BO to OAC has been reported previously (Li et al., 2006). Furthermore, COX-2 induces angiogenesis by promoting vascular endothelial growth factor (VEGF) and basic fibroblast growth factor (bFGF) expression (Tsujii et al., 1998), and facilitates metastatic potential by upregulation of urokinase-type plasminogen activator (uPA) and matrix metalloproteinase-2 (MMP-2, Li et al., 2002, Tsujii et al., 1997). Moreover, COX-2 inhibits apoptosis by upregulation of B-cell lymphoma 2 (bcl-2, Tsujii and DuBois, 1995), and suppresses the host immune response (Sharma et al., 2003). The latter includes PGE2-mediated suppression of tumour surveillance, achieved through inhibition of the functional maturation of natural killer (NK) cells and reduction of their cytotoxicity against target cells (Park et al., 2018, Holt et al., 2011). PGE2 has been reported to induce the proliferation of BO cells (Oyama et al., 2005), which provides an opportunity for these cells to accumulate replication errors. Chronic induction of PGE2 appears to facilitate the accumulation of abnormal cells with genomic instability (Oshima and Oshima, 2013), therefore promoting carcinogenesis.

### 1.7 c-Met and Oesophageal Cancer

c-Met is a transmembrane tyrosine kinase receptor (RTK) encoded by the MET proto-oncogene (p190MET), and is expressed in most epithelial and endothelial cells (Bottaro et al., 1991). c-Met is composed of α- and β-chains connected by a disulphide bond (Organ and Tsao, 2011). It is activated via auto-phosphorylation of its tyrosine kinase

domain upon the binding of its ligand, hepatocyte growth factor (HGF) (Hanna et al., 2009). HGF is mainly produced by mesenchymal cells, acting as a paracrine factor on epithelial tissues (Powell et al., 2011). c-Met receptor activation has mitogenic (Zarnegar and Michalopoulos, 1989), motogenic (Weidner et al., 1990), and angiogenic cellular effects (Gherardi and Stoker, 1991), and has been implicated in promoting tumour development, progression and metastasis. The overexpression of c-Met and/or its correlation with poor prognosis has been reported in various human malignancies, including oesophageal adenocarcinoma (Tuynman et al., 2008).

### 1.7.1 c-Met Signalling

Binding of HGF to c-MET results in the homodimerization of the receptor and phosphorylation of two tyrosine (Y) residues, Y1234 and Y1235, located within the catalytic loop of the tyrosine kinase domain (Rodrigues and Park, 1994). Subsequently, this leads to phosphorylation of Y1349 and Y1356 in the carboxy-terminal tail, causing the formation of a tandem SH2 recognition motif, known to be unique to c-Met (Ponzetto et al., 1994). SH2 recruits the adaptor proteins growth factor receptor-bound protein 2 (GRB2) (Fixman et al., 1996), src homology 2 domain-containing (SHC) (Pelicci et al., 1995), v-crk sarcoma virus CT10 oncogene homolog (CRK) (Garcia-Guzman et al., 1999) and CRK-like (CRKL) (Sakkab et al., 2000); the effector molecules phosphatidylinositol 3-kinase (PI3K), phospholipase Cγ (PLCγ) and SRC (Ponzetto et al., 1994), the src homology 2 domain-containing 5' inositol phosphatase (SHIP-2), and the signal transducer and activator of transcription STAT3 (Hecht et al., 2004). Furthermore, c-Met exclusively associates with the multi-adaptor protein GRB2-associated binding protein 1 (GAB1) which, upon phosphorylation by c-Met, creates

binding sites for more downstream adaptors. GAB1 can bind c-Met directly, or indirectly through GRB2. The downstream response to c-Met activation relies on conventional signalling pathways shared by many RTKs. These include the MAPK cascade and the PI3K/AKT signalling pathway (Chaudhuri et al., 2011). Activation of c-Met stimulates the activation of the rat sarcoma viral oncogene homolog (RAS) via the guanine nucleotide exchanger son of sevenless (SOS) bound by SHC and GRB2. This leads to the indirect activation of v-raf murine sarcoma viral oncogene homolog B1 (Nguyen et al., 2014) kinases, which subsequently activate MAPK effector kinase (MEK), and finally MAPK. This allows nuclear translocation of the latter, activating transcription factors responsible for regulating a large number of genes, including those involved in cell proliferation, cell motility and cell cycle progression, as shown in Figure 1.3 (Organ and Tsao, 2011, Maroun et al., 2003, Schaeper et al., 2000). The AKT/protein kinase B axis is chiefly responsible for the cell survival response to c-Met signalling (Xiao et al., 2001). It has been shown that c-Met is not expressed in regular squamous oesophagus or nondysplastic BO, but is frequently overexpressed in OAC (Herrera et al., 2005), where HGF/c-Met-dependent signalling differentially stimulates proliferation, survival, motility and invasion through ERK and AKT signalling (Watson et al., 2006).

The complex signalling network of HGF/c-Met plays a pivotal role in the normal development but also progression of cancer, controlling biological functions such as survival, proliferation, motility and invasion, which are associated with tumour growth and metastatic progression. Consequently, c-Met is a candidate for therapeutic intervention, and exhibits potential as a diagnostic biomarker. Furthermore, its expression on the cell membrane makes extracellular epitopes accessible for targeting with imaging agents (Han et al., 2017). Increased c-Met expression, as indicated by

intense semiquantitative IHC staining, has been reported in surgical specimens of OAC with a median IHC score of 2.49 as well as BO, in contrast to a minimal staining observed in healthy tissue (Herrera et al., 2005). Furthermore, Mesteri and colleagues reported overexpression of c-Met in 34.4% of OAC, and demonstrated a correlation between increased c-Met expression and shorter disease free, disease specific and overall survival of OAC patients (Mesteri et al., 2014). Moreover, a high number of activated c-Met has been observed in primary OAC and lymph node metastatic cells, whereas lower numbers were seen in metaplastic and dysplastic BO samples (Miller et al., 2006). Finally, gene amplification of the MET oncogene has been reported in 2%–10% of oesophageal adenocarcinoma tumours (Jardim et al., 2014, Forde and Kelly, 2013).

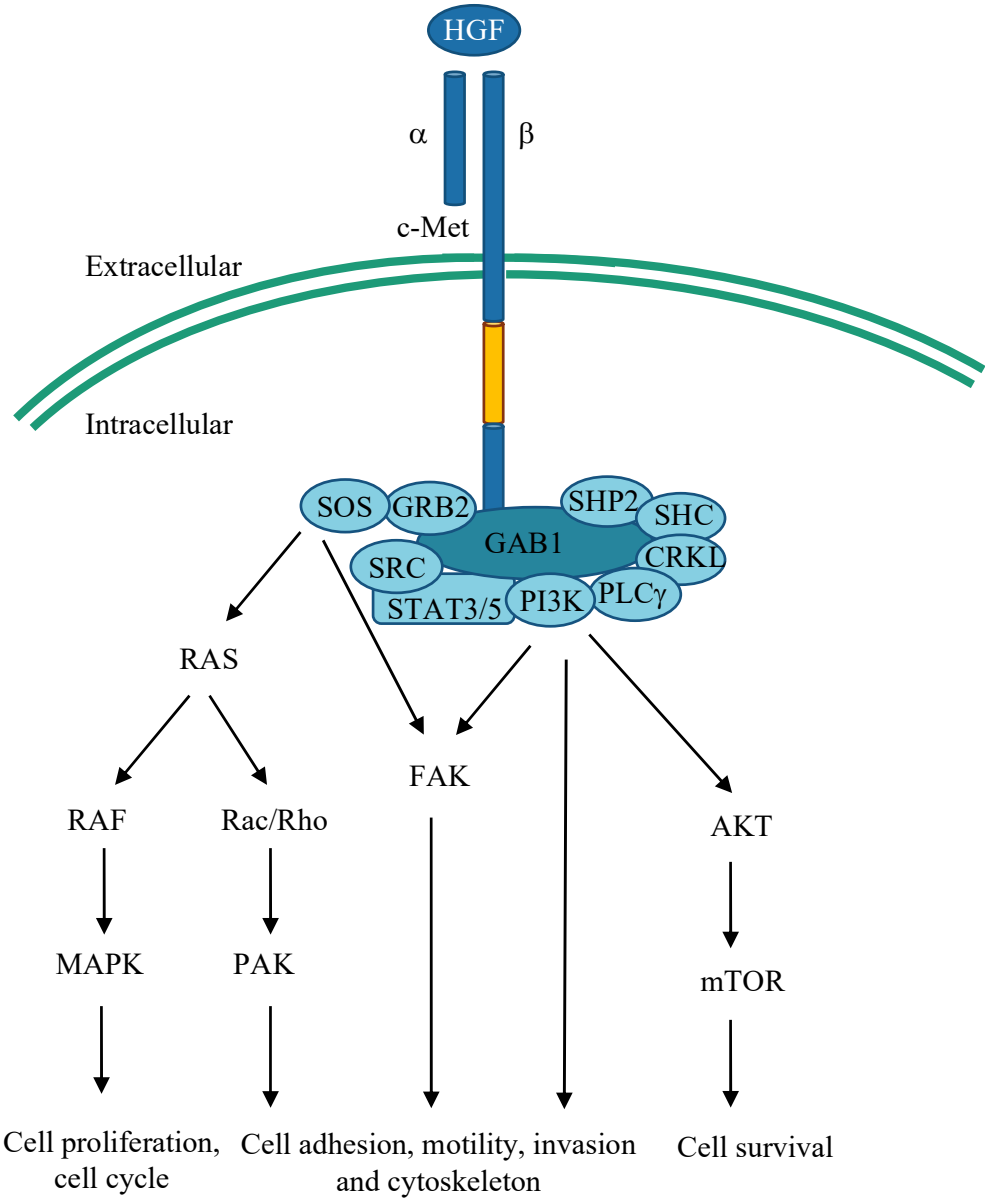



**Figure 1.3 c-Met Signalling.** Binding of HGF to c-Met results in the homodimerization of the receptor and phosphorylation of two tyrosine residues, located within the catalytic loop of the tyrosine kinase domain. Subsequently, this leads to phosphorylation of tyrosines in the carboxy-terminal tail, causing the formation of a tandem SH2 recognition motif. SH2 recruits the adaptor proteins growth factor receptor-bound protein 2 (GRB2), src homology 2 domain-containing (SHC), v-crk sarcoma virus CT10 oncogene homolog (CRK) and CRK-like (CRKL); the effector molecules phosphatidylinositol 3-kinase (PI3K), phospholipase Cγ (PLCγ) and SRC, the src homology 2 domain-containing 5' inositol phosphatase (SHIP-2), and the signal transducer and activator of transcription STAT3. Furthermore, c-Met exclusively associates with the multi-adaptor protein GRB2-associated binding protein 1 (GAB1) which, upon phosphorylation by c-Met, creates binding sites for more downstream adaptors. As a result, activated c-Met regulates a variety of cellular processes, including cell proliferation, survival, motility, invasion, adhesion and cytoskeletal changes. Adapted from Trusolino et al., 2010.

## 1.8 Current Surveillance, Diagnosis and Management of Barrett's Oesophagus

Diagnosis of BO involves both endoscopic examination and histopathological evaluation (Fitzgerald et al., 2014). Regardless of cancer risk, there is a requirement for endoscopic identification of columnar mucosa in the oesophagus for a diagnosis of BO. The main differences in criteria worldwide concern the requirement for histological confirmation of goblet cells in oesophageal biopsies (Naini et al., 2016). In Europe, the presence of non-goblet foveolar (mucus producing) epithelium in biopsies is sufficient to diagnose BO (Naini et al., 2016). However, US medical societies require intestinal metaplasia (IM) with goblet cells for diagnosis. The latter is associated with a higher risk of malignant transformation; therefore, such patients undergo a more intensive surveillance regime (Bansal et al., 2015). The most widely adopted guidelines for the diagnosis and management of BO are published by the British Society of Gastroenterology (BSG, Fitzgerald et al., 2014, Tham, 2015) and by the American Gastroenterology Association (AGA)/American College of Gastroenterologists (AGC, Shaheen et al., 2016). As per the most recent BSG guidelines, BO is diagnosed by the presence of ≥1 cm extension of salmon-coloured mucosa proximal to the gastroesophageal junction on endoscopic examination, and confirmed histopathologically from oesophageal biopsies (Fitzgerald et al., 2014). The key recommendation statements for diagnosis of BO are summarised in Table 2.

As per current BSG guidelines, screening with endoscopy is not feasible or justified for an unselected population with gastro-oesophageal reflux symptoms. However, the BSG recommends that screening for BO may be considered in patients with frequent (weekly

or more) symptoms of GORD and at least three risk factors for BO or OAC: age (50+ years), male sex, Caucasian ethnicity and existence of central obesity (Fitzgerald et al., 2014). Confirmed family history of BO or OAC in a first-degree relative lowers the threshold for multiple rish factors (Fitzgerald et al., 2014).

| | |
|---|---|
| **1.** | Barrett's oesophagus is defined as an oesophagus in which any portion of the normal distal squamous epithelial lining has been replaced by metaplastic columnar epithelium, which is clearly visible endoscopically (≥1 cm) above the GOJ and confirmed histopathologically from oesophageal biopsies |
| **2.** | The proximal limit of the longitudinal gastric folds with minimal air insufflation is the easiest landmark to delineate the GOJ and is the suggested minimum requirement. |
| **3.** | Endoscopic reporting should be performed using a minimum dataset including a record of the length using the Prague criteria (circumferential extent (C), maximum extent (M) of endoscopically visible columnar-lined oesophagus in centimetres and any separate islands above the main columnar-lined segment noted). |
| **4.** | In order to improve the standard of care and to ease discussion between experts, the use of a minimum dataset is recommended to report histopathological findings. |

**Table 2 Recommendation Statements for Diagnosis of Barrett's Oesophagus.** Adapted from Fitzgerald et al., 2014.

Surveillance for patients with BO currently involves repeated endoscopic evaluation using high-definition white light endoscopy. Endoscopic surveillance in patients without dysplasia should include four-quadrant biopsies at 2 cm intervals. For Barrett's patients with dysplasia of any grade, biopsied tissue must be reviewed by two pathologists, including one specialized in GI pathology, due to interobserver variability in the interpretation of dysplasia (Lunedei et al., 2002). Key recommendations for surveillance and management of BO are listed in Table 3. Routine use of advanced imaging techniques such as electronic chromoendoscopy, and use of additional biomarkers for risk stratification of patients with BO is currently not recommended (Fitzgerald et al., 2014, Falk, 2016, Shaheen et al., 2016). Despite their potential to provide more focused

intervention, use of biomarkers have to overcome the issue of the heterogeneity of biomarkers in the genetic patient profiles of those progressing to cancer (Riley et al., 2018).

| | |
|---|---|
| **1.** | For HGD and Barrett's-related adenocarcinoma confined to the mucosa, endoscopic therapy is preferred over oesophagectomy or endoscopic surveillance. |
| **2.** | For BE patients without dysplasia, endoscopic surveillance should take place at intervals of 2 to 5 years, depending on the length of the BO segment. |
| **3.** | For a given patient, whether or not surveillance is indicated should be determined on the basis of an estimate of the likelihood of cancer progression and patient fitness for repeat endoscopies, as well as patient preference |
| **4.** | Patients with a diagnosis of indefinite for dysplasia should be managed with optimisation of antireflux medication and repeat endoscopy in 6 months. If no definite dysplasia is found on subsequent biopsies, then the surveillance strategy should follow the recommendation for non-dysplastic Barrett's oesophagus |
| **5.** | Patients with LGD should have a repeat endoscopy in 6 months' time. If LGD is found in any of the follow up OGDs and is confirmed by an expert GI pathologist, the patient should be offered endoscopic ablation therapy after review by the specialist multidisciplinary team. |

**Table 3 Recommendation Statements for Surveillance and Management of Barrett's Oesophagus.** *Endoscopic therapies include injection, ablation, and mechanical therapy. Adapted from Fitzgerald et al., 2014 and Tham, 2015.

### 1.8.1 Diagnosis of Oesophageal Adenocarcinoma

Progression of BO to invasive OAC is reflected histologically by the metaplasia-dysplasia-carcinoma sequence, as introduced in § 1.4.2. Dysplasia is defined as abnormal epithelium with cytological and architectural atypia confined to the epithelium (Jain and Dhingra, 2017a). Cytological atypia is defined by the presence of nuclei that are large, irregularly shaped and hyperchromic, at times showing binucleation and presenting with absence of a perinuclear halo. Cytological atypia can be found in squamous and metaplastic cells (Fadare and Rodriguez, 2009). In BO, dysplasia is typically classified into one of 4 categories: negative for dysplasia (NDS), indefinite for dysplasia (Jalalabadi

et al., 2018), LGD and HGD (Odze, 2006). Their cytological and architectural features are outlined in Table 4.

| | **Mucosa** | **Cytologic Atypia** | **Architecture** | **Inflammation** |
|---|---|---|---|---|
| *NDS* | Shows preserved surface maturation characterised by darkly staining nuclei with stratification at the base of glands as compared to the surface where nuclei are paler, maintain polarity and lack stratification. | Limited to the basal portion of glands. | The glands are round and surrounded by abundant lamina propria. | If present, may show reactive nuclear changes. |
| *IDS* | Shows changes in deeper glands suggestive/consistent with dysplasia; however, the surface maturation is preserved. | Includes nuclear hyperchromasia, nuclear membrane irregularities and increased mitosis. | Occasionally, crypt budding / branching may be present. Crowded and irregularly shaped crypts may be present. | If present may exaggerate cytologic atypia. |
| *LGD* | Shows loss of surface maturation and architectural distortion with glandular crowding, in absence of active inflammation; there is a sharp contrast between neoplastic and non-neoplastic mucosa. | Nuclei in the surface mucosa show hyperchromasia, nuclear enlargement, stratification and mucin loss. Mitotic figures can be seen on the surface. | Crypt budding / branching may be present. Crowded and irregularly shaped crypts may be present. | Inflammation is less in comparison to the architectural and cytologic atypia. |
| *HGD* | Loss of surface maturation (as in LGD) and glandular crowding. | The nuclei show loss of polarity and are rounded, enlarged, hyperchromatic with inconspicuous nucleoli. Mitoses are frequent. | Crypt budding / branching is present. Crowded and irregularly shaped crypts are present. | Inflammation is less in comparison to the architectural and cytologic atypia. |

**Table 4 Cytological and Architectural Features of NDS, IDS, LGD and HGD in Barrett's Oesophagus.** Adapted from Odze, 2006.

There exist rarer variants of dysplasia, such as deep crypt dysplasia (cytological features of LGD or HGD limited to the deep glands) and foveolar type dysplasia (foveolar glands show mild architectural changes and architectural crowding, the nuclei are round to oval and show prominent nucleoli with typical and atypical mitoses present).

In some instances, the presence of ulceration, active inflammation and/or prominent nucleoli are indicative of reactive and reparative changes due to a benign process such as inflammation. However, these features may also be indicative of the presence of an associated invasive carcinoma. Additional features suggestive of invasive adenocarcinoma on biopsy include cribriform glandular architecture, luminal necrotic debris, ulceration, neutrophils within dysplastic glands and pagetoid spread of neoplastic cells in the overlying squamous mucosa (Jain and Dhingra, 2017).

### 1.8.2 Limitations of Current Screening

Most patients with OAC are diagnosed at an initial endoscopy; in other words, the prevalence (the proportion of cases in a population in a given time period, Noordzij et al., 2010) of OAC is far greater than the incidence (the number of new cases of disease, Noordzij et al., 2010) (Reid et al., 2010). Dulai and colleagues reported, using a random effects model, that the overall percentage of patients with OAC undergoing resection who had a prior diagnosis of BO was only 4.7% ± 2.9% (Dulai et al., 2002). This study provides indirect evidence to suggest that current efforts to identify patients with Barrett's have a had minimal public health impact on the outcomes of OAC. The potential benefits of endoscopic screening seem to only apply to a limited number of the individuals at risk. These data therefore offer a strong and compelling justification for the development of

more effective screening protocols to identify patients with BO. Furthermore, dysplasia and OAC have been reported to be commonly missed at the initial BO diagnosis, particularly in patients with long segment BO and who did not use proton pump inhibitors (PPIs, Lim and Fitzgerald, 2013). PPIs are useful for managing GORD symptoms, are known to reduce oesophageal inflammation thus allowing for more accurate assessment for dysplasia (Lim and Fitzgerald, 2013).

### 1.8.3 Limitations of Current Surveillance

A population-based study by Visrodia et al., evaluating the yield of repeat endoscopy in patients with initial non-dysplastic BO (NDBO), indeterminate dysplasia, and LGD, reported that the miss rates for HGD/OAC (1.9%) and LGD (8.8%) are significant (Visrodia et al., 2016). About 1 in 10 (9.5%) patients with newly diagnosed BO concurrently have a higher grade, undetected dysplasia or OAC (Visrodia et al., 2016). In a follow-up systematic review and meta-analysis of 24 cohort studies in adults with BO (baseline NDBO ± BO + LGD) monitored for at least 3 years after negative index endoscopy (in which BO was diagnosed), it has been further reported that surveillance in patients with BO has not yielded a consistent population-level reduction in the incidence of OAC, with about 25% of OACs classified as missed on diagnosis, that is, diagnosed within 1 year of negative endoscopy (van Putten et al., 2018, Visrodia et al., 2016). Efforts should be made to improve the sensitivity of detection of dysplasia and neoplasia around the time of initial BO diagnosis. Currently white light endoscopy and biopsy is the core diagnostic tool. Yet this approach is ineffective and limited by concerns related to biopsy sampling errors and cost (Sharma et al., 2016). Therefore, in order to overcome these issues, there is a need for an advancement in diagnostic accuracy and

sensitivity, which should address these concerns and ideally enhance risk stratification in order to provide timely management in real time.

### 1.9 Oesophageal cancer: T, N, M staging system

Cancer staging is recognised as crucial in both patient care and cancer research, providing information to determine a patient's prognosis (Sobin, 2009). Consequently, an understanding of its underlying principles is essential for both clinicians and researchers. The Tumour, Node, Metastasis (TNM) classification is the most commonly used staging system worldwide. The T category describes the extent of the primary tumour, which can include size, depth of invasion or invasion of neighbouring structures. The N category specifies the presence and/or extent of metastasis in regional lymph nodes and the M category identifies the absence or presence of distant metastasis (Sellers, 1971). In most cancers, TNM stage and histological grade are combined to give an overall stage at diagnosis, used to determine prognosis and the treatment offered. Table 5 shows TNM and histologic grade definitions for oesophagus and esophagogastric junction cancer, from the 7th edition of the American Joint Committee on Cancer (AJCC) Cancer Staging Manual (Rice et al., 2017, Berry, 2014). Table 6 shows AJCC 7h edition stage groupings based on the TNM status (Rice et al., 2017, Berry, 2014).

**T status**

| | |
|---|---|
| $T_{is}$ | High-grade dysplasia |
| T1 | Invasion into the lamina propria, muscularis mucosae, or submucosa |
| T2 | Invasion into muscularis propria |
| T3 | Invasion into adventitia |
| T4a | Invades resectable adjacent structures (pleura, pericardium, diaphragm) |
| T4b | Invades unresectable adjacent structures (aorta, vertebral body, trachea) |

**N status**

| | |
|---|---|
| N0 | No regional lymph node metastases |
| N1 | 1 to 2 positive regional lymph nodes |
| N2 | 3 to 6 positive regional lymph nodes |
| N3 | 7 or more positive regional lymph nodes |

**M status**

| | |
|---|---|
| M0 | No distant metastases |
| M1 | Distant metastases |

**Histologic grade**

| | |
|---|---|
| G1 | Well differentiated |
| G2 | Moderately differentiated |
| G3 | Poorly differentiated |
| G4 | Undifferentiated |

**Table 5 TNM and Histologic Grade Definitions for OAC.** Adapted from Rice et al., 2017.

| ***Stage*** | **T** | **N** | **M** | **Grade** |
|---|---|---|---|---|
| *0* | is | 0 | 0 | 1 |
| *IA* | 1 | 0 | 0 | 1-2 |
| *IB* | 1 | 0 | 0 | 3 |
| | 2 | 0 | 0 | 1-2 |
| *IIA* | 2 | 0 | 0 | 3 |
| *IIB* | 3 | 0 | 0 | Any |
| | 1-2 | 1 | 0 | Any |
| *IIIA* | 1-2 | 2 | 0 | Any |
| | 3 | 1 | 0 | Any |
| | 4a | 0 | 0 | Any |
| *IIIB* | 3 | 2 | 0 | Any |
| *IIIC* | 4a | 1-2 | 0 | Any |
| | 4b | Any | 0 | Any |
| | Any | 3 | 0 | Any |
| *IV* | Any | Any | 1 | Any |

**Table 6 OAC Stage Groupings Based on the TNM Status.** Adapted from Rice et al., 2017.

## 1.10 Current Treatment

The overall survival for OAC is poor: only 10%–22% of patients survive 5 years after diagnosis (Anderson et al., 2015, Lagergren and Mattson, 2012). The main reason behind poor outcomes is that the diagnosis is made at advanced, often metastatic, stages, with even superficial tumours having a significant susceptibility for metastases (Pennathur et al., 2009).

Despite increased time and resource commitments to improve outcomes and surveillance of patients with BO, there is still no observed reduction in the incidence of OAC at the population level (Visrodia et al., 2016). Indeed, many patients present with symptomatic OAC, at which time they almost always have advanced disease. The most frequently presenting symptom is progressive dysphagia, seen in 74% of patients (Daly et al., 2000). At present, only 20% of patients present with localised disease, allowing for treatment with curative intent, which includes combined modality chemoradiation followed by surgery (Hayeck et al., 2010).

The tumour stage and other tumour and patient characteristics are reviewed by a multidisciplinary team to determine prognosis and treatment (Markl and Martin, 2018). A critical metric is the depth of tumour invasion, which determines the likelihood of nodal metastases.

Multiple chemotherapy regimens have been described for OAC, OSCC, and gastric adenocarcinoma, and these are currently used interchangeably, with considerations for patient functional status, comorbidities, and drug side-effect profiles (Glasgow et al.,

2011). Currently, the majority of OAC patients are prescribed a combination of platinum, taxane, anthracycline, or pyrimidine analogue chemotherapeutics (Abdo et al., 2017). For localized OAC, the combination of cisplatin and 5-fluorouracil is the most studied and commonly used chemotherapeutic regimen, utilised in both neoadjuvant and definitive treatment (Qu et al., 2017). Cisplatin has also been studied and used in combination with taxanes (paclitaxel, docetaxel) and irinotecan. Second-line agents include mitomycin and gemcitabine (Ilson, 2008). As of yet, no combination of chemotherapeutic agents has been proven to be particularly effective in the OAC patient population (Sehdev and Catenacci, 2013).

Radiotherapy can be used either preoperatively or postoperatively and with either curative or palliative intent. Current guidelines recommend the combined use of radiation and chemotherapy as the preferred treatment, with radiotherapy as stand-alone treatment reserved for palliative care or when patients are unfit to receive concomitant chemotherapy (Neuner et al., 2009). For preoperative and definitive therapy (i.e. with curative intent), patients conventionally receive 45.0–50.4 Gy in 1.8–2.0 Gy/day fractions (Fokas and Rodel, 2015). Proton radiotherapy could potentially be used in the future as a superior method aiming at radiotherapy dose escalation while sparing normal tissues (Ask et al., 2005).

Surgery is the treatment of choice in early cancer (Tis-T1a N0) with multiple options available. Carcinoma in situ (Tis) or HGD is usually treated with endoscopic mucosal resection (Shah and Gerdes, 2015) and radiofrequency ablation of associated BO, followed by vigilant endoscopic surveillance. T1 N0 M0 patients must undergo endoscopic biopsy with EMR, if possible (Allum et al., 2014). T1a disease almost never

exhibits nodal involvement and studies have shown disease control with EMR in 93%–99% of cases (Ell et al., 2007, Pech et al., 2007). On the condition that the submucosa has not been breached, local recurrence can be managed by repeat EMR (Lee et al., 2016). Endoscopic submucosal dissection is a more recent development in the treatment of localised superficial OAC and precursor lesions, offering more extensive resection of larger lesions and definitive treatment of precursor lesions including BO metaplasia (Pimentel-Nunes and Dinis-Ribeiro, 2015).

Patients with T1b N1, or T2 or higher (regardless of regional node involvement) are most successfully treated with multimodality therapy (Mawhinney and Glasgow, 2012). Treatment depends on the surgical margins, nodal status, and histology. In patients with high-risk T2 N0 tumours (histopathological examination shows poor differentiation, lymphovascular or neurovascular invasion present, younger age), T3 N0 or any tumour with positive regional lymph node involvement (N1-3), postoperative chemotherapy is also indicated Kleinberg et al. (2003), (Lordick et al., 2016, di Pietro et al., 2018). However, approximately 50% of OAC patients present with incurable disease. This includes an unresectable primary tumour with invasion of the great vessels, heart, or trachea (T4b), distant nodal or metastatic disease or in a patient too frail to undergo surgical resection or intensive chemoradiation (Mawhinney and Glasgow, 2012).

Survival rates, even in candidates suitable for full multimodality treatment, are still poor, with only 37% of patients with localised disease surviving 5 years. With regional nodal involvement this drops to 19%, and to 3% or less if distant metastases are present. These give rise to the aforementioned figure of 20% overall 5-year survival (Mawhinney and Glasgow, 2012). Given the above, it is clear that detecting EAC as early as possible –

and ideally at a pre-cancerous stage – is of paramount importance to improving oncological outcomes.

### 1.11 Optical and Molecular Imaging

One of the main developments in cancer diagnostics has been in the area of molecular imaging. In oncology, molecular imaging can be defined as the *in vivo* characterisation of biomolecules and biological processes that are significant to the malignant state (Kircher et al., 2012). Today, the role of cancer imaging has expanded, moving beyond tumour detection and localisation to include measures of prognosis, prediction of therapeutic success, and early response to therapy (Mankoff et al., 2007).

Several techniques are widely used in cancer imaging, including positron emission tomography (PET), single-photon emission computer tomography (SPECT), magnetic resonance imaging (MRI), and optical modalities (Pysz et al., 2010). Modalities currently used in pre-clinical and clinical settings can be divided into two groups based on the information they provide, i.e. structural and functional. The first group typically includes X-ray computed tomography, MRI, and ultrasound (US, Histed et al., 2012)

The contrast generated in computed tomography utilises difference in X-ray attenuation of tissue, related its physical properties. Magnetic resonance imaging, on the other hand, utilises the properties of atoms when placed in a magnetic field (Plewes and Kucharczyk, 2012). Ultrasound imaging uses high frequency sound waves that are emitted, propagating in the body and reflecting at the interface between regions of different density thus creating contrast. These reflections are detected and mapped temporally and

spatially (O'Brien, 2007). The aforementioned techniques are used to obtain three-dimensional anatomical information and, in some instances, can be further used to obtain information about physiological activity within the imaged region, using techniques such as functional MRI or PET (Crosson et al., 2010). To gain functional information about the tissue of interest, PET relies on detection of two gamma rays, travelling in opposite directions from a position-electron collision. SPECT, on the other hand, detects single gamma rays from a radionuclide (Fahey et al., 2014). The main disadvantages of these modalities include the use of ionising radiation, slow image acquisition times, limited spatial resolution (5-10 nm) and high cost (Arms et al., 2018). Furthermore, PET and SPECT lack the ability to precisely define anatomical landmarks and require integration with either CT or MRI for anatomical correlation (Bererhi, 2008). Molecular imaging can also be achieved using these techniques with an appropriate contrast agent. However, important limitations are poor sensitivity (Seevinck et al., 2007) and large contrast agent dimension (e.g. bubbles in US) often necessitating high imaging agent concentrations (US and CT) which eventually limit clinical translation (Wilson et al., 2018). Furthermore, despite the ability to detect tumours deep within the body, the spatial resolution of most of the currently available imaging modalities is larger than 1 mm (Khalil et al., 2011). In theory, this problem can be resolved as the imaging resolution and contrast can principally be increased. However, in practice, to achieve this, patients risk being exposed to unacceptably high radiation doses, extreme contrast agent concentrations or be subjected to imaging for infeasibly long times. Consequently, these imaging modalities are most suitable to detect larger tumours, usually at a later stage, when survival rates drop dramatically (Hiom, 2015).

It has been reported that, using normal tissue vasculature, tumours cannot grow beyond 1 – 2 mm in size (Forster et al., 2017). Subsequently, to sustain its uncontrollable proliferation, a tumour has to undergo an 'angiogenic switch', where the cancerous mass develops its own vasculature (Fouad and Aanei, 2017). One of the objectives of early cancer detection is tumour identification before the 'switch' happens. This requires a highly sensitive imaging modality with sub-millimetre resolution and molecular probes to target at least one of the unique cancer biomarkers (Schiffman et al., 2015). Improvement of the clinical detection threshold remains of paramount importance. Current, well-established imaging techniques hypothetically allow for detection of a mass which is a few cubic millimetres in size. However, in practice, the threshold can be as large as 1 $cm^3$ for solid tumours (Frangioni, 2008). A typical cell in the human body is 10 μm in diameter, thus every 1 $cm^3$ of solid tumour tissue contains approximately $10^9$ or one billion cells. Hence from an imaging position, the term remission can be understood as presence of anywhere between zero and $10^9$ malignant cells (Frangioni, 2008). A significant improvement in cancer screening, staging, and treatment is unlikely to happen until the detection threshold improves by three to four orders of magnitude. Optical imaging has the potential to provide this level of sensitivity, provided that temporal resolution (which refers to the precision of a measurement with respect to time) is in the range of milliseconds to seconds (Dufort et al., 2010).

### 1.11.1 Optical Imaging

Medical *in vivo* optical imaging exploits contrast that interacts with visible (400 – 700 nm) and near-infrared (700 – 1000 nm) wavelengths of light in living tissues to provide molecular, morphologic, and functional information, probing the absorption, scattering,

and fluorescent properties of cells or tissues (Hillman et al., 2011). Examples include optical microscopy (Combs and Shroff, 2017), spectroscopy, endoscopy, and optical coherence tomography (Gora et al., 2017). Compared with other types of imaging modalities, e.g. CT and MRI, optical imaging has the main benefit of being able to use a wide palette of contrast, as well as using visible light and lower-energy infra-red photons rather than harmful ionising radiation used in many of the approaches previously described – in particular, the radiation doses reported in the CT studies fall in the range which, by direct epidemiological evidence, has been shown to associated with increased cancer risk (Smith-Bindman et al., 2009). The main limitation of optical imaging is its poor ability to penetrate tissue at depth, due to higher absorption and scattering of light in comparison to other techniques (Hillman et al., 2011). The absorption coefficient varies greatly over the visible spectrum, while the scattering coefficient of tissue decreases monotonically as the wavelength increases (Sandell and Zhu, 2011). The scattering seen in tissue is due to the presence of cells and is dependent on the cell morphology (Mourant et al., 1998). The most critical parameters affecting penetration depth in soft tissue are water and haemoglobin absorptions (Zhang et al., 2016). This is particularly relevant when considering clinical translation, as the light mean free path (defined as the average distance travelled by a moving photon between successive collisions, which in turn modify its direction, energy and other properties) is much smaller than dimensions of the human tissues and organs (Newhauser and Zhang, 2015).

For these reasons, the use of long wavelength and near infra-red (NIR) imaging has notably increased. The wavelength range of 650–1450 nm falls in the region of the spectrum with the lowest tissue absorption and therefore enables the deepest tissue

penetration, allowing in some cases for whole animal and deep tissue imaging (Pansare et al., 2012).

Significant improvements in the management of neoplastic disease has caused a move from diagnosing advanced pathology, to detecting early lesions that are potentially amenable to curative treatment (Beg et al., 2016). For OAC, this will require an advance in current diagnostics, with a focus on identifying and characterising subtle mucosal changes. There is great potential in the use of optical technologies to predict histology and enable the formulation of a real-time *in vivo* 'optical biopsy' diagnosis (Wang and Van Dam, 2004).

### 1.12 Antibodies as Imaging Agents

Monoclonal antibodies (mAbs) are attractive cancer-targeting agents due their low toxicity and high specificity (AlDeghaither et al., 2015). Antibodies have been widely considered as the most specific of imaging agents due to their unmatched ability for selectively binding any target. Furthermore, they show a relative lack of toxicity and side effects, and high target affinity and specificity (Kobayashi et al., 2016). Compared to small-molecule compounds, the size of antibodies (150 kDa) facilitates their long plasma half-life (24–56 h) which often results in higher tumour uptake, subsequently leading to better tumour/background contrast (Imai and Takaoka, 2006). However, their clinical utility has been limited primarily due to their slow clearance from the circulation, long retention time in non-targeted tissues and the extensive optimisation necessary for each antibody-tracer (Kaur et al., 2012). Despite these disadvantages, antibodies are thought to be one of the most adaptable targeting vector candidates for conjugation with

numerous biophysical agents, such as fluorescent dyes. Such antibody-based probes are widely used in high-resolution microscopy (Warram et al., 2014).

However, current diagnostic use of antibodies is limited chiefly to immunohistochemical detection of the target of interest in *ex vivo* tissue resected during biopsy, which offers several advantages such as low cost and simplicity of the procedure. However, tissue handling and diagnostic interpretation are major disadvantages of this technique. Furthermore, due to tumour heterogeneity, multiple biopsies are usually required for conclusive results (Cortes et al., 2017). The rapid increase in the number of approved monoclonal antibody-based therapies suggests that mAbs, and their derivatives, are likely to be the focus of the biotherapeutics industry for years to come. The number of therapeutic antibodies being tested in clinical trials in 2017 in the European Union (EU) and United States (US) has reached more than 50 (Reichert, 2017) with 10 such agents being granted a first approval in 2017 alone. This fast pace of therapeutic antibody development is projected to continue (Kaplon and Reichert, 2018). There is no doubt that antibody technology has changed drug development, producing highly targeted and active therapies that can be further advanced through clinical assessment. In parallel, there is an emerging need to access similar targeting agents for diagnostic purposes, including non-invasive imaging in preclinical models and patients. To date, strategies to develop antibody-based imaging agents have focused primarily on extracellular targets such as cell adhesion molecules (Goldenberg , 1995), receptors (Sheng and Liu, 2011) and transporter proteins, mucins, and other membrane-associated proteins (Hischemoller et al., 2012) and have been shown to be effective for visualisation of proteins displaying external antigens (Boonstra et al., 2016). However, there are relatively few tumour-specific or tumour-associated cell surface or soluble antigens available. On the contrary,

intracellular molecules provide a wide range of potential therapeutic targets, provided the issue of access to the cytosol can be successfully resolved (Trenevska et al., 2017). Accessing these targets requires the development of strategies to achieve intracellular delivery. Several methods have been previously described, including electroporation, where electric pulses of duration in microseconds to milliseconds yield a temporary loss of the semi permeability of cell membranes, consequently leading to ion outflow, leakage of metabolites, and increased uptake of drugs, molecular probes, and DNA (Tsong, 1991). Another technique is the delivery of antibodies into individual cells by microinjection (Blose et al., 1984). However, *in vivo* application of these techniques is limited by potential cell damage, the nonspecific transport of molecules into and out of the cell (Hui, 2008), technical difficulties, and poor delivery efficiency (Joo et al., 2014). An alternative, capable of overcoming these limitations, is the use of cell-penetrating peptides (CPPs), also known as protein transduction domains, a class of diverse peptides 5–30 amino acids in length, which have the ability to carry small molecules, proteins, viruses, imaging agents and various nanoparticles across the cellular membrane, facilitating internalisation of the intact cargos (Guo et al., 2016).

### 1.13 Cell-Penetrating Peptides

The need to develop diagnostic and therapeutic tools with significantly improved selectivity and specificity compared to the currently available techniques has driven much of the focus on molecules that are considerably larger than small molecules (< 900 Daltons) and thus unable to freely pass through the lipid bilayer (Yang and Hinner, 2015). Due to size restrictions, many of the molecules of interest are unable to passively diffuse through the cell membrane and gain access to the intracellular components beyond it

(Diamond and Katz, 1974). Nevertheless, the discovery of CPPs has enabled the intracellular delivery of these materials. CPPs are short, positively charged peptides acting through either receptors or energy-independent mechanisms (Zorko and Langel, 2005). Carriers targeting different subcellular domains can be created through various modifications to the CPP sequence (Deshayes et al., 2005). The mechanism of cellular uptake is sequence dependent: CPPs have been reported to deliver cargoes into cells through endosomal pathways, but for some CPPs and smaller cargoes, a direct penetration internalisation mode has also been reported (Duchardt et al., 2007, Fretz et al., 2007). Unanswered questions include the details of the molecular mechanisms underpinning uptake, causes of cell toxicity, and the delivery efficiency of CPPs for different molecules (Guterstam et al., 2009).

Direct membrane transduction or 'delivery' study models have suggested that direct cell penetration occurs via pore formation (Mishra et al., 2011), carpet-like perturbations (Pouny et al., 1992), membrane-thinning (Lee et al., 2005) and micelle formation (Derossi et al., 1996). The direct penetration pathway is energy-independent (El-Andaloussi et al., 2005). In the aforementioned models, the electrostatic interaction (either a local charge neutralisation or the formation of a transient electrical field) between the positively charged CPP and the negatively charged membrane phospholipids is thought to be the initiating event, subsequently leading to changes in the curvature of the membrane and consequent uptake – a mechanism first demonstrated for penetratin in 1996 (Derossi et al., 1996).

The endocytic pathway is energy-dependent and comprises two major categories: phagocytosis and pinocytosis. The former involves uptake of large particles such as

viruses and bacteria and is restricted primarily to cells such as leukocytes and macrophages, whereas the latter is involved in the uptake of solute (Madani et al., 2011). Pinocytosis can be further subdivided into micropinocytosis, clathrin-dependent, caveolin-dependent and clathrin/caveolin-independent pathways (Jones, 2007). Endocytosis describes the de novo creation of internal membranes from the plasma membrane lipid bilayer. Plasma membrane lipids, integral proteins together with extracellular fluid – including the CPP in this case – become fully internalised in early endosomes (Doherty and McMahon, 2009). The majority of CPPs become entrapped in endosomes following delivery into cells and, as a result, any associated cargo also becomes trapped (Lundberg et al., 2003). Usually, agents that become entrapped in endosomes are subsequently degraded by specific enzymes in the lysosome. Therefore, owing to endosomal entrapment, a potential pitfall of using CPPs to deliver cargo may be lysosomal degradation (LeCher et al., 2017). However, this is not always the case, as different mechanisms such as pore formation in the endosomal membrane, and fusion into the lipid bilayer of endosomes, have been proposed to facilitate endosomal escape (Varkouhi et al., 2011).

### 1.13.1 The TAT Peptide

The TAT protein is a transcriptional trans-activator of HIV-1, essential for viral transcription (Kameoka et al., 2002). Additionally, TAT possesses the unusual property of trafficking in and out of the cell (Fittipaldi et al., 2003). The cell penetration and nuclear translocation properties of TAT depend upon the arginine-rich motif, which additionally corresponds to the presumed nuclear localisation signal (NLS, Cardarelli et al., 2007). The mechanisms of entry for TAT and TAT-cargo molecules are a subject of

dispute. Several mechanisms have been proposed, including an endocytosis-independent mechanism (Vives et al., 1997), a temperature-dependant caveolar-mediated pathway (Fittipaldi et al., 2003), and there have been reports that upon different conditions, TAT-membrane interactions vary, resulting in different pathways of internalisation (Mishra et al., 2011). Evidence suggests TAT constructs can successfully deliver cargo both *in vitro* (Asoh et al., 2002, Cao et al., 2002) and *in vivo* (Bolhassani, 2011, Cornelissen et al., 2011), and their use demonstrates potential as a non-invasive approach towards clinical imaging of intracellular targets.

### 1.14 Thesis Aims

Imaging COX-2 and/or c-Met could provide diagnostic benefits in OAC as well other types of cancer. Identification of cancer before significant progression of the tumour or metastasis using these biomarkers has the potential to offer earlier diagnosis and treatment, leading to better outcomes. The current study was designed to test the hypothesis that COX-2 and c-Met are suitable markers for molecular imaging in the context of BO and oesophageal cancer. The following aspects were explored:

i. The properties of selected monoclonal antibodies against exogenous c-Met were evaluated *in vitro*. The specificity and affinity were characterised in OE33 (c-Met high expression) and FLO-1 (c-Met low expression) cells. Following the initial *in vitro* validation, the monoclonal antibodies were conjugated to a Cy5 fluorescent dye and subsequently, the functional characteristics of the Cy5-antibody conjugates were validated (Chapter 3).

ii. Following the initial *in vitro* validation, the ability of Cy5-labelled anti-c-Met antibody conjugates to target c-Met protein *in vivo* were evaluated in two mouse xenograft models using optical imaging (Chapter 4).

iii. The properties of selected monoclonal antibody against endogenous COX-2 protein were evaluated *in vitro*. The specificity and affinity were characterised in OE33 (COX-2 high expression) and FLO-1 (COX-2 low expression) cells. Following the initial *in vitro* validation, the monoclonal antibody was conjugated to a cell penetrating peptide, TAT, and a Cy5 fluorescent dye and the functional characteristics of the Cy5-antibody-TAT conjugates were validated after each modification step. Finally, the ability of Cy5-labelled anti-COX-2-TAT antibody conjugates to target COX-2 protein *in vivo* was evaluated in a mouse xenograft model of OAC using optical imaging (Chapter 5).

# Chapter 2 Materials and Methods

## 2.1 Cell Lines

### 2.1.1 CP (hTert) Cell Lines

Four CP (hTERT) cell lines were a kind gift from Professor Peter Rabinovitch (University of Washington, USA). These cell lines, CP-A, CP-B, CP-C, and CP-D, were established from Barrett's Oesophagus cells isolated from 4 patients. The CP-A cell line (9p Loss of Heterozygosity (LOH), $TP53^{wt}$, 5q LOH) was established from an area of non-dysplastic metaplasia and the CP-B (9p LOH, 17p LOH, $TP53^{mut}$), CP-C (9p LOH, 17p LOH, $TP53^{mut}$), and CP-D (9p LOH, 17p LOH, $TP53^{mut}$) cell lines were established from areas of high-grade dysplasia. All 4 BE lines were maintained at 37°C in 5% $CO_2$ in MCDB 153 medium (Sigma-Aldrich, UK) supplemented with 5% (v/v) foetal bovine serum (FBS, Invitrogen™, UK), 1% (v/v) penicillin/streptomycin/glutamine (Invitrogen™, UK), 20 ng/mL epidermal growth factor (EGF, Gibco, USA), 140 µg/mL bovine pituitary extract (BPE, Sigma-Aldrich, UK), 5 µg/mL insulin, 5 µg/mL transferrin and 5 ng/mL selenium (Sigma-Aldrich, UK) as described previously (Palanca-Wessels et al., 1998).

### 2.1.2 FLO-1 Cell Line

The FLO-1 cell line, a gift from Professor Esther Hammond (University of Oxford, UK), was established in 1991 from a primary distal oesophageal adenocarcinoma in a 68-year-old Caucasian male (Rockett et al., 1997). Cells were maintained at 37°C in 5% $CO_2$ in Dulbecco's Modified Eagle Medium (DMEM, Sigma-Aldrich, UK) supplemented with

10% (v/v) FBS (Invitrogen™, UK) and 1% (v/v) penicillin/streptomycin/glutamine (Invitrogen™, UK).

### 2.1.3 OE33 Cell Line

The OE33 cell line (Sigma-Aldrich, UK) was established from an adenocarcinoma of the lower oesophagus from a 73-year-old female patient. The tumour was identified as pathological stage IIA (UICC) and showed poor differentiation (Rockett et al., 1997). Cell were maintained at 37°C in 5% $CO_2$ in Roswell Park Memorial Institute medium 1640 (RPMI, Sigma-Aldrich, UK) supplemented with 10% (v/v) FBS (Invitrogen™, UK) and 1% (v/v) penicillin/streptomycin/glutamine Invitrogen™, UK).

### 2.1.4 Cell Maintenance

Cell lines were cultured in T-75 flasks (Greiner Bio-One, UK). Once cells had reached approximately 90% confluency, they were washed with phosphate buffer saline (PBS) (37 mM NaCl; 2.7 mM KCl; 4.3 mM $Na_2HPO_4$; 1.47 mM $KH_2PO_4$; pH 7.4) and were detached from the flask by addition of 5mL trypsin-ethylenediaminetetraacetic acid (Trypsin-EDTA) (Sigma-Aldrich, UK). The cell suspension was then transferred to a universal tube and spun at 100 x g (RCF, relative centrifugal force) for 5 min in a Heraeus™ Megafuge™ 40 centrifuge (Thermo Fisher Scientific, UK). Cell pellets were resuspended in 10 mL (FLO-1), 6 mL (OE33) or 5 mL (CP cell lines) of fresh culture media and 1 mL of cell suspension was transferred to a new flask, topped up with fresh culture media to a final volume of 15 mL. Where required, cells were counted using a Countess II automated cell counter (Thermo Fisher Scientific, UK) and the appropriate

number of cells was plated into selected well plates 24 h prior to each experiment. Cells were regularly checked for Mycoplasma infection using a MycoAlert testing kit (Lonza, UK), according to the manufacturer's instructions.

### 2.1.5 Cryopreservation and Storage of Cells

Cells were harvested, as described in § 2.1.4, and counted to ensure cell viability was no less than 90%. The cell suspension was then centrifuged at 100 x g for 5 min in a Heraeus™ Megafuge™ 40 centrifuge (Thermo Fisher Scientific, UK). The cell pellet was re-suspended in appropriate growth media containing 10% (v/v) dimethyl sulfoxide (DMSO) (Sigma-Aldrich, UK) (cell suspension of 1 x $10^6$ cells/mL). One mL aliquots of cell suspension were dispensed into 2mL cryogenic storage vials (Greiner Bio-One, UK), and were placed in a CoolCell® cell freezing container (Bioscion, USA) to ensure a standardised and controlled temperature decrease of -1 °C / minute, to avoid cell damage. Vials were kept at -80°C overnight prior to a long-term storage in the gas phase above liquid nitrogen (-190°C to -135°C).

### 2.1.6 Cell Culture Plastic Ware

Live cell immunocytochemistry assays were performed in 10-well CELLview™ Slides (Greiner Bio-One, UK, 0.32 $cm^2$ growth area) or Thermo Scientific™ Nunc™ MicroWell™ 96-Well Optical-Bottom Plates (Thermo Fisher Scientific, UK, 0.32 $cm^2$ growth area).

## 2.2 Western Blot (WB) Analysis

### Lysis Buffer

RIPA lysis buffer, composed of 10 mM 2-Amino-2-(hydroxymethyl)-1,3-propanedio hydrochloride (Tris-HCl), 1 mM ethylenediaminetetraacetic acid (EDTA), 1% (v/v) Triton X-100, 0.1% sodium deoxycholate, 0.1% sodium dodecyl sulfate (SDS), 140 mM NaCl and 1 mM PMSF, supplemented further with cOmplete™, a protease inhibitor cocktail (Roche, UK).

### SDS Loading Sample Buffer (5 x)

The SDS loading sample buffer, composed of 25 mM Tris-HCL, 1% (v/v) SDS (10% stock solution), 5% (v/v) glycerol, 1mM EDTA (0.5 M stock), 2.5% (v/v) β-mercaptoethanol, and 0.01% (v/v) bromophenol blue (1% stock solution).

### NUPAGE® MES SDS Running Buffer (20 x)

2-(N-morpholino)ethanesulfonic acid (MES) running buffer (20 x, pH 7.2, Thermo Fisher Scientific, UK), composed of 50 mM MES, 50 mM Tris base (pH 7.3), 0.1% (v/v) SDS, and 1 mM EDTA. For gel electrophoresis, the buffer was diluted 1:20 with deionised $H_2O$ ($dH_2O$) from the 20 x stock.

**NUPAGE® Transfer Buffer (20 x)**

NuPage® Transfer buffer (20 x, pH 7.2, Thermo Fisher Scientific, UK), composed of 25 mM bicine, 25 mM Bis-Tris (free base), and 1 mM EDTA. Prior to use, the buffer was diluted 1:20 in $dH_2O$ and in 20% (v/v) methanol.

**Cell Pellet Preparation**

Once cells reached 90% confluency (in T-75 flask, unless otherwise stated), the medium was aspirated, and cells were washed twice with 5 mL of ice-cold PBS. Subsequently, cells were covered in 10 mL of ice-cold PBS and scraped off the dish, using a cell scraper (Greiner Bio-One Ltd, UK) and transferred into a 15 mL centrifugal tube. The samples were then centrifuged at 252 x g at 4°C for 5 min using a 5417R centrifuge (Eppendorf Ltd, UK). The supernatant was discarded, and the pellet was re-suspended in 1 mL of ice-cold PBS, and re centrifuged further at 252 x g at 4°C for 5 min. After the supernatant was decanted, cell pellets were stored at -80°C if not used immediately.

**Cell Lysis**

Cell pellets were prepared as described in § 2.2.5. After determining the packed cell volume (PCV) of the pellet, cells were re suspended in lysis buffer (3 times the PCV) containing cOmplete™ protease inhibitor cocktail (1 tablet/10 mL of RIPA buffer, Roche, UK). The cell suspension was then mixed thoroughly before incubation on ice for 30 min. To separate cell debris, lysates were centrifuged at 15,000 x g at 4°C for 10 min and the supernatant was collected and stored at -80°C if not used immediately.

**BCA Protein Assay**

The protein concentration of each sample was determined using Pierce™ bicinchoninic acid (BCA) Protein Assay Kit (Thermo Fisher Scientific, UK). Albumin standard (BSA) was diluted into several vials, using PBS, to prepare a set of diluted standards for a working range of 20-2000 μg/mL. Volume of 10 μL for each of the standard concentrations and unknown samples was transferred onto a clear 96-well plate and topped up with PBS to a final volume of 25 μL. The Working Reagent (WR) was prepared by mixing 50 parts of BCA Reagent A with 1 part of BCA Reagent B and immediately a volume of 200 μL was dispensed into each well. The plate was incubated for 30 min at 37°C followed by absorbance measurement at 595 nm using an Infinite 200 Pro plate reader (Tecan, Männedorf, Germany). The protein concentration of unknown samples was determined by comparing the net absorbance values with those at 595 nm against the standard curve.

**Sample Loading**

4-12% Bis-Tris protein gels (10 well, NuPAGE™ Novex™, Thermo Fisher Scientific, UK) were used. The samples to be loaded were prepared in the total volume of 20 μL by adding 40 μg of protein unless otherwise stated, 4 μL of 5 x SDS loading sample buffer and 2 μL of the NuPAGE™ Sample Reducing Agent (10X) (Thermo Fisher Scientific, UK). The remaining volume was made up by PBS. The samples were denatured by heating for 5 minutes at 90° C prior to loading.

**Electrophoresis**

Gel cassettes were placed in an XCell SureLock™ Mini-cell system (Thermo Fisher Scientific, UK) after removing the tape covering the back of the gel cassette. The upper buffer chamber was filled with 1 x running buffer, approximately 200 mL prior to filling the lower buffer chamber. The SeeBlue™ Plus2 Pre-stained Protein Standard (Thermo Fisher Scientific, UK) was loaded in the first lane (10 µL) followed by the samples. Gels were run at 125 V for up to 1.5 h, with the voltage controlled by the PowerPac™ High-Current power supply (Bio-Rad Laboratories Ltd., UK).

**Protein Transfer**

Protein Transfer was carried out using the XCell II™ blot module (Thermo Fisher Scientific, UK). Blotting pads and filter papers (2.5 mm thickness, Invitrogen, USA) were pre-soaked in transfer buffer, detailed in § 2.2.4. A hydrophobic immobilon®-P Polyvinylidene difluoride (PVDF) membrane (Millipore, Feltham, UK) were prewet for 30 s in methanol, rinsed in $dH_2O$ and soaked in transfer buffer for 2 min. The cathode core of the blotting module was filled in a specific order, ensuring no air bubbles were introduced, with the following: blotting pad, filter paper, gel, PVDF membrane, filter paper, blotting pad. Additional pre-soaked blotting pads were added to hold and secure the gel-membrane sandwich if necessary, and the anode was placed on top of the pads. The assembled blotting module was subsequently placed inside the Criterion™ blotter (Bio-Rad Laboratories Ltd., UK) and filled with transfer buffer. Cooling pads were placed around the tank to prevent heating of the transfer buffer. Transfer was performed at 90 V for 1 h.

**Enhanced Chemiluminescence Detection**

Pierce™ enhanced luminescence western blotting substrate (Thermo Fisher scientific, UK) was used for ECL detection. After the transfer or upon retrieving from storage in PBS, membrane was incubated with the ECL substrate working solution, prepared immediately before incubation by mixing equal parts of detection reagents 1 and 2. After 1 – 3 min of incubation at room temperature (RT), the membrane was then removed, excess reagent gently blotted onto a tissue pepper, and membrane was placed on a clear Saran wrap and taped into an X-ray cassette (18 x 24 cm) with the protein side facing up. Under red safe light, X-ray film (Fuji Super RX-N, Fujifil, Japan) was then placed on the top of the membrane. Exposure times varied, subject to factors such as quality of the primary antibody and the amount of the protein of interest. Subsequently, the film was removed from the cassette and placed into a Compact X4 film processor (Xograph, UK). The approximate molecular weight of each of the protein bands were marked on the film by placing it over the membrane and using pre-stained protein ladder as guidance.

**Membrane Blocking and Antibody Probing**

Upon completion of the transfer, the PVDF membrane was removed and placed in a blocking solution of 5% w/v BSA (Sigma-Aldrich, UK) in 1 x PBST (PBS with 0.1% (v/v) Tween-20) for 1 hour at RT on the Boekel Scientific Orbital Platform Shaker (Boekel Scientific, USA) before probing with primary antibodies. The antibodies and dilutions used in the COX-2 and c-Met studies are listed in table 2.1. The antibodies were diluted in blocking solution and incubated for 2 h at RT or 24 h at 4°C on a Boekel rotary shaker. After incubation with primary antibodies, membrane was washed 3 x 5 min with

PBST whilst on a Boekel rotary shaker, and subsequently incubated with secondary horseradish peroxidase (HRP) conjugated antibody for 1 h at RT. Finally, membranes were washed again 3 x 5 min with PBST and kept in PBS at 4°C if not developed immediately. Recombinant human COX-2 protein (ab58868, Abcam, UK) was used as a positive control.

| Antibody | Species | Catalogue # | Supplier | Dilution | MW Detected |
|---|---|---|---|---|---|
| **Anti-COX-2 [AS66]** | Mouse | ab90345 | Abcam | 1:750 | 69 kDa |
| **Anti-c-Met (Met13)** | Mouse | MAB1916 | Merck Millipore | 1:700 | low reactivity and specificity towards denatured c-Met by WB. This antibody is not recommended for WB application (Wong et al., 2013) |
| **Anti-c-Met [EP1454Y]** | Rabbit | ab51067 | Abcam | 1:750 | 240 kDa |
| **β-Actin** | Rabbit | ab8227 | Abcam | 1:5000 | 42 kDa |
| **Anti-Rabbit IgG (H/L):HRP** | Goat | 65-6120 | Invitrogen | 1:5000 | N/A |
| **Anti-Mouse IgG (H/L):HRP** | Rabbit | 61-6520 | Invitrogen | 1:5000 | N/A |

**Table 7 Antibody Dilutions Used for COX-2 and c-Met Western Blotting.** Catalogue number, company, dilutions used, and the molecular weight of protein recognised by each antibody are provided (when applicable).

## 2.3 Antibodies

### 2.3.1 Main Antibodies Used

Antibodies were chosen based on review publications (antibody data and references) and vendor information regarding antibody usability for both species used and desired applications. The antibody used for COX-2 studies was the anti-COX-2 (AS66) mouse monoclonal antibody (ab90345, Abcam, UK). The main antibody used for c-Met study was the anti-c-Met (Met13) mouse monoclonal antibody (MAB1916, Merck Millipore, USA). Another antibody tested in parallel with the MAB1916 was anti-Met (c-Met) [EP1454Y] rabbit monoclonal antibody (ab51067, Abcam, Cambridge, UK). Product information, reactivity and immunogenicity for each antibody are provided in Table 2.2.

| Name | Species Cross-Reactivity | Isotype | Immunogen |
|---|---|---|---|
| **Anti-COX-2 / Cyclooxygenase-2 antibody [AS66]** | Human | IgG1κ | Recombinant Human COX2/ Cyclooxygenase 2 protein |
| **Anti-c-Met (Met13) antibody** | Human | IgG1κ | His-tagged recombinant human c-Met α chain (Wong et al., 2013) |
| **Anti-c-Met [EP1454Y] antibody** | Mouse, Rat, Human | IgG1κ | Synthetic peptide (the amino acid sequence is considered to be commercially sensitive) corresponding to Human Met (c-Met) aa 1-100 (N terminal) |

**Table 8 Anti-COX-2 [AS66], Anti-c-Met (Met13) and Anti-c-Met [EP1454Y] Product Information.**

### 2.3.2 Non-Specific Control Antibodies

The non-specific control antibodies used for all COX-2 and c-Met experiments were purified mouse IgG antibodies (Sigma-Aldrich, UK), similarly diluted and known to be unreactive to COX-2 and c-Met proteins.

### 2.3.3 Antibody Labelling with the Cy5-NHS Dye – Anti-c-Met Antibodies

Cyanine 5 mono-reactive dye (Cy5-NHS, GE Healthcare, UK), dissolved in dimethyl sulfoxide (DMSO, 1 mg/mL), was reacted with a solution of 1 mg/mL TAT-conjugated antibody (in 0.1 M sodium bicarbonate buffer, pH 9) at a 20:1 ratio for overnight at 4°C on an orbital platform shaker (Boekel Scientific, USA). The excess non-reactive reagent was removed using Sephadex® $G_{50}$ gel filtration (Sigma-Aldrich, UK) in PBS (500-10,000 fractionation range) and eluted with PBS (100 μL/fraction, 16 fractions). The absorbance of the Cy5-antibody conjugate was measured at 280 nm and 670 nm using the Nanodrop 1000 spectrophotometer (Thermo Fisher Scientific, UK). The efficiency of labelling was estimated using the method described in Amersham CyDye™ mono-reactive NHS Esters Product Booklet (GE Healthcare, UK).

### 2.3.4 Conjugation of TAT Penetrating Peptide – Anti-COX-2 [AS66]

The anti-COX-2 [AS66] (ab90345, Abcam, UK) and mouse IgG1 non-specific control antibodies (Sigma-Aldrich, UK) were dissolved in 0.1 M MES acid (pH 6) using an Amicon ultracentrifugal filter with a nominal molecular weight cut off of 30 kDa, (0.5

mL, Merck Millipore). The filter was centrifuged for 8 min at 12,300 × g using a MicroStar 12 desktop microcentrifuge (VWR, USA) for three consecutive rounds of concentration and dilution. The final concentration of antibodies was maintained at approximately 1 mg/mL in 100 µL total volume. Subsequently, the antibodies were diluted to 200 µL with 0.1 M MES (pH 6) and then 3.1 µL of 1-Ethyl-3-(3-dimethylaminopropyl)carbodiimide (EDC, 130 mM in 0.1 M MES, pH 6) (Thermo Fisher Scientic, UK) and 8.8 µL of Sulfo-NHS (115 mM, in 0.1 M MES, pH 6) (Thermo Fisher Scientic, UK) were added to give a final concentration of 2 mM and 5 mM, respectively. The resultant solutions were then mixed by vortexing for 15 min at RT. The Sulfo-NHS modified antibodies were then buffer exchanged to PBS (pH 7.4) in a final volume of 100 µL and the cell penetrating peptide TAT (GRKKRRQRRRPPQGYG, molecular weight = 1996.3 g/mol, Cambridge Peptides, UK) was reacted with the antibody for 2 h at RT (TAT:antibody ratio at 5:1, TAT stock concentration = 2 mg/mL in PBS). Unreacted TAT was removed using Sephadex® G50 gel filtration (Sigma-Aldrich, UK) in PBS (500-10,000 MW fractionation range), eluted with 0.1 M sodium bicarbonate buffer at pH 9 (100 µL/fraction, 16 fractions). The fractions with the highest antibody concentration, as determined by Nanodrop 1000 (A280) (Thermo Fisher Scientific, UK), were combined, concentrated and used for the labelling with Cy5 NHS Ester (GE Healthcare, UK).

### 2.3.5 TAT Radiolabelling

TAT radioactive labelling with Iodine-123 involves incorporation of $^{123}I$ into tyrosine residue within the TAT peptide (Escher, 1984). Pierce™ Iodogen Iodination Tubes (Thermo Fisher Scientific, UK) were rinsed with 500 µL Iodogen buffer (0.1 M $K_2HPO_4$,

pH 8.45) and 100 μL of TAT (in iodogen buffer, final concentration of 1 mg/mL) were added. For radiolabelling, $Na^{123}I$ solution was added to each tube to the desired amount (1 MBq) and left to incubate at RT for 30 min. Excess $Na^{123}I$ was removed using Bio-Gel P-4 Gel filtration (Bio-Rad, UK) in PBS (800–4,000 MW fractionation range), eluted with PBS (100 μL/fraction, 20 fractions). The radioactivity of each collected fraction was determined using Wizard γ Counter (Perkin Elmer, MA, USA).

### 2.3.6 Evaluation of TAT- anti-COX-2 [AS66] antibody conjugation using $^{123}$I-TAT

$^{123}$I-TAT was radiolabelled as described in § 2.3.5. The fractions with the highest radioactivity were combined, concentrated and used for the conjugation of $^{123}$I-TAT to the anti-COX-2 [AS66] antibody, as described in § 2.3.4. Subsequently, unreacted $^{123}$I-TAT was removed using Sephadex® $G_{50}$ gel filtration (Sigma-Aldrich, UK) in PBS (500-10,000 fractionation range), eluted with PBS (100 μL/fraction, 20 fractions). The protein concentration and radioactivity of each fraction were determined by Nanodrop 1000 ($A_{280}$) (Thermo Fisher Scientific, UK) and Wizard γ Counter (Perkin Elmer, MA, USA), respectively.

## 2.4 Enzyme-Linked Immunosorbent Assay (ELISA)

### 2.4.1 Indirect ELISA – Anti-COX-2 and Anti-c-Met

An ELISA plate, Maxisorp (Sigma-Aldrich, UK) was coated with either COX-2 human full-length protein (ab58868, Abcam, UK) at 1 μg/mL or human Met (c-Met) peptide (ab167073, Abcam, UK) at 1 μg/mL in bicarbonate buffer (pH 9.6; 0.2 M $Na_2CO_3$; 0.2

M $NaHCO_3$), 100 µL/well, and left to incubate overnight at 4°C. The next day, 300 µL of the blocking buffer (2% BSA in PBS) was added to each well for 1 hr at 37°C to block any non-specific binding. Subsequently, native, unlabelled anti-COX-2 [AS66] or anti-c-Met antibodies was added in a range of concentrations (100 nM – 0.2 nM), 100 µL/well, and left to incubate overnight at 4°C. The next day, the plate was washed with washing buffer (Tween 20 (1% v/v) in PBS) and biotinylated IgG antibody (anti-rabbit or anti-mouse, BA-1000 and BA-9200, Vector Laboratories, UK) was incubated for an hour at RT, at 1 µg/mL, 100 µL/well to allow it to bind to mouse anti-COX-2 [AS66] / mouse anti-c-Met (Met13) / rabbit anti-c-Met [EP1454Y]. The plate was washed x 3 and streptavidin-HRP conjugate (N100, Thermo Fisher Scientific, UK) was added at 1 µg/mL; 100 µL/well for 25 min at RT. This was followed by 4 washes to remove excess streptavidin. The bound antibody was detected colorimetrically with substrate [1:1 ($H_2O_2$ : tetramethylbenzidine)] 100 µL/well at RT for 10 min. The reaction was terminated by addition of 2 N $H_2SO_4$. Absorbance was measured spectrophotometrically at 450 nm with correction at 570 nm (to remove the optical background of the plate), using an Infinite 200 Pro plate reader (Tecan, Germany).

### 2.4.2 Direct ELISA – Anti-COX-2 and Anti-c-Met

An ELISA plate was coated and blocked as detailed in § 2.4.1. Subsequently, native, unlabelled anti-COX-2 [AS66] or anti-c-Met antibodies was added in a range of concentrations (100 nM – 0.2 nM), 100 µL/well, and left to incubate overnight at 4°C. The next day, the plate was washed with washing buffer (Tween 20 (1% v/v) in PBS) and fluorescence intensity was measured at 670 nm (exposure 30s), using an Infinite 200 Pro plate reader (Tecan, Germany).

### 2.4.3 Competition Binding ELISA – Anti-COX-2 and Anti-c-Met

An ELISA plate was coated and blocked as detailed in § 2.4.1. Subsequently, Cy-5 labelled anti-COX-2-TAT antibodies (1nM) plus increasing concentrations of native COX-2 or anti-COX-2-TAT were added overnight at 4°C (range 100 nM – 0.2 nM). Alternatively, Cy-5 labelled anti-c-Met antibodies (1nM) plus increasing concentrations of native anti-c-Met mAbs were added overnight at 4°C (range 100 nM – 0.2 nM). Next day, the plate was washed with washing buffer (Tween 20 (1% v/v) in PBS) and fluorescence intensity was measured at 670 nm (exposure 30s), using an Infinite 200 Pro plate reader (Tecan, Germany).

## 2.5 Immunohistochemistry

### 2.5.1 Ligand Binding Assays

OE33 cells were seeded at 1 x $10^4$ per well (for plastic ware, refer to § 2.1.6) and left to adhere overnight at 37°C in a 5% $CO_2$ humidified chamber. The following day, Cy5 labelled anti-c-Met antibodies were added in a range of concentrations (100 nM – 0.2 nM), 100 µL/well, and left to incubate for 3 h at 37 degrees in a 5% $CO_2$ humidified chamber. Subsequently, treatments were washed gently using sterile PBS, 3 x 1 minute, and cells nuclei and cytoplasms were stained as detailed in § 2.6.1 prior to imaging with fluorescence microscope, as described in § 2.6.2.

### 2.5.2 Competition Binding Assay

OE33 cells were seeded at 1 x $10^4$ per well (for plastic ware, refer to § 2.1.6) and left to adhere overnight at 37 degrees in a 5% $CO_2$ humidified chamber. The following day, the media was replaced with a solution of Cy-5 labelled anti-c-Met antibodies (1nM) plus increasing concentrations of native c-Met mAbs (range 100 nM – 0.2 nM) were added and cells were left to incubate overnight at 37°C. In the morning, treatments were washed gently using sterile PBS, 3 x 1 minute, and cells nuclei and cytoplasms were stained as detailed in § 2.6.1 prior to imaging with fluorescence microscope, as described in § 2.6.2.

### 2.5.3 Blocking Assay – Anti-c-Met (Met13)

Cells were seeded at 1 x $10^4$ per well (for plastic ware, refer to § 2.1.6) in either DMEM (FLO-1) or RPMI (OE33) medium and left to adhere overnight. The following day, the medium was replaced with a solution of either 7.5 μg/mL or 15 μg/mL of anti-c-Met (Met13) or anti-c-Met [EP1454Y]. Control cells were treated with unlabelled IgG from mouse or rabbit serum; please refer to § 2.3.2 for more details. Unlabelled antibodies were washed off either 3 or 24 hours later, and matching Cy5-labelled anti-c-Met antibodies were added and left to incubate for an additional 3 hours. After treatment was complete, samples were washed gently using sterile PBS, 3 x 1 minute, and cells nuclei and cytoplasms were stained as detailed in § 2.6.1 prior to imaging with fluorescence microscope, as described in § 2.6.2.

## 2.6 Fluorescent Imaging

### 2.6.1 Live Cell Imaging

Cells were seeded at 5 x $10^4$ per well (for plastic ware, refer to § 2.1.6) in either DMEM (FLO-1) or RPMI (OE33) medium and left to adhere overnight. The following day, the medium was replaced with a solution of 3 μg/mL of Cy5-anti-COX-2-TAT, Cy5-Met13 or Cy5-EP1454Y in corresponding cell medium and left to incubate for 24 hours. Control cells were treated with Cy5-anti-COX-2, Cy5-IgG-TAT or Cy5-IgG (ms, mouse) solutions (3 μg/mL). Alternatively, for c-Met experiments, control cells were treated with Cy5-IgG (ms, mouse) or Cy5-IgG (rb, rabbit) solutions (3 μg/mL). After 24 hours, treatments and controls were washed gently using sterile PBS, 3 x 1 minute, and cells nuclei and cytoplasms were stained with the mixture of 20 nM Hoechst 33342 (Thermo Fisher Scientific, UK) and 50 nM Calcein (Thermo Fisher Scientific, UK), cell-permeant dyes, in sterile PBS for 10 min at 37°C after which Hoechst/Calcein stains were removed and cells were washed 3 x 1 min in PBS. Subsequently, 200 uL of fresh RPMI 1640 medium, no phenol red (Thermo Fisher Scientific) or FluoroBrite™ DMEM medium was added prior to imaging with a fluorescence microscope (Barber et al., 2013).

### 2.6.2 Image Acquisition

Cell cultures were imaged on the Gray's Institute 'open' high-content, fluorescence microscope, Abbe. Abbe is equipped with a fluorescence excitation illuminator (Lumen 200, Prior Ltd, UK) and fluorescence filter cube changing unit, with suitable filters arranged to give required wavelength discrimination, with filters (Semrock Inc.,

Rochester, USA) and filter cubes (Nikon UK Ltd, UK). The cubes used were a UV-2A longpass filter cube (centre wavelength (CWL)/ bandwidth (BW) = 355/50 nm, barrier filter barrier filter = 410 nm) for Hoechst stain (λex = 350 nm, λem = 460 nm), fluorescein isothiocyanate (Fitch, #242) bandpass filter cube (CWL/BW = 480/30 nm, barrier filter = 535/45 nm) for Calcein (λex = 490 nm, λem = 520 nm), and Cy5 HQ cube (CWL/BW = 620/60 nm, barrier filter = 700/75 nm) for Cy5 (λex = 640 nm, λem = 670 nm) detection. The objective lens used was 20 x 0.75 NA S Fluor (Nikon UK Ltd, UK). Images were acquired using Prior Lumen 200 at 100% position shutter, minimal gain setting, Cy5, FITC and UV-2A channel acquisition times of 500 ms, 100 ms and 50 ms, respectively, unless otherwise stated. The autofocus range was set to 20 μm with 0.5 μm accuracy. Images were acquired every 15 minutes for a period of up to 60 minutes, unless otherwise stated. Cells were maintained at 37°C in 5% $CO_2$ using an in-house developed incubation accessory. Image data acquisition and processing were performed using in-house developed software. In addition, a stand-alone program, TRI2, was used for post processing and manual quantification of the fluorescence data (Barber et al., 2009).

### 2.7 Small-Interfering RNA (siRNA)-Mediated Gene Silencing

OE33 cells were seeded in a 6-well plate (1 x $10^5$ per well) and left to adhere overnight. All COX-2 and c-Met siRNAs were synthesized and chemically modified by Dharmacon Inc. Transfections were carried using DharmaFECT transfection reagent (Dharmacon Inc., USA), and solutions were prepared following Dharmacon Basic siRNA Resuspension Protocol. Stock concentrations of 20 μM siRNA solutions were prepared in 1 x siRNA buffer (60 mM KCl, 6 mM HEPES-KOH, pH 7.5, and 0.2 mM $MgCl_2$). Upon resuspension, the siRNA was aliquoted into small volumes and stored at -20 °C to

-80 °C if not used immediately. siRNA pre-mixed samples were prepared by mixing 10 μL of 5 μM siRNA and 190 μL serum-free RPMI medium (Sigma-Aldrich, UK). DharmaFECT transfection reagent at a volume of 5 μL was mixed with 195 μL of serum-free media to prepare a solution with a final concentration of 25 nM. Each mix was incubated for 5 min at room temperature before siRNA pre-mixed samples were added to DharmaFECT transfection reagent and incubated for further 20 min at RT. The siRNA-transfection buffer complex was then added to the well, and topped up with 1600 μL serum-free RPMI medium to a final volume of 2 mL. Control transfections were performed using the above method, but the COX-2/c-Met siRNA targeting mix was replaced by non-targeting siRNA control (ON-TARGET*plus* Non-Targeting Pool, Dharmacon Inc., USA) or GAPDH siRNA (ON-TARGET*plus* GAPDH Control Pool, Dharmacon Inc., USA) for a positive transfection control.

### 2.8 *In Vivo* Imaging

OE33 and FLO-1 murine xenograft mouse models were used for *in vivo* studies. All animal experiments were performed in accordance with the UK Animal Act (Scientific Procedures) 1986 and approved by the local ethics committee. All animals were housed under a 12 h light/dark cycle and supplied with purified alfalfa free diet (Invigo, UK) and water *ad libitum*. Mice were checked daily for health and behavioural changes throughout the experiments.

### 2.8.1 Cell Preparation for Inoculation

Culture medium was aspirated; cells were washed with sterile PBS and trypsinised as described in § 2.1.4. Trypsin was neutralised by addition of appropriate cell medium supplemented with FBS. Cells were counted using an automated Countess II automated cell counter (Thermo Fisher Scientific, UK). Cells were centrifuged (100 × g, 5 min), using a Heraeus™ Megafuge™ 40 centrifuge (Thermo Fisher Scientific), media was removed and cell pellet was re-suspended in PBS to a final concentration of $30 \times 10^6$ cells/mL.

### 2.8.2 OE33 and FLO-1 Xenograft Models

Bagg Albino (BALB)/c Nude or Non-Obese Diabetic, Severe Combined Immunodeficiency (NOD SCID) γ mice (22 - 28 g) (Charles River, UK) were anaesthetised using 3-4% (v/v) isoflurane in oxygen. Previously prepared cell suspensions (§ 2.5.1) were agitated and 100 μL ($3 \times 10^6$ cells/ mouse) of OE33 or FLO-1 cells were inoculated subcutaneously, using a 21 G needle, behind the right upper limb of the mouse. To prevent hypothermia, animals were placed on a heated pad during inoculations. Mice were then observed for 10 - 15 min to ensure full recovery from anaesthesia.

### 2.8.3 Growth Rate of OE33 and FLO-1 Xenografts

Under isoflurane anaesthesia, mice were inoculated subcutaneously in the flank with appropriate number of cells, as detailed in § 2.8.2. Tumour growth was monitored using

callipers twice weekly for up to 10 weeks. Tumour volumes were calculated according to the equation (Euhus et al., 1986):

$$\text{Tumour Volume } (mm^3) = \text{length} \times (\text{width}^2) / 2$$

### 2.8.4 *In Vivo* Experimental Design

OE33 and FLO-1 tumour-bearing mice were randomised into experimental groups and received either Cy5-labelled probes or Cy5-IgG non-specific control probes intravenously (iv), 10 μg, unless otherwise specified. All animals were weighed weekly. The Mouse Grimace Score was used to assess pain. Mice were imaged for fluorescence when tumour volume was more than 62.5 $mm^3$. This involved iv injection of the antibody-conjugated dyes at the required concentration, followed by imaging using a novel multiwavelength fluorescence imaging system. Anaesthetised animals were imaged periodically for a total duration of 3 - 4 days, unless otherwise stated, at the end of which, the mice were euthanised. Tumour development was assessed by a combination of visual inspection and measurement by callipers and fluorescence imaging.

### 2.8.5 *Ex Vivo* Biodistribution Studies

After the last imaging session, animals were euthanised and tissues of interest were removed. *Ex vivo* whole-organ imaging was used to compare the relative concentrations of fluorescently labelled antibodies within tissues and between multiple types of tissues or treatment groups, using a multiwavelength fluorescence imaging system (Volpi et al., 2014).

### 2.8.6 Image Acquisition

A novel optical filtering arrangement allowed real-time simultaneous detection of bright-field colour images and fluorescence images from Cy5 dye (λex=640 nm, λem=670 nm) using a single camera (Volpi et al., 2014). Exposure time during fluorescence acquisition ranged between 320 and 640 ms, depending on the emission intensity and imaging depth, which allowed for reduced recording time. In a subset of mice, percutaneous Cy5 fluorescence imaging of the tumour was performed prior to experimental procedure and injection of the Cy5-labelled probes. To improve the signal detected from the regions of interest during imaging, all NSG animals were shaven; once the animals were fully anesthetised, electric clippers were used to shave their backs.

### 2.8.7 Image Processing and Analysis

#### 2.8.7a Gamma Correction

Numerous video instruments use conventional cameras, and to present white image correctly, conventional intensity compression / decompression techniques are applied because of the poor dynamic range of the video systems used. In the past, signal intensity was compressed such that:

$$\text{output}_{\text{intensity}} = (\text{input}_{\text{intensity}})^{\text{gamma}}$$

Once video signals arrived at monitor they were inherently linearised, such that monitor intensity = (output signal)$^{1/\text{gamma}}$ . This standard has been adapted in all video systems

since 1950s, and has continued on into the modern electronic era. The images thus acquired have a non-linear response to the intensity seen by the camera. The latter is proportional to a first approximation to the concentration of the fluorophore of interest, therefore in order to derive that from the recorded signal, the inverse gamma factor must be applied. Consequently, each image analysed was gamma corrected, as demonstrated in Figure 2.1.

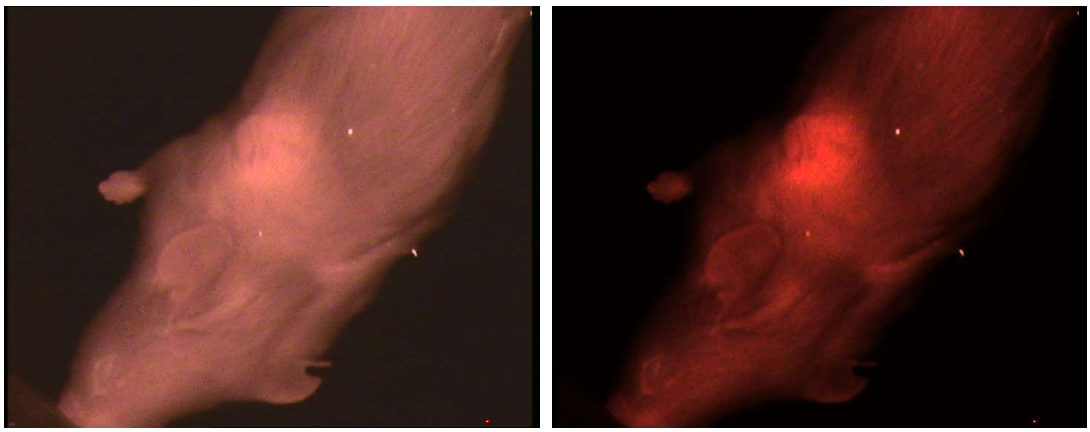


**Figure 2.1 Gamma Correction.** Gamma Correction is the non-linear logarithmic processing), done to correct for cathode-ray tube (CRT) monitors (corrected image on the right) which show data as if it had been raised to the power of gamma (in this case, exponent of 2.2, image on the left).

### 2.8.7b Region of Interest (ROI) analysis

ImageJ (Fiji, Japan) software was used to select for the same region of interest (ROI) in each animal. ROI was defined as the area covering most of the tumour. Fluorescence intensity within ROI was quantified by using ImageJ software as shown in Figure 2.2. Each tumour or background sample was quantified thrice, and the average was taken. A)

Standardized ROI of the fluorescence was measured by capturing the same $mm^2$ area for each mouse. Background fluorescence was removed by subtracting the fluorescence of the background capture area (consisting of skin or B) exposed muscle tissue) from each articular reading. Calculations were represented graphically as fluorescence intensity (arbitrary units) or C) Standardized ROI of the fluorescence was measured by capturing the same area for each mouse. Calculations were represented graphically as tumour fluorescence to background fluorescence (average) ratios, arbitrary units.

### 2.9 Statistical Analysis

All statistical analyses and non-linear regression were performed using GraphPad Prism 7 (GraphPad Software, USA) and the details of specific tests and methods are presented in relevant chapters. The data were obtained in at least triplicates and results are reported and graphed and mean ± standard error of the mean, unless otherwise stated.

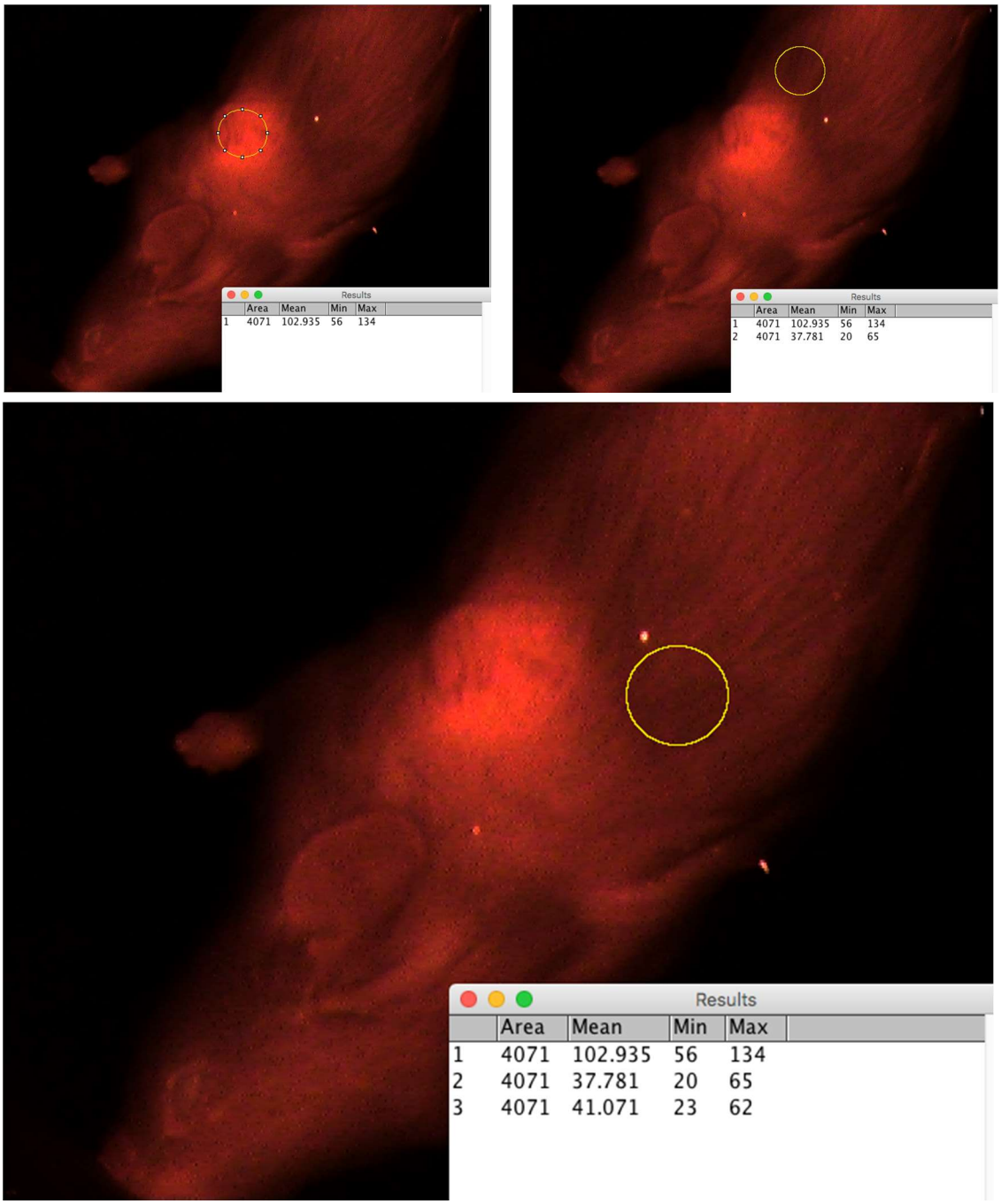



**Figure 2.2 Region of Interest (ROI) Analysis.** Each tumour or background sample was quantified thrice, and the average was taken. A) Background fluorescence was removed by subtracting the fluorescence of the background capture area (consisting of skin or B) exposed muscle tissue) from each articular reading. Calculations were represented graphically as fluorescence intensity (arbitrary units) i.e. 102.935 – average background fluorescence i.e. 39.426 = 63.509 AU or C) Standardized ROI of the fluorescence was measured by capturing the same area for each mouse. Calculations were represented graphically as tumour fluorescence to background fluorescence (average) ratios i.e. TBR = 102.935 / average background fluorescence i.e. 39.426 = 2.61.

# Chapter 3 *In Vitro* Imaging of Oesophageal Cancer by Targeting c-Met Receptors

## 3.1 Introduction

Although primarily developed for preclinical research and therapeutic use (Chapman et al., 2009), antibodies, with their high antigen specificity, can be used as a courier to selectively deliver a diagnostic probe (Warram et al., 2014). For the purpose of diagnostic imaging, novel antibody-based probes can be developed to visualise expression of biomarkers for the detection of cancer. It is generally accepted that an optimal biomarker for imaging will be overexpressed in the tumour relative to normal tissue, indicating a change that corelates with the risk or progression of disease, and is expressed consistently between patients (Karley et al., 2011). In this chapter, the first step towards achieving an optimal antibody-based probe to be used as a c-Met-targeting vector is the characterisation of commercially available antibodies. To achieve this, a number of assays were used to validate the specificity, affinity and binding parameters of two monoclonal anti-c-Met antibodies: the anti-c-Met [EP1454Y] rabbit mAb and anti-c-Met (Met13) mouse mAb in two cell lines with positive (OE33) or negative (FLO-1) c-Met expression.

### 3.1.1 Selective Optical Imaging of c-Met

Diagnostic imaging offers exciting opportunities for selective detection of certain cell populations, such as those bearing markers indicative of cancer (Weissleder and Ntziachristos, 2003). Technical aspects of endoscopic imaging have a major role in determining pre-malignant lesion detection rate, together with human factors. Imaging at endoscopy is currently performed using white light (WL), and lesions are detected by operators who are trained to discriminate pre-malignant or cancerous lesions from normal

oesophageal tissue by recognizing characteristics such as protrusion into the lumen and mucosal colour changes (Ballester and Cruz-Correa, 2014). However, these features are less discriminatory in smaller and early lesions, leading to miss rates of up to 12% (Sekiguchi and Oda, 2017). Combining targeted optical probes and advanced imaging technology has the potential to significantly improve oesophageal lesion detection by improving the visualisation of dysplastic lesions (Espino et al., 2014).

Mesenchymal–epithelial transition factor – also named c-Met – is a receptor tyrosine kinase for the hepatocyte growth factor that plays a pivotal role in tumorigenesis, as described previously in § 1.7, c-Met overexpression has been shown to occur as an early event in the oesophageal adenoma-carcinoma sequence (Delitto et al., 2014), making it a suitable biomarker for oesophageal neoplasia (Nagaraja and Eslick, 2014). A recent meta-analysis of 14 studies focussing on c-Met overexpression in gastric cancers revealed a negative correlation between levels of c-Met expression and survival (Huang et al., 2001). Furthermore, it has been reported that c-Met is overexpressed in 34%-70% of OAC, although these data have been obtained using random biopsies, so the true overexpression may in fact be higher (Xu et al., 2016, Mesteri et al., 2014). Finally, its expression on the cell membrane makes extracellular epitopes accessible for targeting with imaging agents (Han et al., 2017).

Table 9 shows representative molecular imaging agents developed for c-Met imaging in various cancers. Amongst these, there are only three fluorescent imaging agents including Ms20-QD, a fluorescent-labelled single chain variable fragment (scFv) of an anti-c-Met antibody, and two fluorescent-labelled peptides: cMBP-AOC-Cy5.5 and GE-137. In 2018 there have been reports of several new c-Met imaging radiotracers in

development, including $^{99m}$Tc-HYNIC-cMBP for SPECT (Han et al., 2018) and [$^{18}$F]FP-Met-pep1 for PET imaging (Li et al., 2018). Only one – GE-137 – has been tested in humans so far (Burggraaf et al., 2015).

| Name | Nature | T/C | Imaging technique | Clin |
|---|---|---|---|---|
| $^{64}$Cu-NOTA-rh-HGF | rh-ligand | T/M =13.5 ± 6.1 | PET | No |
| $^{125}$I-mAb | mAb | T/TB = 0.37 | Gamma camera | No |
| $^{125}$I-Met3 | mAb | T/TB = 0.32 ± 0.13, | Gamma camera | No |
| $^{125}$I-Met5 | mAb | T/TB = 0.146 ± 0.097 | Gamma camera | No |
| $^{125}$I-hFab-Met-1 | Fab fragment | – | Gamma camera | No |
| $^{125}$I-MET4 | mAb | – | Gamma camera | No |
| $^{89}$Zr-DN30 | mAb | T/M = 17.5 | PET | No |
| $^{89}$Zr-df-onartuzumab | mAb | T/M = 27 | PET | No |
| $^{89}$Zr-DFO-H2cys-diabody | scFv | T/M =27 ± 14 | PET | No |
| **Ms20-QD** | **scFv** | **T/$T_n$ = 4.3** | **NIR fluorescence** | **No** |
| anti-MET-Gd-DTPA-albumin | mAb | SIC(T/$T_n$) ≈ 5 | MRI | No |
| SPIO-anti-c-MET | PcAb | SIC(T/$T_n$) ≈ 2 | MRI | No |
| $^{125}$I-Met-pep1 | Peptide | – | Gamma camera | No |
| $^{125}$I-cMBP-GGG | Peptide | T/Bl = 2.94 | SPECT | No |
| **cMBP-AOC-Cy5.5** | **Peptide** | **T/M =33.711 ± 3.34** | **NIR fluorescence** | **No** |
| **GE-137** | **Peptide** | **T/Ba = 1.6** | **NIR fluorescence** | **Yes** |
| $^{18}$F-AH113804 | Peptide | T/M ≈ 2 | PET | No |
| $^{99m}$Tc-AH113018 | Peptide | T/M =55.2 ± 13.4 | SPECT | No |
| $^{89}$Zr-PRS-110 | s-protein | T:M = 29 | PET | No |
| $^{11}$C- SU11274 | smTKI | T/$T_N$ = 2.6 | PET | No |

**Table 9 Representative Molecular Imaging Agents Developed for c-Met Imaging in Cancer.** T/C - tumour control area activity ratio; Clin - clinical transformation; T/M - tumour to muscle; T/TB - tumour to total body; T/$T_n$ - tumour to tumour with non-specific probe; SIC - signal intensity changes; T/Bl - tumour to blood; T/Ba - tumour to background fluorescence; T/$T_N$ - tumour to negative tumour. Adapted from (Han et al., 2017)

### 3.1.2 GE-137 Peptide

Clinical utility of the antibody-based probes can be limited primarily due to their slow clearance from the circulation, long retention time in non-targeted tissues, due to their size, and the extensive optimisation necessary for each antibody-tracer (Kaur et al., 2012). Peptide therapies, though not as prevalent in cancer therapies as antibodies (AlDeghaither et al., 2015), have been widely utilized in imaging, offering the advantage of small size, ease of synthesis and modification, tumour-penetrating ability and good biocompatibility (Borghouts et al., 2005). Thus, alongside anti c-Met antibody-based probes, we have assessed the potential of optical imaging of c-Met using GE-137 peptide. GE-137 is a 26 amino acid cyclic peptide conjugated with a modified cyanine 5 as the fluorescent dye (Esfahani et al., 2016), and has high affinity for the extracellular domain of c-Met, with reported $K_d$ of 3 nM in humans (Burggraaf et al., 2015). The fluorophore reporter of GE-137 - Cy5.5 - exhibits optical characteristics similar to Cy5, with peak excitation at 653 nm and peak emission at 675 nm (Liu et al., 2015). The probe – originally developed by General Electric Healthcare – was a gift from Edinburgh Molecular Imaging. Compared to antibody, a peptide such as GE-137 offers several theoretical advantages, including rapid distribution, reduced or absent immunogenicity, and ease and scalability of synthesis.

### 3.1.3 Cy5, a Far-Red Fluorescent Dye

Fluorescence techniques have been extensively used in a range of biological applications. The main benefit of these methods is the ability to observe events with high temporal resolution (Sanderson et al., 2014). The higher the temporal resolution, the shorter the

time between the acquisition of successive images (Men et al., 2017). When combined with microscopy, fluorescence methods are also capable of high spatial resolution. Since the detection of fluorescence is non-invasive, dynamic processes can be followed in living cells and organisms, generating high-quality data (Haustein et al., 2007).

The cyanine dyes have many advantageous properties which make them suitable for use in fluorescent probes. They have a high extinction coefficient (ε) (> 200,000 $cm^{-1}M^{-1}$), moderate quantum yields and photostability. These dyes can be synthesised with excitation maxima ranging from approximately 500 nm to beyond 750 nm (Peng et al., 2005).

The far-red dye Cy5 was used to label anti-c-Met mAbs, with the intention of ultimately developing NIR labelled probes. NIR fluorophores have several advantages over visible-light fluorophores, including superior light penetration in tissue and minimal tissue autofluorescence (Sato et al., 2016). For the purpose of probe development, Cy5 has proven to be bright (with a quantum yield of 0.20, Mujumdar et al., 1993 and high extinction coefficient of 250,000 $cm^{-1}M^{-1}$, Berlier et al., 2003) and has demonstrated a significant advantage over shorter wavelength dyes such as FITC (green, Billinton and Knight, 2001) due the low autofluorescence of biological specimens in the far-red region of the spectrum (Peng et al., 2005).

### 3.1.4 Overall Aim

Taken together, the aim of the investigations in this chapter is to validate the c-Met binding ability of the Cy5-labelled anti-c-Met [EP1454Y] and anti-c-Met (Met13) probes, following initial *in vitro* characterisation. The antibodies, both of which detect epitopes in the extracellular domain of c-Met, were selected from a large number of commercially available antibodies due to their application range (including flow cytometry, immunohistochemistry, western blotting and ELISA), literature references indicating high performance, and availability. Considering the variable quality of commercially available antibodies, the anti-c-Met [EP1454Y] rabbit mAb and anti-c-Met (Met13) mouse mAb were validated using set criteria: their specificity, reproducibility and affinity were assessed in two cell lines, with either a positive (OE33) (Anderson et al., 2006) or negative (FLO-1) c-Met profile. Considering the important role of c-Met in the carcinogenesis and progression of oesophageal cancer, as described in § 1.7, an imaging agent against c-Met would provide an invaluable tool for early detection of neoplastic changes in the oesophagus.

### 3.2 Experimental Set Up

Compared with fixed cell microscopy, live cell imaging offers several advantages, allowing for observation of cellular processes as they happen, as well as providing information about the pharmacokinetics and toxicity of given stimuli. Furthermore, live cell imaging is less prone to experimental artefacts, offering more reliable information (Drummen, 2012, Miyawaki et al., 2003).

However, successful live cell imaging experiments can be technically challenging. It is important to ensure cells are healthy and function normally while on the microscope stage, often in the presence of synthetic fluorophores or fluorescent proteins. The conditions under which cells are maintained on the microscope stage often dictate the success or failure of an experiment.

To acquire live cell images, the Oxford Institute for Radiation Oncology high content open microscopy design was used (Figure 3.1 A). This approach demonstrates the first implementation of time-domain fluorescence microscopy in a flexible automated platform to use in routine biology applications (Barber et al., 2013). Abbe microscope design allows for easy expansion and modification of the platform capabilities, as demonstrated by the addition of custom-built live cell imaging chamber (Figure 3.1 C). The chamber allows an investigator to maintain the conditions necessary for normal growth of cells, a pre-requisite for experimental success. The chamber was designed to maintain a constant temperature and high humidity for the growth of tissue culture cells under a 5% $CO_2$ atmosphere. Relative humidity was controlled by bubbling $CO_2$ through a water bath, thus feeding humidified $CO_2$ into the chamber. Temperature was regulated

through a heating element with thermostatic control. Figure 3.2 shows OE33 cells successfully maintained for up to 48 hours in the custom-built live cell imaging chamber. This imaging chamber kept the cells growing normally throughout all experiments.




**Figure 3.1 The Open Microscope 'Abbe'.** A) External photograph without light shielding in place, showing the optical components inside. B) Photograph of part of the internal optics: stage, inverted objective and fluorescent cube changer (arrow point). C) Photograph of live cell imaging chamber in place, on the top of the stage, with light shielding around the optical components.

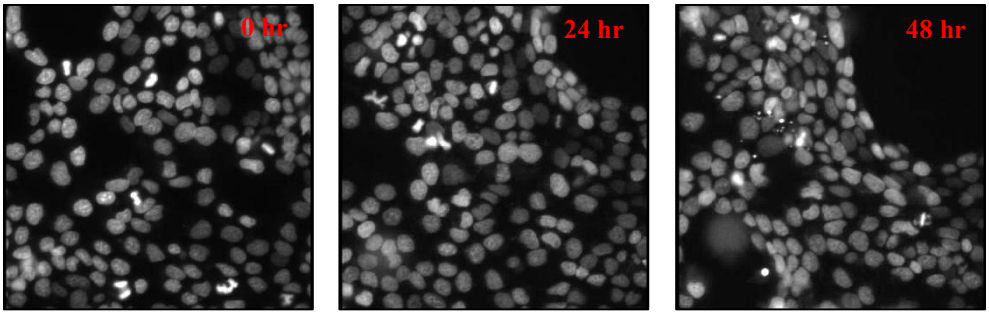



**Figure 3.2 Maintaining Live Cells Using Live Cell Imaging Chamber.** A series of images was captured from OE33 cells left for 48 hours in the live cell imaging chamber. The imaging chamber kept the cells functioning normally for the duration of experiment.

## 3.3 Results

### 3.3.1 Validation of the Anti c-Met [EP1454Y] and (Met13) Antibodies

The anti-c-Met [EP1454Y] rabbit monoclonal and anti-c-Met (Met13) mouse monoclonal antibodies were validated using set criteria. Their specificity, reproducibility, and affinity were assessed, prior and after labelling with Cy5 fluorescent dye. The oesophageal adenocarcinoma cell lines OE33 and FLO-1, were used throughout as c-Met positive and negative control cell types, respectively (Anderson et al., 2006).

#### 3.3.1.1 Specificity of the Anti-c-Met [EP1454Y] and (Met13) Antibodies Tested in a Panel of Cancer Cell Lines

To confirm the endogenous expression level of c-Met and test specificity of the anti-c-Met antibodies, western blot analyses were performed in a panel of neoplastic cell lines as the first verification. Whole cell extracts were collected from OE33, FLO-1, HTC116 (colon carcinoma) and T47D (invasive ductal carcinoma cell line, reported negative for c-Met expression, Beviglia et al., 1997) and samples (50 μg/lane) were loaded onto 4-12% Bis-Tris protein gels followed by immunoblotting for c-Met, using anti-c-Met [EP1454Y] antibody as described in § 2.2. The expression of c-Met protein was relatively high in the OE33, low in HTC116 and undetectable in FLO-1 and T47D cell lines (Figure 3.3). The specificity of the antibody was confirmed by a presence of a single band at a corresponding molecular weight of the protein of interest (approx. 156 kDa). Anti-c-Met (Met13) antibody exhibited low reactivity and specificity towards denatured c-Met by

western blotting (data not shown). This monoclonal antibody has been previously described as not recommended for western blotting (Wong et al., 2013).

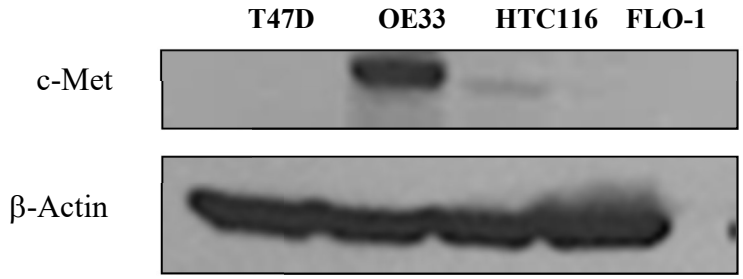



**Figure 3.3 [EP1454Y] Antibody Validation and c-Met Protein Expression Levels for Neoplastic Cell Lines, Detected by Western Blot.** Equal amounts of whole cell extracts (50 μg total protein) were compared and β-actin was used as a loading control. The expression of c-Met protein was high in the OE33, low in HTC116 and undetectable in FLO-1 and T47D cell lines. The specificity of the antibody was confirmed by a presence of a single band at a corresponding molecular weight of the protein of interest (approx. 156 kDa).

### 3.3.1.2 Determination of Anti-c-Met [EP1454Y] and (Met13) Affinity by ELISA

In order to gain insight of the interaction between the antigen binding site of anti-c-Met [EP1454Y] and (Met13) antibodies and the c-Met epitope, the equilibrium dissociation constant ($K_d$) was characterised. An interaction of high affinity is represented by a low $K_d$, where the association rate ($K_{on}$) is many orders of magnitude faster compared to the dissociation rate ($K_{off}$) (Salahudeen and Nishtala, 2017).

Indirect enzyme-linked immunosorbent assay (ELISA) was used, as described in § 2.4. In this experiment, an antigen – synthetic peptide within human c-Met – was immobilised on the surface and recognised by the anti-c-Met [EP1454Y] and (Met13) monoclonal antibodies. Subsequently, anti-c-Met [EP1454Y] and (Met13) monoclonal antibodies were bound by a secondary, enzyme linked antibody (horseradish peroxidase, HRP). This allowed for detection using a substrate-chromogen reagent that recognises the conjugated enzyme and allows for development of colour, and successively, a colometric analysis. The absorbance was measured at 450 nm.

The $K_d$ values for the anti-c-Met [EP1454Y] and (Met13) monoclonal antibodies were determined by testing a range of concentrations for anti-c-Met [EP1454Y] and (Met13). Figure 3.4 displays representative binding curves, showing binding of anti-c-Met [EP1454Y] and (Met13) antibodies to their c-Met epitopes, with the equilibrium dissociation constants $K_d$ of 2.804 ± 0.62 nM and 1.88 ± 0.28 nM for [EP1454Y] and (Met13), respectively, *versus* $K_d$ of 3 ± 0.5 nM for GE-137 as reported by Burggraaf and colleagues (2015).

The data was fitted to a saturation binding curve using a non-linear regression fitting model of the GraphPad Prism 7 software using the following equation:

$$Y = B_{max} \times X_n \, (K_d + X_n)$$

Where $B_{max}$ stands for the maximum specific binding, X for the concentration (Pedersen et al., 1994), n represents the curve slope factor, and $K_d$ is the dissociation constant. The background was considered equal to the reading obtained where no antibody was added,

representing non-specific binding. Low $K_d$ value represents greater binding affinity of the ligand to its target (Salahudeen and Nishtala, 2017); consequently, it is concluded that the nanomolar range $K_d$ of the anti-c-Met [EP1454Y] and (Met13) antibodies indicates anti-c-Met [EP1454Y] and (Met13) antibodies have high affinity for c-Met antigen.

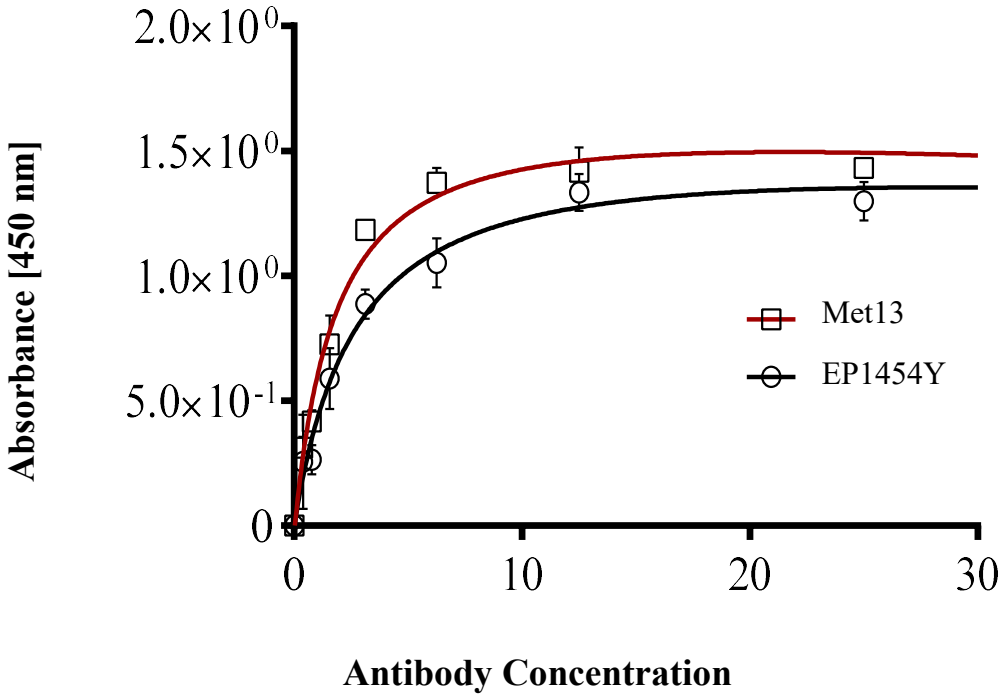



**Figure 3.4 Evaluation of Binding Affinity by ELISA.** Saturation binding curves representing the binding of the anti-c-Met [EP1454Y] and (Met13) monoclonal antibodies to the c-Met antigen immobilised on the surface of the ELISA plate. The $K_d$ values were 2.804 ± 0.62 nM and 1.88 ± 0.28 nM for EP1454Y and Met13, respectively (mean ± SEM, n = 3 independent biological experiments). These values compare favourably with GE-137 peptide, with a reported $K_d$ value of 3 ± 0.5 nM (Burggraaf et al., 2015)

### 3.3.2 Fluor-Labelling with Cy5 Fluorophore and *In Vitro* Validation of Cy5-EP1454Y and Cy5-Met13 Probes

#### 3.3.2.1 Cy5 Labelling

Anti-c-Met [EP1454Y] and (Met13) antibodies were labelled with the fluorescent dye, Cy5, as described in § 2.3.3. Subsequently, OE33 cells were seeded and left to adhere overnight, and the following day incubated for 3 h with 2 μg/mL of either Cy5-EP1454Y, Cy5-Met13 or native, unmodified [EP1454Y] or (Met13) antibody (as described in § 2.4) and subsequently analysed using an Infinite 200 Pro plate reader. Native, unlabelled anti-c-Met [EP1454Y] and (Met13) did not emit fluorescence beyond the background level of 70 ± 20 AU and 84 ± 22 AU, respectively. In contrast, the Cy5-labelled anti-c-Met probes emitted red fluorescence when excited at 640 nm. The means values were 1,368 ± 197 AU and 1,889 ± 242 AU, for Cy5-Met13 and Cy5-EP1454Y, respectively (mean ± SD, n = 3 independent biological experiments, $P < 0.0001$, one-way ANOVA) (Figure 3.5). This result confirms successful labelling of anti-c-Met [EP1454Y] and (Met13) antibodies with Cy5 fluorescent dye.

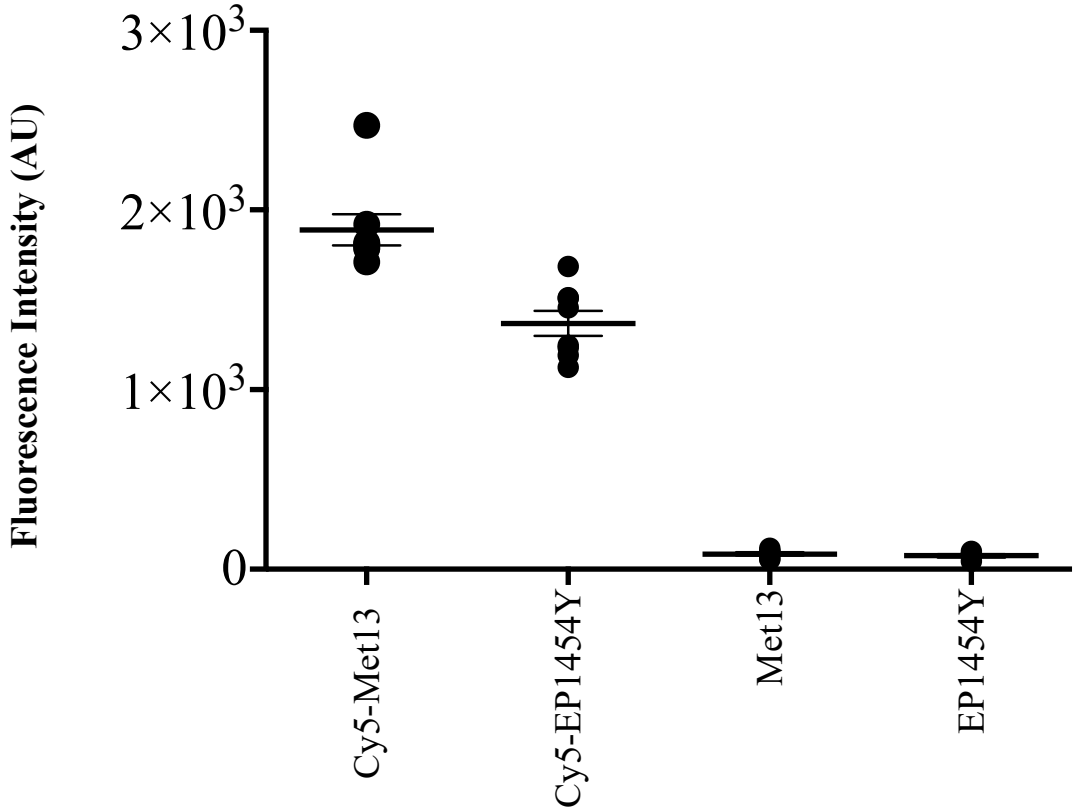



**Figure 3.5 Fluorescence Intensity of Anti-c-Met Cy5-Labelled Constructs.** OE33 cells were seeded and left to adhere overnight, and the following day incubated for 3 h with 2 μg/mL of either Cy5-EP1454Y, Cy5-Met13 or native, unmodified [EP1454Y] or (Met13) antibody (as described in § 2.4) and subsequently analysed using anInfinite 200 Pro plate reader**.** Cy5-labelled anti-c-Met probes emitted red fluorescence when excited at 640 nm. (mean ± SEM, n = 3 independent biological experiments, $P < 0.0001$, one-way ANOVA).

### 3.3.2.2 Determination of Cy5-EP1454Y and Cy5-Met13 Affinity by Immunocytochemistry (ICC)

To determine whether the interaction between the antigen binding site of the anti-c-Met [EP1454Y] and (Met13) antibodies and the c-Met epitope changed due to addition of Cy5, the $K_d$ value of Cy5-EP1454Y and Cy5-Met13 was determined. ICC was used, as

described in § 2.5. In this experiment, an antigen – c-Met protein on the surface of OE33 cells – was immobilised to the surface by allowing OE33 cells to adhere to the plate overnight. The attachment of Cy5 far-red dye allowed for detection using a microscope as described in § 2.6.

The $K_d$ values for the Cy5-EP1454Y and Cy5-Met13 antibodies were determined by testing a range of concentrations of Cy5-EP1454Y and Cy5-Met13. Figure 3.6 displays representative binding curves, showing binding of the Cy5-EP1454Y and Cy5-Met13 antibodies to the c-Met epitope, with an affinity constants $K_d$ of 11.24 ± 2.59 nM and 7.25 ± 1.99 nM for Cy5-EP1454Y and Cy5-Met13, respectively (mean ± SEM, n = 3 independent biological experiments). Low $K_d$ values within the same order of magnitude as native anti-c-Met [EP1454Y] and (Met13) mAbs (2.804 nM and 1.88 nM) indicate that the high binding affinity of the ligand to its target has been retained despite the Cy5 modifications (P = 0.0339 and P = 0.557, unpaired t-test), demonstrating that the synthesized anti-c-Met probes have high affinity for c-Met antigen.

Finally, the $IC_{50}$ values were evaluated to determine the sensitivity, which represented the concentration of Cy5-EP1454Y and Cy5-Met13 antibodies that produced 50% inhibition of native antibody binding to the antigen, c-Met protein expressed on the surface of OE33 cells, as described in § 2.4 and § 2.5. The $logIC_{50}$ values recorded were of 0.21 ± 0.12 nM and -0.12 ± 0.07 nM (mean ± SEM, n = 2 independent biological repeats) for Cy5-EP1454Y (Figure 3.7 A) and Cy5-Met13 (Figure 3.7 B), respectively. The Cy5-Met13 antibody has shown to be more sensitive, and thus has been scored as more favourable for future use.

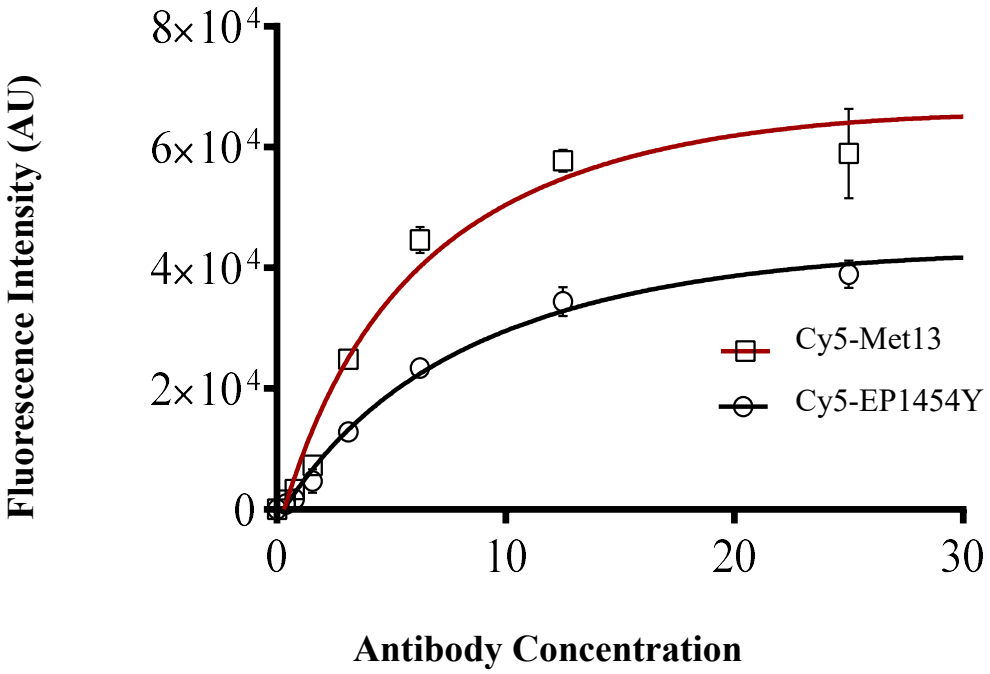



**Figure 3.6 Evaluation of Binding Affinity by ICC.** Saturation binding curves representing the binding of the Cy5-EP1454Y and Cy5-Met13 probes to the c-Met antigen, expressed on the surface of OE33 cells. The attachment of Cy5 far-red dye allowed for detection using a fluorescent microscope. The $K_d$ values were 11.24 ± 2.59 nM and 7.25 ± 1.99 nM for Cy5-EP1454Y and Cy5- Met13, respectively (mean ± SEM, n = 3 independent biological experiments).

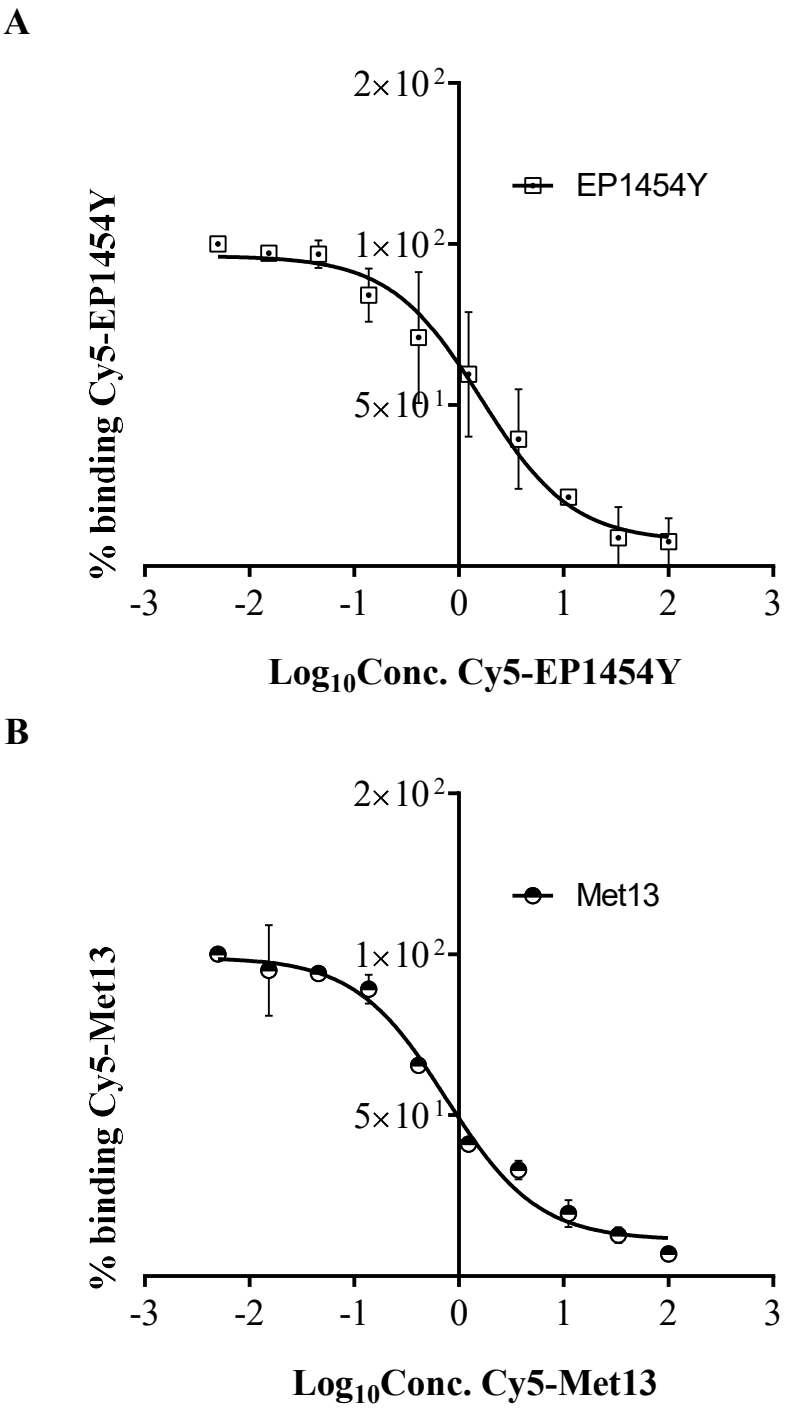



**Figure 3.7 Competition Binding Assay.** A) ICC showing binding of Cy5-EP1454Y to c-Met epitope, expressed on the surface of OE33 cells, in competition with increasing concentrations of anti-c-Met [EP1454Y]. The $logIC_{50}$ value recorded was of 0.21 ± 0.12 nM. B) ICC showing binding of Cy5-Met13 to c-Met epitope, expressed on the surface of OE33 cells, in competition with increasing concentrations of anti-c-Met (Met13). The $logIC_{50}$ value recorded was of -0.12 ± 0.07 nM (mean ± SEM, n = 2 independent biological experiments).

### 3.3.3 Cy5-EP1454Y and Cy5-Met13 Antibodies Bind OE33 but Not FLO-1 Cells

The ability of the Cy5-EP1454Y and Cy5-Met13 conjugates to bind c-Met was validated by live-cell fluorescence imaging. Direct visualisation of the antibody and its cellular localisation was achieved by using Cy5-labelled antibody conjugates and Hoechst 33342 nuclear stain.

#### 3.3.3.1 Cy5-EP1454Y and Cy5-Met13 Demonstrate Uptake in OE33 but Not FLO-1 Cells

The c-Met binding properties of the antibody constructs were evaluated in OE33 and FLO-1 cells. Both cells lines were exposed to Cy5-EP1454Y and Cy5-Met13 or controls, Cy5-IgG (rabbit, rb) or Cy5-IgG (mouse, ms), for 3 hours at 37°C (3 μg/mL). Hoechst 33342 stain and Calcein, a cell-permeant dye, were used to determine the number of nuclei and to assess gross cell morphology. Prior to imaging with fluorescent microscope, standard cell media was replaced with fresh, phenol red free cell media, as described in § 2.6. OE33 cells showed high uptake of anti-c-Met Cy5-EP1454Y and Cy5-Met13 probes, but not the respective Cy5-IgG controls (Figure 3.8). FLO-1 cells showed low uptake of anti-c-Met Cy5-EP1454Y and Cy5-Met13 probes and their respective Cy5-IgG controls (Figure 3.9).

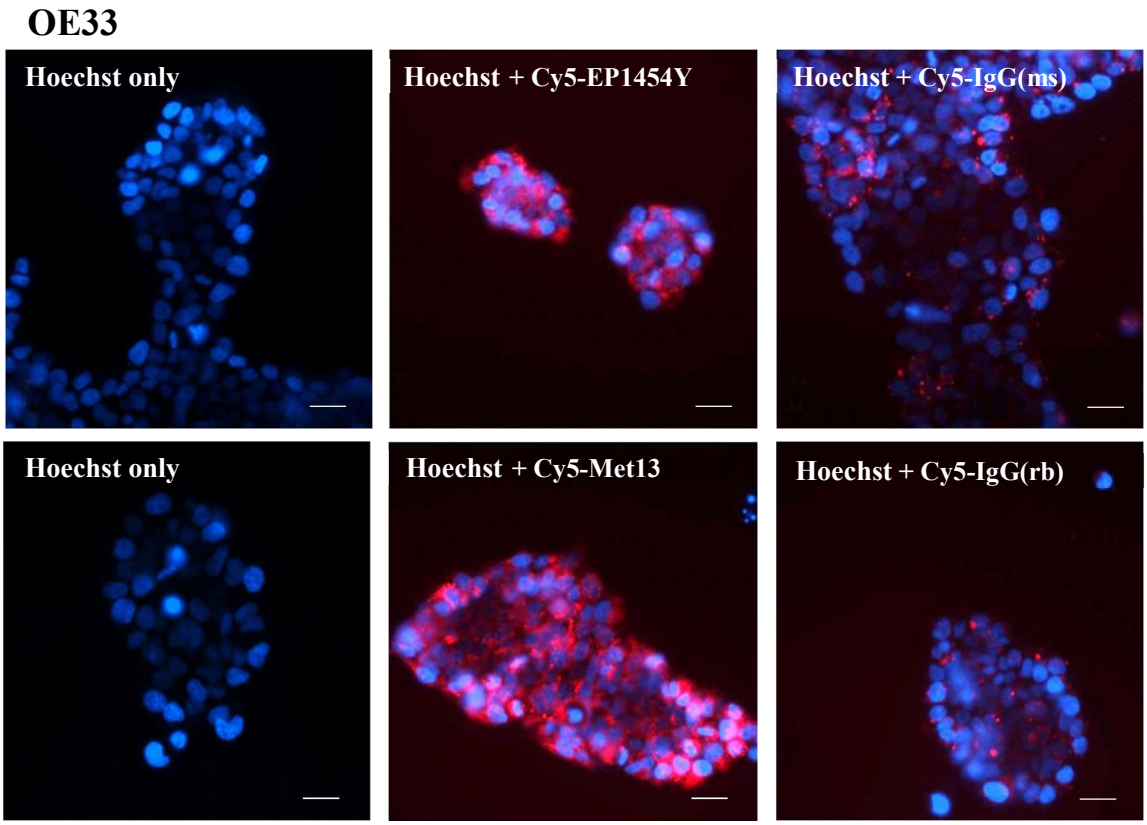



**Figure 3.8 Binding Properties of the Cy5-EP1454Y and Cy5-Met13 in OE33 Cells.** Immunofluorescence microscopy: OE33 cells were exposed to Cy5-EP1454Y and Cy5-Met13 or control conjugates, non-specific Cy5 labelled IgG constructs, for 3 h at 37°C (3 µg/mL). Hoechst 33342 staining was used to determine the number of nuclei and to assess gross cell morphology. OE33 show high uptake of anti-c-Met Cy5-Ep1454Y and Cy5-Met13 probes, but not their respective Cy5-IgG controls. Bar size is 20 µm.

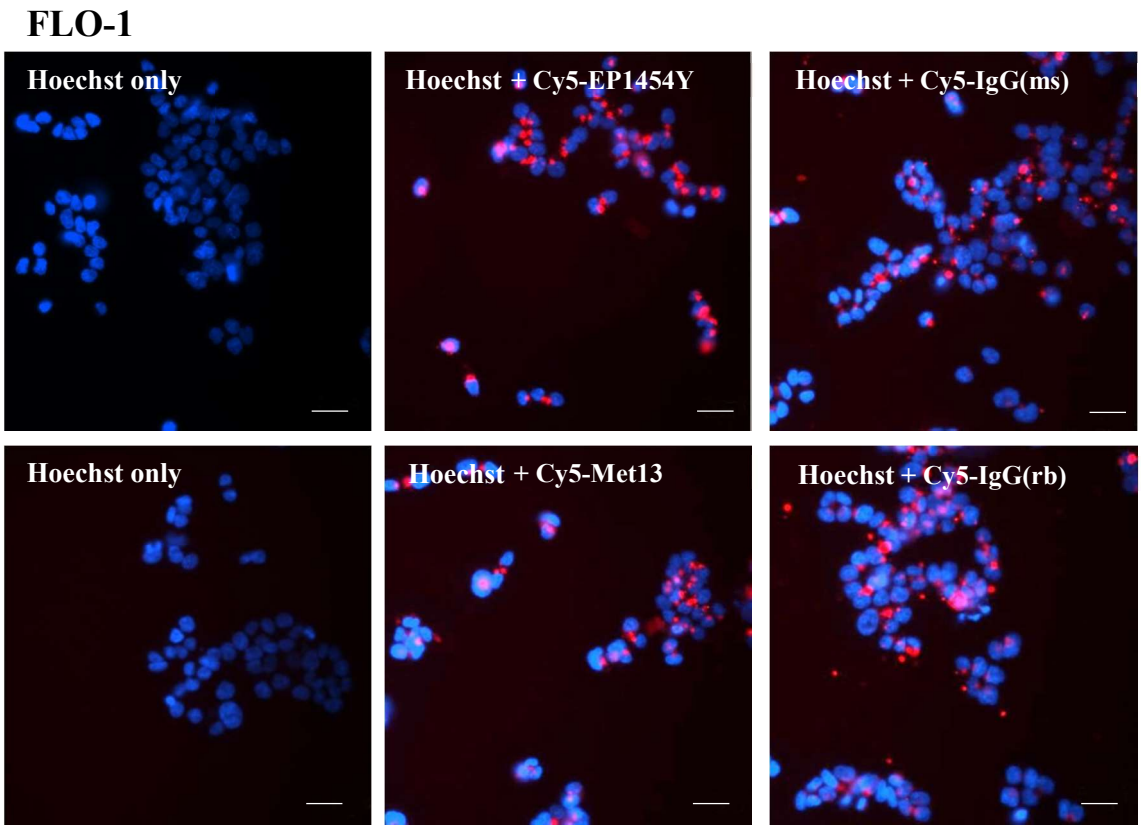



**Figure 3.9 Binding Properties of the Cy5-EP1454Y and Cy5-Met13 in FLO-1 Cells.** Immunofluorescence microscopy: FLO-1 cells were exposed to Cy5-EP1454Y and Cy5-Met13 or control conjugates, non-specific Cy5 labelled IgG constructs, for 3 h at 37°C (3 μg/mL). Hoechst 33342 staining was used to determine the number of nuclei and to assess gross cell morphology. FLO-1 cells show low uptake of anti-c-Met Cy5-Ep1454Y and Cy5-Met13 probes and their respective Cy5-IgG controls. Bar size is 20 μm.

Figure 3.10 shows fluorescent intensity per cell averaged from three independent experiments, where the c-Met binding properties of the antibody constructs from different antibody batches were evaluated and assessed for reproducibility. Both OE33 and FLO-1 cells were exposed to Cy5-EP1454Y and Cy5-Met13 or their respective controls, Cy5-IgG (rb) or Cy5-IgG (ms), for 3 hours at 37°C (3 μg/mL). OE33, a high c-Met expressing cell line, shows high average fluorescent intensity per cell of 169,564 ± 25,839 AU and 156,784 ± 3,613, for Cy5-EP1454Y and Cy5-Met13, respectively. In comparison, OE33 cells show significantly lower staining when exposed to control conjugates, non-specific Cy5 labelled IgG constructs, with mean values of 50,834 ± 4,259 AU for Cy5-IgG (rb) and 57,826 ±10,620 AU for Cy5-IgG (ms) (Mean ± SEM, n = 3 independent biological repeats, $P < 0.01$, two-way ANOVA). FLO-1, a low c-Met expressing cell line, shows lower average intensities per cell in comparison to OE33 cells, with average intensity per cell of 40,034 ± 13,656 AU and 28,003 ± 17,237, for Cy5-EP1454Y and Cy5-Met13, respectively. The level of probes uptake in FLO-1 cells is comparable to their uptake of the control, non-specific Cy5 labelled IgG constructs, with averages of 30,381 ± 7,855 AU for Cy5-IgG (rb) and 38,993 ± 23,132 AU for Cy5-IgG (ms) (Mean ± SEM, n = 3 independent biological repeats, $P < 0.001$, two-way ANOVA).

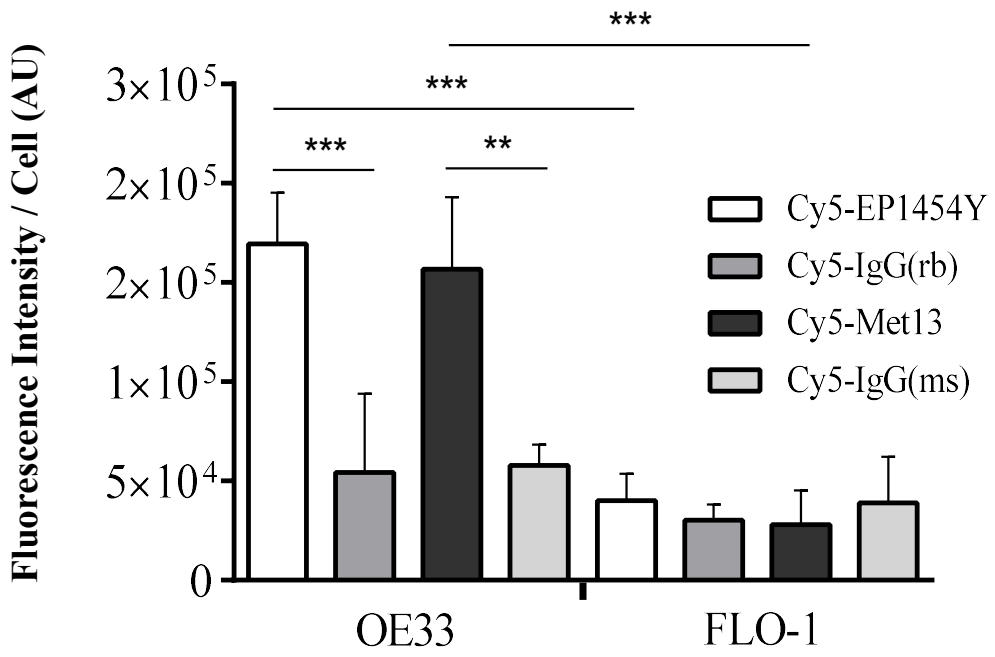



**Figure 3.10 The c-Met Binding Properties of the Antibody Constructs Were Evaluated in OE33 and FLO-1 Cells.** Both cell lines were exposed to Cy5-EP1454Y and Cy5-Met13 or their respective controls, Cy5-IgG (rb) or Cy5-IgG (ms), for 3 hours at 37˚C (3 μg/mL). OE33, a high c-Met expressing cell line, shows high average fluorescent intensity per cell after treatment with Cy5-EP1454Y and Cy5-Met13 but lower average fluorescent intensity when pre-treated with Cy5-IgG (rb) and Cy5-IgG (ms) (Mean ± SEM, n = 3 independent biological repeats, $^{**}$ $P < 0.01$, one-way ANOVA). FLO-1, a low c-Met expressing cell line, shows lower average intensities per cell in comparison to OE33 cells, for Cy5-EP1454Y and Cy5-Met13, respectively. The level of probes uptake in FLO-1 cells is comparable to the uptake of the control probes (Mean ± SEM, n = 3 independent biological repeats, $^{***}$ $P < 0.001$, one-way ANOVA).

### 3.3.3.2 Investigation of the Specificity of the Cy5-EP1454Y and Cy5-Met13 Probes in OE33 Cells

To test whether down regulation of c-Met protein abrogates signal from Cy5-EP1454Y and Cy5-Met13 antibodies, a siRNA knockdown method was used. This technique is extensively used for antibody validation, and relies on a mechanism in which the expression of a target protein is suppressed by siRNA selectively binding and subsequently leading to degradation of the target mRNA (Bernstein et al., 2001). OE33 cells were treated with siRNA-transfection buffer as described in § 2.7 and c-Met knockdown was confirmed by western blot analysis (Figure 3.11). Subsequently, non-transfected and transfected OE33 cells were exposed to Cy5-EP1454Y and Cy5-Met13 for 3 h at 37°C (3 μg/mL). As shown in Figure 3.12, successful knockdown of c-Met protein caused a three-fold decrease of the probe uptake in the knockdown OE33 cells, but not in untreated, control OE33 cells (non-transfected, NT). Furthermore, as shown in Figure 3.13, there is a significant difference in the average fluorescence intensity per cell between c-Met knockdown and untreated OE33 cells (Mean ± SD, $P < 0.0001$, one-way ANOVA) for both Cy5-EP1454Y (154,044 ± 23,628 for NT versus 46,825 ± 17,432 for OE33 si.MET) and Cy5-Met13 (120,397 ± 19,519 for NT versus 12,122 ± 8,359 for OE33 si.MET) probes. There is no significant difference in fluorescence intensity per cell between untreated and control (si.NS, non-specific siRNA) OE33 cells. Taken together, these results indicate that Cy5-EP1454Y and Cy5-Met13 probes have high specificity for c-Met and show low off-target binding.

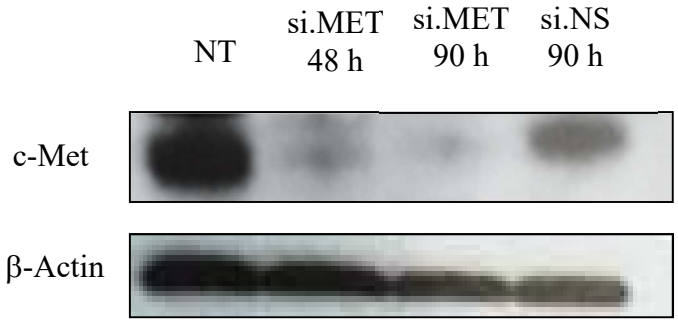



**Figure 3.11Validation of siRNA-Mediated c-Met Knockdown in OE33 Cell Line.** OE33 cells were incubated with either a c-Met-targeting siRNA pool (si.MET) or Non-Specific pool (si.NS), and harvested at different times for western blot analysis. Non-transfected cells (NT) were used as a control. Equal amounts of whole cell extracts (50 μg total protein) were compared and β-actin was used as a loading control.

To further determine whether binding of Cy5-EP1454Y and Cy5-Met13 was specific, an unlabelled anti-c-Met [EP1454Y] and (Met13) antibody blocking experiment was performed. Before proceeding with the staining protocol using Cy5-EP1454Y and Cy5-Met13 probes, the c-Met epitope on the surface of OE33 cells was blocked by a 3 h incubation with a 5-fold excess of unlabelled anti-c-Met [EP1454Y] or (Met13) antibody before further 3 h incubation with a corresponding, Cy5-labelled probe, that recognizes the same epitope, with a washing step in between. In principle, the unlabelled anti-c-Met [EP1454Y] and (Met13) antibody that is bound to the c-Met epitope should prevent binding by Cy5-EP1454Y and Cy5-Met13 probes. As shown in Figure 3.14, incubation with unlabelled anti-c-Met (Met13) antibody prior to incubation with Cy5-Met13 probe resulted in almost 50% decrease in average intensity per cell, with the values of 147,088

± 21,041 AU versus 71,035 ± 6,610 AU for untreated and 'blocked' OE33 cells (Mean ± SD, $P < 0.0001$, one-way ANOVA). However, there was no significant difference in the average fluorescent intensity per cell between untreated and 'blocked' OE33 cells when cells were pre-incubated with unlabelled anti-c-Met [EP1454Y] antibody prior to incubation with its labelled equivalent (189,000 ± 13,000 AU versus 202,000 ± 6,000 AU, respectively), suggesting that anti-c-Met [EP1454Y] antibody possible recognises another epitope, resulting in a degree of the off-target, non-c-Met-specific binding.

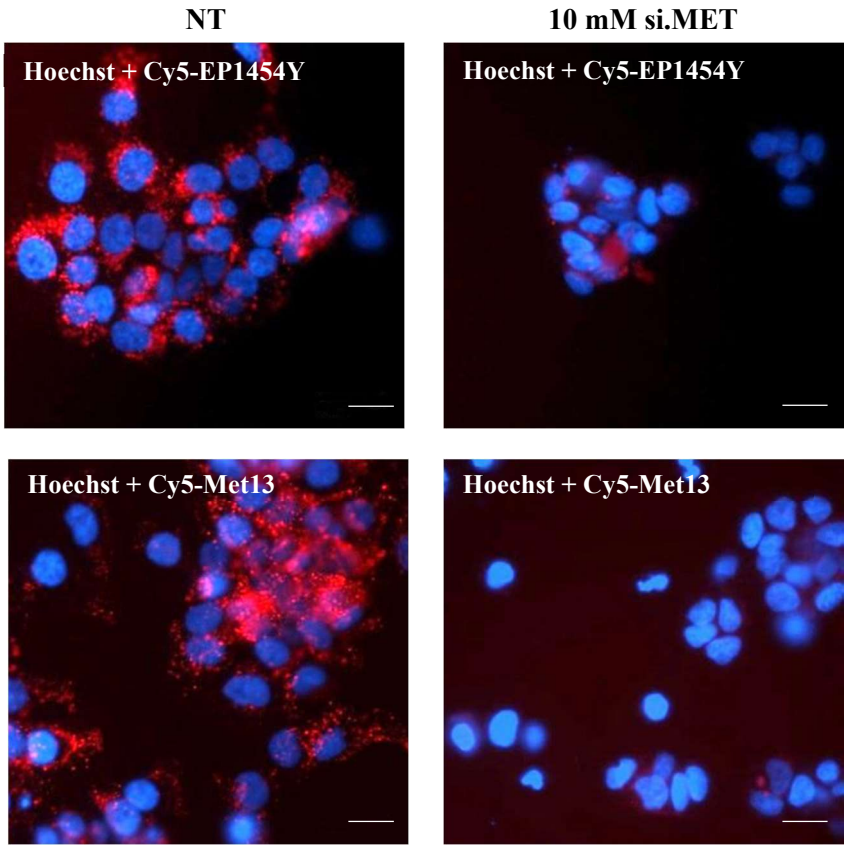



**Figure 3.12 Validation of the Off-Target Binding of Cy5-EP1454Y and Cy5-Met13, Immunofluorescence Microscopy.** Untreated, non-transfected and si.MET transfected OE33 cells were exposed to Cy5-EP1454Y and Cy5-Met13 for 3 h at 37˚C (3 µg/ml). Hoechst 33342 staining was used to determine the number of nuclei and to assess gross cell morphology. si.MET transfected OE33 cells show lower uptake of anti-c-Met Cy5-EP1454Y and Cy5-Met13 probes, when compared to non-transfected OE33 cells. Bar size is 20 µm.

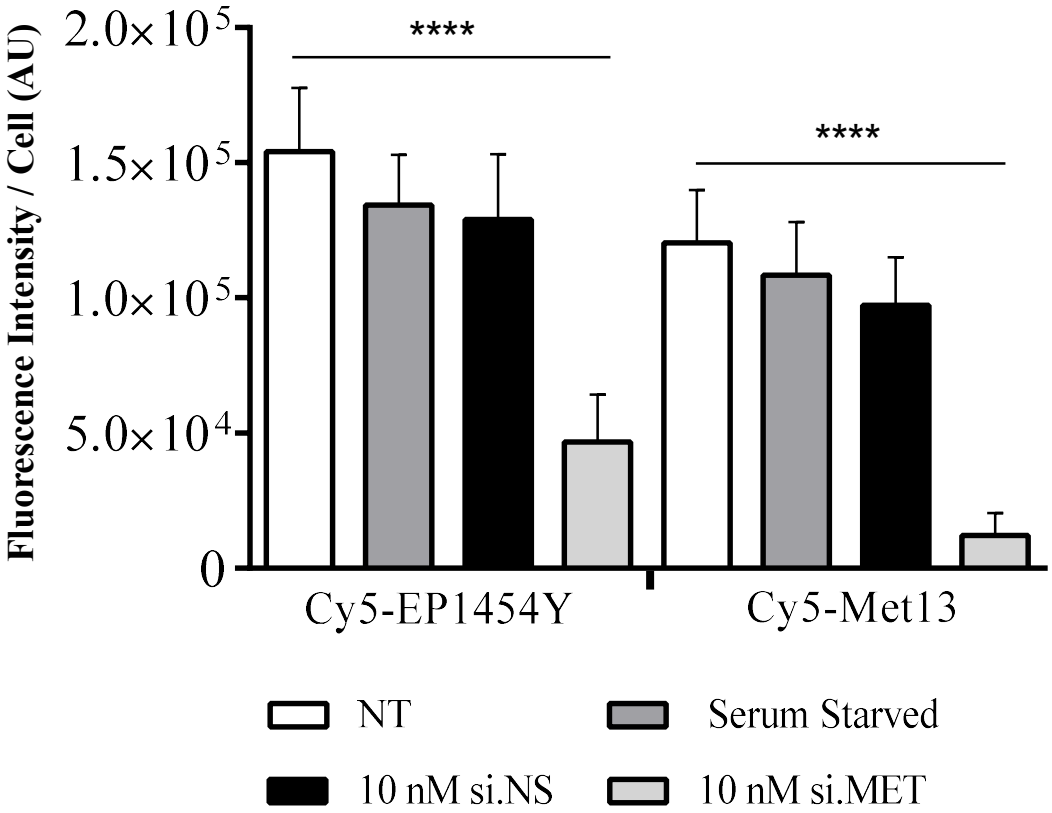



**Figure 3.13 Validation of the Off-Target Binding of Cy5-EP1454Y and Cy5-Met13, siRNA Knockdown.** Untreated, non-transfected (NT, 10 nM) and si.MET transfected (10 nM) OE33 cells were exposed to Cy5-EP1454Y and Cy5-Met13 (3 h at 37°C, 3 μg/ml) and the binding of the probe was subsequently determined using the Abbe microscope and further analysed to give average fluorescent intensity per cell of untreated, control and c-Met knockdown OE33 cells (Mean ± SD, **** $P < 0.0001$, one-way ANOVA).

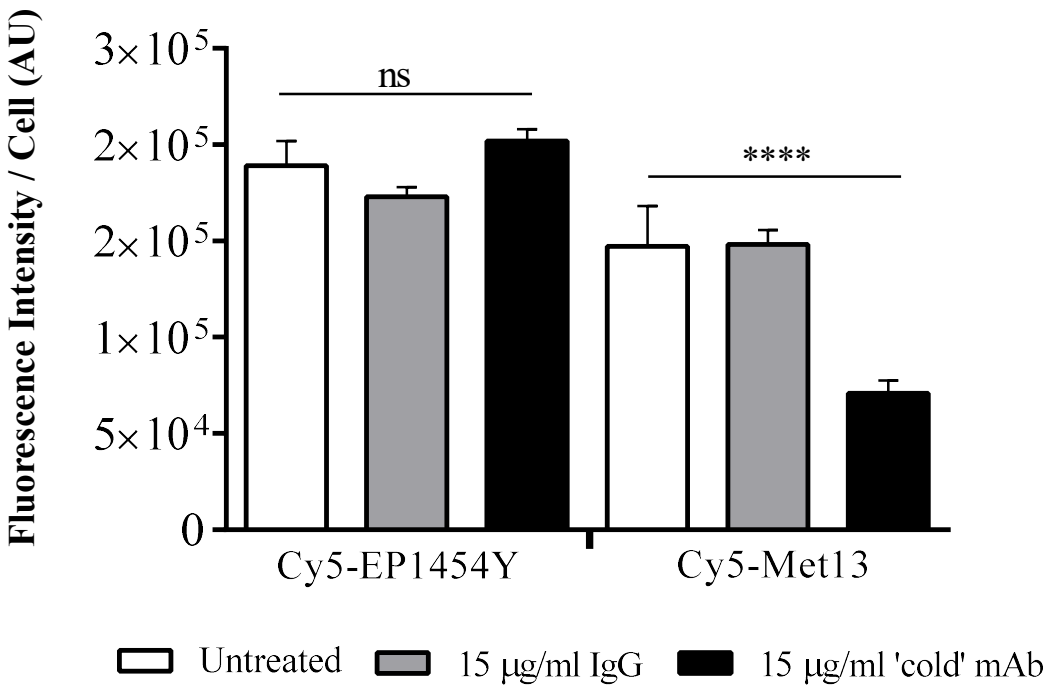



**Figure 3.14 Validation of the Off-Target Binding of Cy5-EP1454Y and Cy5-Met13, Blocking Experiment.** OE33 cells were pre-incubated with a 5-fold excess of unlabelled anti-c-Met (Met13) or anti-c-Met [EP1454Y] antibodies (3 h at 37°C, 15 μg/mL) prior to treatment with Cy5-Met13 or Cy5-EP1454Y probes (3 h at 37°C, 3 μg/mL). The binding of the fluorescent probes was subsequently determined using Abbe microscope and further analysed to give average fluorescent intensity per cell between 'blocked' and control OE33 cells. (Mean ± SD, **** $P < 0.0001$, one-way ANOVA).

## 3.4 Discussion

In this chapter, mouse monoclonal anti-c-Met (Met13) and rabbit monoclonal anti-c-Met [EP1454Y] antibodies were validated *in vitro* using several assays, to investigate their potential suitability as the c-Met-targeting vector for a diagnostic probe.

### 3.4.1 Specificity of the Anti-c-Met [EP1454Y] and (Met13) Antibodies Tested in a Panel of Cancer Cell Lines

The anti-c-Met [EP1454Y] antibody was shown to be specific, giving a single band at approx. 156 kDa in Western blot analysis of OE33 cell lysate (Figure 3.3). No other bands were present across the membrane at different molecular weights, which suggests a lack of sample degradation or splice or other variants (Ghosh et al., 2014). There was no detectable c-Met in the FLO-1 cell line, and this was comparable to a known negative control cell line T47D (Beviglia et al., 1997). This has challenged the existing literature, which shows FLO-1 to be a c-Met positive cell line (Herrera et al., 2005, Watson et al., 2006). However, repeated western blots analysis of the verified FLO-1 cells further confirmed low c-Met expression in FLO-1 cells used throughout this chapter. Anti-c-Met (Met13) antibody exhibited low reactivity and specificity towards denatured c-Met by western blotting (data not shown). This monoclonal antibody has been previously described as not recommended for western blotting application (Wong, 2013). These results suggest that anti-c-Met (Met13) antibody recognizes a conformational epitope, where key amino acid residues are brought together by protein folding (Forsstrom et al., 2015), whereas anti-c-Met [EP1454Y] recognizes linear epitope, where a stretch of amino acids is sufficient for binding of the antibody (Sela, 1969). Antibodies directed

towards linear epitopes give WB bands (Forsstrom et al., 2015). In contrast, antibodies towards conformational epitopes did not bind their target proteins in the WB assays, demonstrating the advantage of using antibodies recognizing linear epitopes for immunoassays involving whole or partial denaturation of the protein targets – a process shown to destroy conformational epitopes by unfolding the protein structure (Fowler et al., 2011, Freire et al., 1990).

### 3.4.2 Determination of the Anti-c-Met [EP1454Y] and (Met13) Affinity by ELISA

An imperative part of antibody characterisation includes the determination of antibody-antigen affinity constants and binding kinetics, which may be predictive of antibody performance in biotechnological applications (Neri et al., 1996). Representative binding curves in Figure 3.4 demonstrate good affinity of both anti-c-Met [EP1454Y] and (Met13) antibodies to the c-Met epitope, and were generated using a solid-phase ELISA method, which provides reproducible and precise estimates of $K_d$ for antigen-antibody complexes (Kim et al., 1990). Low $K_d$ values in the nM range obtained for both mAbs represents high binding affinity, however, (Met13) antibody, having lower $K_d$ value, seems to be have more translational potential than [EP1454Y]. *In vivo* detection of biomarkers is complex, owing to molecular imaging agents being exposed to host's physiology before they are delivered to the tumour site, where $K_d$ (molecular affinity) and specificity against the target will determine the interaction between the probe and the biomarker expressed by the neoplastic cells (Chauhan et al., 2013). Factors affecting the clinical performance of diagnostic probes include molecular weight, conformation, and interaction with other molecules in serum, and specificity and affinity for antigen of interest (Leelawattanachai et al., 2015, Lammers et al., 2012).

### 3.4.3 Fluor-Labelling with Cy5 Fluorophore and *In Vitro* Validation of Cy5-EP1454Y and Cy5-Met13 Probes

Fluorescence-based assays are essential experimental tools which allow the detailed analysis of molecular mechanisms (Toseland, 2013). Proteins have intrinsic fluorescence, dominated by tryptophan residues (Ray et al., 2009). However, extrinsic labels provide much greater advantages for studying biological processes, due to enhanced fluorescence intensity observed. Successful labelling of the anti-c-Met [EP1454Y] and (Met13) antibodies with Cy5 allowed for a visualisation of the c-Met internalisation using live cell fluorescence microscopy. Upon activation, c-Met has been shown to be internalised and recycled through endocytic pathways and mechanisms (Viticchie et al., 2015) – this explains why fluorescent signal was detected in the cytoplasms rather than on the cell membranes of OE33 cells. In the future, low-temperature condition (4 degrees C) and endocytosis inhibitors could be utilised to futher investigate the mechanism of Cy5-EP1454Y and Cy5-Met13 probes uptake by OE33 cells. The chemistry applied to facilitate Cy5 conjugation utilised primary amine groups present in the antibody, including its active site, hence leading to random distribution of Cy5 molecules across antibody domains. Therefore, this has the potential to result in alterations in the binding capacity of the antibody to its target or even complete inactivation of the antibody (Vira et al., 2010). However, the analysis of § 3.3.2.2 shows that immunoreactivity of the anti-c-Met [EP1454Y] and (Met13) antibodies was not affected to a significant degree by Cy5 modification. The dye-to-protein labelling ratio varied between 8 and 10 – within the 'ideal' range suggested by the manufacturer. This is important, as the number of copies of a fluorophore conjugated to an antibody effects the fluorescence quantum yield (Szabo et al., 2018). Furthermore, the $IC_{50}$ values were

evaluated to determine the potency of the Cy5-labelled conjugates, which represented the concentration of Cy5-EP1454Y and Cy5-Met13 antibodies that produced 50% inhibition of native antibody binding to the antigen, c-Met protein expressed on the surface of OE33 cells. The Cy5-Met13 antibody was shown to be more potent, and thus has been scored as more favourable for future use. Potency of a drug or a compound can be defined by *in vitro* $IC_{50}$ value, which represents a 50% inhibitory concentration (Webb et al., 2015) or, in the case describe in this chapter, a concentration at which Cy5-labelled anti-c-Met probes can compete with native, unlabelled antibodies to successfully bind to half of the available c-Met receptors. Lower relative $IC_{50}$ value of Cy5-Met13 represents higher potency when compared to a higher $IC_{50}$ value of Cy5-EP1454Y as the inhibitory potencies are lower when $IC_{50}$ values are higher (Mullol et al., 1995).

### 3.4.5 Cy5-EP1454Y and Cy5-Met13 Antibodies Bind OE33 but Not FLO-1 Cells

The ability of the Cy5-EP1454Y and Cy5-Met13 conjugates to bind c-Met was validated by quantitative fluorescence imaging. Direct visualisation showed high uptake of anti-c-Met Cy5-Ep1454Y and Cy5-Met13 probes in OE33 cells, with low uptake of the Cy5-IgG control probes (Figure 3.8). FLO-1 cells demonstrated low relative uptake of anti-c-Met Cy5-Ep1454Y and Cy5-Met13 probes as well as their respective Cy5-IgG control (Figure 3.9). The mean fluorescence intensity per cell, averaged from three independent experiments, evaluating and assessing antibody constructs from different batches for reproducibility, was confirmed to be high in OE33 cells exposed to anti-c-Met probes, but significantly lower when exposed to control conjugates. FLO-1 cells consistently demonstrated lower average intensities per cell in comparison to OE33 cells. The fold difference in average fluorescence intensity per cell between OE33 and FLO-1 cells was

4.2 and 5.6, for Cy5-EP1454Y and Cy5-Met13, respectively. These differences are statistically significant ($P < 0.001$) and are encouraging enough to consider taking both probes into further development and *in vivo* experiments.

### 3.4.6 Further Investigation of the Specificity of the Cy5-EP1454Y and Cy5-Met13 Probes

In § 3.3.3.2, western blot analysis of c-Met expression showed siRNA knockdown of the protein in OE33 cells with the non-transfected (NT) OE33 used as a control. Subsequently, a strong reduction in staining was observed in knockdown cells exposed to Cy5-EP1454Y or Cy5-Met13 when compared to NT control. The visual difference in staining was striking, as confirmed by quantification of the fluorescence signal, with no difference between untreated and control, si.NS (non-specific siRNA) treated, OE33 cells. The siRNA knockdown method is widely used for antibody validation, and relies on a mechanism in which siRNA suppresses the expression of a target protein by stimulating the specific degradation of the target mRNA (Bernstein et al., 2001). A strong signal for the NT cells next to a weak signal for the siRNA-transfected cells in a WB and immunofluorescence means that the antibody is specific and that the knockdown experiment was successful (Olds and Li, 2016). Finally, we tested whether Cy5-EP1454Y and CY5-Met13 probes still bind their antigen when the relevant epitope is blocked, or made unavailable by pre-incubation with a non-labelled, unmodified antibody before proceeding with the Cy5-EP1454Y and Cy5-Met13 staining protocol. The reduction in fluorescent signal was only achieved for the OE33 cells pre-treated with (Met13) antibody, but not when the blocking antibody used was anti-c-Met [EP1454Y]. This indicates that Cy5-Met13 antibody is favoured for future use, as off-target binding,

such as demonstrated for Cy5-EP1454Y, has been reported to significantly affect the pharmacokinetics, tissue distribution, efficacy and toxicity of a therapeutic antibody (Bumbaca et al., 2011). However, it should be noted that the experimental protocol for the blocking experiment could benefit from further optimisation, as some published blocking/competition protocols suggest blocking the antigen/binding site by pre-incubating the epitope/active site with a higher (50- up to a 100-fold) molar excess of unlabelled antibody/ligand than used in the current study, in order to properly determine the extent of the non-specific binding (Hulme and Trevethick, 2010, Sorkin and Duex, 2010, Kislinger et al., 1999).

### 3.4.7 Conclusions

The work presented in this chapter demonstrated, through a number of assays, that a critical condition required to utilise labelled antibodies (that the conjugation reaction has no deleterious effects on antibody affinity) has been met. Furthermore, Cy5-EP1454Y and Cy5-Met13 probes demonstrated suitability for the purposes of this study as a high-quality c-Met-targeting vectors, proving good specificity, reproducibility, and affinity. Notably, Cy5-Met13 probe has shown to be superior over Cy5-EP1454Y, demonstrating greater affinity, potency and specificity. Finally, both probes, Cy5-Met13 more so than Cy5-EP1454Y, demonstrated good signal to background ratios, achieved consistently when applied to *in vitro* live-cell experiments. In conclusion, the data in this chapter support the feasibility of applying Cy5-Met13 probe to *in vivo* studies.

# Chapter 4 *In vivo* Evaluation of the Cy5-EP1454Y, Cy5-Met13 and GE-137 in the Oesophageal Adenocarcinoma Xenograft Models

## 4.1 Introduction

Oesophageal cancer has a notably poor prognosis, with many patients being diagnosed at a stage that is too advanced for curative therapy, often with symptoms of oesophageal obstruction at first presentation (Loffeld and Dekkers, 2013). The 5-year survival rate following the combination of neoadjuvant chemoradiotherapy and surgery in patients with symptomatic oesophageal cancer is only 20% (Thrift, 2016, Muller et al., 1990). On the contrary, survival rates are markedly higher in patients with early disease, reaching over 90% (Wang et al., 2009). Traditional WL endoscopy, currently the most commonly-used modality for detection of OAC, relies on identification of characteristics such as mucosal colour changes, nodules or ulcers (Bird-Lieberman and Fitzgerald, 2009). However, these features are less discriminatory in smaller and early lesions, which in many cases appear morphologically normal (Jain and Dhingra, 2017). Given the rising incidence of oesophageal cancer, especially in the Western world, developing new and more sensitive diagnostic techniques is necessary (Edwards et al., 2010).

In the past 20 years, imaging has become an unprecedentedly powerful tool in preclinical cancer research and clinical practice and there has been a significant increase in the number of imaging technologies and their applications in the field of oncology, but perhaps the biggest breakthroughs are new developments in optical molecular imaging, for example, the intraoperative optical image-guided surgery, which has been shown to improve both sensitivity and accuracy of tumour detection (Wang et al., 2015).

### 4.1.1 Current Treatment

Currently only about 25% of patients with OAC present with early-stage, localised disease that allows for treatment with curative intent. This usually comprises combined modality chemoradiation followed by surgery (Shaikh et al., 2017, Hur et al., 2013). For localized OAC, the combination of cisplatin and 5-fluorouracil is the most studied and commonly used chemotherapeutic regimen, utilised both pre-oesophagectomy and for definitive treatment (Qu et al., 2017). Moreover, multiple surgical procedures exist for performing esophagectomy, carrying their own advantages and potential complications (Mawhinney and Glasgow, 2012).

The remainder of patients present with advanced TNM stage disease, i.e. distant organ or nodal metastatic disease (Cho et al., 2014) and/or tumour invasion of critical surrounding structures such as the great vessels, heart, or trachea (Cho and Kim, 2015). The advanced stage of cancer, in addition to the physiologically frail state of the majority of affected patients, disqualifies them from surgical resection or intensive chemoradiation (Galli et al., 2017).

Survival rates, even in candidates suitable for full multimodality treatment, are still poor, with only 37% of patients with localized disease surviving 5 years. With regional nodal involvement, this drops to 19%, and to 3% or less if distant metastases are present. These give rise to the aforementioned figure of 20% overall 5-year survival (Mawhinney and Glasgow, 2012). The majority of patients with advanced OAC will require palliative treatment due to both local recurrence and the aggressive nature of tumours, giving rise to metastases (Chen et al., 2017). The median survival after non-invasive palliative

treatment for dysphagia is only 3–6 months and is comparable to the survival of patients with untreated advanced oesophageal cancer (Polee et al., 2003).

Given the above, it is clear that detecting OAC as early as possible –and ideally at a pre-cancerous stage – is of paramount importance to improving oncological outcomes.

### 4.1.2 'Early' Oesophageal Cancer and c-Met

For the purpose of this chapter 'early' oesophageal cancer is defined as either high-grade dysplasia, tumour limited to the mucosa ($T_{is}$) or to the submucosa (T1). The stage of OAC (classified according to the TNM system) at which oesophageal cancer is detected is the most important factor in determining prognosis (Galli et al., 2017). In the majority of symptomatic cases, there is tumour invasion of the muscularis propria (T3) and disease has already spread to local lymph nodes (N1) (Luna et al., 2012), highlighting why it is essential to pursue detection before the onset of symptoms.

c-Met overexpression has been shown to occur as an early event in the oesophageal adenoma-carcinoma sequence (Delitto et al., 2014). Herrera reports minimal c-Met IHC staining in the proliferative zone of areas of non-dysplasia (ND) and LGD, but diffuse intense staining in areas of HGD and OAC in matching samples from a cohort of patients who underwent esophagectomy for OAC (Herrera et al., 2005). Gene expression profiles have demonstrated evidence for a significant level of c-Met activation, both in primary OAC and in cells that have metastasised to lymph nodes. High level of c-Met activation has also been observed – albeit to a lesser extent – in a subset of metaplastic and dysplastic Barrett's mucosa (Lu and Wang, 2008), suggesting that c-Met plays an

important role in the development and progression of OAC. Indeed, c-Met overexpression has been reported to be a main oncogene in about 35% of OAC (Mesteri et al., 2014). Taken together, the current literature suggests that c-Met presents a highly promising diagnostic and therapeutic target in patients with HGD and 'early' OAC.

### 4.1.3 Advanced Endoscopic Imaging in Gastrointestinal Neoplasia and Preneoplasia

Conventional WL endoscopy remains the current standard for early detection of OAC in routine clinical practice (Espino et al., 2014). However, it does not accurately diagnose preneoplastic lesions (Sekiguchi and Oda, 2017). The technological advancements in the field of endoscopic imaging for gastrointestinal lesions are increasing rapidly. Currently available advanced endoscopic imaging modalities include chromoendoscopy, narrow band imaging (NBI) and optical molecular endomicroscopy. Chromoendoscopy involves the application of stains or dyes capable of selective light absorption (Trivedi and Braden, 2013) to improve the visualization of the gastrointestinal mucosa as well as its characterisation through differential dye uptake (Davila, 2009) or use of acetic acid (Chedgy et al., 2016). It has been first used for the visualization of the cervix, where 5% dilute acetic acid is instilled onto cervix to highlight dysplastic areas during screening for cervical neoplasia (Megevand et al., 1996). First use of acetic acid in the digestive tract was reported in 2000, aiding in the identification of small islands of BO following ablative therapy (Guelrud et al., 2000). More recently, there have been some compelling evidence for the use of combination of acetic acid and chromoendoscopy, which has been shownt to reduce number of biopsies required to detect one neoplasia by the factor of 15,

when comparing Acetic Acid Chromoendoscopy cohort versus the Random Four Quadrant Biopsies cohort (40 biopsies vs 604 biopsies, Chedgy et al., 2016).

NBI aims to enhance the mucosal features and blood vessels by utilization of a smaller portion of the visible spectrum. Blue and green wavelengths are selected by optical filters, with the elimination of red light. Thus, light with narrowed bandwidth penetrates the superficial mucosal structures and are better absorbed by haemoglobin, highlighting the characteristics and vascular patterns of the gastrointestinal mucosa (Singh et al., 2009). Some preliminary studies have provided encouraging results for NBI alone or in combination with other advanced endoscopic techniques in the screening and surveillance of Barrett's oesophagus patients (Wani and Sharma, 2007). However, in a recent meta-analysis of patients with ulcerative colitis (n = 305), the sensitivity of NBI for the detection of neoplasia was merely comparable to conventional WL colonoscopy (Har-Noy et al., 2017). Furthermore, despite the potential of NBI to more accurately detect metaplastic and dysplastic tissue within BO segments compared to WL endoscopy, it does not provide predictive information about the cancerous potential of these lesions.

Recent advances in optical and multimodality molecular imaging include research and development of optical molecular probes against biomarkers of cancer such as cell surface receptors, extracellular acidosis, hypoxia and secreted proteases (Wang et al., 2018). This has led to development of a variety of optical imaging probes targeting these biomarkers to improve tumour contrast over background tissue (Hellebust and Richards-Kortum, 2012). Fluorescent optical imaging methods are safer, have higher spatial resolution and real-time capability in comparison to molecular imaging technologies such as PET, SPECT and MRI, and therefore have become a promising modality for

tumour detection and image-guided surgery in clinics (Wang et al., 2018). However, main disadvantage of fluorescent imaging is that if a lesion or a tumour is completely embedded in tissue, this will result in a significant attenuation of the fluorescent signal and may require the surgeon to first remove the overlying tissue such as fat or vessels (van der Poel et al., 2011). For non-superficial tumour dissection, a multimodality imaging technology based on a combination of optical imaging and molecular imaging modalities could facilitate and optimise tumour dissection (Li et al., 2016, van der Poel et al., 2011).

Confocal fluorescence endomicroscopy attempts to obtain high magnification and resolution images of the morphological changes in tissue which occur in dysplasia, through imaging of tissue autofluorescence or administration of iv fluorophores (Thekkek et al., 2011). Potentially suitable agents are fluorescein, acriflavine, tetracycline, or cresyl violet (De Palma, 2009). In theory, confocal laser endomicroscopy has the potential to eliminate the need for biopsy, facilitating diagnosis at the point-of-care setting (Leggett and Gorospe, 2014). However, in comparison to wide-field fluorescence detection, the confocal scanning endoscope scans specimens point-by-point, compromising speed for improved resolution and sensitivity, which is useful in laboratory setting but may require further refinement to compete with wide-field endoscope's ability to achieve real-time imaging of the tumour in the clinic (Risi et al., 2014).

### 4.1.4 Overall Aim

The purpose of this chapter was to evaluate the fluorescent optical imaging capability of the Cy5-EP1454Y, Cy5-Met13 and GE-137 (as described in § 3.1.2) fluoroconjugates *in vivo*, in two animal models: subcutaneous xenografts of the OAC-derived cell lines OE33 and FLO-1.

Work presented in Chapter 3 demonstrated, through a number of assays, that the Cy5 conjugation reaction had no deleterious effects on antibody affinity and that Cy5-Met13 and Cy5-EP1454Y probes are high-quality c-Met-targeting vectors, showing good specificity, reproducibility, and affinity. Notably, the Cy5-Met13 probe has shown to be superior to Cy5-EP1454Y, demonstrating greater affinity and specificity. In summary, this chapter will explore the use of Cy5-EP1454Y, Cy5-Met13 and GE137 probes for *in vivo* real-time tumour detection.

## 4.2 Experimental Set Up

Fluorescence image-guided surgery (FIGS) has recently emerged as a complementary imaging technique to WL reflectance imaging and it aims to provide the surgeon with an extra tool to enable real-time intra-operative assessment of tumour margin (Keereweer et al., 2011). Tumour-specific intraoperative fluorescence imaging modality is based on the use of clinically approved contrast agents that are excited in the visible – near infrared region of the electromagnetic spectrum (van Dam et al., 2011). Contrast agents or fluorescently-labelled antibodies can be used to identify tumour tissue or to detect lymph nodes in a non-specific manner (Debie et al., 2019). The NIR region of the electromagnetic spectrum has several advantages over the visible: these include higher penetration depths, lower scattering and lower tissue autofluorescence (Volpi et al., 2014). The multiwavelength fluorescence image-guided surgery imaging system developed by Dr Davide Volpi and Professor Boris Vojnovic has been adapted for use as an *in vivo* imaging system that delivers high-standard performance and versatility for preclinical imaging studies.

To acquire real-time, non-invasive tumour images *in vivo*, we used the aforementioned imaging device, composed of the control unit (Figure 4.1 A) and widefield imaginer (camera) that is connected to the control unit during the experiment (Figure 4.1 B). OE33 tumour xenografts imaged with anti-c-Met Cy5-Cy13 antibody: brightfield (4.1 C) and brightfield and fluorescence emission displayed simultaneously (4.1 D). Volpi's device demonstrates the first implementation of white light reflectance imaging and multispectral fluorescence imaging simultaneously using a single colour CCD camera,

without the need for software image overlays, as required by systems employing multiple cameras (Volpi et al., 2014).

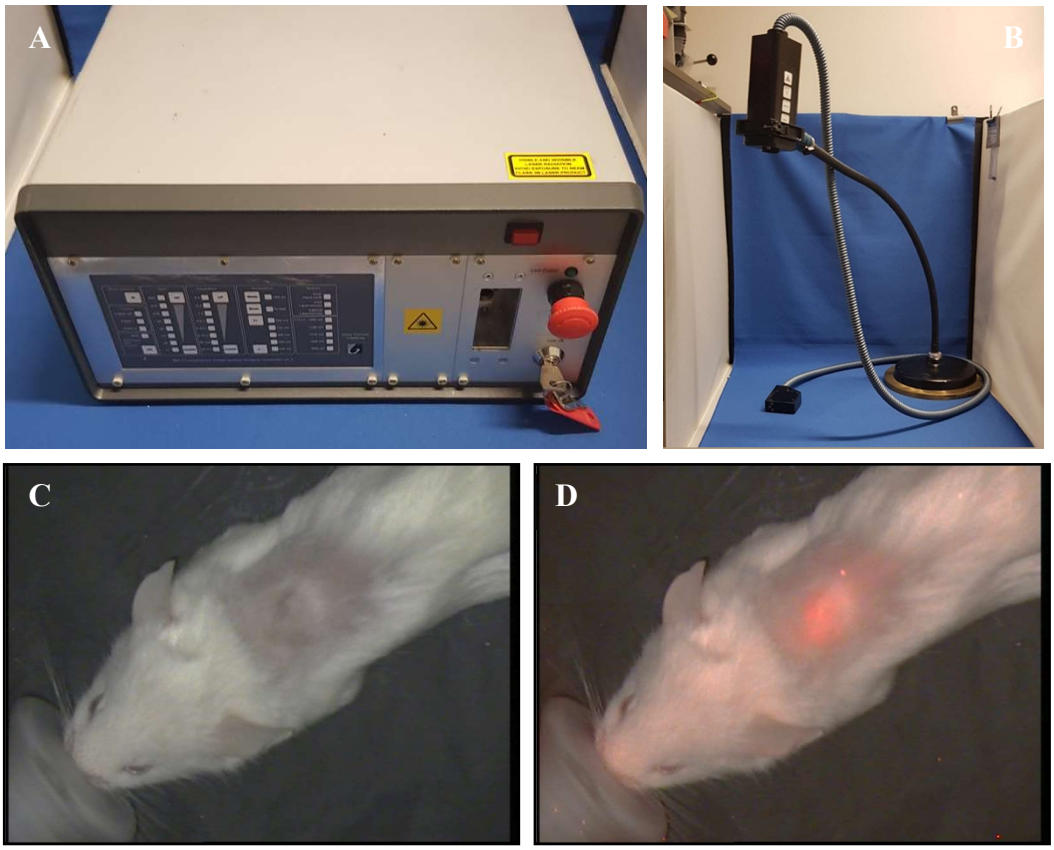



**Figure 4.1 Imaging Device, Final Design.** A) The control unit. B) The widefield imager. Real-time imaging of OE33 xenografts using Cy5-labelled anti-c-Met mAb. C) Brightfield D) Brightfield and fluorescence emission (white arrow points to tumour) displayed simultaneously. Camera exposure time: 40 ms.

## 4.3 Results

### 4.3.1 Growth Rate of Subcutaneous Oesophageal Adenocarcinoma Derived Xenografts

Following subcutaneous inoculation of OE33 cells, longitudinal measurements of tumour volume were performed over a period of 5 weeks to assess the tumour growth rate in two different mouse strains: BALB/c Nude and NOD/SCID γ. Furthermore, once xenografts were successfully established in NOD/SCID γ mice, tumours were harvested, cut up and non-necrotic fragments of the tumour were inoculated subcutaneously to BALB/c Nude mice (designated BALB/c Nude T), as described previously (Santander et al., 2012). All animals developed palpable tumours at the site of injection after one week and measurements were obtained, as described in §2.5.3. As shown in Figure 4.2, the tumour growth rate follows different trends for different groups of mice, making both BAL/c Nude and BALB/c Nude T groups unsuitable for future experiments, due to tumour shrinkage or very slow growth. Consequently, NOD/SCIDγ mice were used for both OE33 and FLO-1 xenograft models. For FLO-1 xenografts, mice were inoculated, as described in § 2.8.2, and all animals developed palpable tumours at the site of injection after one week and by approximately the end of week three tumours had reached the maximum allowed geometric mean diameter. No signs of distress or weight loss were observed during that period.

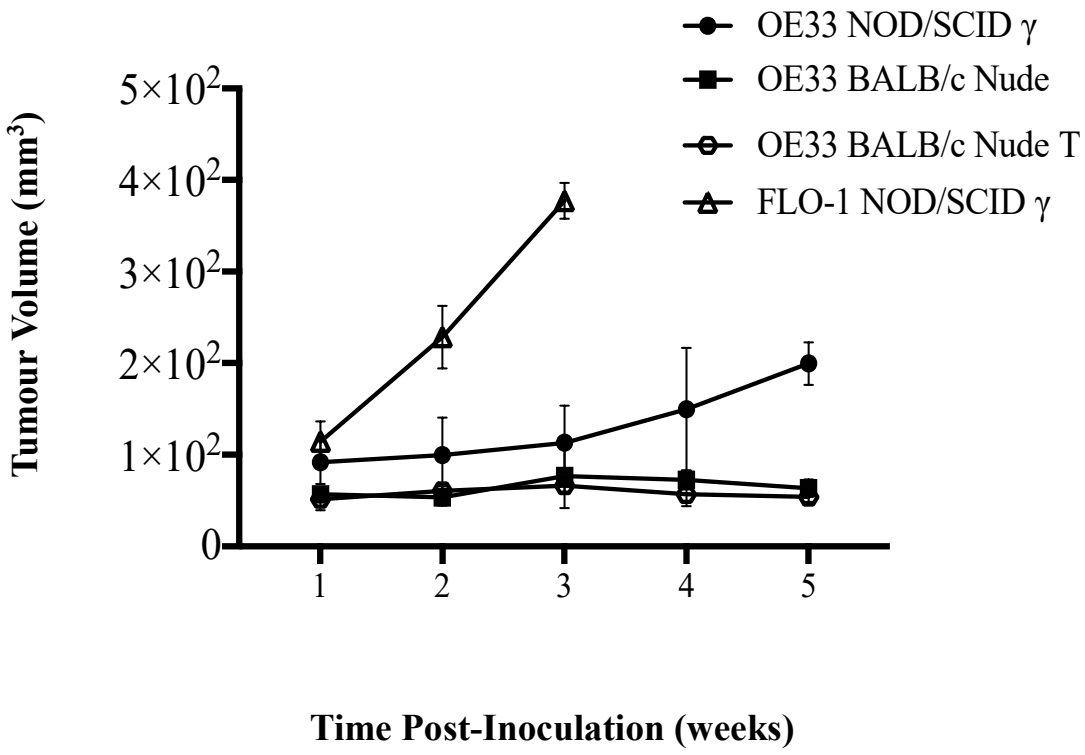



**Figure 4.2 Tumour Growth Curves for the OE33 and FLO-1 Xenografts.** Athymic nude or SCID mice were subcutaneously inoculated with either OE33 or FLO-1 lines or OE33 tumour fragments and tumour volume ($mm^3$) measurements were acquired throughout a 5-week period. Tumour volumes are reported as Mean ± SD (n = 3).

### 4.3.2 *Ex Vivo* Biodistribution Analysis and Dose Study

In order to select the antibody most suited for *in vivo* studies and the optimal amount to be injected, biodistribution analyses were conducted. OE33 xenograft bearing mice were imaged using Volpi's imaging system at 24, 48 and 72 h after iv administration of either Cy5-EP1454Y (5 and 10 μg doses) or Cy5-Met13 (5 and 10 μg doses).

#### 4.3.2.1 Cy5-Met13

Whole-body optical images were acquired at 24 h, 48 h, and 72 h post iv of Cy5-Met13 (5 and 10 μg). After imaging organs were harvested for *ex vivo* evaluation of fluorophore uptake. As shown in Figure 4.3, the OE33 tumour uptake and retention of the Cy5-Met13 probe was recorded as tumour to background ratio (TBR) at 24, 48 and 72 h post iv. TBRs recorded for the lower injected amount (5 μg) were 3.43 ± 0.28, 1.92 ± 0.06 and 1.52 ± 0.36 at 24, 48 and 72 h, respectively. To compare, TBRs recorded for the greater injected amount (10 μg) were 3.1 ± 0.89, 3.5 ± 0.35 and 4.56 ± 0.48 at 24, 48 and 72 h post iv, respectively.

Tumour, stomach, large and small intestines were noted as the main organs of uptake after administration of Cy5-Met13 at 72 h post iv (Figure 4.4). Highest signal was observed in the stomach, with organ to muscle ratio of 185.23 ± 5.11, large intestine (28.31 ± 1.13), tumour II (10 μg of Cy5-Met13, 11.69 ± 0.56), tumour I (5 μg of Cy5-Met13, 4.67 ± 0.82) and small intestine (3.75 ± 1.71). No significant accumulation in other organs was observed including liver, kidneys and heart.

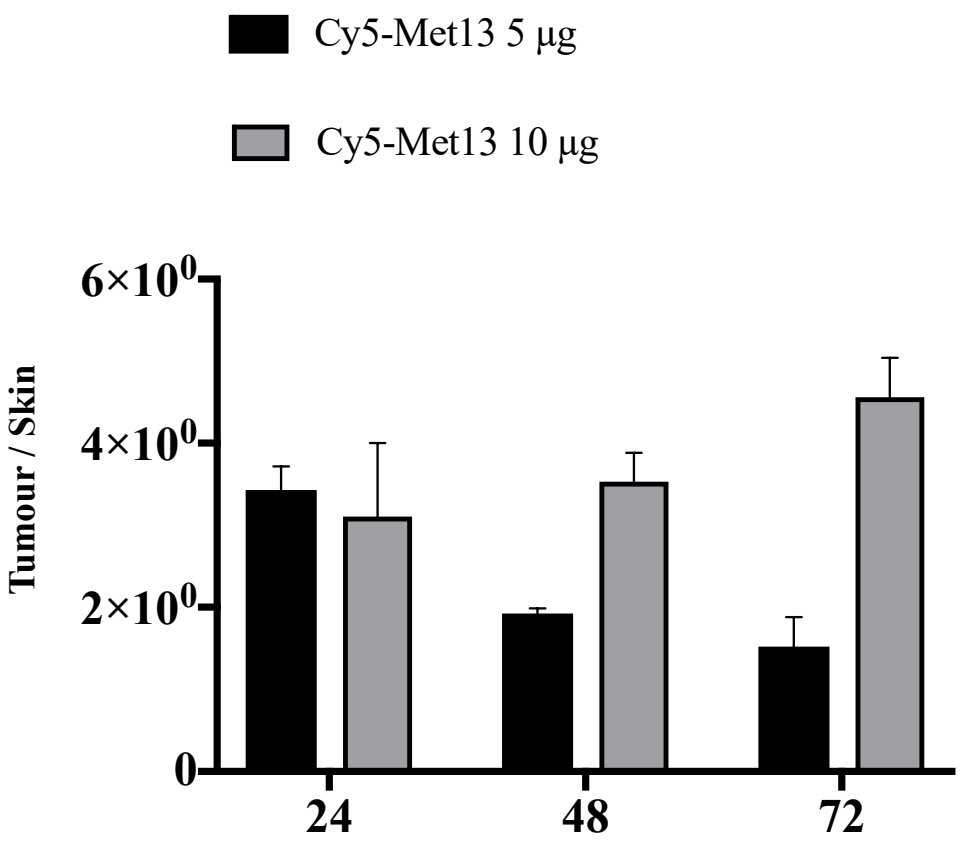



**Figure 4.3 Biodistribution Study, Cy5-Met13.** Quantification of optical intensities of tumour volumes by image analysis was performed at 24, 48 and 72 h post iv for an injected amount of 5 and 10 µg of Cy5-Met13 per mouse. Data are expressed as TBR and bars represent mean ± SD (n = 2 mice).

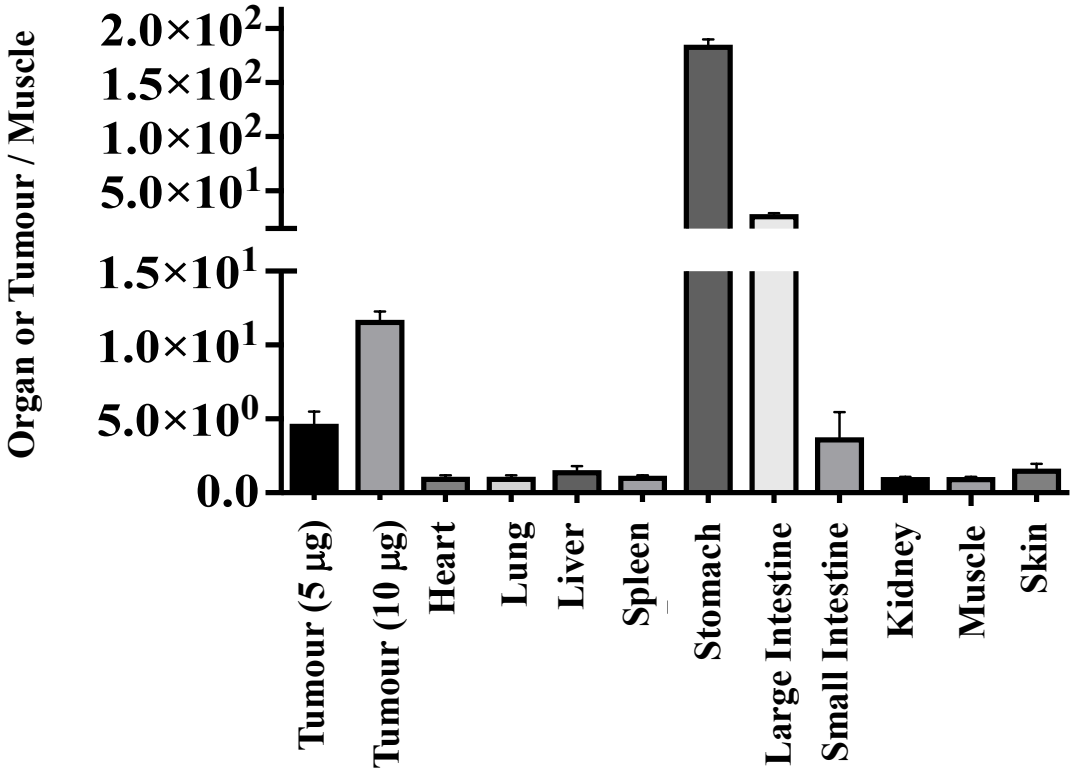



**Figure 4.4 Ex Vivo Tissue Biodistribution, Cy5-Met13.** *Ex vivo* biodistribution analysis was performed at 72 h post iv of 5 and 10 µg of Cy5-Met13. Tumours and major tissues are shown. Data presented as organ or tumour to muscle ratios, expressed as mean ± SD (n = 2 mice).

Representative optical images of mice injected with different amounts of Cy5-Met13 are shown in Figure 4.5. In each case the WL image is shown on the left and the optical image on the right. Pre-injection images show no tumour uptake. In contrast, 24 h post iv of the anti-c-Met fluorescent probe, tumour uptake was observed ($P < 0.0001$, two-way ANOVA, data quantified from the images in Figure 4.5 using ImageJ).

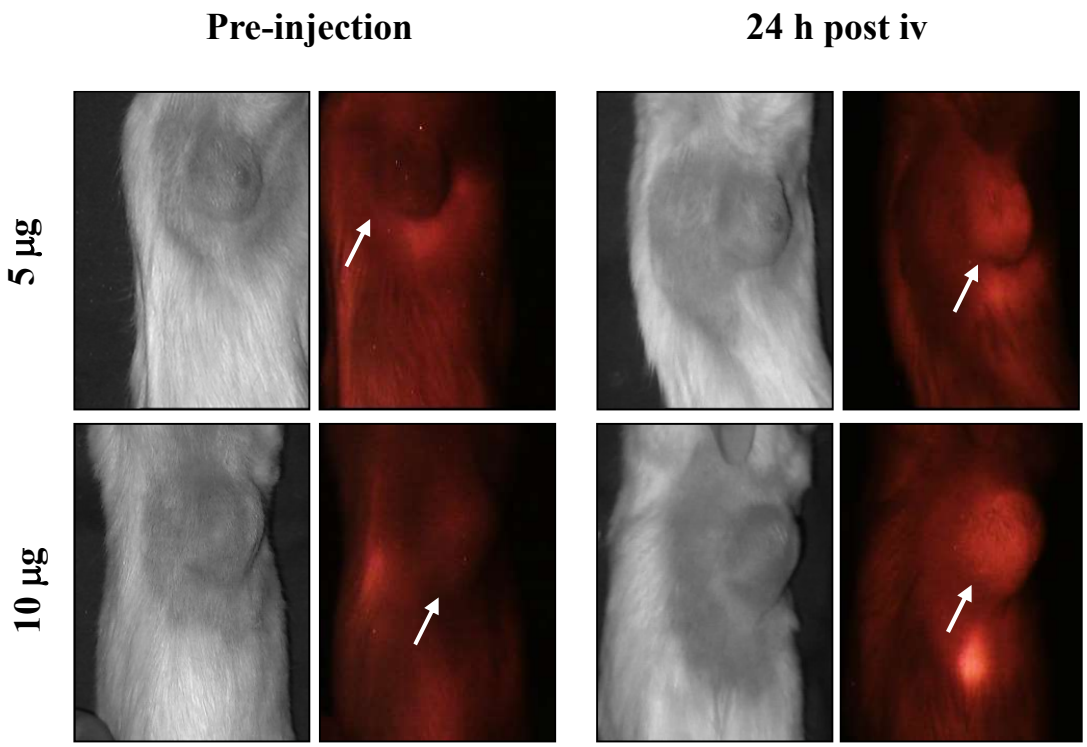



**Figure 4.5 Optical Images Showing Tumour Uptake of Cy5-Met13.** Representative optical images of OE33 xenograft bearing mice, pre - and 24 h post iv of 5 and 10 µg of Cy5-Met13. WL image on the left, and fluorescent image on the right, arrows point to tumour. Pre-injection images show no tumour uptake. In contrast, 24 h post iv of the anti-c-Met fluorescent probe, tumour uptake was observed.

#### 4.3.2.2 Cy5-EP1454Y

Whole-body optical images were acquired at 24 h, 48 h, and 72 h post iv of Cy5-EP1454Y (5 or 10 μg). After imaging organs were harvested for *ex vivo* evaluation of fluorophore uptake. As shown in Figure 4.6, the OE33 tumour uptake and retention of the Cy5- EP1454Y probe was recorded as TBR at 24, 48 and 72 h post iv. Optical intensity ratios observed following injection of 5 μg Cy5-EP1454Y were 4.68 ± 0.77, 1.78 ± 0.22 and 2.48 ± 0.61 at 24, 48 and 72 h, respectively. In comparison, optical intensity ratios observed for the higher injected amount (10 μg) were 5.56 ± 1.15, 2.9 ± 0.18 and 3.02 ± 0.39 at 24, 48 and 72 h post iv, respectively.

Tumour, stomach, large and small intestines were noted as the main organs of uptake after administration of Cy5-EP1454Y at 72 h post iv (Figure 4.7). Highest signal was observed in the stomach, with organ to muscle ratio of 220.67 ± 10.79, large intestine (33.87 ± 5.60), small intestine (8.64 ± 0.59), tumour II (10 μg of Cy5-EP1454Y, 8.29 ± 0.38) and tumour I (5 μg of Cy5-EP1454Y, 1.62 ± 0.63). No significant accumulation in other organs was observed including liver, kidneys and heart.

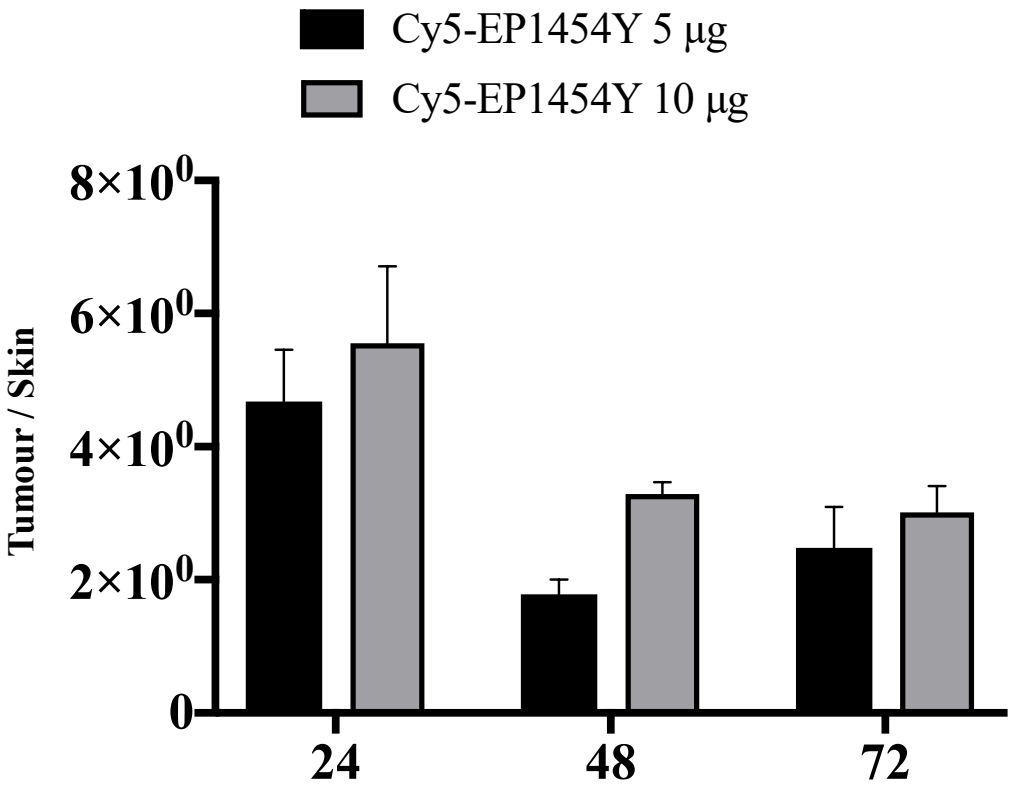



**Figure 4.6 Biodistribution Study, Cy5-EP1454Y.** Quantification of optical intensities of tumour volumes by image analysis was performed at 24, 48 and 72 h post iv for an injected amount of 5 and 10 µg of Cy5-EP1454Y per mouse. Data are expressed as TBR and bars represent mean ± SD (n = 2 mice).

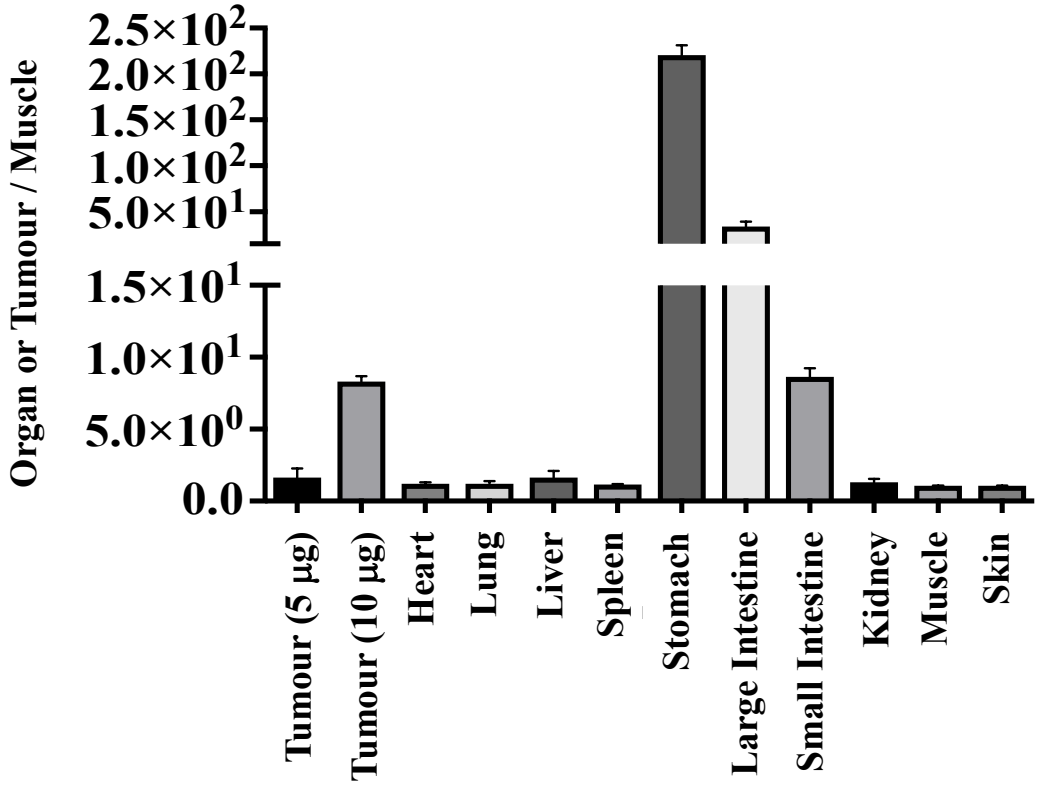



**Figure 4.7 Ex vivo Tissue Biodistribution, Cy5-EP1454Y.** *Ex vivo* biodistribution analysis was performed at 72 h post iv of 5 and 10 µg of Cy5-EP1454Y. Tumours and major tissues are shown. Data presented as organ or tumour to muscle ratios, expressed as mean ± SD (n = 2 mice).

Representative optical images of mice injected with different amounts doses of Cy5-EP1454Y are shown in Figure 4.8. In each case the WL image is shown on the left and the optical image on the right. Pre-injection images show no tumour uptake. In contrast, 24 h post iv of the anti-c-Met fluorescent probe, tumour uptake was observed ($P < 0.0001$, two-way ANOVA, data quantified from the images in Figure 4.8 using ImageJ).

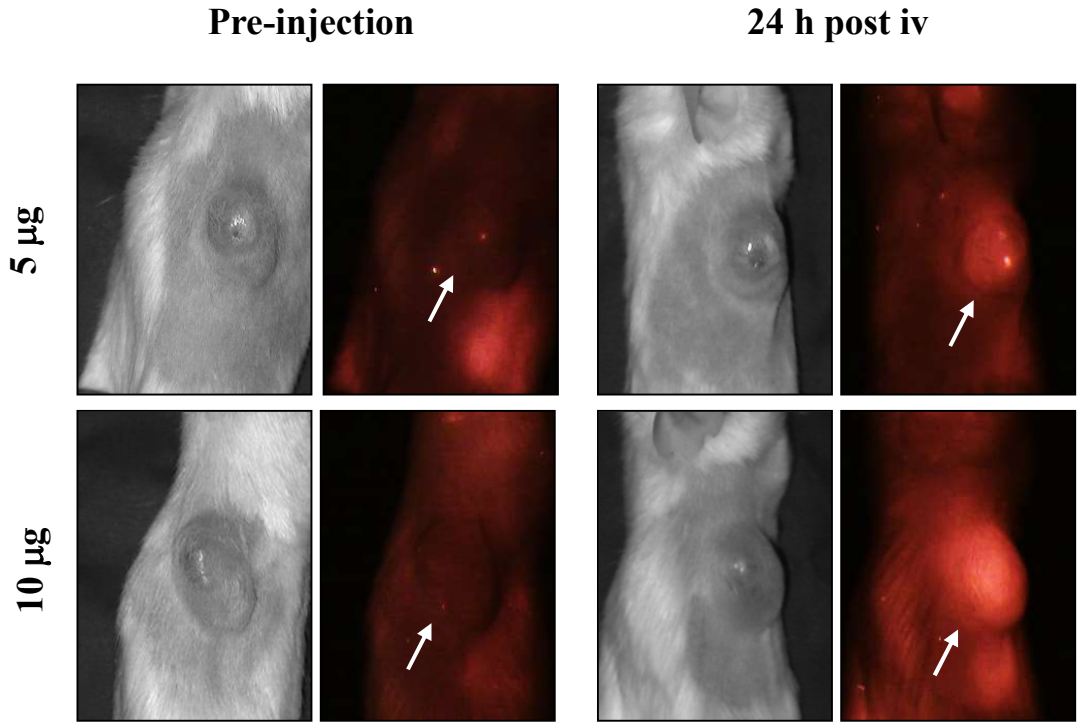



**Figure 4.8 Optical Imaging Showing Tumour Uptake of Cy5-EP1454Y.** Representative optical images of OE33 xenograft bearing mice, pre - and 24 h post iv of 5 and 10 µg of Cy5-EP1454Y. WL image on the left, and fluorescent image on the right, arrows point to tumour. Pre-injection images show no tumour uptake. In contrast, 24 h post iv of the anti-c-Met fluorescent probe, tumour uptake was observed.

### 4.3.3 Investigation of the Specificity of the Cy5-Met13 Probe in OE33 Xenografts

Whole-body optical images of 3 mice were acquired at 24 h, 48 h, and 72 h post iv of Cy5-Met13 (10 μg) and were used to quantify tumour uptake and retention of Cy5-Met13, recorded as Fluorescence Intensity (FI) at 24, 48 and 72 h post iv, using ROI analysis as described in § 2.8.7b A). A control group received 10 μg of Cy5-labelled mouse IgG. Furthermore, second control group received 20 μg of unlabelled anti-c-Met (Met13) antibody to occupy the c-Met epitope on the surface of OE33 cells, 24 h before proceeding with the staining protocol using Cy5-Met13 probe. In this study, probes were randomly allocated to individual mice and administered by a research assistant who identified each mouse using a unique reference number. In this way image acquisition and analysis was performed in a blinded manner to eliminate subjective bias in imaging data interpretation. Treatments were prepared in advance and randomised, and mice were examined and imaged post iv using only reference numbers. The study was unblinded once the experiment was completed. FI at 24, 48 and 72 h post iv are shown in Figure 4.9. There were no significant differences in FI between the groups that received Met13 + Cy5-Met13 or Cy5-Met13 alone (71.65 ± 32.42 AU *versus* 101.89 ± 15.84 AU at 24 h, P = 0.9216, 68.77 ± 45.12 AU *versus* 95.51 ± 10.27 AU at 48 h, P = 0.9670 and 81.67 + 55.14 AU *versus* 93.41 ± 28.86 AU at 72, P = 0.9998, skin on). FI was significantly reduced in Cy5-IgG control group at 72 h with values of 11.09 ± 5.23 AU (mean ± SD, n = 3 mice, $P < 0.05$, two-way ANOVA), but there were not significant differences at 24 and 48 h with values of 20.28 ± 6.11 AU and 16.11 ± 4.99 AU, respectively (mean ± SD, n = 3 mice, P = 0.0520 and 0.0735, respectively, two-way ANOVA).

Furthermore, at 72 h the skin was removed to expose muscle, and images were taken and analysed as described in § 2.8.7b B). Figure 4.10 shows FI at 72 h post iv, and demonstrates a significant difference between c-Met specific Cy5-Met13 accumulation and non-specific IgG control (mean ± SD, n = 3 mice, ** $P < 0.01$, one-way ANOVA) with values of 209. 53 ± 29.54 AU *versus* 23.08 ± 14.71 AU, and 177.09 ± 48.87 AU for 'blocked' group.

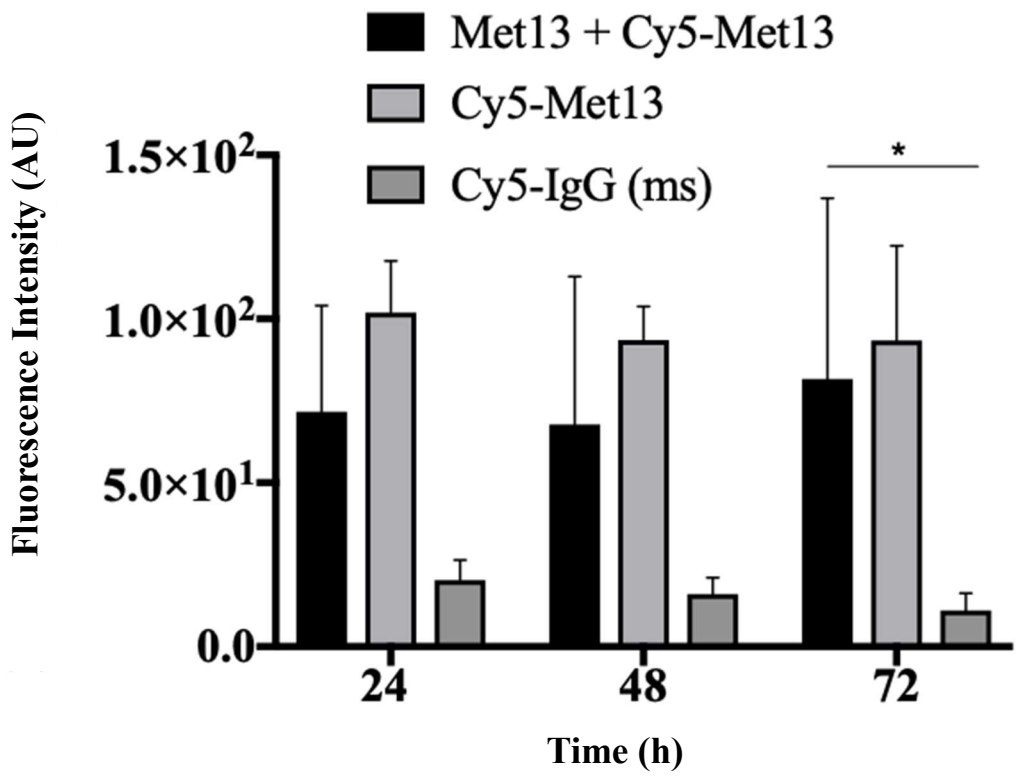



**Figure 4.9 Specificity of the Cy5-Met13 Probe in OE33 Xenografts.** Quantification of optical intensities of tumour areas by image analysis was performed at 24, 48 and 72 h post iv of Cy5-Met13 (10 μg) and were used to evaluate tumour uptake and retention of Cy5-Met13, as described in § 2.8.7b A). Control groups received 10 μg of Cy5-labelled mouse IgG or 20 μg of unlabelled anti-c-Met (Met13) (administered 24 h before the imaging dose of fluorescent Cy5-Met13 antibody, mean ± SD, n = 3 mice, * $P < 0.05$, two-way ANOVA).

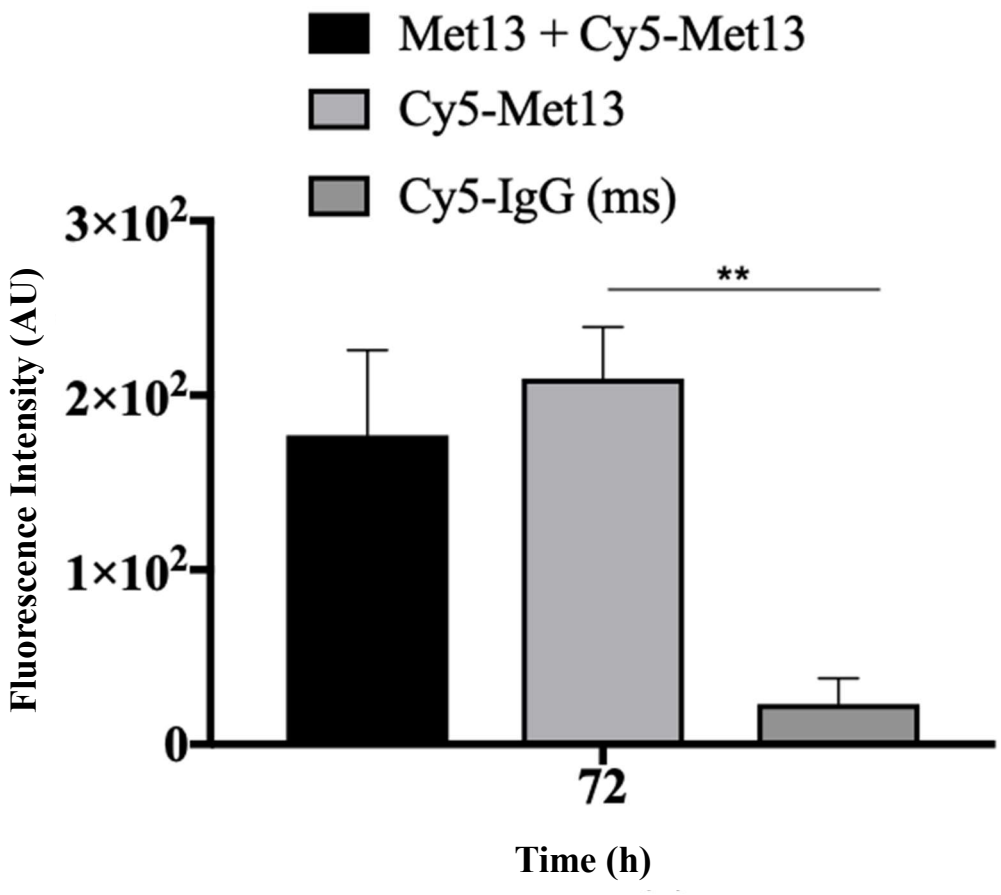



**Figure 4.10 Specificity of the Cy5-Met13 Probe in OE33 Xenografts, Skin Removed.** Quantification of optical intensities of tumour areas by image analysis was performed at 72 h post iv of Cy5-Met13 (10 μg) and was used to evaluate tumour uptake and retention of Cy5-Met13, as described in § 2.8.7b B). Control groups received 10 μg of Cy5-labelled mouse IgG or 20 μg of unlabelled anti-c-Met (Met13) (administered 24 h before the imaging dose of fluorescent Cy5-Met13 antibody, mean ± SD, n = 3 mice, ** $P < 0.01$, one-way ANOVA).

Representative optical images of mice injected with Cy5-Met13 (10 μg), Cy5-labelled mouse IgG (10 μg) or 20 μg of unlabelled anti-c-Met (Met13) + the imaging dose of fluorescent Met13, are shown in Figure 4.11. In each case the WL image is shown on the left, highlighting the location of the tumour. Fluorescent images on the right show high tumour uptake for mice injected with CyMet13 + Cy5-Met13 and Cy5-Met13, but for Cy5-IgG (mouse, ms), tumour uptake was significantly lower ($P < 0.01$, Two-Way ANOVA, data quantified from the image in Figure 4.11 using ImageJ).

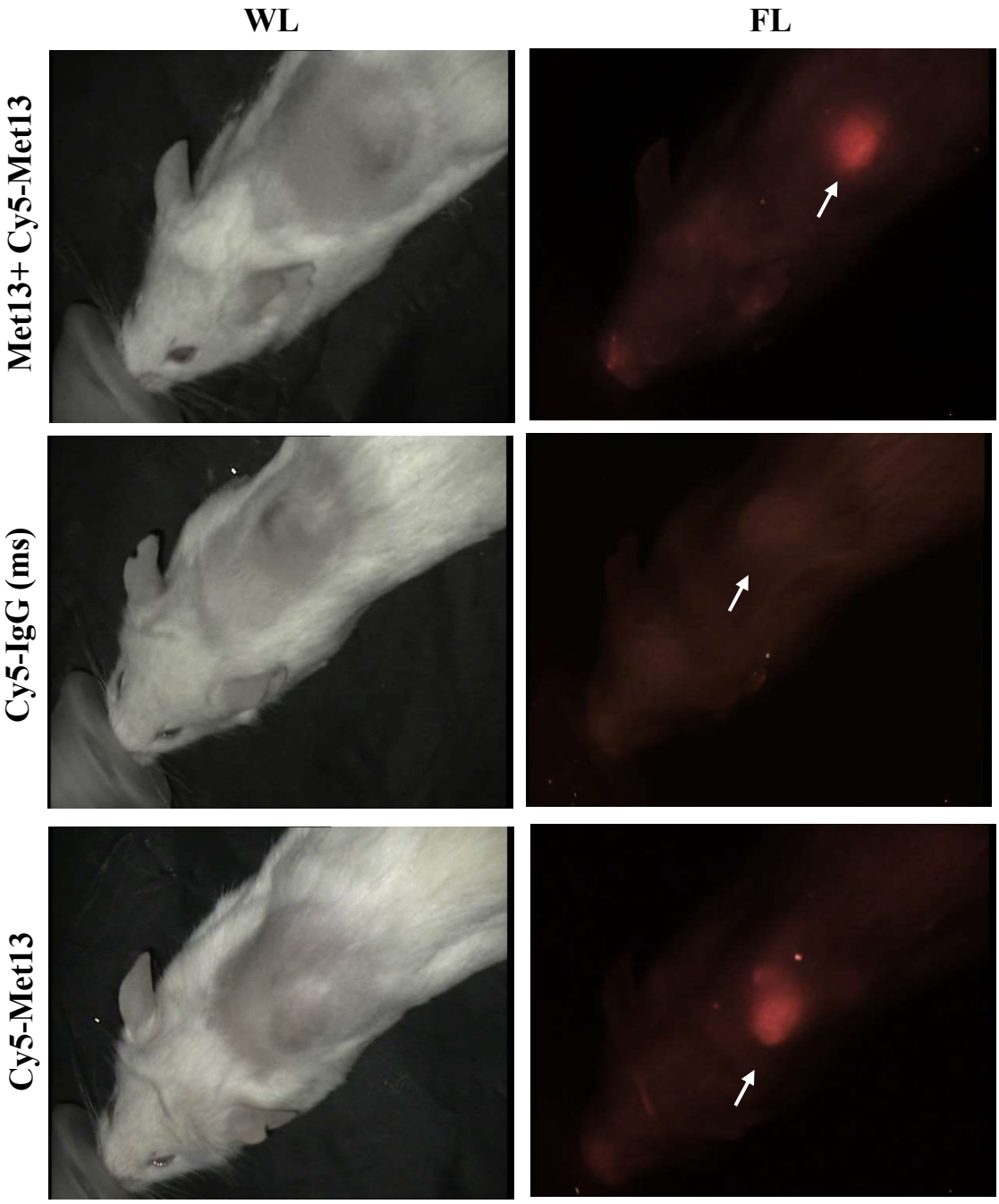



**Figure 4.11 Optical Images Showing Tumour Uptake of Cy5-Met13 and Cy5-IgG.** Representative optical images of OE33 xenograft bearing mice, 24 h post iv with Cy5-Met13 (10 μg), Cy5-labelled mouse IgG (10 μg) and 20 μg of unlabelled anti-c-Met (Met13) + the imaging dose of fluorescent Met13. WL image on the left, and fluorescent image on the right, arrows point to tumour showing marked uptake of the Cy5-Met13 probe (± Met13).

### 4.3.4 Investigation of the Specificity of the Cy5-Met13 Probe in OE33 and FLO-1 Xenografts

For the final experiment, designed to evaluate the performance of the Cy5-Met13 probe *in vivo*, whole-body optical images were acquired at 24 h and 48 h post iv of Cy5-Met13 (10 μg) or Cy5-IgG (10 μg) in either OE33 or FLO-1 xenograft mouse models. This study was conducted to investigate the specificity of uptake of Cy5-Met13 in a c-Met positive *versus* a c-Met negative tumour model. Figure 4.12 shows average FI (n = 4 mice) with significantly higher probe accumulation and retention in c-Met expressing OE33 xenografts (621.34 ± 164.83 AU, TBR = 20.37 ± 4.34) in comparison to FLO-1, a low c-Met expressing cell line, with the average fluorescence intensity of 98.99 ± 8.75 AU (TBR = 5.47 ± 1.13, mean ± SD, $P < 0.0001$, two-way ANOVA). The non-specific Cy5-labelled IgG control did not accumulate significantly in OE33 (40.12 ± 5 AU) nor FLO-1 (71.11 ± 29.99 AU) xenografts (mean ± SD).

Tumour, stomach, large and small intestines and liver were noted as the main organs of uptake after administration of Cy5-Met13 and Cy5-IgG at 48 hours post injection in OE33 and FLO-1 xenograft models (data not shown). Highest fluorescent signal was consistently observed in the stomach, regardless of the treatment or cell line. No significant accumulation in other organs was observed including bladder, kidneys and heart (representative data from one mouse that received Cy5-Met13 shown in Figure 4.13).

Representative optical images of mice bearing OE33 or FLO-1 xenografts, injected with either Cy5-Met13 (10 μg) or Cy5-labelled mouse IgG (10 μg) are shown in Figure 4.14.

On the left, images show the white light image of the same mouse to highlight the location of the tumour. Fluorescent images on the right show high tumour uptake of Cy5-Met13 in OE33 but not FLO-1 xenografts ($P < 0.0001$, Two-Way ANOVA, data quantified from the image in Figure 4.14 using ImageJ).

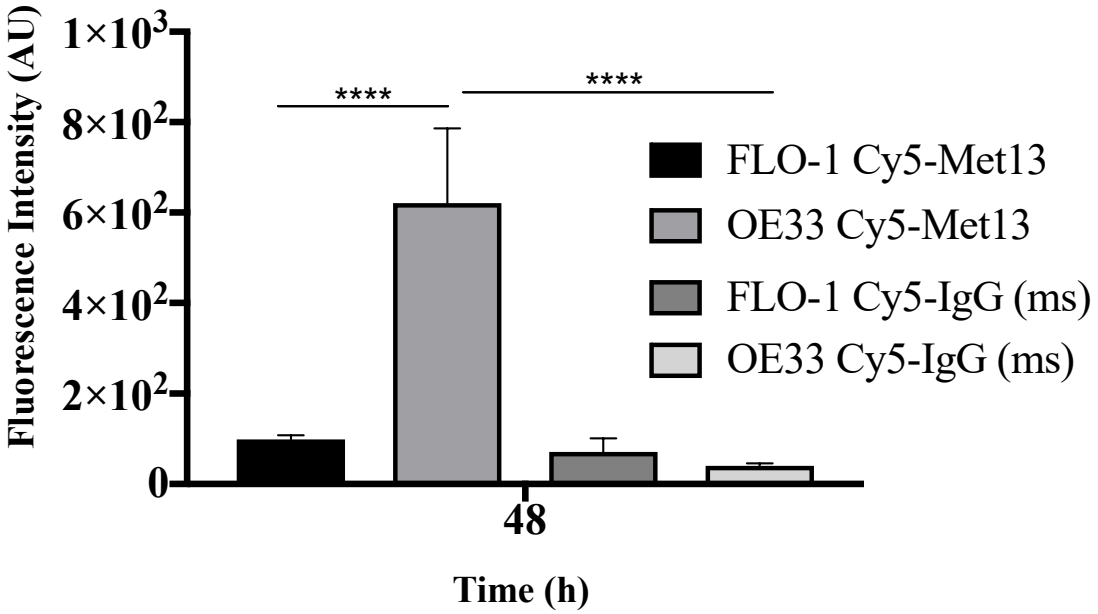



**Figure 4.12 Uptake of the Cy5-Met13 Probe in OE33 and FLO-1 Xenografts, Skin Removed.** Quantification of optical intensities of tumour areas by image analysis was performed at 48 h post iv as described in § 2.8.7b B), and was used to evaluate tumour uptake and retention of Cy5-Met13. Control groups received 10 μg of Cy5-labelled mouse IgG (mean ± SD, n = 4 mice, **** $P < 0.0001$, one-way ANOVA).

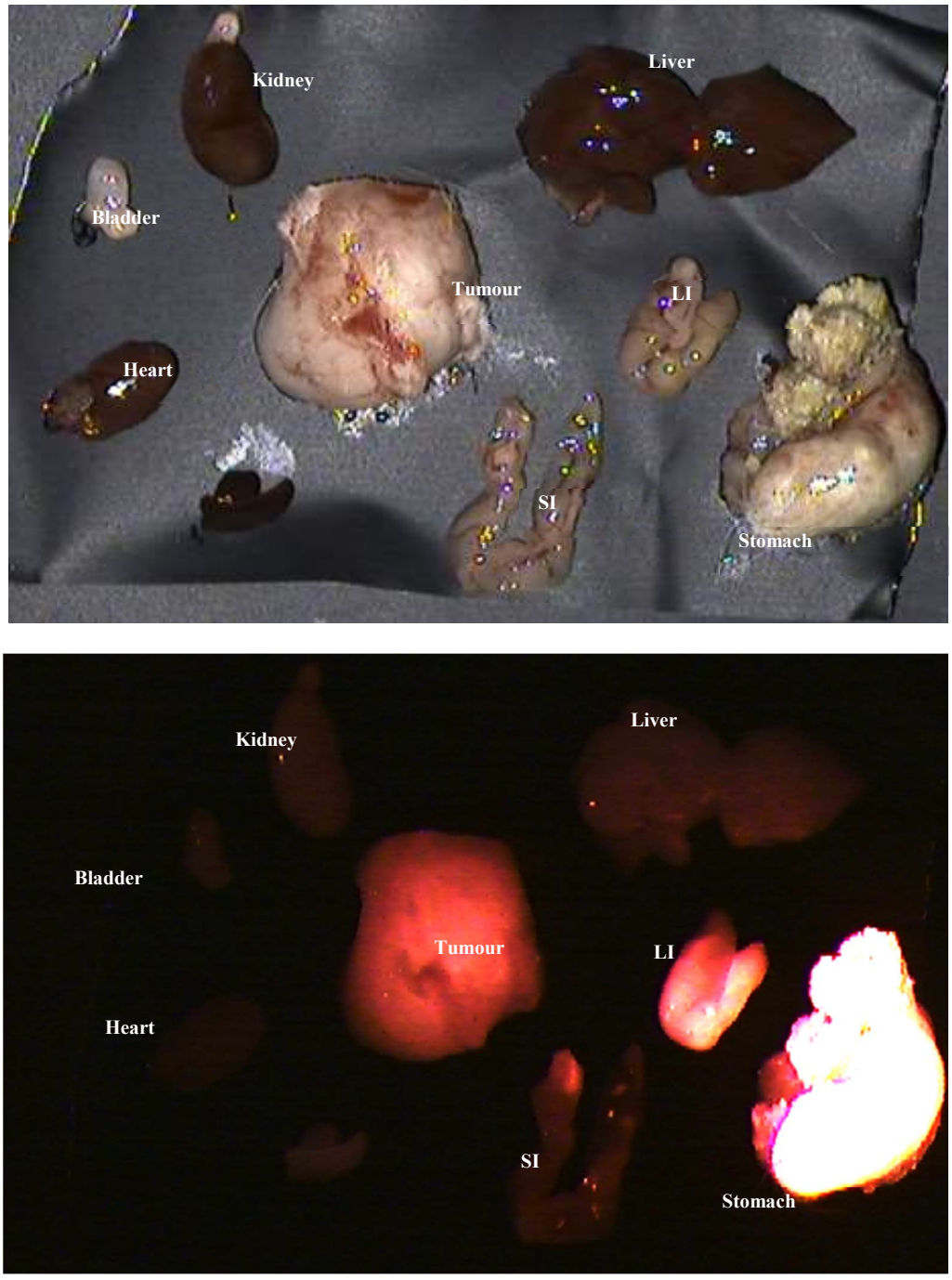



**Figure 4.13 Optical Images Showing *Ex Vivo* Biodistribution.** *Ex vivo* biodistribution images were taken at 48 h post iv of 10 µg of Cy5-Met13. Tumour and major tissues are shown: A) WL image and B) fluorescent image. SI - small intestine, LI - large intestine.

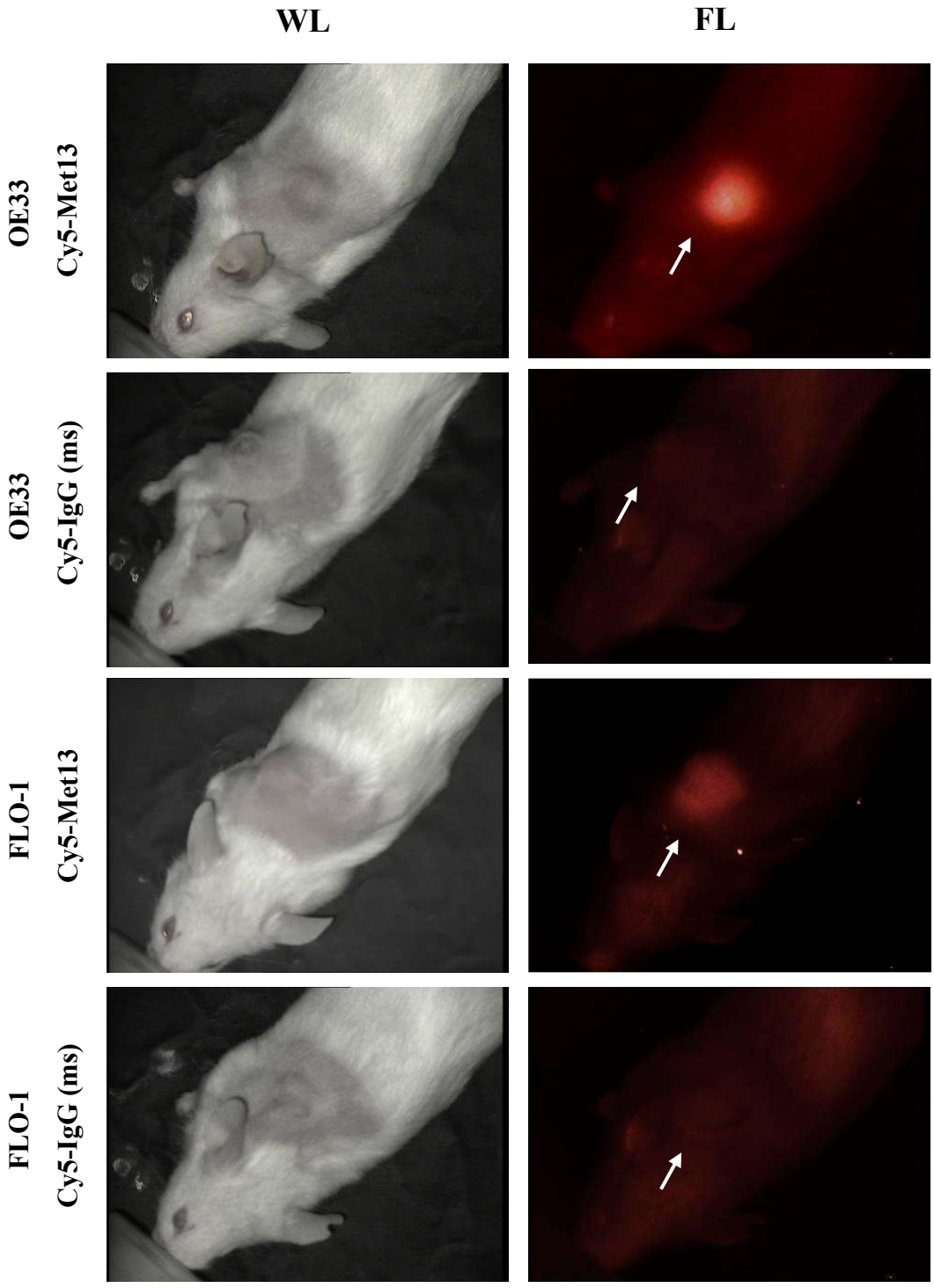



**Figure 4.14 Optical Imaging Showing Tumour Uptake of Cy5-Met13 and Cy5-IgG in OE33 and FLO-1 Xenografts.** Representative optical images of OE33 and FLO-1 xenograft bearing mice, 24 h post iv of Cy5-Met13 (10 μg) or Cy5-IgG (10 μg). WL image on the left, and fluorescent image on the right, arrows point to tumours, showing marked uptake of the Cy5-Met13 in OE33 xenograft.

### 4.3.5 Optical Imaging of GE-137

Whole-body optical images were acquired at 6 h post iv of GE-137 (5 μg) in mice bearing either OE33 or FLO-1 xenografts. The images were used to evaluate the *in vivo* bio-distribution of the GE-137 peptide. As shown in Figure 4.15, the OE33 tumour to muscle contrast provided by GE-137 probe at 6 h p.i. was high with an average of 28.6 ± 8.08 (mean ± SD). The TBR observed for the c-Met low expressing FLO-1 xenograft control was lower at 16.6 ± 7.57 (mean ± SD). Tumour, kidneys, bladder and stomach were noted as the main organs of uptake after administration of GE-137 at the time of imaging. Representative optical images of mice bearing either OE33 or FLO-1 xenograft, injected with GE-137 peptide are shown in Figure 4.16. There is significant difference between the amount of GE-137 internalised in the OE33 and FLO-1 xenografts ($P < 0.05$, one-way ANOVA) and between OE33 tumour and muscle (background tissue) ($P < 0.0001$, one-Way ANOVA).

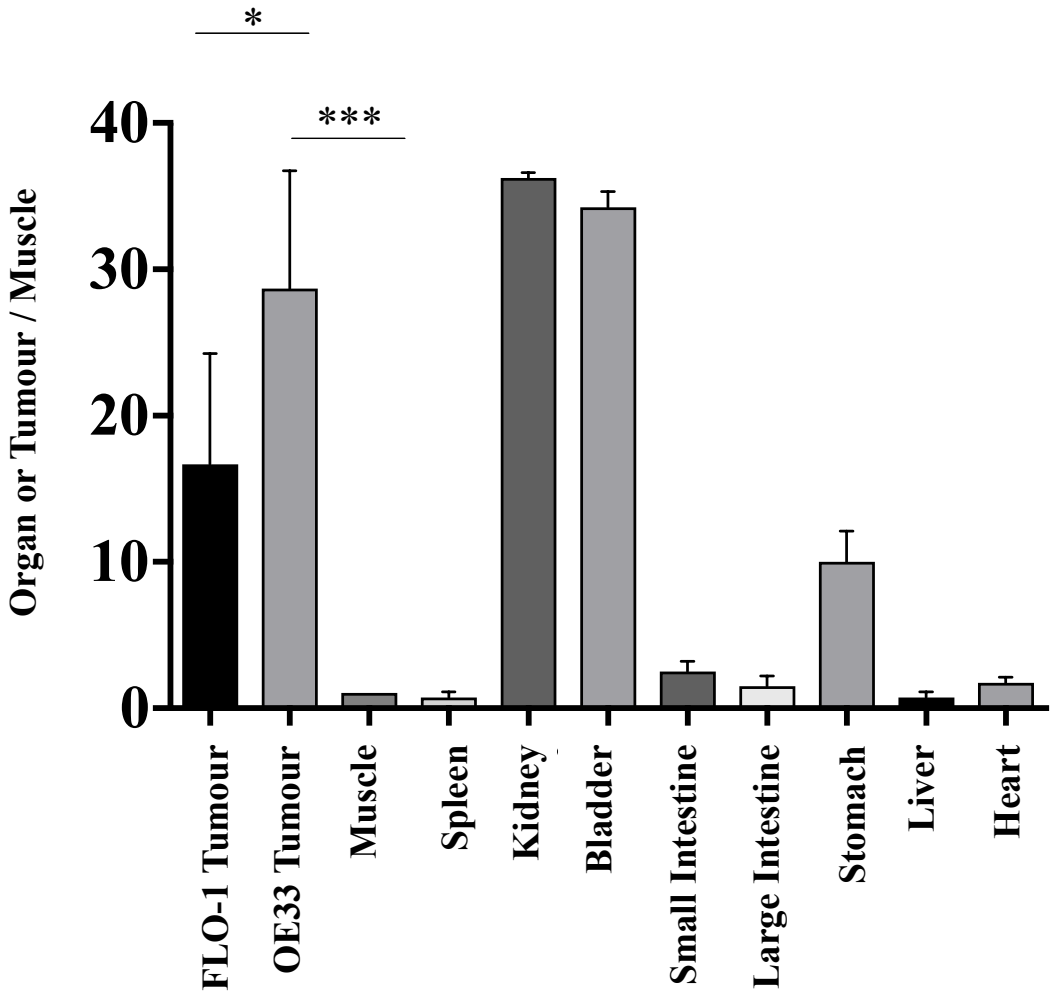



**Figure 4.15 *Ex Vivo* Biodistribution Analysis, GE-137.** *Ex vivo* biodistribution analysis was performed at 6 h post iv of 5 μg of GE-137. Tumours and major tissues are shown. Data are expressed as organ or tumour / muscle and bars represent mean ± SD (n = 3 mice). There is significant difference between the amount of GE-137 internalised in the OE33 and FLO-1 xenografts ($^{*}$ $P < 0.05$, one-way ANOVA) and between OE33 tumour and muscle ($^{***}$ $P < 0.001$, one-way ANOVA).

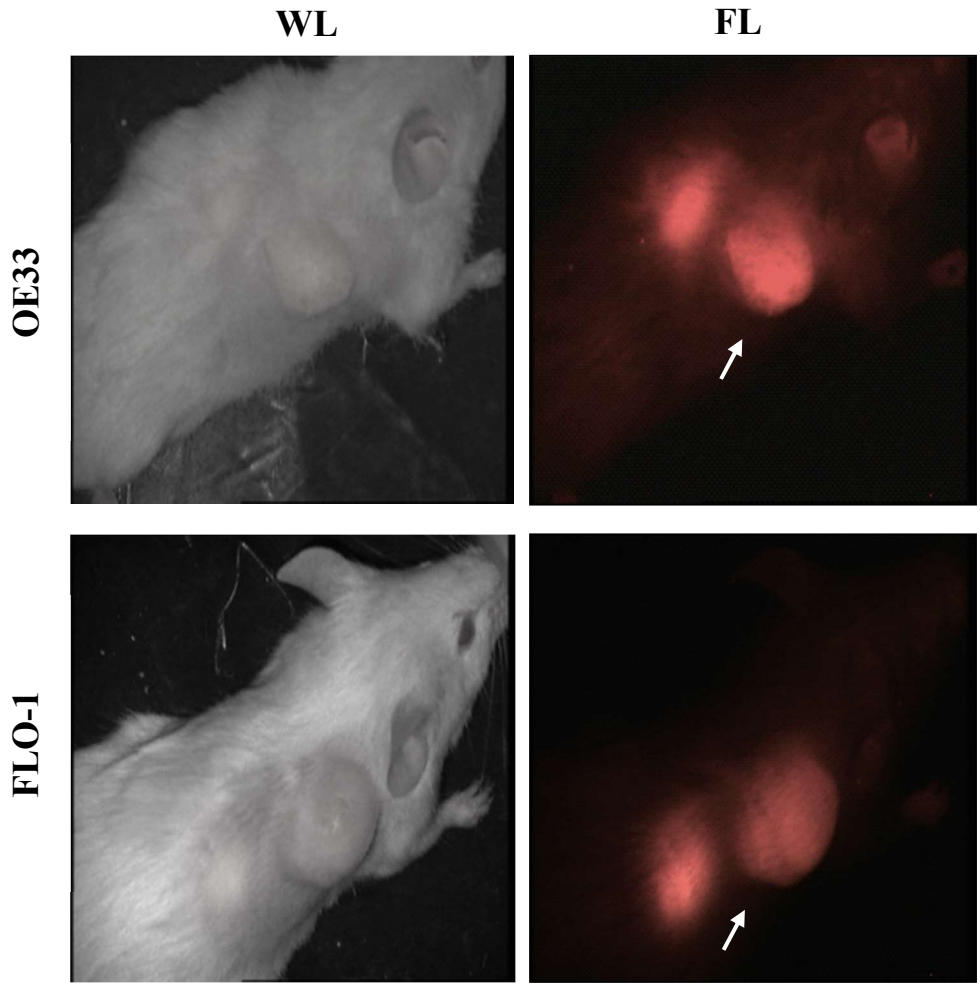



**Figure 4.16 Optical Images Showing Uptake of GE-137 in OE33 and FLO-1 Xenografts**. Representative optical images of OE33 and FLO-1 xenograft bearing mice, 6 h post iv of GE-137 (5 μg). WL image on the left, and fluorescent image on the right, arrows point to tumours, showing uptake of GE-137 peptide in both OE33 and FLO-1 xenografts.

## 4.4 Discussion

Despite extensive research, there is currently no molecular biomarker approved in clinical practice for OAC, with the exception of human epidermal growth factor receptor 2 (HER2) in GOJ cancer (Bartley et al., 2017). Multiple studies have been conducted to explore the genomic profile of OAC, which have resulted in highlighting the presence of mutations in several cancer-related genes and brought to attention distinctive gene signatures, as extensively described in § 1.5. However, despite their potential, none has so far been adopted into practise in the clinic as a biomarker for targeted treatment or diagnostic purposes (Battaglin et al., 2018). The advanced optical imaging technique described in this chapter, in combination with Cy5-labelled monoclonal antibodies against c-Met, presents a method of real-time *in vivo* tumour characterisation to aid diagnosis. This chapter has explored the translational potential and *in vivo* suitability of Cy5-Met13, Cy5-EP1554Y and GE-137 probes to be utilised as a c-Met targeting vector.

### 4.4.1 Establishing a Model of Subcutaneous OAC-Derived Xenografts

When planning the experimental design for *in vivo* validation, significant consideration should be given to the animal model to be used. As a result of the absorption and diffraction limitations of optical imaging tissues greater than 10 mm deep cannot be imaged (Chen and Thorne, 2012). For pragmatic reasons such as cost and availability, and owing to aforementioned restrictions, a small rodent model was selected as being most suitable. Athymic nude mice such as BALB/c Nude offer several advantages for use in pre-clinical studies, offering ease of validation in a relatively short time period, accurate monitoring of tumour growth, and low cost (Vandamme et al., 2014).

In order to estimate the parameters of the OE33 tumour growth model, we used data from a total of 9 tumours under three different conditions (3 tumours each) as represented in Figure 4.3. OE33 xenografts failed to develop in BALB/c Nude model inoculated with either OE33 cells or tumour fragments transplanted from a NOD/SCID γ mice, in line with previously established protocols (Santander et al., 2012). Difficulty in growing viable OE33 tumours in nude mice has been reported before (Melsens et al., 2017). However, it was found that xenografts developed successfully in the NOD/SCID γ model. Consequently, SCID mice were used in all *in vivo* imaging experiments presented in this chapter. Difficulty in developing successful xenografts in nude mice is not uncommon, and many tumour lines have been reported to grow better in SCID mice (Garofalo et al., 1993), likely due to their significantly greater immune system impairment (Romano et al., 2012). Their limitations, however, include higher cost and the presence of thick fur. Animal fur diffracts light (Chen and Thorne, 2012), and so shaving the area around the tumour was performed for all experiments, to maximise signal.

Subsequently, the FLO-1 tumour growth model was developed in the NOD/SCID γ model, as dictated by the results obtained for OE33 xenografts. FLO-1 xenografts have a higher growth rate when compared to OE33 xenograft, likely owing to shorter doubling time, as observed during routine cell culture.

The findings from the above pilot studies allowed improved experimental planning, so that OE33 and FLO-1 xenografts reached the same size at the same time, permitting

probe administration and subsequent imaging of all experimental groups within the same week.

### 4.4.*2 Ex Vivo* Biodistribution Analysis and Dose Study

Whole-body optical images were acquired at 24 h, 48 h, and 72 h post iv injection of Cy5-Met13 or Cy5-EP1454Y (5 and 10 μg doses) and were used to evaluate tumour to background ratios. As shown in Figures 4.3 and 4.6, retention of Cy5-Met13 in OE33 tumours was higher when compared to Cy5-EP1454, but the difference was not significant. However, there was a significant difference between two injected amounts, with higher tumour to background contrast achieved at 48 and 72 h post iv at the 10 μg rather than 5 μg dose. Figures 4.5 and 4.8 show representative optical images of OE33 xenograft bearing mice, pre- and 24 h post iv injection of either Cy5-Met13 (Fig. 4.5) or Cy5-EP1454Y (Fig. 4.8) at the two aforementioned amounts, demonstrating visibly higher fluorescence intensity in the tumour region at the higher injected amount. The 10 μg administered per mouse (with an approximate weight of 20 g) translates into a dose of 0.5 mg/kg. This value falls within the range of FDA-approved doses for therapeutic monoclonal antibodies e.g. trastuzumab, which is given to patients with metastatic breast cancer at a 4 mg/kg loading dose, followed by 2 mg/kg weekly until disease progression (Goldenberg, 1999). There are no available data or current guidelines pertaining to mAbs used diagnostically – consequently this area of the project needs further optimisation and development. However, a lower mass amount would be expected to be needed for an imaging antibody, based on current literature, as e.g. imaging dose in radiation therapy has traditionally been ignored due to its low magnitude and frequency in comparison to therapeutic dose used to treat patients (Alaei and Spezi, 2015). Many therapeutic mAbs

are not considered cost-effective, due to existing difficulty in identifying patents most likely to respond (e.g. use of bevacizumab, cetuximab and panitumumab for metastatic colorectal cancer, Lange et al., 2014). However, this may differ for a single-dose application required for mAb used as a diagnostic agent. Furthermore, based on current evidence, it can be safe to assume that a dose of 0.5 mg/kg would be well-tolerated and unlikely to cause a toxic reaction (Newsome and Ernstoff, 2008). However, some reports suggest that the animal dose should not be translated to a human equivalent dose (HED) by a simple conversion based on body weight (Reagan-Shaw et al., 2008, Contrera et al., 2004). Instead, the body surface area (BSA) normalization method should be used (Reagan-Shaw et al., 2008, Contrera et al., 2004):

$$\text{HED (mg/kg)} = \text{animal dose (mg/kg)} \times (\text{animal } K_m / \text{human } K_m)$$

Where $K_m$ factors for human and mouse are 37 and 3, respectively (Reagan-Shaw et al., 2008, Contrera et al., 2004). Consequently, HED calculated from a dose used *in vivo* could be closer to = 0.5 x (37/3) = 6.2 mg/kg. However, this seems to be a much less realistic dose when compared to doses used in current clinical trials, for example, 4.5 mg of bevacizumab-IRDye 800CW for breast cancer (Clinicaltrials.gov: NCT01508572). However, it is difficult to speculate and compare dosages at this stage of development of the anti-c-Met probe, particularly when pre-clinical data available on bevacizumab-IRDye 800CW does not specify doses used in animal models (Korb et al., 2014).

*Ex vivo* biodistribution analysis of Cy5-Met13 and Cy5-EP1454Y in the OE33 xenograft model was evaluated and compared: tumour, stomach, large and small intestines were noted as the main organs of uptake after administration of Cy5-Met13 and Cy5-EP1454Y

at 72 hours post iv (Figures 4.4 and 4.6, respectively). The highest signal was observed in the stomach, followed by large intestine, tumour and small intestine. No significant accumulation in other organs was observed including the liver, kidneys and heart, which was unexpected. The biodistribution of full-length monoclonal antibodies has been well documented *in vivo* (Hassan et al., 1999, Fawwaz et al., 1985), including those labelled with fluorescent dyes (Peterson et al., 2016, Vasquez et al., 2011). These data generally show strong retention in healthy tissues, especially liver and kidneys, and relatively slow circulation, which affects the tumour to background contrast of imaging at early time points after administration. However, this can differ for antibodies that target extracellular markers (Tabrizi et al., 2006) such as c-Met. Monoclonal antibodies are characterised by the high specificity conferred by the antibody interaction with an epitope (Lipman et al., 2005). Hence, it is not surprising that among the factors regulating mAb pharmacokinetics and pharmacodynamics (PK/PD), antigen distribution (soluble versus membrane associated) can influence mAb retention (Kamath, 2016). In contrast to soluble antigens, membrane-associated internalizing antigens can greatly enhance antibody clearance through a target-mediated, specific process (Tabrizi et al., 2006).

The strong gastrointestinal tract signal seen during *ex vivo* biodistribution analysis was most likely due to the presence of auto fluorescent compounds in the animals' diet. The mice were fed an alfalfa-free diet, as this has been shown to substantially reduce intestinal autofluorescence (Volpi et al., 2012). To potentially further improve collected *in vivo* data, the use of a low-fluorescence diet, especially a purified diet, should be considered in the future (Inoue et al., 2008). It was speculated whether the probe may bind c-Met in the mouse intestinal tract, as it has been reported that c-Met is overexpressed in some patients with gastric cancers (Awazu et al., 2013, Janjigian et al., 2011) and increased c-

Met expression has been shown in rats with methotrexate-induced gut mucosal damage (Xian et al., 2000). However, not only these specific conditions did not apply to our murine model, we also tested human the Met13 antibody for cross reactivity with mouse c-Met and we found there was none (data not shown). Furthermore, high intensity signal from the stomach has been observed in studies using both antibodies based Cy5-Met13 probe and GE-137 peptide. Despite TBRs for the stomach being different between these two experiments, showing lower TBR for the stomach in the GE-137 experiment relatively to Cy5-Met13 experiment, these cannot be directly compared. This is because tissue (stomach) to background ratios calculated in these two experiments used different background values generated by two different agents with different brightness but using a similar optical intensity value for the stomach, as it was full of fluorescent animal feed in both cases, generating a very similar, overexposed image. Additional side by side testing combined with a purified diet could be useful in providing a convincing data for the lack of c-Met expression in the stomach.

### 4.4.3 Investigation of the Specificity of the Cy5-Met13 Probe in OE33 and FLO-1 Xenografts

The ability of the Cy5-Met13 conjugates to bind c-Met was validated by quantitative fluorescent imaging. Direct visualisation showed significantly ($P < 0.001$) higher uptake of anti-c-Met Cy5-Met13 probe in OE33 xenografts, with low uptake of the Cy5-IgG controls over the course of the experiment (Figures 4.9, 4.10 and 4.11). However, when tested, Cy5-Met13 probe still binds its antigen when the relevant epitope was blocked, or made unavailable, by pre-incubation with a non-labelled, unmodified (Met13) antibody before proceeding with Cy5-Met13 staining protocol. The achieved reduction

in fluorescent signal was insignificant. This could indicate that Cy5-Met13 antibody demonstrates off-target binding *in vivo*, a potential issue which has been reported to significantly affect the pharmacokinetics, tissue distribution, efficacy and toxicity of a therapeutic antibody (Bumbaca et al., 2011). However, it should be noted that the experimental protocol for the blocking experiment must be further optimised, as published blocking protocols suggest blocking the antigen/binding site by pre-incubating the epitope/active site with a much higher (50- up to a 100-fold) molar excess of unlabelled antibody/ligand than used in the aforementioned study, in order to properly determine the extent of the non-specific binding (Hulme and Trevethick, 2010, Sorkin and Duex, 2010, Kislinger et al., 1999).

Figure 4.12 shows average fluorescence intensity (n = 4 mice) with significantly higher probe accumulation and retention in c-Met expressing OE33 xenografts in comparison to FLO-1 xenografts, which demonstrated low uptake of both anti-c-Met Cy5-Met13 probe and Cy5-IgG control. In Cy5-Met13 uptake and retention studies, FLO-1 cells consistently demonstrated lower average FI *in vivo* and *in vitro* in comparison to OE33 cells. The difference in TBR between OE33 and FLO-1 xenografts was 4-fold, with TBR of $20.37 \pm 4.34$ and $5.47 \pm 1.13$, respectively ($P < 0.001$, one-way ANOVA). This result suggests that Cy5-Met13 probe is c-Met specific. Low level uptake was observed in c-Met-negative FLO-1 xenografts may be suggestive of non-specific tumour uptake due to the enhanced permeability and retention (EPR) effect, a phenomenon attributed to abnormal tumour vasculature that causes leakage

of long circulating molecules into tumour tissue and retention due to limited lymphatic drainage (Kobayashi et al., 2014). Since the EPR effect depends on the physical characteristics (size, charge, polarity) of the injected molecules and not on their binding properties, it was hard to discriminate between the specific binding and non-specific uptake of these antibodies (Heneweer et al., 2011, Ogawa et al., 2009).

Furthermore, the TBR offered is clinically translatable, being on average comparable if not higher than some of the tumour-to-background ratios reported for molecular imaging modalities; such as Breast-Specific Gamma Imaging (BSGI), used to investigate the correlations between TBR obtained from BSGI and the prognostic factors of breast cancer (TBR in the range of 1.4 – 6.3, Lee et al., 2017) or F18-fluorodeoxyglucose positron emission tomography/computed tomography (FDG-PET/CT) in colorectal liver metastasis (TBR in the range of 1.8 to 16.9, Rogasch et al., 2015). Furthermore, amongst representative molecular imaging agents developed for c-Met imaging in various cancers (Table 9, § 3.1.1) there are only three fluorescent imaging agents including Ms20-QD, a fluorescent-labelled single chain variable fragment (scFv) of an anti-c-Met antibody, and two fluorescent-labelled peptides: cMBP-AOC-Cy5.5 and GE-137. The difference in $T/T_n$ (tumour / tumour with non-specific probe) between Ms20-QD and the Cy5-Met13 probe characterised herein is 2-fold, with $T/T_n$ of 4.3 (Lu et al., 2011) and 9.8 respectively. In 2018 there have been reports of several new c-Met imaging radiotracers in development, including $^{99m}$Tc-HYNIC-cMBP for SPECT (Han et al., 2018) and [$^{18}$F]FP-Met-pep1 for PET imaging (Li et al., 2018). However, to our knowledge, no new optical imaging agents have been synthesised and evaluated and none of the imaging agents described so far have been applied to the clinic. Only one – GE-137 – has been tested in humans (Burggraaf et al., 2015). However, we have shown that our antibody-

based Cy5-Met13 offers greater specificity over the peptide GE-137, as discussed in § 4.4.4. below.

### 4.4.4 Optical Imaging of GE-137

Figure 4.15 shows TBR with significantly higher GE-137 accumulation and retention in c-Met expressing OE33 xenografts in comparison to FLO-1 xenografts, which however still demonstrated significantly higher uptake of GE-137 in comparison to background. FLO-1 cells and xenografts consistently demonstrated lower average intensities per cell and xenograft in comparison to OE33 cells. Tumour, kidneys, bladder and stomach were noted as the main organs of uptake after administration of GE-137 at 6 hours post iv. Fluorescence agents are excreted from the body typically through the liver and the kidneys. Excretion time varies depending on the water solubility of the drug and on the injected dose. Our biodistribution studies showed renal clearance of the probe consistent with previous reports (Esfahani et al., 2016).

Compared to antibodies, peptides offer a multitude of advantages including rapid distribution, reduced or absent immunogenicity, ease and scalability of synthesis and affordable labelling (Reubi and Maecke, 2008) however, the difference in TBR between OE33 and FLO-1 xenografts was only 2-fold, suggesting high tumour uptake but low c-Met specificity of GE-137. As reported previously, cytoplasmic accumulation of GE-137 may be a possible reason for a nonlinear relationship between the expression level of c-Met and the GE-137 signal intensity when comparing xenografts with higher and lower number of c-Met receptors (Liu et al., 2015). The cytoplasmic accumulation may be a cause of longer retention of GE-137 peptide and high TBR, which may have some application in the clinic, allowing for detection of lesions for targeted biopsy (Liu et al.,

2015). This could explain the high signal observed in FLO-1 tumours, however, this theory has not been tested in the xenograft models used. Even so, it is very likely however, that antibody-based Cy5-Met13 probe shows better specificity and correlation between signal intensity and the expression level of c-Met on a linear scale. This was based on normalising the signal observed to c-Met expression between OE33 and FLO-1 xenografts, as determined by WB using cell pellets (Fig. 3.3). In order to determine this relationship with more precision, expression of c-Met in *ex vivo* tumour tissue should be measured using WB or, if possible, using a different technique that offers quantification of the amount of protein detected for more accurate results.

### 4.4.5 Conclusions

In summary, this chapter demonstrated feasibility of applying anti-c-Met probes in i*n vivo* studies. The non-invasive *in vitro* imaging of c-Met was attempted using Cy5-labelled monoclonal antibodies and GE-137 peptide. *In vivo* internalisation studies with fluorophore-labelled anti-c-Met antibody conjugates showed the superiority of the Cy5-Met13 over Cy5-EP1454Y to selectively bind c-Met receptor, and high affinity and specificity when compared to non-specific IgG fluorophore-labelled molecules. Furthermore, the Cy5-Met13 probe showed low accumulation in a control group (mice bearing FLO-1 derived xenografts). Finally, an antibody-based probe has shown to be more c-Met specific than GE-137, a c-Met targeting fluorescently-labelled peptide.

# Chapter 5 *In Vitro* and *In Vivo* Imaging of Oesophageal Cancer by Targeting Cyclooxygenase 2 (COX-2)

## 5.1 Introduction

Monoclonal antibodies are considered among the most clinically useful biomolecules for molecular imaging, including for the detection of cancer. However, their target repertoire is limited as there are relatively few tumour-specific or tumour-associated cell surface or soluble antigens. Intracellular molecules represent almost half of the human proteome and provide an unexploited reservoir of potential therapeutic and diagnostic targets (Trenevska et al., 2017). One potentially attractive intracellular target is COX-2. COX-2 is a membrane-bound endoplasmic reticulum (ER)-resident, prostaglandin-endoperoxide synthase (PTGS) enzyme, which is implicated in cancer. In particular, the expression of COX-2 is shown to increase with tumour progression and is thought to be of prognostic value, correlating with poor survival in cancers of the oesophagus (Hu et al., 2017). To carry an antibody inside the cell in order to target COX-2, we used TAT, which is a well-described CPP. CPPs have been widely studied as a means of delivering cargoes to the interior of the cell via the plasma membrane (Hallbrink et al., 2001).

This chapter describes the development of the rabbit mAb Cy5-anti-COX-2[AS66]-TAT antibody for real time detection of intracellular COX-2, including the extensive characterisation and validation of synthetized Cy5-COX-2-TAT probe *in vitro* and *in vivo*.

### 5.1.1 Cyclooxygenase 2

COX enzymes are responsible for formation of a number of molecules, including prostacyclins, thromboxanes and prostaglandins, the latter known for their function as major effectors of cancer initiation and progression. Both COX isoforms are membrane-bound and ER-resident glycoproteins (Smith et al., 2000, Narumiya and FitzGerald, 2001). Structural and biochemical studies have shown that COX-1 and COX-2 are integral membrane proteins, associated with the luminal surfaces of the ER and the adjoining inner membrane of the nuclear envelope (Picot et al., 1994). In healthy tissues, COX-1 is the predominant isoform, whereas COX-2 expression has been shown to be increased in malignant cells, including cells of the oesophagus (Kurumbail et al., 2001). COX-2 is widely expressed in inflammatory cells, cancer and in cancer-associated blood vessels and fibroblasts. The importance of COX-2 in tumour progression has been thoroughly documented, especially in cancers of the colon and oesophagus, where the expression level of COX-2 is shown to increase with tumour progression and COX-2 expression is thought to have a prognostic value and correlates with poor survival (Hu et al., 2017). The results from a recent study further indicate that expression of COX-2 in oesophageal tumour tissue significantly exceeds the expression of COX-2 in normal tissue of the baseline biopsy. Patients whose tumours show high expression of COX-2 are less responsive to treatment compared to patients with lower expression of COX-2 (Jalalabadi et al., 2018). Poor treatment response and patient outcome is associated with a link between COX-2 and aggressive cancers (Boland et al., 2004, Marrogi et al., 2000), where COX-2 overexpression is associated with inhibition of apoptosis (Tsujii and DuBois, 1995), neoangiogenesis (Liu et al., 2000), and increased metastatic potential (Tsujii et al., 1997).

### 5.1.2 Diagnostic Potential of Intracellular Targets

Historically the dogma in the field has been that antibody therapy is amenable to targeting only extracellular antigens that are easily accessible for antibody binding. This is due to the fact that the large size of antibodies prevents them from crossing the cell membrane to access intracellular targets (Trenevska et al., 2017). Consequently, the targets of approved antibody therapies are predominantly extracellular antigens. Cell membranes are impermeable to most large molecules, in fact, only small uncharged molecules can diffuse freely through phospholipid bilayers (Cooper, 2000), therefore current approaches to target intracellular targets are focused mainly on the use of small molecules that are able to passively diffuse into cells (Yang and Hinner, 2015). However, despite the fact that small molecules have been used to target many intracellular antigens, in comparison to antibodies, they are at times not as selective for their targets (Lau and Dunn, 2018). They can demonstrate unpredictable off-target activities, consequently leading to adverse side effects and thus usually require a more tailored clinical development strategy (Trenevska et al., 2017). In contrast, antibodies have greater binding specificity thus offering minimal off-target binding (Lau and Dunn, 2018). However, majority of the antibodies cannot penetrate living cells, thus limiting their ability to targeting molecules that are secreted or located on the cell membrane (Marschall et al., 2011). Gene therapy has been used to generate intracellular antibodies, used as research tools and therapeutic agents against pathogens such as HIV-1, but their use is still experimental because of potential toxicity (Weisbart et al., 2012).

Different mechanisms of cellular uptake have been discussed extensively in the literature and in § 1.13. It follows from this discussion that clinical imaging of a target in the

cytosol, or in the nucleus, pose a great challenge even in cases where successful imaging has been obtained in cells *in vitro* (Duncan and Richardson, 2012). This is due to the problem of getting sufficient of the targeting agent to reach the tumour without also being administered in too high concentrations (Bae and Park, 2011).

Because COX-2 exists within the luminal surface of the ER, adjacent to the inner membrane of the nuclear envelope, it is separated from circulating imaging probes by the cell and ER membranes, rendering it inaccessible, particularly to high-molecular-weight antibody-based agents. However, this barrier is manageable. The intent of the work presented in this chapter was to synthesize a monoclonal anti-COX-2 probe capable of penetrating living cells and localizing in the rough ER adjacent to the nucleus.

### 5.1.3 TAT Cell-Penetrating Peptide

CPPs or protein transduction domains (PTDs) have been widely studied as a means of cargo delivery into cells. CPP are able to deliver genes and biologically active proteins to cytoplasmic compartments via the plasma membrane (Kadkhodayan et al., 2017). A representative CPP is TAT, which is derived from the transactivator of transcription (TAT) of human immunodeficiency virus (Green and Loewenstein, 1988). TAT contains the two positively-charged amino acids, arginine and lysine (YGRKKRRQRRR) and has been reported to deliver various cargos into the cell both *in vitro* and *in vivo* (Cornelissen et al., 2011, Mann and Frankel, 1991).

### 5.1.4 Overall Aim

The aim of the investigations in this chapter was to validate real-time COX-2 imaging using a Cy5-labelled anti-COX-2 [AS66] probe, following initial *in vitro* characterisation. The antibody was selected from a large number of commercially available antibodies on account of the range of applications for which it has been used including WB and ICC, favourable literature reports of its use and availability. Considering the variable quality of commercially available antibodies, the anti-COX-2 [AS66] rabbit mAb was validated using several criteria: specificity, batch-to-batch reproducibility and affinity. It was assessed in two cell lines, one with a positive (OE33) and the other a negative (FLO-1) COX-2 profile, both *in vivo* and *in vitro*. Considering the important role of COX-2 in cancer associated inflammation and progression of oesophageal cancer, as described in § 1.6 and § 1.6.1, a robust and sensitive imaging agent against COX-2 would provide an invaluable diagnostic and prognostic tool to detect and characterise neoplastic changes in the oesophagus.

## 5.2 Experimental Set Up

To acquire live cell images, the Oxford Institute for Radiation Oncology high content open microscopy design (Figure 3.1 (A), § 3.2) with custom built live-cell imaging chamber was used (Figure 3.1 (C), § 3.2). The imaging chamber maintained the cells at a constant temperature and high humidity under a 5% $CO_2$ atmosphere throughout all experiments.

To acquire real-time *in vivo* images, the multiwavelength fluorescence image-guided surgery imaging system developed by Dr Davide Volpi and Professor Boris Vojnovic was used, as described in Chapter 4 (Figure 4.1, § 4.2).

## 5.3 Results

### 5.3.1 Validation of the Anti-COX-2 [AS66] Antibody

The anti-COX-2 [AS66] rabbit monoclonal antibody was validated using a series of criteria. Its specificity, batch-to-batch reproducibility, and affinity were assessed, prior and after labelling with TAT peptide and Cy5 fluorescent dye. The oesophageal adenocarcinoma (OAC) cell lines OE33 and FLO-1, COX-2 high and low-expressing respectively, were used throughout as positive and negative controls.

#### 5.3.1.1 Specificity of Anti-COX-2 [AS66] Tested in a Panel of Cancer Cell Lines

To determine the endogenous expression level of COX-2 and test specificity of the anti-COX-2 [AS66] antibody, western blot analysis was performed in a panel of oesophageal cancer cell lines. Whole cell extracts were collected from OE33, FLO-1 and CP (A-D) and samples (50 μg/lane) were loaded onto 4-12% Bis-Tris protein gel followed by immunoblotting for COX-2, as described in § 2.2. Additionally, recombinant human COX-2 protein was used as a positive control. The expression of COX-2 was high in the OE33 and low in FLO-1 cell lines (Fig 5.1 A). CP cell lines showed varying levels of COX-2 protein expression with the exception of CP-B, in which COX-2 was not detected (Fig. 5.1 B). The specificity of the antibody was confirmed by a presence of a single band at the expected molecular weight of the protein of interest (approx. 69 kDa). CP-A, CP-B, CP-C, and CP-D cell lines were established from Barrett's Oesophagus cells isolated from 4 patients, one from an area of non-dysplastic metaplasia (CP-A), remaining three from areas of high-grade dysplasia (Palanca-Wessels et al., 1998). After the initial

characterisation for COX-2 expression, these cells were not used for work presented in this chapter. Generally, work presented in this thesis is preliminary, proof on concept data and for pragmatic reasons, such as need for more robust cell lines to grow xenografts *in vivo,* CP cell lines were set aside to be used in the future, once initial protocols have been suitably optimised.

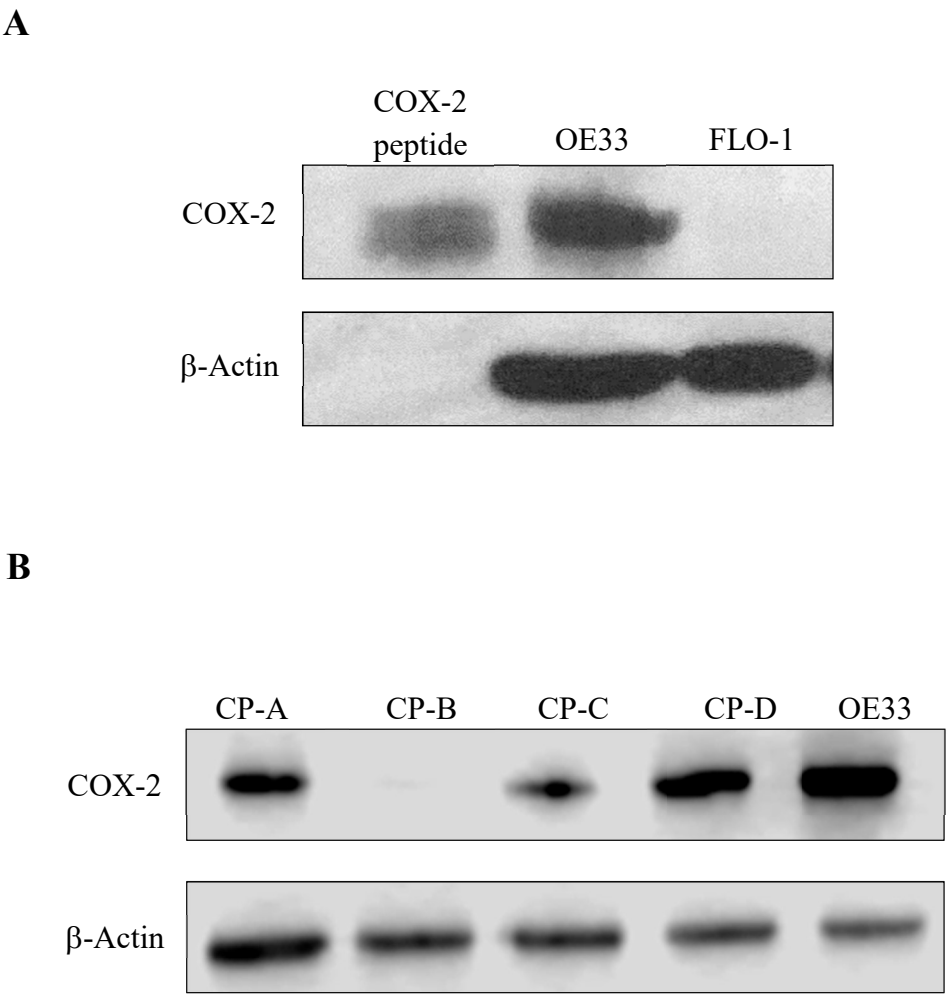



**Figure 5.1[AS66] Antibody Validation and COX-2 Protein Expression Levels in Oesophageal Cancer Cell Lines, Detected by Western Blot Analysis.** Equal amounts of whole cell extracts (50 μg total protein) were compared and β-actin was used as a loading control. Most cell lines, with the exception of FLO-1 (A) and CP-B (B), express COX-2; the expression of COX-2 was greatest in the OE33 cell line. The specificity of the antibody was confirmed by the presence of a single band at a molecular weight corresponding to COX-2, the protein of interest (approx. 69 kDa).

### 5.3.1.2 Determination of Anti-COX-2 [AS66] Affinity by ELISA

In order to gain insight into the interaction between the antigen binding site of anti-COX-2 [AS66] and the COX-2 epitope, the equilibrium dissociation constant ($K_d$) was characterised. An interaction of high affinity is represented by a low $K_d$, where the association rate ($K_{on}$) is many orders of magnitude faster compared to the dissociation rate ($K_{off}$) (Salahudeen and Nishtala, 2017).

ELISA was used, as described in § 2.4. In this experiment, an antigen – recombinant human COX-2 protein – was immobilised on the surface of an ELISA plate and recognised by the anti-COX-2 [AS66] monoclonal antibody. Subsequently, anti-COX-2 [AS66] was bound by a secondary, enzyme linked antibody (HRP). This allowed for subsequent detection using a substrate-chromogen reagent that recognises the conjugated enzyme and allows for development of colour, and successively, a colometric analysis. The absorbance was measured at 450 nm.

The $K_d$ value for the anti-COX-2 [AS66] antibody was determined by testing a range of concentrations for anti-COX-2 [AS66]. Figure 5.2 displays a representative binding curve, showing binding of the anti-COX-2 [AS66] antibody to the COX-2 epitope, reaching saturation at approximately 2 nM with an affinity constant $K_d$ of 0.26 ± 0.03 nM. The data was fitted to a saturation binding curve using a non-linear regression fitting model as described in § 3.3.1.2. The background was considered equal to the reading obtained where no antibody was added, representing non-specific binding. Low $K_d$ value represents greater binding affinity of the ligand to its target (Salahudeen and Nishtala,

2017); consequently, it is concluded that the nanomolar range $K_d$ of the anti-COX-2 [AS66] antibody indicates anti-COX-2 [AS66] has high affinity for COX-2 antigen.

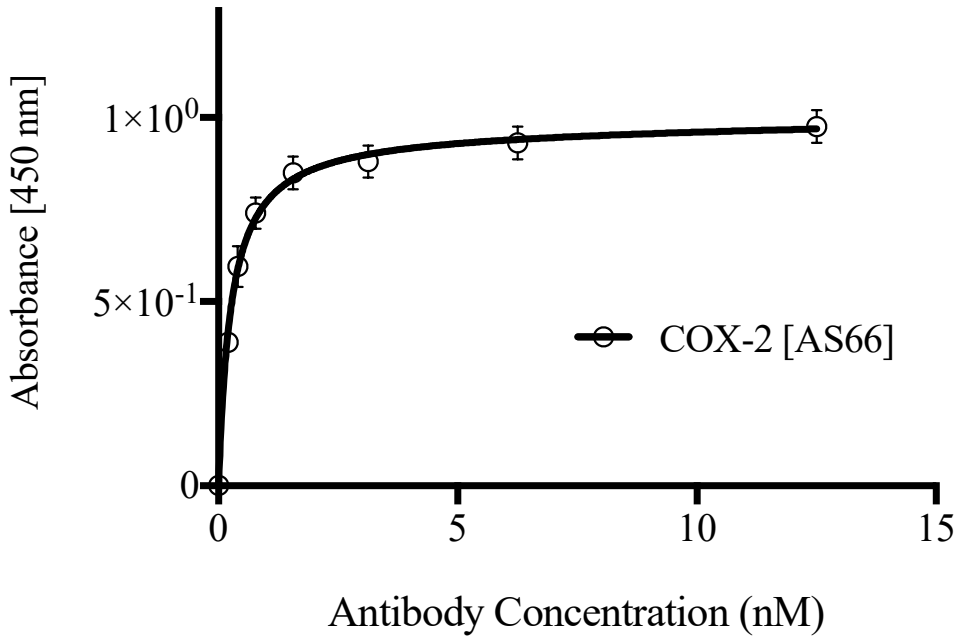



**Figure 5.2 Evaluation of Binding Affinity of Anti-COX-2 [AS66] Antibody by ELISA.** Saturation binding curve representing the binding of the anti-COX-2 [AS66] monoclonal antibody to the COX-2 antigen immobilised on the surface of the ELISA plate. The $K_d$ value was 0.26 ± 0.03 nM (mean ± SEM, n = 3 independent biological repeats).

### 5.3.2 TAT-Antibody Conjugation

The essential step towards targeting COX-2 for imaging was the conjugation of the anti-COX-2 [AS66] mAb to TAT CPP. TAT peptide (GRKKRRQRRRPPQGYG) incorporation was achieved using N-(3-dimethylaminopropyl)-N'-ethylcarbodiimide/ N-hydroxysuccinimide activation, where EDC, a crosslinking agent, is used to couple carboxyl groups, present at the side chains of the biomolecule, to primary amines resulting in the formation of an active intermediate. To increase the stability of the intermediate, Sulfo-NHS was used converting it into an amine-reactive Sulfo-NHS ester which then reacted with the amines from the TAT peptide forming an amide bond.

#### 5.3.2.1 Evaluation of TAT-Anti-COX-2 [AS66] Antibody Conjugation Using $^{123}$I-TAT

Following modification of the anti-COX-2 [AS66] antibody by addition of TAT, a successful antibody : TAT conjugation was determined through $^{123}$I radiolabelling of tyrosine residues in the TAT peptide as previously described (Cornelissen et al., 2011).

Initially, TAT was radiolabelled with $^{123}$I, as detailed in § 2.2.5 and subsequently, anti-COX-2 [AS66] antibody was conjugated to $^{123}$I-TAT, as described in § 2.2.4. Following incubation, a mixture containing $^{123}$I-TAT-labelled antibody and an excess of free $^{123}$I-TAT was purified, using $G_{50}$ gel filtration. Figure 5.3 shows the fractions collected during $G_{50}$ size exclusion chromatography. Fig. 5.3 (A) shows the amount of radioactivity (counts per minute) associated with each of the eluted fractions, as measured by Wizard γ Counter. Fig. 5.3. (B) shows the protein concentration corresponding to each fraction.

The highest CPM was observed in fractions 9 – 13, the same fractions that showed the highest antibody concentrations, suggesting successful labelling of the anti-COX-2 [AS66] with $^{123}$I-TAT.

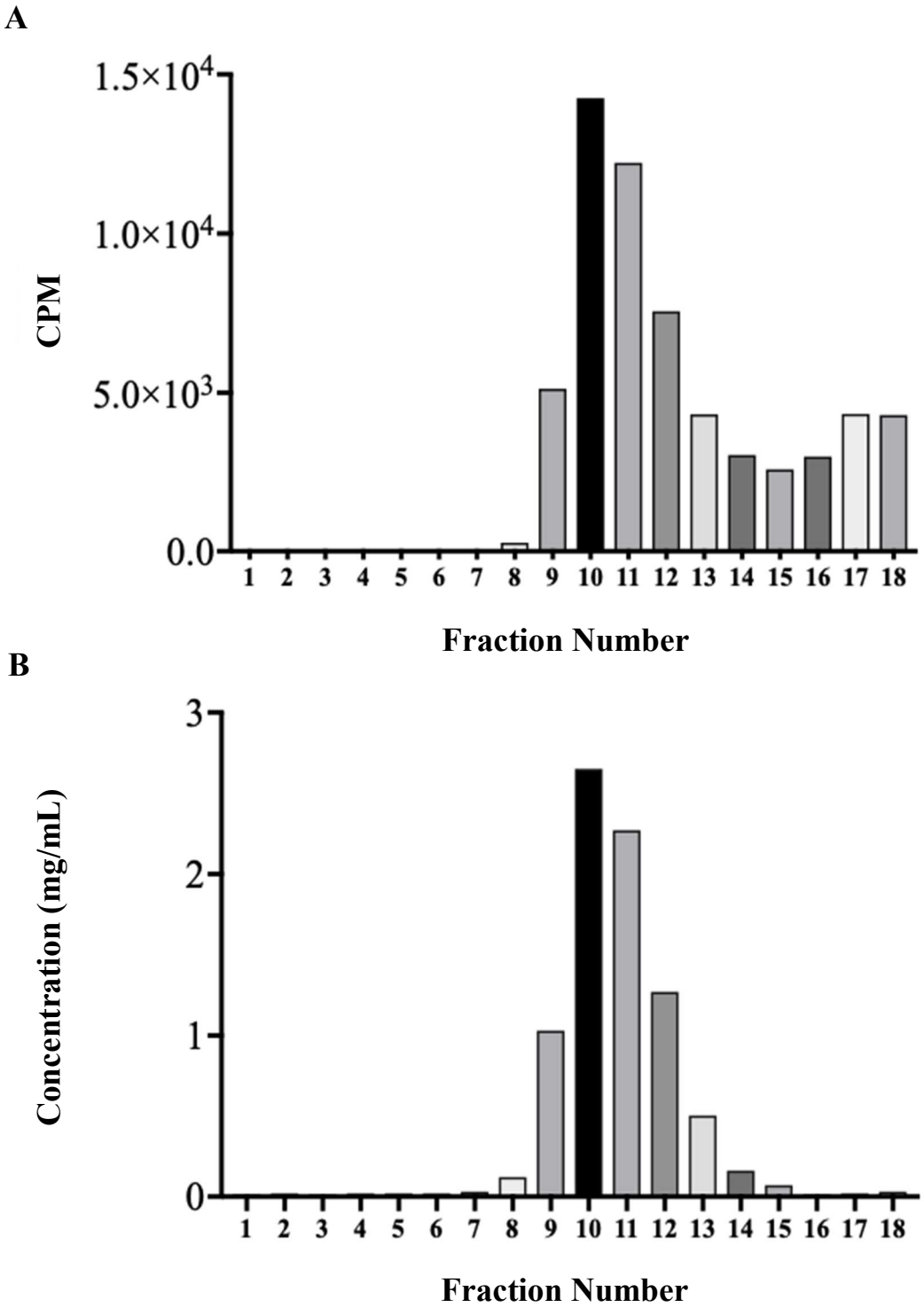



**Figure 5.3 Evaluation of TAT-Anti-COX-2 [AS66] Antibody Conjugation Using $^{123}$I-TAT.** (A) the amount of radioactivity of each eluted fraction, represented as counts per minute (CPM), was measured and compared against the protein concentration each fraction (B) Highest CPM was observed in fractions 9 – 13, the fractions with highest antibody concentration, suggesting successful labelling of the anti-COX-2 [AS66] with $^{123}$I-TAT.

### 5.3.3 Labelling with Cy5 Fluorophore and *In Vitro* Validation of Cy5-COX-2-TAT Probe

#### 5.3.3.1 Cy5 Labelling

TAT-labelled anti-COX-2 [AS66] antibodies were next labelled with Cy5 fluorescent dye. Following incubation, a mixture containing Cy5-labelled antibody and an excess of Cy5 was purified using a $G_{50}$ SEC column. Cy5 labelled antibodies eluted in fractions 8-12, followed by elution of the remaining, free Cy5, in fractions 14-16 (data not shown). Afterwards, an ELISA plate that had been coated with COX-2 protein was incubated with 2 μg/mL of either Cy5-COX-2-TAT, COX-2-TAT or unmodified anti-COX-2 [AS66] antibody (as described in § 2.4) and analysed using an Infinite 200 Pro plate reader. Native, unlabelled anti-COX-2 [AS66] and anti-COX-2-TAT antibodies did not emit fluorescence beyond background levels of 79 ± 5.5 AU and 101 ± 7.8 AU, respectively. In contrast, the Cy5-labelled COX-2-TAT probe emitted red fluorescence when excited at 640 nm, with the mean FI of 3,235 ± 210.6 AU (Figure 5.4). This result confirms successful labelling of anti-COX-2-TAT with Cy5 fluorophore (mean ± SD, n = 1 independent biological experiment, P value < 0.0001, one-way ANOVA).

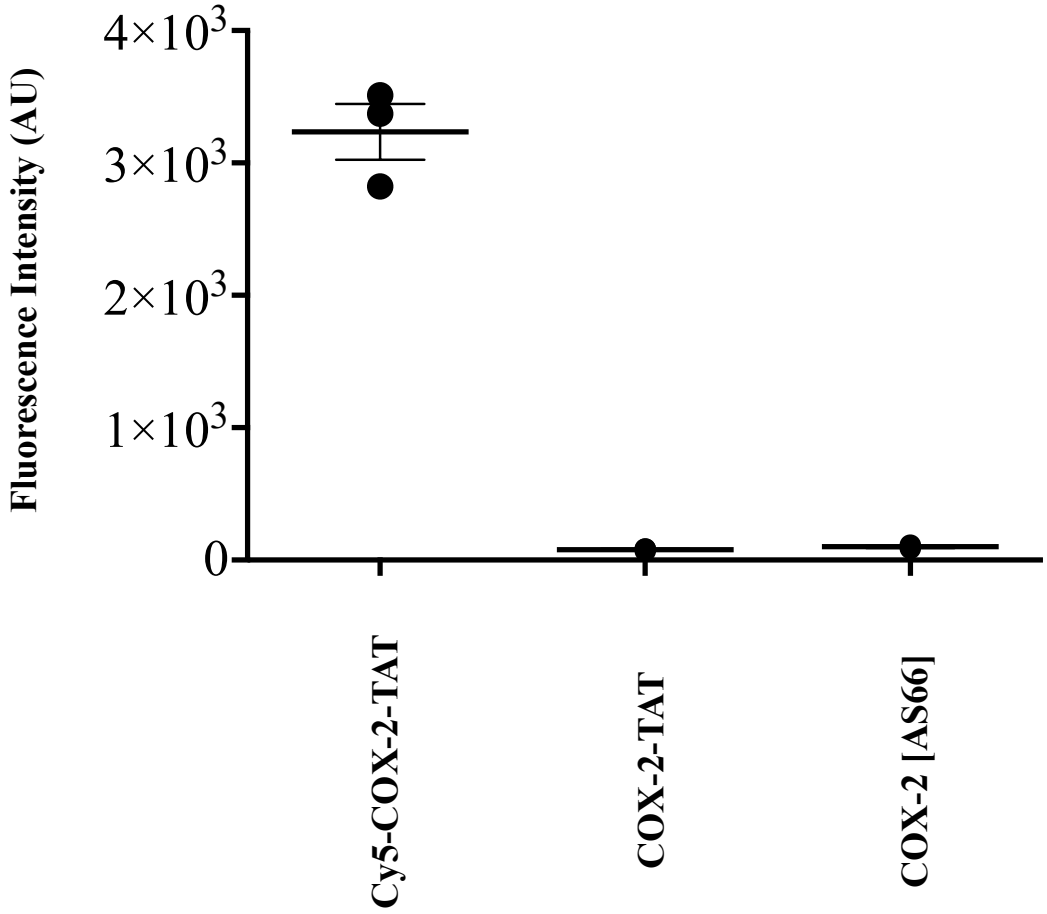



**Figure 5.4 Fluorescence Intensity of Cy5-COX-2-TAT Constructs.** COX-2 antigen, immobilised on the surface of the ELISA plate, was incubated for 3 h with 2 μg/mL of either Cy5-COX-2-TAT, COX-2-TAT or native, unmodified [AS66] antibody (as described in § 2.4) and subsequently analysed using an Infinite 200 Pro plate reader**.** The Cy5-labelled COX-2-TAT probe emitted red fluorescence when excited at 640 nm (mean ± SD, n = 1 independent biological experiment, P value < 0.0001, One-way ANOVA).

### 5.3.3.2 Determination of Cy5-COX-2-TAT Affinity by ELISA

In order to determine whether the interaction between the antigen binding site of anti-COX-2 [AS66] and the COX-2 epitope was altered by addition of Cy5 and TAT, the $K_d$ value of the Cy5-COX-2-TAT was determined.

ELISA was used, as described in § 3.3.2.2. In this experiment, an antigen – recombinant COX-2 protein – was immobilised to the surface and recognised by the Cy5-COX-2-TAT antibody. The attachment of Cy5 far-red dye allowed for a detection using an Infinite 200 Pro plate reader.

The $K_d$ value for the Cy5-COX-2-TAT antibody was determined by testing a range of concentrations of Cy5-COX-2-TAT. Figure 5.5 displays a representative binding curve, showing binding of the Cy5-COX-2-TAT antibody to the COX-2 epitope, reaching saturation at approximately 5 nM with an affinity constant $K_d$ of 0.79 ± 0.16 nM. Low $K_d$ value within the same order of magnitude as native anti-COX-2 [AS66] (0.26 nM and 0.79 nM for anti-COX-2 [AS66] and Cy5-COX-2-TAT, respectively) suggests the good binding affinity of the ligand to its target has been retained despite the Cy5 and TAT modifications; consequently, it is concluded that nanomolar range $K_d$ of the Cy5-COX-2-TAT construct indicates the synthesized anti-COX-2 probe has high affinity for COX-2 antigen (mean ± SEM, n = 3 independent biological experiments, P = 0.5468, unpaired t-test).

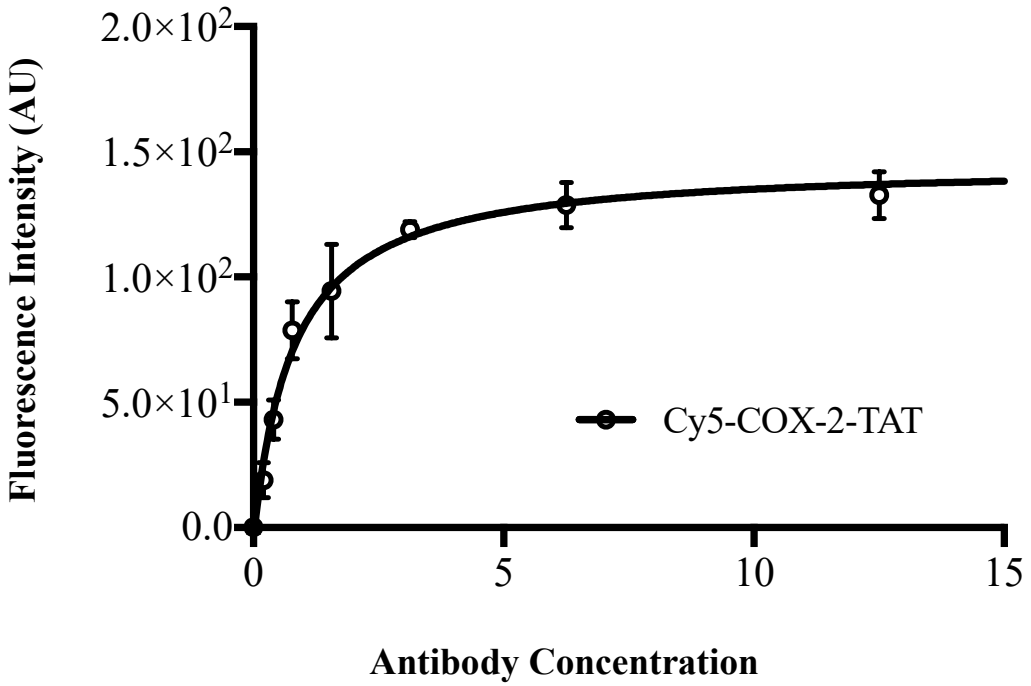



**Figure 5.5 Evaluation of Binding Affinity by ELISA.** Saturation binding curve representing the binding of the Cy5-COX-2-TAT probe to the COX-2 antigen, immobilised on the surface of the ELISA plate. The attachment of Cy5 far-red dye allowed for detection using a fluorescent microscope. The $K_D$ value was 0.79 ± 0.16 nM (mean ± SEM, n = 3 independent biological experiments, P = 0.5468, unpaired t-test).

Finally, the ability of anti-COX-2-TAT and anti-COX-2 [AS66] to compete with Cy5-COX-2-TAT for binding to COX-2 was determined to be similar with $IC_{50}$ values of 1.39 ± 0.16 and 1.74 ± 0.11 (Figure 5.6, mean ± SEM, n = 3 independent biological experiments, P = 0.1458, unpaired t-test), respectively. This indicates that the Cy5 and TAT additions to anti-COX-2 [AS66] antibody did not significantly change its affinity for the target epitope.

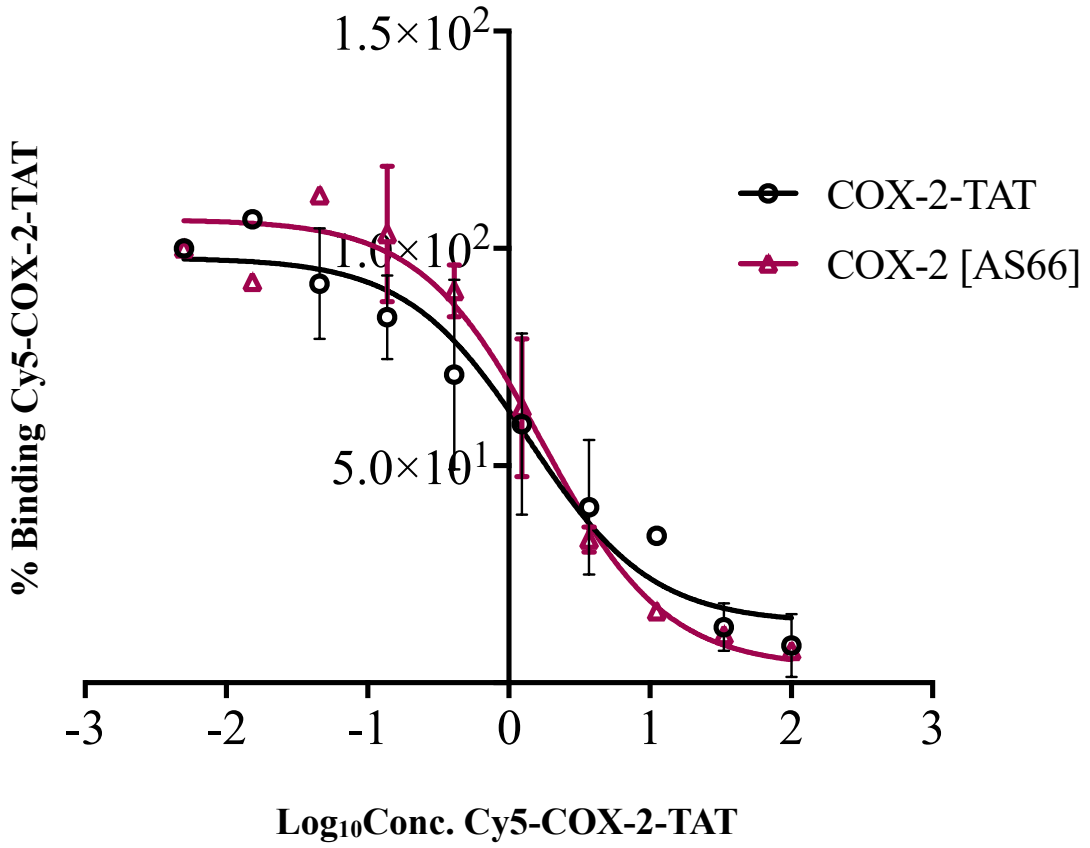



**Figure 5.6 Competitive Binding Study.** ELISA showing binding of Cy5-COX-2-TAT and COX-2-TAT to the COX-2 antigen, immobilised on the surface of an ELISA plate, in competition with increasing concentrations of anti-COX-2 [AS66]. The $\log IC_{50}$ values recorded were 1.74 ± 0.11 and 1.39 ± 0.16, respectively (mean ± SEM, n = 3 independent biological experiments, P = 0.1458, unpaired t-test).

### 5.3.4 Evaluating the COX-2 Binding and Internalising Properties of Cy5-COX-2-TAT Antibody Constructs in OE33 and FLO-1 Cells

The ability of the Cy5-COX-2-TAT conjugate to penetrate the cell membrane and undergo nucleocytoplaasmic transport was validated using live cell fluorescence imaging. Direct visualisation of the antibody and its cellular localisation was achieved by using Cy5 labelled antibody conjugates and Hoechst nuclear stain.

#### 5.3.4.1 Cy5-COX-2-TAT Internalises Efficiently in OE33 but Not FLO-1 Cells

The internalisation properties of the antibody constructs were evaluated in OE33 and FLO-1 cells. Both cells lines were exposed to Cy5-COX-2-TAT for 3 or 24 hours at 37°C (3 μg/mL). Hoechst 33342 staining and Calcein, a cell-permeant dye, were used to determine the number of nuclei and to assess gross cell morphology. Prior to imaging with a fluorescence microscope, standard culture medium was replaced with fresh, phenol red-free culture medium, as described in § 2.6. OE33 cells show good internalisation of Cy5-COX-2-TAT probe, with cytoplasmic staining, with much lower signal observed in FLO-1 cells (Figure 5.7). The average FI per cell in OE33 cells was 136,681 ± 49,427 AU. In comparison, FLO-1, which shows very little uptake of the Cy5-COX-2-TAT construct, had an average FI of 7,543 ± 6,516 AU per cell (Figure 5.8, Mean ± SD, $P < 0.05$, one-way ANOVA).

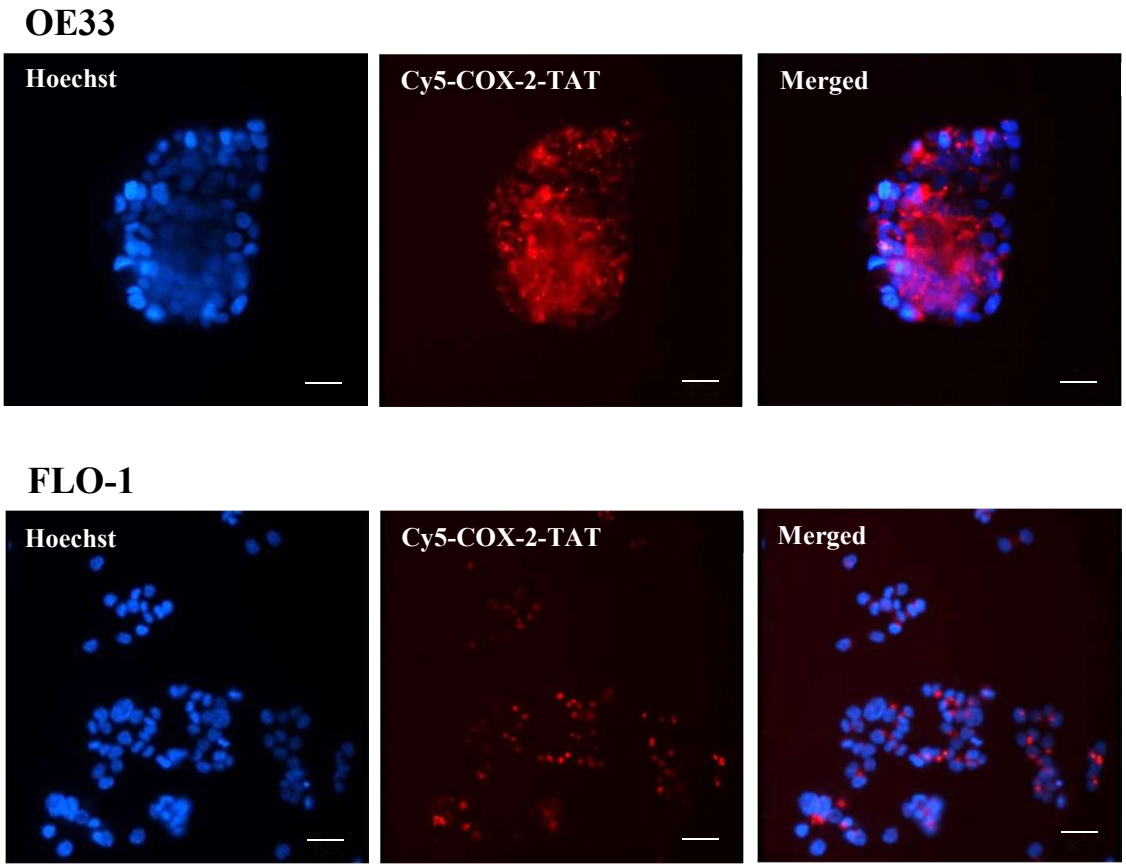



**Figure 5.7 Internalisation of Cy5-COX-2-TAT in OE33 and FLO-1 Cells.** Immunofluorescence microscopy: OE33 and FLO-1 cells were exposed to Cy5-COX-2-TAT for 3 h at 37°C (3 μg/mL). Hoechst 33342 staining was used to determine the number of nuclei and to assess gross cell morphology. FLO-1, a low COX-2 expressing cell line, shows minor internalisation of the Cy5-COX-2-TAT in comparison to OE33 cells. Bar size is 20 μm.

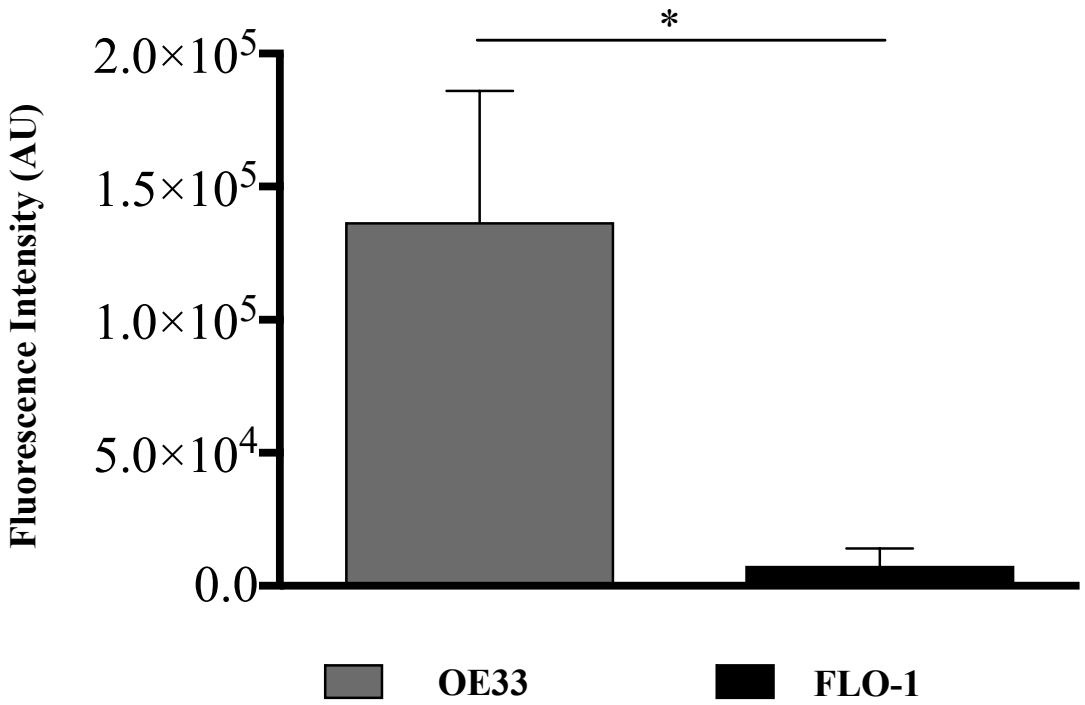



**Figure 5.8 Uptake of Cy5-COX-2-TAT in OE33 and FLO-1 Cells.** Both cell lines were exposed to Cy5-COX-2-TAT for 3 hours at 37°C (3 μg/mL). OE33, a high COX-2 expressing cell line, shows significantly higher average fluorescence intensity per cell after treatment with CY5-COX-2-TAT in comparison to FLO-1, a low COX-2 expressing cell line (Mean ± SD, $P < 0.05$, n = 1 independent biological experiment).

### 5.3.4.2 Specificity and Internalisation of Cy5-COX-2-TAT in OE33

Specify of the Cy5-COX-2-TAT antibody constructs was further evaluated in vitro using OE33 and FLO-1 cells. Both cells lines were exposed to Cy5-COX-2-TAT, Cy5-IgG-TAT, Cy5-IgG or Cy5-COX-2 for 3 h at 37°C (3 μg/mL). Figure 5.9 shows the difference in uptake of the Cy5-COX-2-TAT probe compared to control constructs in OE33 and FLO-1 cells. Despite the fact that OE33 cell line shows significantly higher uptake of the Cy5-COX-2-TAT antibody when compared to FLO-1 cells (139,900 ± 15,880 AU and 14,500 ± 1,542 AU, $P < 0.0001$) and significantly higher uptake of Cy5-COX-2-TAT *versus* non-specific Cy5-IgG ± TAT (35,900 ± 9,590 AU and 11,700 ± 1,619 AU for Cy5-IgG-TAT and Cy5-IgG, respectively, mean ± SEM, n =3 independent biological experiments, $P < 0.0001$, two-way ANOVA), there was no significant difference in OE33 uptake of Cy5-COX-2-TAT or Cy5-COX-2 (AFI, 139,900 ± 15,880 AU *versus* 125,200 ± 12,833 AU, respectively (P value = 0.3854).

Figure 5.10 shows immunofluorescence microscopy of OE33 cells immuno-labelled with Cy5-COX-2-TAT, Cy5-IgG-TAT or Cy5-COX-2. FLO-1 cells and Cy5-IgG control treatment are not shown. Hoechst 33342 staining and Calcein, a cell-permeant dye, were used to determine the number of nuclei and to assess gross cell morphology. Prior to imaging with fluorescence-lifetime imaging microscopy, standard culture medium was replaced with fresh, phenol red-free culture medium, as described in § 2.6. OE33 cells show marked internalisation of Cy5-COX-2-TAT probe, with perinuclear staining. However, a similar signal intensity was observed in OE33 cells immuno-labelled with Cy5-COX-2 without TAT.

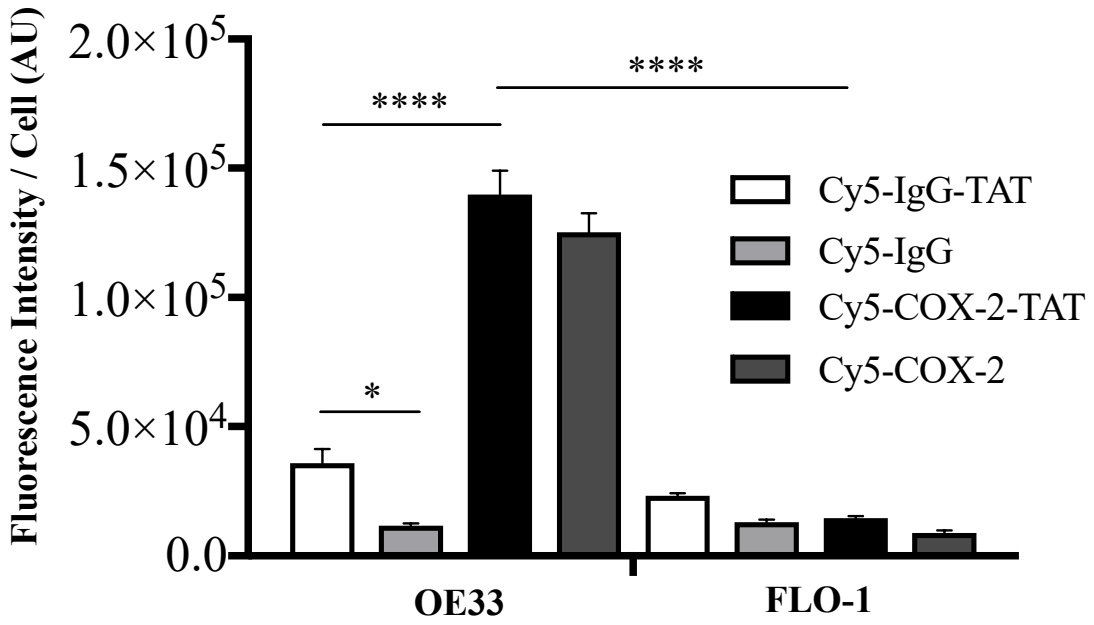



**Figure 5.9 COX-2 Binding and Internalisation Properties of the Cy5-COX-2-TAT Antibody Constructs in OE33 and FLO-1 Cells.** Both cell lines were exposed to Cy5-COX-2-TAT, Cy5-IgG-TAT, Cy5-IgG or Cy5-COX-2 for 3 hours at 37˚C (3 μg/mL). OE33, a high COX-2 expressing cell line, shows significantly higher uptake of the Cy5-COX-2-TAT antibody when compared to FLO-1 cells (Mean ± SEM, $P < 0.0001$, two-way ANOVA). Uptake of Cy5-COX-2-TAT was higher *versus* Cy5-IgG ± TAT (Mean ± SEM, $P < 0.0001$, Two-way ANOVA), there is no significant difference between OE33 uptake of TAT labelled and TAT-unlabelled Cy5-COX-2 antibody (Mean ± SEM, P value = 0.3854, Two-Way ANOVA, n = 3 independent biological experiments).

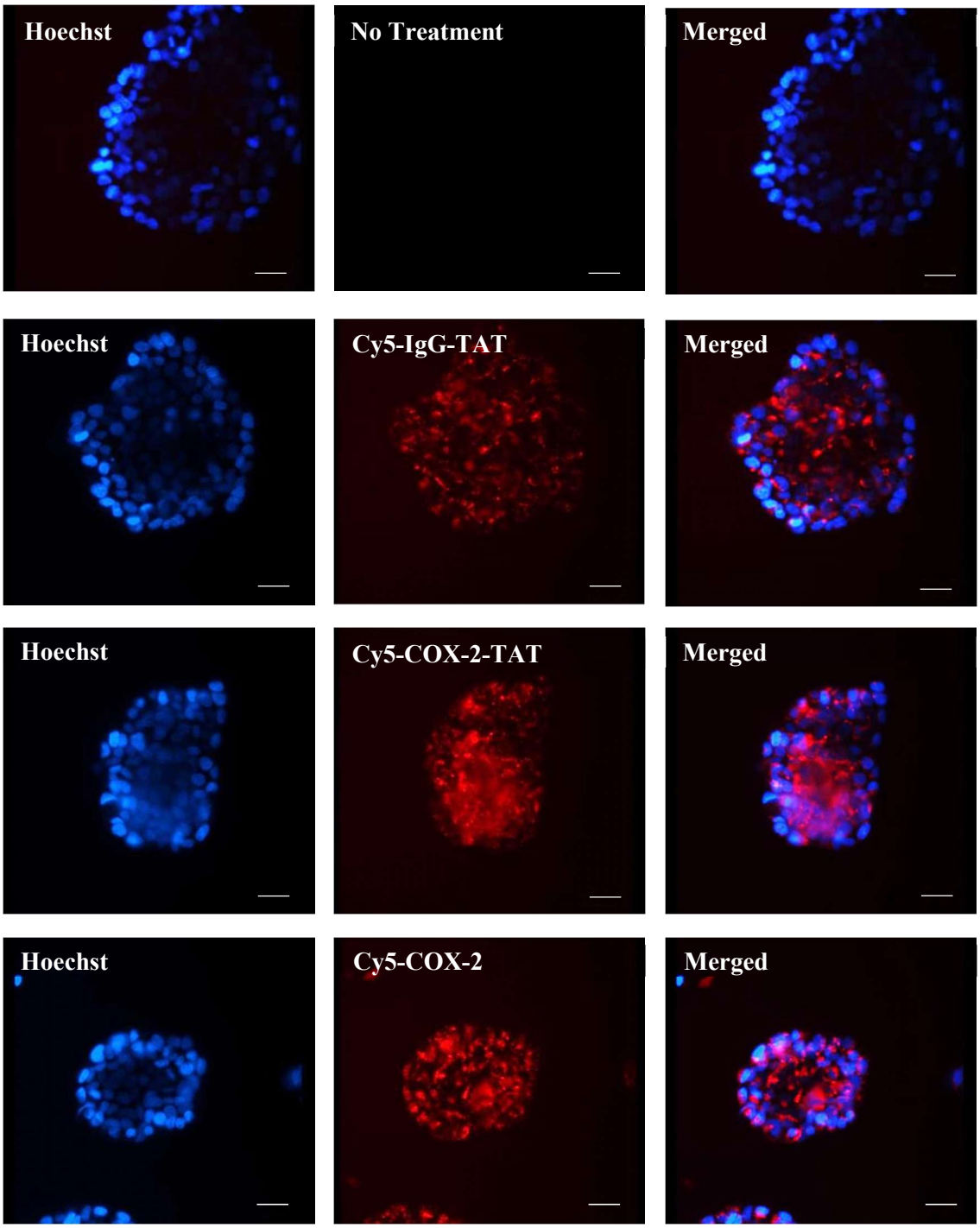



**Figure 5.10 Internalisation of Cy5-COX-2-TAT in OE33 Cells.** Immunofluorescence microscopy: OE33 cells were exposed to Cy5-IgG-TAT, Cy5-COX-2-TAT and Cy5-COX-2 for 3 h at 37°C (3 µg/mL). Hoechst 33342 staining was used to determine the number of nuclei and to assess gross cell morphology. OE33 cells show good internalisation of Cy5-COX-2-TAT probe, with cytoplasmic staining, however, similar signal intensity was observed in OE33 cells immuno-labelled with Cy5-COX-2 without TAT. Scale bar = 20 µm.

### 5.3.5 Investigation of Specificity of COX-2 [AS66] Antibody

To test whether COX-2 [AS66] antibody uptake is abrogated when COX-2 protein is removed, a siRNA knockdown method was used. This technique is extensively used for antibody validation, as described in § 3.3.3.2.

OE33 was treated with siRNA-transfection buffer as described in § 2.7, and the knockdown was confirmed by Western Blot analysis (Figure 5.11).

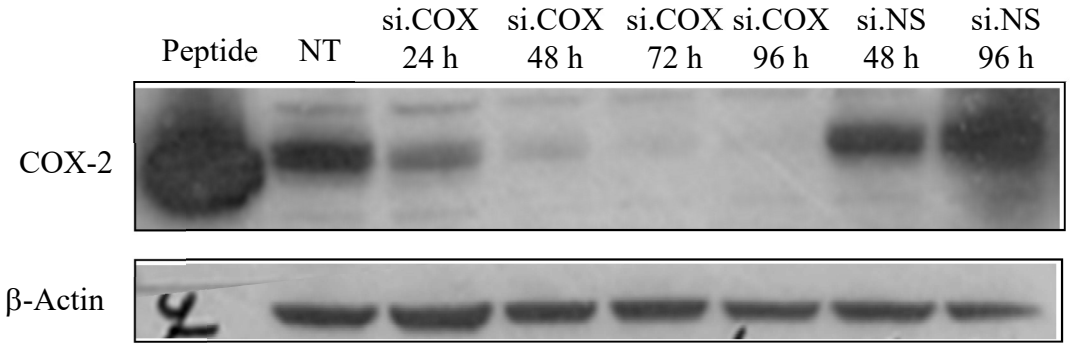



**Figure 5.11 Validation of siRNA-Mediated COX-2 Knockdown in the OE33 Cell Line.** OE33 cells were incubated with either a COX-2-targeting siRNA pool (si.COX) or non-specific pool (si.NS), and harvested at different times for western blot analysis. Non-transfected cells (NT) and COX-2 peptide were used as controls. Equal amounts of whole cell extracts (50 μg total protein) were compared and β-actin was used as a loading control.

Subsequently, non-transfected (NT) and transfected OE33 cells (10 nM si.COX) were exposed to Cy5-COX-2-TAT for 3 h at 37°C (3 μg/mL). As shown in Figure 5.12, despite successful knockdown confirmed by WB, there was no difference in AFI per cell between NT and si.COX treated OE33 cells (130,969 ±12,907 AU and 140,404 ± 5,467 AU for NT and OE33 si.COX, respectively, mean ± SD, n = 1 independent biological experiment, P = 0.6523, one-way ANOVA). Furthermore, there was no significant difference in AFI per cell between si.COX knockdown and si.NS (non-specific siRNA) treated OE33 cells (140,404 ± 5,467 AU *versus* 133,281 ± 11,825 AU, mean ± SD, n = 1 independent biological experiment, P = 0.8082, One-way ANOVA). Finally, there was no difference in AFI between si.COX knockdown cells and OE33 cells grown in media without serum (serum starved, 128,887 ± 6,654 AU, mean ± SD, n = 1 independent biological experiment, P = 0.5082, one-way ANOVA). Taken together, these results suggest that Cy5-COX-2-TAT has low specificity for COX-2 and shows off-target binding. These changes are not driven by the addition of TAT, but rather, by the poor quality of the COX-2 [AS66] antibody, which most likely binds multiple epitopes.

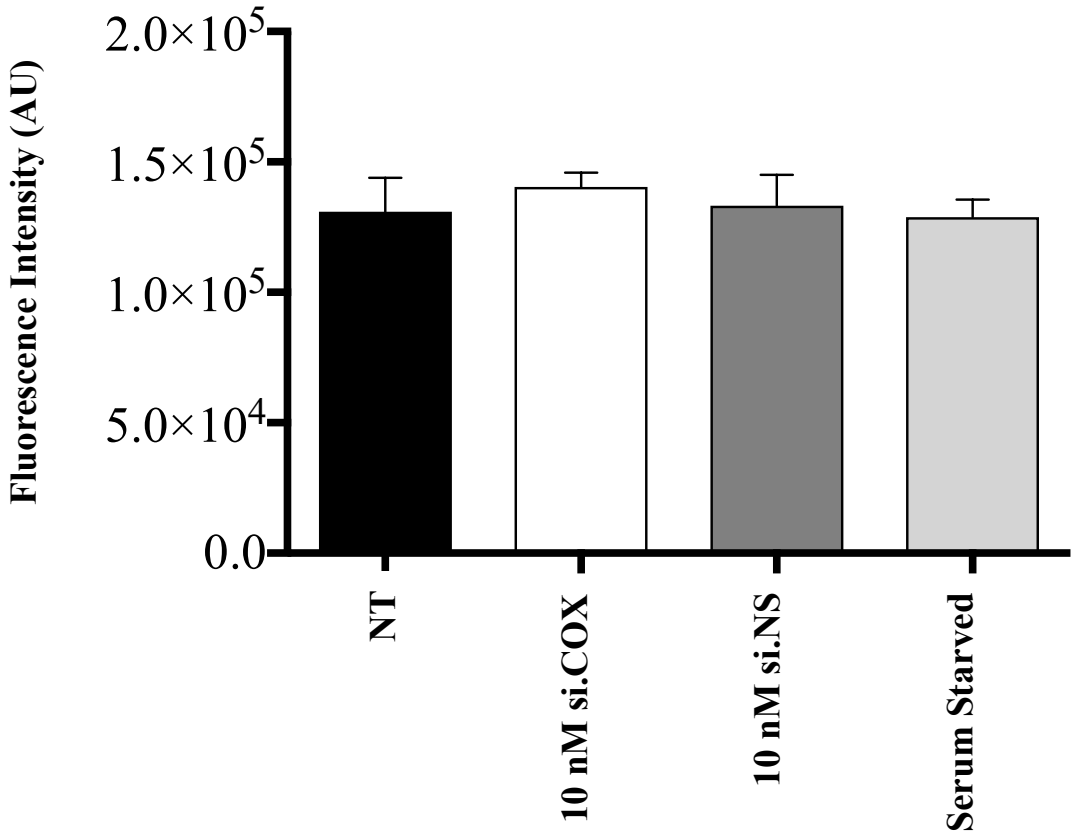



**Figure 5.12 Demonstration of the Off-Target Binding of Cy5-COX-2-TAT, siRNA Knockdown.** Non-transfected (NT), si.COX or si.NS transfected, and serum starved OE33 cells were exposed to Cy5-COX-2-TAT (3 h at 37°C, 3 μg/mL) and the binding of the probe was subsequently determined using fluorescence microscopy and further analysed to give quantitative data i.e. average fluorescent intensity (AFI) per cell between NT, si.NS, serum starved and COX-2 knockdown OE33 cells. There is no significant difference in AFI per cell between NT and si.COX treated OE33 cells (mean ± SD, n = 1 independent biological experiment, $P > 0.05$, one-way ANOVA).

### 5.3.6 *In Vivo* Evaluation of the Cy5-COX-2-TAT in an OE33 Xenograft Model

NOD/SCID/γ mice were used to grow OE33 xenografts, as detailed in § 4.3.1. For this purpose, mice were inoculated, as described in § 2.8.2, and all animals developed palpable tumours at the site of injection after one week and measurements were obtained, as described in § 2.8.3. No signs of distress or weight loss were observed during that period.

#### 5.3.6.1 *In Vivo* and *Ex Vivo* Biodistribution of Cy5-COX-2-TAT

Whole-body optical images were acquired at 24 h, 48 h, and 72 h post iv injection of Cy5-COX-2-TAT, Cy5-IgG or Cy5-COX-2 (20 μg) and were used to evaluate *in vivo* biodistribution. As shown in Figure 5.13, the OE33 tumour to skin contrast provided by Cy5-COX-2-TAT at 72 h post injection was low with an average of 3.15 ± 1.2 (mean ± SD, n = 3 animals) and did not change significantly for the duration of the experiment (3.12 ± 1.3 at 24 h and 3.10 ± 0.9 at 48 h, mean ± SD). The ratios observed for the non-specific control agents, Cy5-IgG-TAT and Cy5-COX-2, were not significantly different from Cy5-COX-2-TAT with 4.99 ± 0.79 (P = 0.7659, one-way ANOVA) and 2.68 ± 0.16 (P = 0.1299, one-way ANOVA), respectively, and were unchanged throughout the duration of the experiment (4.8 ± 0.56 at 24 h, and 4.77 ± 0.91 at 48 h for Cy5-IgG-TAT and 2.8 ± 0.2 at 24 h, and 2.77 ± 0.35 at 48 h for Cy5-COX-2).

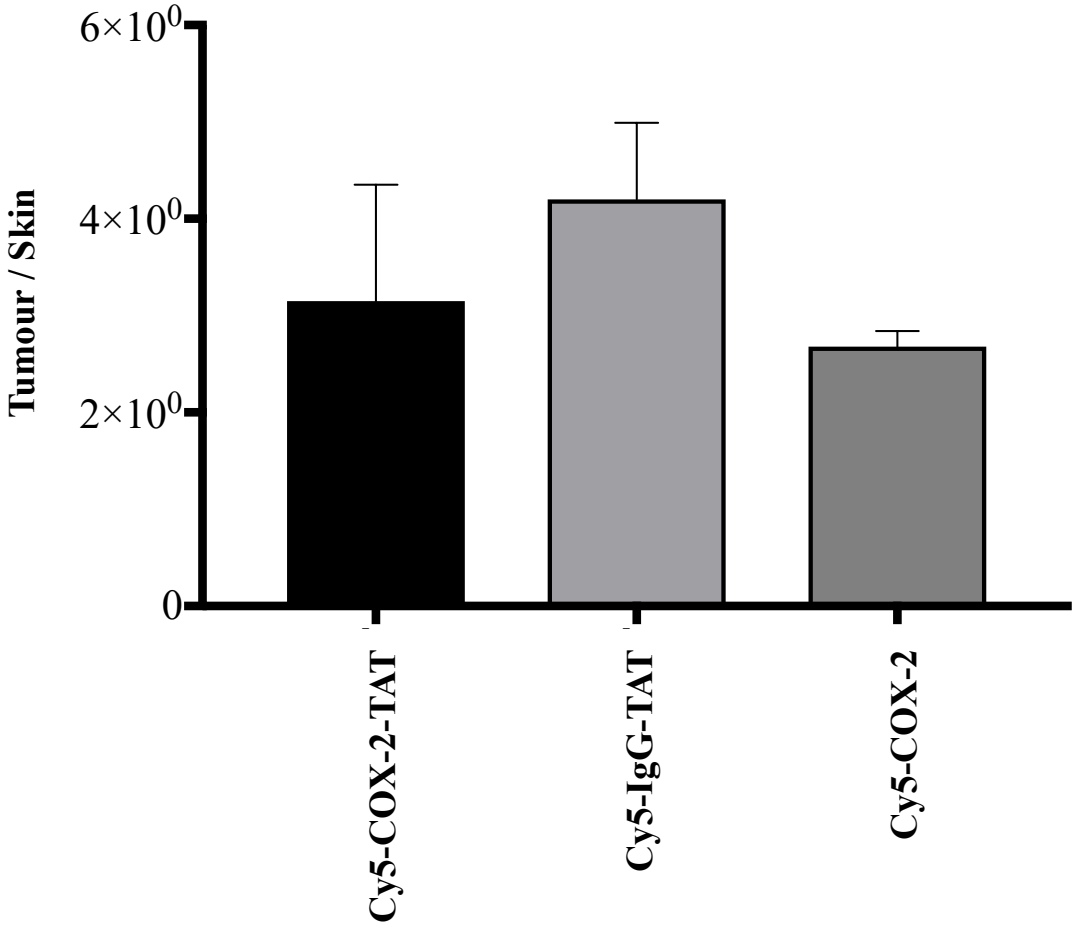



**Figure 5.13 *In Vivo* Biodistribution of Cy5-COX-2-TAT.** Quantification of optical intensities of tumour areas by image analysis was performed at 72 h post iv of Cy5-COX-TAT, Cy5-IgG or Cy5-COX-2 (20 μg). Data are expressed as TBR and bars represent mean ± SD (n = 3 mice).

Tumour, stomach, large intestines and liver were noted as the main organs of uptake after administration of Cy5-COX-2-TAT at 72 h post iv (Figure 5.14). The highest signal was observed in the stomach, with organ to muscle ratio of 16.38 ± 4.96, large intestine (6.7 ± 0.85), tumour (3.93 ± 0.89) and liver (3.10 ± 0.36). No significant accumulation in other organs was observed including kidneys and heart. A similar tissue distribution was observed for Cy5-IgG-TAT and Cy5-COX-2, where the highest accumulation of optical tracers was also observed in the stomach, tumour, large intestines and liver (data not shown).

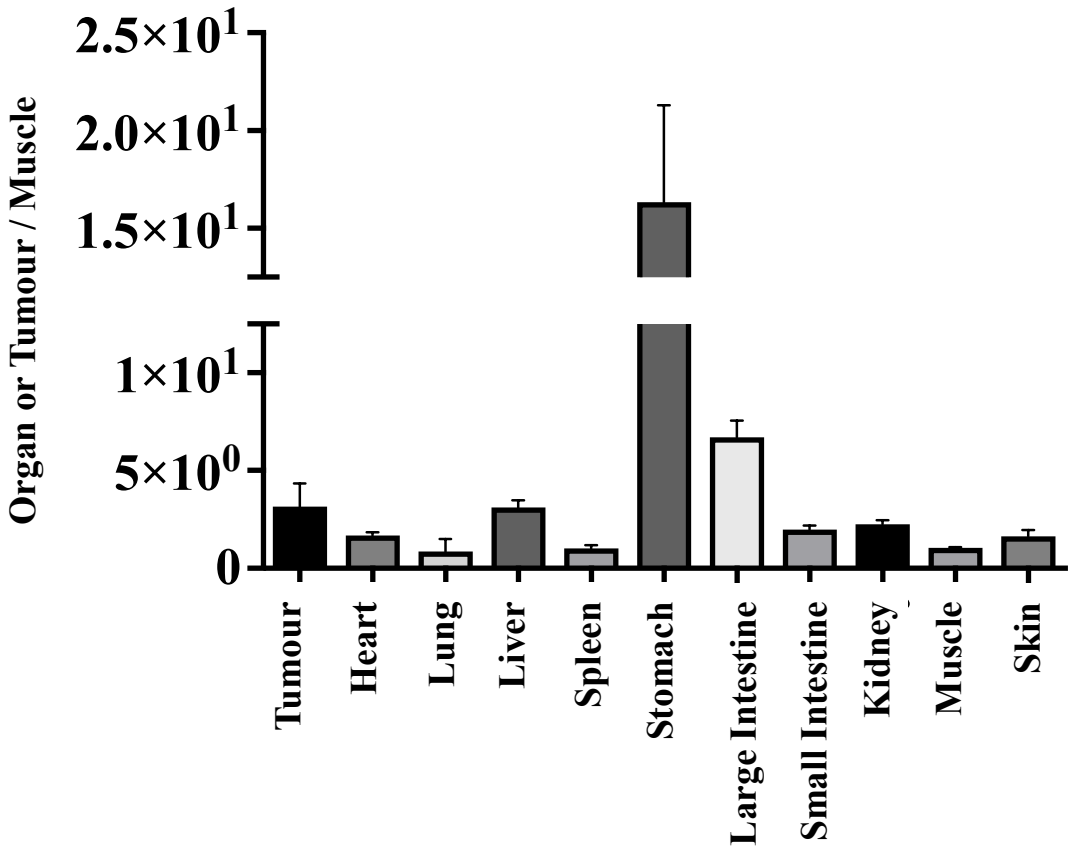



**Figure 5.14 *Ex Vivo* Biodistribution of Cy5-COX-2-TAT.** *Ex vivo* biodistribution analysis was performed at 72 h post iv of 20 μg of Cy5-COX-2-TAT. Tumour and major tissues are shown. Data are expressed as organ or tumour/ muscle and bars represent mean ± SD (n = 3 mice for each group).

Representative optical images of mice injected with Cy5-COX-2-TAT, Cy5-IgG-TAT and Cy5-COX-2 (20 μg) are shown in Figure 5.15. A WL image is shown on the left, highlighting the location of the tumour. Fluorescent images on the right show low tumour uptake with no significant difference in signal intensity between mice injected with Cy5-COX-2-TAT, Cy5-IgG-TAT or Cy5-COX-2 (P = 0.2818, one-way ANOVA, data quantified from the image in Figure 5.15 using ImageJ).

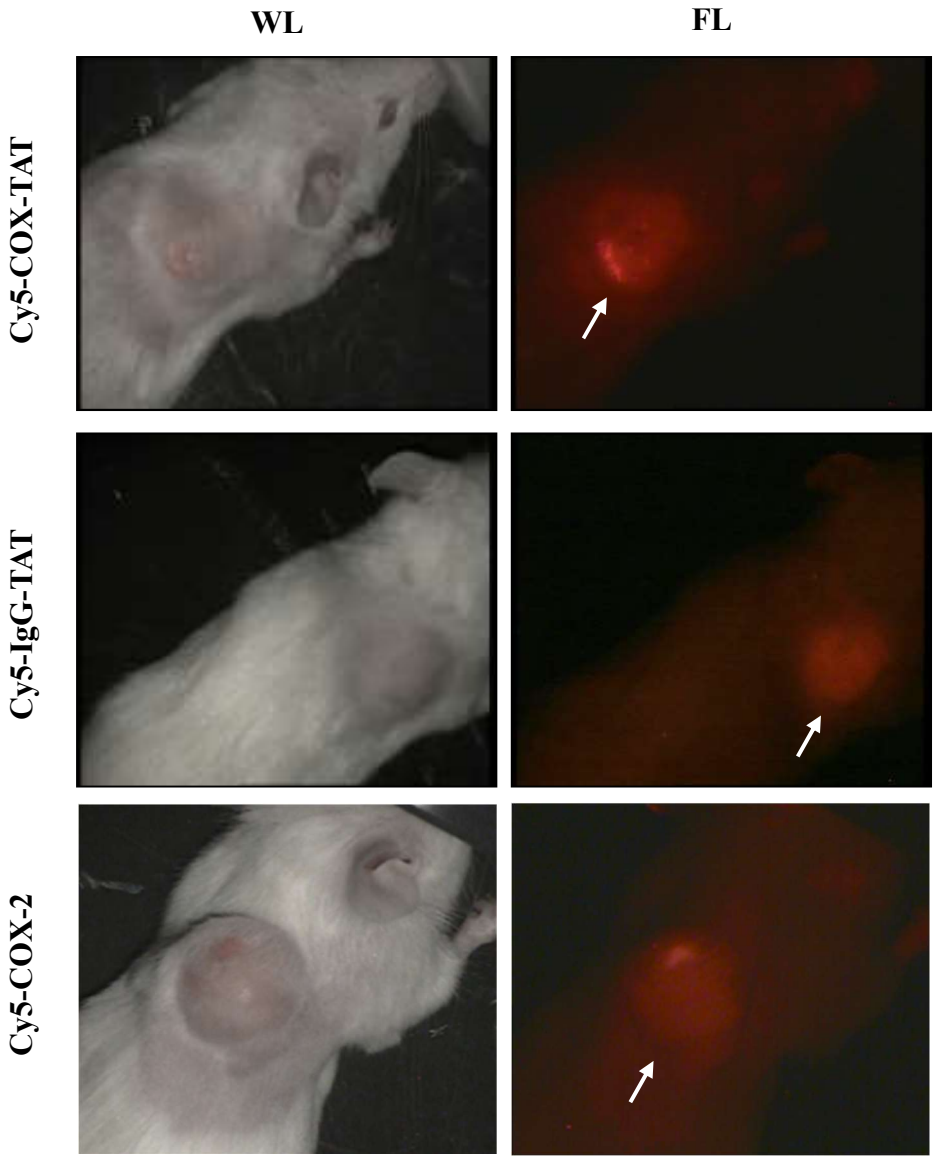



**Figure 5.15 Optical Images Showing Tumour Uptake of Cy5-COX-2-TAT, Cy5-IgG-TAT and Cy5-COX-2 in OE33 Xenografts.** Representative optical images of OE33 xenograft bearing mice, 24 h post iv with Cy5-COX-2-TAT, Cy5-IgG-TAT or Cy5-COX-2 (10 μg). WL image on the left, and fluorescent image on the right, arrows point to tumours, showing no significant difference in signal intensity between OE33 xenograft injected with different antibody constructs.

## 5.4 Discussion

In this chapter, rabbit monoclonal anti-COX-2 [AS66] antibody was investigated *in vitro* and *in vivo* using several assays, to explore its potential suitability as a diagnostic COX-2-targeting probe.

### 5.4.1 Specificity of Anti-COX-2 [AS66] Antibody Tested in a Panel of Cancer Cell Lines

The anti-COX-2 [AS66] antibody was shown to be specific, with a single band at approx. 69 kDa observed for OE33 cells (Figure 5.1), in line with a positive control, synthetic full-length COX-2 enzyme. COX-2 expression in the OE33 cell line is well documented in the current literature (Abdalla et al., 2005, Cheong et al., 2004). No other bands were present across the membrane at different molecular weights, which suggests a lack of breakdown products, sample degradation or splice variants (Ghosh et al., 2014). The FLO-1 cell line had undetectable levels of COX-2, consistent with previous reports (Aggarwal et al., 2000). Further Western blots and ELISA analysis, using recombinant human COX-2 protein, showed high binding activity and specificity of anti-COX-2 [AS66] towards both folded and denatured COX-2. This suggests that anti-COX-2 [AS66] antibody recognises a linear, (rather than conformational) epitope, where a stretch of amino acids is sufficient for binding of the antibody (Sela, 1969). Antibodies directed towards linear epitopes give WB bands (Forsstrom et al., 2015). In contrast, antibodies towards conformational epitopes did not bind their target proteins in the WB assays, demonstrating the advantage of using antibodies recognizing linear epitopes for immunoassays involving whole or partial denaturation of the protein targets – a process

shown to destroy conformational epitopes by unfolding the protein structure (Fowler et al., 2011, Freire et al., 1990).

### 5.4.2 Determination of Anti-COX-2 [AS66] Affinity by ELISA

The determination of antibody-antigen affinity constants and binding kinetics is an important part of antibody characterisation and may be predictive of antibody performance in biotechnological applications (Neri et al., 1996). Representative binding curves in Figure 5.2 demonstrate good affinity of anti-COX-2 [AS66] antibody to the COX-2 epitope, and have been generated using the solid-phase ELISA method, which provides reproducible and precise estimates of $K_d$ for antigen-antibody complexes (Kim et al., 1990). A low $K_d$ value in the nM range represents high binding affinity, and is arguably the expected standard amongst commercially available antibodies.

### 5.4.3 Evaluation of TAT-Anti-COX-2 [AS66] Antibody Conjugation Using $^{123}$I-TAT

The TAT/IgG labelling was determined by radioiodination of the TAT peptide as previously described (Cornelissen et al., 2007). Figure 5.3 shows antibody-TAT conjugation with (A) amount of radioactivity of each of the eluted fractions, as measured by Wizard γ Counter, and (B) shows the corresponding protein concentration of each fraction. The greatest radioactivity was observed in the same fractions that showed highest antibody concentrations, suggesting successful labelling of anti-COX-2 [AS66] with $^{123}$I-TAT, as previously reported (Cornelissen et al., 2011).

### 5.4.5 Cy5 Labelling and Determination of Cy5-COX-2-TAT Affinity by ELISA

Fluorescent labels provide significant advantages for studying biological processes, providing greater contrast as compared to visualising cells with brightfield microscopy alone. Successful labelling of the anti-COX-2 [AS66] antibody with Cy5 (Figure 5.4) allowed for visualisation of COX-2 in OE33 cells, using live cell fluorescence microscopy. During Cy5-labelling, random distribution of Cy5 molecules across antibody domains, including the antigen-binding site, has the potential to result in alterations in the binding capacity of the antibody to its target or even complete inactivation of the antibody (Vira et al., 2010). However, Figure 5.5 shows that immunoreactivity of anti-COX-2 [AS66] was not affected to a significant degree by Cy5 modification, with a $K_d$ similar to that of the native COX-2 [AS66] antibody (Figure 5.2). Furthermore, $LogIC_{50}$ values were generated to further evaluate the potency (affinity) of the Cy5-COX-2-TAT and Cy5-COX-2 constructs when in competition with native COX-2 [AS66] for binding recombinant human COX-2 protein (Gubler et al., 2013). The final construct, Cy5-COX-2-TAT, was shown to retain a high affinity despite Cy5- and TAT additions to the COX-2 [AS66] antibody, as previously reported (Cornelissen et al., 2011).

### 5.4.6 Evaluating the COX-2 Binding and Internalising Properties of Cy5-COX-2-TAT Antibody Constructs in OE33 and FLO-1 Cells

#### 5.4.6.1 Cy5-COX-2-TAT Internalises Efficiently in OE33 but Not FLO-1 Cells

The TAT protein of HIV-1 has been described as a cell-penetrating peptide, which facilitates intracellular and intranuclear delivery of biomolecules (Heitz et al., 2009, Frankel and Pabo, 1988). Figures 5.7 and 5.8 demonstrate in live cells that TAT peptide conjugated to anti-COX-2 [AS66] antibody was able to facilitate delivery of the antibody into the cell. The anti-COX-2-TAT construct was labelled with Cy5 dye (Figure 5.4) to visualise its intracellular distribution. The conjugate was shown to localise in the cytoplasm and perinuclear region of OE33 cells (Figure 5.7). The internalization of Cy5-COX-2-TAT into cells is not influenced by COX-2 expression, because TAT peptide is able to penetrate almost any cell (Heitz et al., 2009). However, Cy5-COX-2-TAT constructs are retained only in the cells that express COX-2, resulting in target/nontarget contrast. This explains our findings of significantly lower average fluorescence intensity in FLO-1 cells, that do not express COX-2 under normal conditions (Aggarwal et al., 2000).

#### 5.4.6.2 Specificity and Internalisation of Cy5-COX-2-TAT in OE33 Cells

The COX-2 binding and TAT internalising properties of the Cy5-COX-2-TAT antibody constructs were evaluated in OE33 and FLO-1 cells. The retention of Cy5-COX-2-TAT was validated by quantitative fluorescence imaging, showing marked retention of the anti-COX-2 probe in OE33 cells as compared to FLO-1 cells (Figure 5.8). However,

despite the fact that mean fluorescence intensity per cell was significantly higher in OE33 compared to FLO-1 cells when exposed to Cy5-COX-2-TAT, OE33 cells demonstrated comparably high uptake when exposed to Cy5-COX-2 without TAT (Figure 5.9).

The significant difference between uptake of Cy5-IgG with TAT (higher) and without TAT (lower) in OE33 cells confirmed TAT's ability to carry the cargo through cell membrane, and shows that the non-specific IgG control is not retained, for the reasons described in § 5.4.6.1. The uptake process of TAT proceeds both through temperature-independent and temperature-dependent mechanisms. The temperature independent process is attributed to a direct passive translocation of TAT through the plasma membrane, whereas the temperature-dependent process is ascribed to a yet unidentified endocytic process (Fischer et al., 2004). As elucidated by Brock in 2014, one of the conditions which can have an effect on inducing different pathways is concentration of TAT – it has been shown that below 2 μM, the uptake is energy-independent and relies on membrane interactions and pore formation. Interestingly, concentrations ranging from 2 μM to 20 μM were shown to induce an endocytic pathway, with mechanism changing back to energy-independent above 20 μM (Brock, 2014). These changes were explained by the accumulation of the peptide on the extracellular surface, leading to membrane disturbance. This phenomenon has been shown indecently, reporting membrane interactions resulting in direct penetration with arginine-rich CPPs and polyarginine (Zeller et al. 2015, Chakrabarti et al. 2014, Herce et al. 2014). This could further explain why TAT-IgG is not retained in the OE33 nor FLO-1 cells, which were incubated for 3 h with 20 nM of Cy5-IgG-TAT suggesting Cy5-IgG-TAT enters and leaves cells through directive passive translocation and does not bind epitopes inside the cells. That a small

amount of fluorescence was detected may be attributed to the fact that this dynamic process requires some time for all of the Cy5-IgG-TAT to leave the cells.

Despite this encouraging result, a high signal shown in OE33 cells exposed to the Cy5-COX-2 control suggests either low specificity of the antibody *in vitro* when applied to a cell-based assay rather than ELISA, likely due to high off-target binding or perhaps internalisation of the Cy5-antibody constructs, independent but comparable to that of TAT-labelled probe. The ELISA plate was coated with a single antigen (COX-2 full length protein) and thus did not provide any information regarding off-target binding of the antibody in development. While the issue of epitope specificity is complex, we anticipated that the use of a monoclonal over polyclonal anti-COX-2 antibody would reduce the likelihood of off-target binding. Polyclonal antibodies represent a pool of antibodies against the immunogen (targeting various epitopes) and typically demonstrate a higher probability for detection in a range of different conditions i.e. WB, ELISA and ICC, whereas a monoclonal antibody is more likely to work in only one set of conditions. Monoclonal antibodies are purer, being produced from single clones of fused cells producing immunoglobulins (Ramos-Vara, 2005, Saper and Sawchenko, 2003). Lack of antibody specificity in commercially available antibodies has been reported before. A study by Spicer et al. demonstrated that seven of 20 monoclonal antibody preparations analysed had staining patterns localised to the Golgi cisternae unrelated to the antigenic specificity of the antibody, and that five of these cross-reactive antibodies failed to even stain the antigen of interest (Spicer et al., 1994). Similarly, a more recent review highlights the lack of target specificity for 49 antibodies against 19 subtypes of G protein–coupled receptors, calling for more stringent antibody validation criteria (Michel et al., 2009).

### 5.4.7 Further Investigation of the Specificity of the Cy5-COX-2-TAT Probe

In § 5.3.5, WB analysis showed successful siRNA knockdown of COX-2 expression in OE33 cells compared to NT OE33 controls. However, subsequently, no reduction in staining was observed in knockdown cells exposed to Cy5-COX-2-TAT when compared to NT controls (data not shown). There was no significant difference in staining, as confirmed by quantification of the fluorescent signal, between siRNA knockdown and any of the controls: si.NS (non-specific siRNA) treated, serum starved or NT OE33 cells (Figure 5.12). The siRNA knockdown technique has been extensively used for antibody validation, and relies on a phenomenon in which siRNA suppresses the expression of a target protein by stimulating the specific degradation of the target mRNA (Bernstein et al., 2001). A strong immunostaining signal in siRNA knockdown OE33 cells despite the lack of COX-2 band in WB analysis suggests that the antibody recognises another epitope or multiple epitopes. The epitope recognised by anti-COX-2 [AS66] is likely conformational – i.e. composed of key amino acid residues brought together by protein folding – as WB does not show any additional bands. The sample preparation for WB denatures proteins and therefore interferes with conformational epitopes (Forsstrom et al., 2015).

### 5.4.8 *In Vivo* Evaluation of the Cy5-COX-2-TAT in the OE33 Xenograft Models

Whole-body optical images were acquired at 24 h, 48 h, and 72 h post iv of Cy5-COX-2-TAT, Cy5-IgG-TAT and Cy5-COX-2 (20 μg doses) and were used to evaluate tumour to background ratios. As shown in Figures 5.13 and 5.14, TBR in OE33 tumours was comparable between treatments and the difference was not significant. Figure 5.15 shows

representative optical images of OE33 xenograft bearing mice at 24 h post iv of Cy5-COX-2-TAT, Cy5-IgG-TAT and Cy5-COX-2, with low TBRs and a lack of visible difference in fluorescence intensity between treatments. Cy5-IgG-TAT (control) internalisation is expected due to the presence of the TAT peptide, and the extent of this uptake and subsequent egress from the tumour is dependent on factors such as tumour size and blood flow (Hagan et al., 1986). In addition, it has been previously suggested that the positive charge of the TAT peptide itself may affect tumour permeability leading to poor tumour uptake of TAT-labelled conjugates (Niesner et al., 2002). It is therefore challenging to discriminate between specific and non-specific uptake of Cy5-COX-2-TAT and Cy5-IgG-TAT in the OE33 xenograft model. Similar uptake observed for Cy5-COX-2 may be attributed to high off-target binding, discussed above.

*Ex vivo* biodistribution analysis of Cy5-COX-2-TAT in the OE33 xenograft model was evaluated and compared: tumour, stomach, large intestines and liver were noted as the main organs of uptake at 72 h post iv (Figure 5.14). The biodistribution of full-length monoclonal antibodies has been well documented *in vivo* (Hassan et al., 1999, Fawwaz et al., 1985), including those labelled with fluorescent dyes (Peterson et al., 2016, Vasquez et al., 2011). These data generally show strong retention in healthy tissues, especially liver and kidneys, which explains lower tumour to background contrast at earlier time points after administration, consistent with our results. This may be due to a relatively slow circulation of antibodies (Kaur et al., 2012).

### 5.4.9 Conclusions

The work presented in this chapter demonstrated, through a number of assays, that a critical condition required to utilise labelled antibodies (that the conjugation reaction has no deleterious effects on antibody affinity) has been met. However, despite the fact that the Cy5-COX-2-TAT probe was able to internalise and potentially target COX-2 in OE33 cells, its suitability as a high-quality COX-2-targeting vector was lacking, due to low specificity caused by high off-target binding. In conclusion, the data in this chapter do not support the utilisation of COX-2 [AS66] for further *in vitro* and *in vivo* studies; however, successful conjugate synthesis and TAT-facilitated internalisation serve as a proof of concept for the future development of an anti-COX-2 fluorescent probe, on the condition of selecting an antibody with better specificity. Only then, further investigation into TATs ability to deliver anti-COX-2 antibody could be conducted, and colocalisation experiments could be completed, to determine whether fluorescently labelled antibody construct conjugated to CPP TAT have potential to be applied as diagnostic probe *in vivo.*

# Chapter 6 Conclusions and Future Work

The anti-c-Met [EP1454Y] rabbit monoclonal, anti-c-Met (Met13) mouse monoclonal and the anti-COX-2 [AS66] rabbit monoclonal antibodies were validated using set criteria. Validation procedures included specificity analysis in multiple cell lines, antibody and modified-antibody competition experiments, and lot-to-lot consistency analysis. These factors were tested through a number of assays including WB, live-cell immunochemistry, and ELISA. Specificity, reproducibility, and affinity of the antibody constructs were assessed, prior to and after labelling with Cy5 fluorescent dye and the cell penetrating peptide TAT (COX-2 only). The oesophageal adenocarcinoma cell lines OE33 and FLO-1 – c-Met and COX-2 high- and low-expressing cell lines – were used throughout as positive and negative controls, respectively (Anderson et al., 2006; Abdalla et al., 2005; Cheong et al., 2004; Aggarwal et al., 2000).

Taken together, the aim of the investigation presented in this thesis was to validate a novel method for the detection of biomarkers of OAC using a monoclonal antibody (mAb) approach. The potential of *in vivo* optical imaging of c-Met and COX-2 was investigated using the Cy5-labelled anti-c-Met [EP1454Y] rabbit monoclonal, anti-c-Met (Met13) mouse monoclonal (Chapter 4), and the anti-COX-2 [AS66] - TAT rabbit monoclonal (Chapter 5) constructs, following initial *in vitro* characterisation (Chapter 3 for c-Met and Chapter 5 for COX-2).

### 6.1 Determining the Affinity of Selected Antibodies

The antibodies were selected from a large number of commercially available antibodies due to their application range (from flow cytometry and immunohistochemistry to western blotting and ELISA), literature references indicating high performance, and

availability. Considering reports suggesting variable quality of commercially available antibodies (Weller, 2016, Groff et al., 2015), the first aim of this study was to evaluate anti-c-Met [EP1454Y] and anti-c-Met (Met13) mAbs against their extracellular epitopes, as discussed in Chapter 3, and anti-COX-2 [AS66] mAb against its intracellular epitope, as discussed in Chapter 5.

The anti-c-Met [EP1454Y] rabbit monoclonal, anti-c-Met (Met13) mouse monoclonal, and the anti-COX-2 [AS66] rabbit monoclonal antibodies all showed good specificity for their targets in a number of assays. All three antibodies achieved good experimental reproducibility between different antibody batches, and demonstrated high affinity towards the antigens of interest – as demonstrated by low $K_d$ values in the nM range. Furthermore, the immunoreactivity of the anti-c-Met (Met13), and anti-COX-2 [AS66] antibodies was not affected to a significant degree by Cy5 (§ 3.3.2.2, § 5.3.3.2) and TAT (§ 5.3.4) modifications. This supported the selection of these particular antibodies for subsequent studies.

## 6.2 Evaluating the COX-2 Binding and TAT Internalising Properties of Cy5-COX-2-TAT

The intracellular distribution of COX-2 suggests the necessity for cell membrane penetration and near-nuclear translocation. Therefore, design of the COX-2 targeting imaging agent required the use of CPPs to achieve this. In Chapter 5, the anti-COX-2 [AS66] antibody was conjugated to TAT, facilitating entry into the cell. Whole serum rabbit IgG labelled with Cy5 and TAT was used as isotype control. Internalisation of TAT-labelled antibody constructs into cells is not influenced by epitope expression, because the TAT peptide is able to penetrate almost any cell (Heitz et al., 2009).

However, antibody-TAT constructs are retained only in the cells that express the epitope of interest, resulting in target/nontarget contrast. As expected, the IgG-TAT isotype control demonstrated a significantly lower degree of retention in OE33 cells when compared to Cy5-COX-2-TAT. Importantly, there was a significant difference between uptake of Cy5-IgG with TAT (higher) and without TAT (lower) in OE33 cells, demonstrating TAT's ability to carry its cargo through cell membrane. However, no such difference was observed between internalisation and retention of Cy5-COX-2-TAT and Cy5-COX-2, suggesting off-target binding. These results support the need for extensive validation of chosen targeting vectors, as cross-reactivity is a commonly reported issue among antibody-based imaging agents. Antibodies' affinity is determined by their epitope's amino acid sequence and/or conformational state. Consequently, it is very difficult to find antibodies that react exclusively to one protein, as this requires a unique epitope. Most antibodies do not bind to unique epitopes and so a degree of cross-reactivity is difficult to avoid (Voskuil, 2014). A profile of cross-reactivity in several commercially available antibodies across proteins that are expressed in a wide range of cell lines has been recently demonstrated using high content protein microarrays (Chen et al., 2018).

### 6.3 Investigation of the Specificity of the Cy5-EP1454Y, Cy5-Met13 and Cy5-COX-2-TAT probes

The epitope binding and retention properties of the Cy5-mAb ± TAT antibody constructs were evaluated in OE33 and FLO-1 cells by quantitative fluorescent imaging, as described in § 3.3.3 and § 5.3.4. Significantly higher binding of anti-c-Met probes was observed in OE33 but not FLO-1 cells. Similarly, high internalisation and retention of

the Cy5-COX-2-TAT constructs was observed in OE33 with almost no signal detected in FLO-1 cells. Considering the unexpected uptake of Cy5-COX-2 in OE33 cells (§ 6.2), the antigen specificity of all primary antibodies used was further investigated. To determine whether these primary antibodies bind exclusively to their target antigen, a molecular approach, siRNA knockdown, was utilised to manipulate the expression of the antigen protein. siRNA knockdown is extensively used for antibody validation (Burry, 2011), and relies on a phenomenon in which siRNA suppresses the expression of a target protein by stimulating the specific degradation of its mRNA (Bernstein et al., 2001). A strong signal for the NT cells next to a weak signal for the siRNA-transfected cells in WB means that the knockdown experiment was successful (Olds and Li, 2016). To demonstrate primary antibody specificity, loss of protein expression shown by WB should be followed by decreased protein expression visualised with immunofluorescence (Bordeaux et al., 2010), following the principle that if the protein of interest is not expressed, the primary antibody should not bind to the cells (Moore et al., 2007).

WB analysis demonstrated successful siRNA knockdown of c-Met and COX-2 protein expression in OE33 cells as compared to NT OE33 controls (§ 3.3.3.2 and § 5.3.5, respectively). Subsequently, a significant reduction in Cy5-EP1454Y and Cy5-Met13 staining was observed in c-Met knockdown OE33 cells, as compared to NT controls. However, no significant reduction in Cy5-COX-2-TAT staining was observed in COX-2 knockdown OE33 cells, as compared to NT controls. Taken together, these results corroborate the findings described in § 6.1, demonstrating high specificity of anti-c-Met antibodies and lack of specificity for COX-2 [AS66] antibody (§ 6.2). These results are in line with extensive reports in the literature which show that commercially available antibodies can often lack sensitivity and/or specificity (Weller, 2016, Schonbrunn, 2014,

Herrera et al., 2013, Bordeaux et al., 2010). Therefore, user validation is a necessary step in developing a novel antibody-based probe.

### 6.4 Investigating Specificity of the Cy5-COX-2-TAT Probe *In Vivo*

Whole-body optical images were acquired at 24 h, 48 h, and 72 h post iv of Cy5-COX-2-TAT, Cy5-IgG-TAT and Cy5-COX-2, and were used to evaluate TBRs. TBRs in OE33 xenografts were similarly low between the treatment conditions, and the differences were not significant. A degree of Cy5-IgG-TAT (control) internalisation is expected due to the presence of the TAT peptide, and the extent of this uptake and subsequent egress from the tumour area is dependent on factors such as tumour size and blood flow (Hagan et al., 1986). In addition, it has been previously suggested that the positive charge of the TAT peptide itself may affect tumour permeability leading to poor tumour uptake of TAT-labelled conjugates (Niesner et al., 2002). It is therefore challenging to discriminate between specific and non-specific uptake of Cy5-COX-2-TAT and Cy5-IgG-TAT in the OE33 xenograft model. Similar uptake observed for Cy5-COX-2 may be attributed to high off-target binding, as discussed above.

In conclusion, despite data in Chapter 5 not supporting the utilisation of anti-COX-2 [AS66] for further *in vitro* and *in vivo* studies, we have presented a feasible idea for the new approach to optical imaging of COX-2. Successful conjugate synthesis and TAT-facilitated internalisation serve as a proof of concept for the future development of an anti-COX-2 fluorescent probe, on the condition of selecting an antibody with better specificity. The use of selective inhibitors of COX-2 as imaging agents, based on the selective uptake by COX-2-expressing neoplastic lesions, has been reported before. The

first synthesis and characterisation of radioactively-labelled COXIBs as cancer imaging agents was reported in 2006 (Kuge et al., 2006, Schuller et al., 2006). Schuller and colleagues used a derivative of celecoxib as a SPECT radiotracer to identify COX-2-expressing, carcinogen-induced, lung and pancreatic lesions *in vivo* (Schuller et al., 2006). Furthermore, novel anti-COX-2 PET and SPECT imaging radiotracers have been synthesised and evaluated using rodent models (Uddin et al., 2009, Uddin et al., 2011, Tietz et al., 2013). In the field of optical imaging, derivatives of nonsteroidal anti-inflammatory drugs (NSAIDs) labelled with rhodamine dyes have been evaluated for detection of COX-2 (Uddin et al., 2010, Uddin and Marnett, 2008). Fluorocoxib, a strong inhibitor of purified human COX-2 enzyme, is one such optical imaging agent (Cekanova et al., 2012). However, to our knowledge, we are the first group that has pursued the development of antibody based optical imaging agents against COX-2, showing promising results. This work, however, is not a simple task of transporting imaging probe into the cytosol of cells. Rather, one must make ensure several conditions have been met, one of which is that the imaging agent can escape the endosome if internalised through energy-depended pathway (Skotland, 2012). Secondly, decreased activity and reduced toxicity to healthy tissues must be ensured while it is expected for the drug or agent to localise and accumulate preferentially only in the tumour site (Ruoslahti, 2017). This specificity could be achieved in the future by exploring the idea that tissues and organs contains organ- or disease-specific molecular tags on its vasculature that acts as a vascular 'postcode' (Enback and Laakkonen, 2007). The number of peptides that recognise specific cell types ("homing peptides") increases every day (Martín et al., 2010). The advantage of these peptides is that they have the ability to recognize specific phenotypes and subsequently arrive at a desired location (Enback and Laakkonen, 2007). CPPs are a real possibility for delivery of imaging agents and drugs into cells. However,

inducing selective cell delivery into CPP-mediated strategies must be addressed immediately, as there is need for improved delivery systems, which can deliver imaging agents safely, decreasing side effects in healthy cells and reducing the amount of agent required to achieve an optimum signal to noise ratio required for imaging.

### 6.5 Investigating Specificity of the anti-c-Met Probes *In Vitro*

Work presented in Chapter 3 demonstrated, through several assays, that the Cy5 conjugation reaction had no deleterious effects on antibody affinity and that Cy5-Met13 and Cy5-EP1454Y probes are high-quality c-Met-targeting vectors, showing good specificity, reproducibility, and affinity. Notably, the Cy5-Met13 probe was shown to be superior over Cy5-EP1454Y, demonstrating greater affinity and specificity. Chapter 4 explored the feasibility of applying the Cy5-Met13 probe to *in vivo* real-time tumour detection studies. Furthermore, Cy5-Met13 was compared to a peptide-based probe GE-137 in diagnostic imaging of c-Met.

In Cy5-Met13 uptake and retention studies, FLO-1 xenografts consistently demonstrated lower average fluorescence intensity in comparison to OE33 xenografts. The difference in TBR between OE33 and FLO-1 xenografts was 4-fold, with TBRs of 20.37 ± 4.34 and 5.47 ± 1.13, respectively (mean ± SD, $P< 0.001$). Compared to Cy5-Met13, GE-137 peptide offered an advantage of rapid distribution, lower dose, and higher TBR, particularly in OE33 xenografts. However, the difference in TBR for GE-137 between OE33 and FLO-1 xenografts was only 2-fold, with an average of 28.6 ± 8.08 (mean ± SD) in OE33 and 16.6 ± 7.57 (mean ± SD) in FLO-1 xenografts, suggesting GE-137 had high tumour but low c-Met specificity. The cytoplasmic accumulation of GE-137,

reported previously, may be a cause of longer retention of GE-137 peptide and high TBRs overall (Liu et al., 2015).

The antibody-based Cy5-Met13 probe showed better correlation between signal intensity and the expression of c-Met on a linear scale. Amongst imaging agents against c-Met currently in development, there are only three fluorescent imaging agents – Ms20-QD, a fluorescent-labelled single chain variable fragment (scFv) of an anti-c-Met antibody, and two fluorescent-labelled peptides: cMBP-AOC-Cy5.5 and GE-137. The difference in $T/T_n$ (tumour / tumour with non-specific probe) between Ms20-QD and the Cy5-Met13 probe characterised herein is 2-fold, with $T/T_n$ of 4.3 (Lu et al., 2011) and 9.8 respectively. In 2018 there have been reports of several new c-Met imaging radiotracers in development, including $^{99m}$Tc-HYNIC-cMBP for SPECT (Han et al., 2018) and [$^{18}$F]FP-Met-pep1 for PET imaging (Li et al., 2018). However, to our knowledge, no new optical imaging agents have been synthesised and evaluated and none of the imaging agents described so far have been applied to the clinic. Only one – GE-137 – has been tested in humans (Burggraaf et al., 2015). However, we have shown that our antibody-based Cy5-Met13 offers greater specificity over the peptide GE-137.

There are various factors that must be considered when developing fluorescent tracers, including brightness, optical and *in vivo* stability, together with pharmacokinetic properties (van Leeuwen et al., 2017). However, from a clinical point of view, it is important to consider the potential cost of a clinical trial, and further down the line, whether proposed new diagnostic method is cost effective. The amount of antibody-based tracer required will directly impact cost – a critical factor for both clinical reimbursement and wider acceptance as the first choice of treatment/regime (van

Leeuwen et al., 2017). Health economical assessments are an extremely useful inclusion when clinical trials with novel imaging agents are proposed. A simplified estimation of potential reimbursement cost for effective surveillance of patients with BO in UK would be as follows:

(number of cancer from BO x cost of treatment for one patient) / (estimate of the number of patients with BO who would have to be given the tracer)

where incidence of BO has been estimated to be around 120,000 annually (Masclee et al., 2014), of which approx. 0.5% will progress to OAC (Schoofs et al., 2017), giving a number of 6,000 cases of cancer from BO per year. Assuming the cost of treatment for one patient is approx. £30,000 (Inadomi et al., 2009, at the time 10 USD = 6.1977 GBP), the cost of a tracer would have to be less than:

(6,000 x £30,000) / (120,000) = £180,000,000 / 120,000 = £1,500 / patient – endoscopic examination at approx. £500 (Cook et al., 2011) = £1000 / patient

Obviously, the estimation would never be that simple, and it is difficult to predicts what would be the cost of a tracer if it was to be manufactured to the clinical standards. On the other hand, patient's quality of life should also be considered.

In conclusion, we have shown a non-invasive means for optical imaging of c-Met, which could have important diagnostic implications for various types of gastrointestinal cancer. However, despite promising *in vivo* results, there are other factors that need to be thought about carefully, such as health economics, which considers issues related to efficiency,

effectiveness and value when assessing true translational potential of any novel diagnostic probe (van Leeuwen et al., 2017).

## 6.6 Future Work

Imaging biomarkers have been described as “integral to routine management of patients with cancer” (O'Connor et al., 2017). The use of biomarkers in field of oncology includes early diagnosis, or prediction of patients ‘at risk’ i.e BRCA1 germline mutation for estimate risk of developing breast and ovarian cancer (Selleck et al., 2017, Easton et al., 1995), staging of cancer, prediction and monitoring of response to therapy i.e. HER2 expression and anti-Her2 therapy in breast and gastric cancer (Bang et al., 2010), and disease prognosis (Karlikova et al., 2015). However, despite extensive use of several existing biomarkers (Henry et al., 2012), and a tremendous effort to discover and develop new ones, the fact is that very few biomarkers are successfully translated to the clinic. Many promising biomarkers, described in the academic literature, lack real application, owing to a lack of effective and applicable strategies for biomarker translation (Waterton et al., 2012). COX-2 and c-Met hold great potential for *in vivo* tumour diagnosis, however, several key steps involved in the preclinical validation of biomarkers have to be explored before they can be selected and approved as clinically applicable candidates. For imaging, the technical and biological/clinical validation occur in parallel rather than sequentially. Extensive clinical/biological evaluation aims to link biomarkers to tumour biology and outcome variables; technical validation step, partially accomplished as described herein, is achieved when the assay for the identification of the biomarker in clinical samples can be performed precisely and accurately, and whether it is widely available in all geographical territories (Parkinson et al., 2012). A biomarker with limited availability or poor reproducibility cannot sensibly be translated into clinic, hence large multicentre trials do not happen until technical validation is completed (O'Connor et al., 2017). Finally, strategies must exist to identify, mitigate and measure the uncertainty,

risk and cost associated with any given biomarker in making research or clinical decision (Hayes, 2015).

While this thesis demonstrated feasibility of non-invasive imaging of intracellular COX-2 and extracellular c-Met *in vivo*, several points remain to be addressed that could extend the scope of this project and make it more translational. Ideally, an imaging agent should exhibit high absorption and appropriate clearance rates to produce high target-to-background ratio *in vivo*. When targeting neoplastic lesions by selectively binding to tumour biomarkers, the signal generated by contrast probes should be higher than the background produced by non-specific uptake. Hence, the development of a successful imaging probe needs to overcome the challenges of slow blood clearance, non-specific uptake (e.g. liver, spleen, bone marrow), and low levels of target expression (Frangioni, 2008). In the present study, the basal abundance of COX-2 and c-Met proteins in the tumour model used remains to be elucidated, and even though *in vitro* immunofluorescence studies were performed in OAC-derived cell lines, no quantification of the copy numbers was conducted at that time. Absolute protein quantification using mass spectrometry (MS)-based proteomics (Wisniewski et al., 2014) could be used to deliver COX-2 and c-Met protein concentrations or copy numbers per cell.

Although the internalisation properties of TAT-conjugated antibodies were demonstrated, quantitative analysis of the number of TAT peptides per antibody was not performed. Evaluation of the conjugation efficiency, combined with live-cell validation of the TAT internalisation mechanism could provide further insights into the delivery and retention of the TAT-antibody conjugate into cells.
The possible endosomal entrapment of the TAT-conjugated antibodies, potentially

leading to an inability to exit these vesicles and bind to intracellular targets must be investigated. If the latter is observed, future work will necessitate use of a CPP with successful escape mechanisms, allowing its cargo to properly interact with the target molecule (El-Sayed et al., 2009).

Despite the reduction in fluorescent signal during the blocking experiment being non-significant (§ 4.3.3), this result does not necessary indicate that Cy5-Met13 antibody demonstrates off-target binding in vivo. Rather, the experimental protocol for the blocking experiment must be further optimised, in line with published blocking protocols, which use a 10 – 15 molar excess of unlabelled antibody (Hulme and Trevethick, 2010, Sorkin and Duex, 2010, Kislinger et al., 1999), rather than the 2-fold excess used in the aforementioned study. This is of utmost importance, in order to properly determine the presence and potential extent of the non-specific binding.

Furthermore, an additional *in vivo* study could offer further insights, using a novel transgenic mouse model for BO and OAC developed by a collaborator (Quante et al., 2012). Quante and colleagues have established a mouse line that carries the EBV-L2-IL-1β transgene, leading to IL-1β overexpression in the oesophageal and squamous forestomach mucosa. These mice exhibit esophagitis, and with no additional intervention, progress to BO by 12 months, and spontaneously develop adenocarcinoma with older age. However, with the addition of bile acids to the drinking water (0.2% deoxycholic acid), the mice develop accelerated BO and earlier onset tumorigenesis. The investigation into whether EBV-L2-IL-1β mice overexpress c-Met is ongoing, and carries the promise of a more translatable alternative to xenograft studies, and has the potential to drive the development of a novel endoscopic imaging device.

The high cost of the monoclonal antibody used in addition to the large amounts required for *in vivo* studies, will ultimately necessitate collaboration with another group, in order to create in-house monoclonal antibodies against targets of interest. The antibodies would require extensive validation in-house, using the same model system and protocols as described herein. Additionally, the immunogenicity of murine and rabbit mAbs to humans largely limits their clinical application (Chames et al., 2009). Therefore, the in-house antibodies should be humanised to enable a translational application.

Finally, targeting tumour cells remains difficult for antibody-based imaging agents due to their size. This severely affects tissue penetration, resulting in increased antibody plasma levels that can lead to difficulties in regulatory approval (Wu, 2014). The development of recombinant DNA techniques has enabled production of antibody fragments of various sizes and avidities (Wu and Yazaki, 2000). Recombinant antibody fragments have been shown to exhibit high tumour retention and fast blood clearance (Olafsen and Wu, 2010). These are desirable properties for imaging that result in high tumour to blood ratios in mice bearing human tumour xenografts. A novel engineered antibody fragment consisting of variable regions of light and heavy chains with fewer constant regions (VL-VH-CH3, or "minibody") with bivalent binding to either COX-2 or c-Met could be produced by genetic fusion of the single-chain variable fragment (scFv – i.e. VL and VH) to the human IgG1 CH3 domain (Chames et al., 2009). These shorter structures may be able to penetrate deeper into tumours and could enhance the TBR and thus improve both safety and performance of antibody-based diagnostic imaging.

## Bibliography


Abdalla SI, Sanderson IR, Fitzgerald RC. Effect of inflammation on cyclooxygenase (COX)-2 expression in benign and malignant oesophageal cells. Carcinogenesis. 2005;26(9):1627-33.

Abdel-Latif MM, O'Riordan J, Windle HJ, Carton E, Ravi N, Kelleher D, et al. NF-kappaB activation in esophageal adenocarcinoma: relationship to Barrett's metaplasia, survival, and response to neoadjuvant chemoradiotherapy. Ann Surg. 2004;239(4):491-500.

Abdo J, Agrawal DK, Mittal SK. "Targeted" Chemotherapy for Esophageal Cancer. Front Oncol. 2017;7.

Abnet CC, Arnold M, Wei WQ. Epidemiology of Esophageal Squamous Cell Carcinoma. Gastroenterology. 2018;154(2):360-73.

Aggarwal S, Taneja N, Lin L, Orringer MB, Rehemtulla A, Beer DG. Indomethacin-induced apoptosis in esophageal adenocarcinoma cells involves upregulation of Bax and translocation of mitochondrial cytochrome C independent of COX-2 expression. Neoplasia. 2000;2(4):346-56.

Alaei P, Spezi E. Imaging dose from cone beam computed tomography in radiation therapy. Phys Medica. 2015;31(7):647-58.

Alao JP. The regulation of cyclin D1 degradation: roles in cancer development and the potential for therapeutic invention. Mol Cancer. 2007;6:24.

AlDeghaither D, Smaglo BG, Weiner LM. Beyond peptides and mAbs--current status and future perspectives for biotherapeutics with novel constructs. J Clin Pharmacol. 2015;55 Suppl 3:S4-20.

Allum WH, Bonavina L, Cassivi SD, Cuesta MA, Dong ZM, Felix VN, et al. Surgical treatments for esophageal cancers. Ann N Y Acad Sci. 2014;1325:242-68.

Anderson LA, Tavilla A, Brenner H, Luttmann S, Navarro C, Gavin AT, et al. Survival for oesophageal, stomach and small intestine cancers in Europe 1999-2007: Results from EUROCARE-5. Eur J Cancer. 2015;51(15):2144-57.

Anderson MR, Harrison R, Atherfold PA, Campbell MJ, Darnton SJ, Obszynska J, et al. Met receptor signaling: a key effector in esophageal adenocarcinoma. Clin Cancer Res. 2006;12(20 Pt 1):5936-43.

Appleby SB, Ristimaki A, Neilson K, Narko K, Hla T. Structure of the human cyclo-oxygenase-2 gene. Biochem J. 1994;302 ( Pt 3):723-7.

Arms L, Smith DW, Flynn J, Palmer W, Martin A, Woldu A, et al. Advantages and Limitations of Current Techniques for Analyzing the Biodistribution of Nanoparticles. Front Pharmacol. 2018;9:802.

Ask A, Johansson B, Glimelius B. The potential of proton beam radiation therapy in gastrointestinal cancer. Acta Oncol. 2005;44(8):896-903.

Asoh S, Ohsawa I, Mori T, Hiraide T, Katayama Y, Kimura M, et al. Protection against ischemic brain injury by protein therapeutics. P Natl Acad Sci USA. 2002;99(26):17107-12.

Awazu Y, Nakamura K, Mizutani A, Kakoi Y, Iwata H, Yamasaki S, et al. A novel inhibitor of c-Met and VEGF receptor tyrosine kinases with a broad spectrum of in vivo antitumor activities. Mol Cancer Ther. 2013;12(6):913-24.

Badillo R, Francis D. Diagnosis and treatment of gastroesophageal reflux disease. World J Gastrointest Pharmacol Ther. 2014;5(3):105-12.

Bae YH, Park K. Targeted drug delivery to tumors: Myths, reality and possibility. J Control Release. 2011;153(3):198-205.

Ballester V, Cruz-Correa M. Endoscopic surveillance of gastrointestinal premalignant lesions: current knowledge and future directions. Curr Opin Gastroen. 2014;30(5):477-83.

Bang YJ, Van Cutsem E, Feyereislova A, Chung HC, Shen L, Sawaki A, et al. Trastuzumab in combination with chemotherapy versus chemotherapy alone for treatment of HER2-positive advanced gastric or gastro-oesophageal junction cancer (ToGA): a phase 3, open-label, randomised controlled trial. Lancet. 2010;376(9742):687-97.

Bani-Hani K, Martin IG, Hardie LJ, Mapstone N, Briggs JA, Forman D, et al. Prospective study of cyclin D1 overexpression in Barrett's esophagus: association with increased risk of adenocarcinoma. J Natl Cancer Inst. 2000;92(16):1316-21.

Bansal A, Fitzgerald RC. Biomarkers in Barrett's Esophagus Role in Diagnosis, Risk Stratification, and Prediction of Response to Therapy. Gastroenterol Clin N. 2015;44(2):373-+.

Barber PR, Ameer-Beg SM, Gilbey J, Carlin LM, Keppler M, Ng TC, et al. Multiphoton time-domain fluorescence lifetime imaging microscopy: practical application to protein–protein interactions using global analysis. J R Soc Interface. 2009;6(Suppl 1):S93-S105.

Barber PR, Tullis IDC, Pierce GP, Newman RG, Prentice J, Rowley MI, et al. The Gray Institute "open' high-content, fluorescence lifetime microscopes. J Microsc-Oxford. 2013;251(2):154-67.

Bartley AN, Washington MK, Colasacco C, Ventura CB, Ismaila N, Benson AB, 3rd, et al. HER2 Testing and Clinical Decision Making in Gastroesophageal Adenocarcinoma: Guideline From the College of American Pathologists, American Society for Clinical Pathology, and the American Society of Clinical Oncology. J Clin Oncol. 2017;35(4):446-64.

Battaglin F, Naseem M, Puccini A, Lenz HJ. Molecular biomarkers in gastro-esophageal cancer: recent developments, current trends and future directions. Cancer Cell Int. 2018;18:99.

Beg S, Wilson A, Ragunath K. The use of optical imaging techniques in the gastrointestinal tract. Frontline gastroenterology. 2016;7(3):207-15.

Bererhi H. Molecular Anatomic Imaging: Pet-CT and SPECT-CT Integrated Modality Imaging: 2(nd) Edition, 2007. Sultan Qaboos University Medical Journal. 2008;8(2):237-9.

Berlier JE, Rothe A, Buller G, Bradford J, Gray DR, Filanoski BJ, et al. Quantitative comparison of long-wavelength Alexa Fluor dyes to Cy dyes: Fluorescence of the dyes and their bioconjugates. J Histochem Cytochem. 2003;51(12):1699-712.

Bernsen MR, Kooiman K, Segbers M, van Leeuwen FWB, de Jong M. Biomarkers in preclinical cancer imaging. European journal of nuclear medicine and molecular imaging. 2015;42(4):579-96.

Bernstein E, Caudy AA, Hammond SM, Hannon GJ. Role for a bidentate ribonuclease in the initiation step of RNA interference. Nature. 2001;409(6818):363-6.

Berry MF. Esophageal cancer: staging system and guidelines for staging and treatment. J Thorac Dis. 2014;6:S289-S97.

Beviglia L, Matsumoto K, Lin CS, Ziober BL, Kramer RH. Expression of the c-Met/HGF receptor in human breast carcinoma: correlation with tumor progression. Int J Cancer. 1997;74(3):301-9.

Bianco R, Damiano V, Gelardi T, Daniele G, Ciardiello F, Tortora G. Rational combination of targeted therapies as a strategy to overcome the mechanisms of resistance to inhibitors of EGFR signaling. Curr Pharm Des. 2007;13(33):3358-67.

Billinton N, Knight AW. Seeing the wood through the trees: A review of techniques for distinguishing green fluorescent protein from endogenous autofluorescence. Anal Biochem. 2001;291(2):175-97.

Bird-Lieberman EL, Fitzgerald RC. Early diagnosis of oesophageal cancer. Br J Cancer. 2009;101(1):1-6.

Blose SH, Meltzer DI, Feramisco JR. 10-nm filaments are induced to collapse in living cells microinjected with monoclonal and polyclonal antibodies against tubulin. J Cell Biol. 1984;98(3):847-58.

Boland GP, Butt IS, Prasad R, Knox WF, Bundred NJ. COX-2 expression is associated with an aggressive phenotype in ductal carcinoma in situ. Brit J Cancer. 2004;90(2):423-9.

Bolhassani A. Potential efficacy of cell-penetrating peptides for nucleic acid and drug delivery in cancer. Bba-Rev Cancer. 2011;1816(2):232-46.

Boonstra MC, de Geus SW, Prevoo HA, Hawinkels LJ, van de Velde CJ, Kuppen PJ, et al. Selecting Targets for Tumor Imaging: An Overview of Cancer-Associated Membrane Proteins. Biomark Cancer. 2016;8:119-33.

Bordeaux J, Welsh AW, Agarwal S, Killiam E, Baquero MT, Hanna JA, et al. Antibody validation. Biotechniques. 2010;48(3):197-209.

Borghouts C, Kunz C, Groner B. Current strategies for the development of peptide-based anti-cancer therapeutics. J Pept Sci. 2005;11(11):713-26.

Bottaro DP, Rubin JS, Faletto DL, Chan AM, Kmiecik TE, Vande Woude GF, et al. Identification of the hepatocyte growth factor receptor as the c-met proto-oncogene product. Science (New York, NY). 1991;251(4995):802-4.

Bray F, Ferlay J, Soerjomataram I, Siegel RL, Torre LA, Jemal A. Global cancer statistics 2018: GLOBOCAN estimates of incidence and mortality worldwide for 36 cancers in 185 countries. CA Cancer J Clin. 2018;68(6):394-424.

Brock R. The Uptake of Arginine-Rich Cell-Penetrating Peptides: Putting the Puzzle Together. Bioconjugate Chem. 2014;25(5):863-8.

Brown VL, Harwood CA, Crook T, Cronin JG, Kelsell DP, Proby CM. p16INK4a and p14ARF tumor suppressor genes are commonly inactivated in cutaneous squamous cell carcinoma. J Invest Dermatol. 2004;122(5):1284-92.

Bumbaca D, Wong A, Drake E, Reyes AE, 2nd, Lin BC, Stephan JP, et al. Highly specific off-target binding identified and eliminated during the humanization of an antibody against FGF receptor 4. mAbs. 2011;3(4):376-86.

Burggraaf J, Kamerling IM, Gordon PB, Schrier L, de Kam ML, Kales AJ, et al. Detection of colorectal polyps in humans using an intravenously administered fluorescent peptide targeted against c-Met. Nat Med. 2015;21(8):955-61.

Burry RW. Controls for Immunocytochemistry: An Update. J Histochem Cytochem. 2011;59(1):6-12.

Buskens CJ, Van Rees BP, Sivula A, Reitsma JB, Haglund C, Bosma PJ, et al. Prognostic significance of elevated cyclooxygenase 2 expression in patients with adenocarcinoma of the esophagus. Gastroenterology. 2002;122(7):1800-7.

Buttar NS, Wang KK. Mechanisms of disease: Carcinogenesis in Barrett's esophagus. Nat Clin Pract Gastroenterol Hepatol. 2004;1(2):106-12.

Callejas NA, Castrillo A, Bosca L, Martin-Sanz P. Inhibition of prostaglandin synthesis up-regulates cyclooxygenase-2 induced by lipopolysaccharide and peroxisomal proliferators. The Journal of pharmacology and experimental therapeutics. 1999;288(3):1235-41.

Cameron AJ, Ott BJ, Payne WS. The incidence of adenocarcinoma in columnar-lined (Barrett's) esophagus. N Engl J Med. 1985;313(14):857-9.

Cao G, Pei W, Ge H, Liang Q, Luo Y, Sharp FR, et al. In Vivo Delivery of a Bcl-xL Fusion Protein Containing the TAT Protein Transduction Domain Protects against Ischemic Brain Injury and Neuronal Apoptosis. J Neurosci. 2002;22(13):5423-31.

Car LT, Papachristou N, Urch C, Majeed A, El-Khatib M, Aylin P, et al. Preventing delayed diagnosis of cancer: clinicians' views on main problems and solutions. J Glob Health. 2016;6(2):020901.

Cardarelli F, Serresi M, Bizzarri R, Giacca M, Beltram F. In vivo study of HIV-1 Tat arginine-rich motif unveils its transport properties. Mol Ther. 2007;15(7):1313-22.

Cekanova M, Uddin MJ, Legendre AM, Galyon G, Bartges JW, Callens A, et al. Single-dose safety and pharmacokinetic evaluation of fluorocoxib A: pilot study of novel cyclooxygenase-2-targeted optical imaging agent in a canine model. J Biomed Opt. 2012;17(11).

Chames P, Van Regenmortel M, Weiss E, Baty D. Therapeutic antibodies: successes, limitations and hopes for the future. Br J Pharmacol. 2009;157(2):220-33.

Chapman K, Pullen N, Coney L, Dempster M, Andrews L, Bajramovic J, et al. Preclinical development of monoclonal antibodies: considerations for the use of non-human primates. MAbs. 2009;1(5):505-16.

Chaudhry SR, Bordoni B. Anatomy, Thorax, Esophagus. [Updated 2019 Apr 8]. In: StatPearls [Internet]. Treasure Island (FL): StatPearls Publishing; 2019 Jan-. Available from: https://www.ncbi.nlm.nih.gov/books/NBK482513/

Chaudhuri A, Xie MH, Yang B, Mahapatra K, Liu JF, Marsters S, et al. Distinct Involvement of the Gab1 and Grb2 Adaptor Proteins in Signal Transduction by the Related Receptor Tyrosine Kinases RON and MET. Journal of Biological Chemistry. 2011;286(37):32762-74.

Chen F, Chang D, Goh M, Klibanov SA, Ljungman M. Role of p53 in cell cycle regulation and apoptosis following exposure to proteasome inhibitors. Cell Growth Differ. 2000;11(5):239-46.

Chen H, Thorne SH. Practical Methods for Molecular In Vivo Optical Imaging. Curr Protoc Cytom. 2012;59(1224):12 24 1-12 24 11.

Chen YH, Lu HI, Chien CY, Lo CM, Wang YM, Chou SY, et al. Treatment Outcomes of Patients with Locally Advanced Synchronous Esophageal and Head/Neck Squamous Cell Carcinoma Receiving Curative Concurrent Chemoradiotherapy. Sci Rep. 2017;7:41785.

Cheong E, Ivory K, Doleman J, Parker ML, Rhodes M, Johnson IT. Synthetic and naturally occurring COX-2 inhibitors suppress proliferation in a human oesophageal adenocarcinoma cell line (OE33) by inducing apoptosis and cell cycle arrest. Carcinogenesis. 2004;25(10):1945-52.

Cho JH, Kim TN. Long-term survival after concurrent chemoradiation therapy for esophageal cancer with tracheal invasion. Korean J Intern Med. 2015;30(6):931-3.

Cho JW, Choi SC, Jang JY, Shin SK, Choi KD, Lee JH, et al. Lymph Node Metastases in Esophageal Carcinoma: An Endoscopist's View. Clin Endosc. 2014;47(6):523-9.

Clemons NJ, Phillips WA, Lord RV. Signaling pathways in the molecular pathogenesis of adenocarcinomas of the esophagus and gastroesophageal junction. Cancer Biol Ther. 2013;14(9):782-95.

Combs CA, Shroff H. Fluorescence Microscopy: A Concise Guide to Current Imaging Methods. Curr Protoc Neurosci. 2017;79:2 1 -2 1 25.

Cook C, Hatton C, Hendy P, Makins R. National Guidelines for Capsule Endoscopy: Cost Implications of Non-Compliance. Gut. 2011;60.

Cooper GM. The Cell: A Molecular Approach. 2nd edition. Sunderland (MA): Sinauer Associates; 2000. Cell Membranes. Available from: https://www.ncbi.nlm.nih.gov/books/NBK9928/

Cornelissen B, Kersemans V, Darbar S, Thompson J, Shah K, Sleeth K, et al. Imaging DNA Damage In Vivo Using gamma H2AX-Targeted Immunoconjugates. Cancer research. 2011;71(13):4539-49.

Cornelissen B, Hu M, McLarty K, Costantini D, Reilly RM Cellular penetration and nuclear importation properties of 111In-labeled and 123I-labeled HIV-1 tat peptide immunoconjugates in BT-474 human breast cancer cells. Nucl Med Biol, 2007;34, 37-46.

Cortes JM, de Petris G, Lopez JI. Detection of Intratumor Heterogeneity in Modern Pathology: A Multisite Tumor Sampling Perspective. Front Med (Lausanne). 2017;4:25.

Cronin J, McAdam E, Danikas A, Tselepis C, Griffiths P, Baxter J, et al. Epidermal Growth Factor Receptor (EGFR) Is Overexpressed in High-Grade Dysplasia and Adenocarcinoma of the Esophagus and May Represent a Biomarker of Histological Progression in Barrett's Esophagus (BE). American Journal of Gastroenterology. 2011;106(1):46-56.

Crosson B, Ford A, McGregor KM, Meinzer M, Cheshkov S, Li X, et al. Functional imaging and related techniques: an introduction for rehabilitation researchers. J Rehabil Res Dev. 2010;47(2):vii-xxxiv.

Csendes A, Smok G, Quiroz J, Burdiles P, Rojas J, Castro C, et al. Clinical, endoscopic, and functional studies in 408 patients with Barrett's esophagus, compared to 174 cases of intestinal metaplasia of the cardia. Am J Gastroenterol. 2002;97(3):554-60.

D'Errico A, Barozzi C, Fiorentino M, Carella R, Di Simone M, Ferruzzi L, et al. Role and new perspectives of transforming growth factor-alpha (TGF-alpha) in

adenocarcinoma of the gastro-oesophageal junction. Brit J Cancer. 2000;82(4):865-70.

Daly JM, Fry WA, Little AG, Winchester DP, McKee RF, Stewart AK, et al. Esophageal cancer: Results of an American College of Surgeons patient care evaluation study. J Am Coll Surgeons. 2000;190(5):562-72.

Darnton SJ, Hardie LJ, Muc RS, Wild CP, Casson AG. Tissue inhibitor of metalloproteinase-3 (TIMP-3) gene is methylated in the development of esophageal adenocarcinoma: Loss of expression correlates with poor prognosis. International Journal of Cancer. 2005;115(3):351-8.

Davelaar AL, Calpe S, Lau L, Timmer MR, Visser M, Ten Kate FJ, et al. Aberrant TP53 detected by combining immunohistochemistry and DNA-FISH improves Barrett's esophagus progression prediction: a prospective follow-up study. Genes Chromosomes Cancer. 2015;54(2):82-90.

Davila RE. Chromoendoscopy. Gastrointest Endosc Clin N Am. 2009;19(2):193-208.

Debie P, Hernot S. Emerging Fluorescent Molecular Tracers to Guide Intra-Operative Surgical Decision-Making. Frontiers in Pharmacology. 2019;10.

De Giorgi F, Palmiero M, Esposito I, Mosca F, Cuomo R. Pathophysiology of gastro-oesophageal reflux disease. Acta Otorhinolaryngol Ital. 2006;26(5):241-6.

De Ledinghen V, Liu H, Zhang F, Lo CR, Subbaramaiah K, Dannenberg AJ, et al. Induction of cyclooxygenase-2 by tumor promoters in transformed and cytochrome P450 2E1-expressing hepatocytes. Carcinogenesis. 2002;23(1):73-9.

Dent J, El-Serag HB, Wallander MA, Johansson S. Epidemiology of gastro-oesophageal reflux disease: a systematic review. Gut. 2005;54(5):710-7.

De Palma GD. Confocal laser endomicroscopy in the "in vivo" histological diagnosis of the gastrointestinal tract. World J Gastroenterol. 2009;15(46):5770-5.

De Smet B, Sarovich DS, Price EP, Mayo M, Theobald V, Kham C, et al. Whole-genome sequencing confirms that Burkholderia pseudomallei multilocus sequence types common to both Cambodia and Australia are due to homoplasy. J Clin Microbiol. 2015;53(1):323-6.

Delitto D, Vertes-George E, Hughes SJ, Behrns KE, Trevino JG. c-Met signaling in the development of tumorigenesis and chemoresistance: Potential applications in pancreatic cancer. World journal of gastroenterology. 2014;20(26):8458-70.

Derossi D, Calvet S, Trembleau A, Brunissen A, Chassaing G, Prochiantz A. Cell internalization of the third helix of the antennapedia homeodomain is receptor-independent. Journal of Biological Chemistry. 1996;271(30):18188-93.

DeSantis C, Ma J, Bryan L, Jemal A. Breast cancer statistics, 2013. CA Cancer J Clin. 2014;64(1):52-62.

Deshayes S, Morris MC, Divita G, Heitz F. Cell-penetrating peptides: tools for intracellular delivery of therapeutics. Cell Mol Life Sci. 2005;62(16):1839-49.

DeWitt DL, Meade EA, Smith WL. PGH synthase isoenzyme selectivity: the potential for safer nonsteroidal antiinflammatory drugs. The American journal of medicine. 1993;95(2a):40s-4s.

DeVault KR, Castell DO, American College of G. Updated guidelines for the diagnosis and treatment of gastroesophageal reflux disease. Am J Gastroenterol. 2005;100(1):190-200.

Di Leo M, Maselli R, Ferrara EC, Poliani L, Al Awadhi S, Repici A. Endoscopic Management of Benign Esophageal Ruptures and Leaks. Curr Treat Options Gastroenterol. 2017;15(2):268-84.

Di Pietro M, Fitzgerald RC, group BSGBsgw. Revised British Society of Gastroenterology recommendation on the diagnosis and management of Barrett's oesophagus with low-grade dysplasia. Gut. 2018;67(2):392-3.

Diamond JM, Katz Y. Interpretation of Nonelectrolyte Partition-Coefficients between Dimyristoyl Lecithin and Water. J Membrane Biol. 1974;17(2):121-54.

Dodds WJ, Dent J, Hogan WJ, Helm JF, Hauser R, Patel GK, et al. Mechanisms of gastroesophageal reflux in patients with reflux esophagitis. N Engl J Med. 1982;307(25):1547-52.

Doherty GJ, McMahon HT. Mechanisms of endocytosis. Annu Rev Biochem. 2009;78:857-902.

Domper Arnal MJ, Ferrandez Arenas A, Lanas Arbeloa A. Esophageal cancer: Risk factors, screening and endoscopic treatment in Western and Eastern countries. World J Gastroenterol. 2015;21(26):7933-43.

Drewitz DJ, Sampliner RE, Garewal HS. The incidence of adenocarcinoma in Barrett's esophagus: a prospective study of 170 patients followed 4.8 years. Am J Gastroenterol. 1997;92(2):212-5.

Drummen GPC. Fluorescent Probes and Fluorescence (Microscopy) Techniques - Illuminating Biological and Biomedical Research. Molecules. 2012;17(12):14067-90.

Duchardt F, Fotin-Mleczek M, Schwarz H, Fischer R, Brock R. A comprehensive model for the cellular uptake of cationic cell-penetrating peptides. Traffic. 2007;8(7):848-66.

Dufort S, Sancey L, Wenk C, Josserand V, Coll JL. Optical small animal imaging in the drug discovery process. Bba-Biomembranes. 2010;1798(12):2266-73.

Dulak AM, Stojanov P, Peng SY, Lawrence MS, Fox C, Stewart C, et al. Exome and whole-genome sequencing of esophageal adenocarcinoma identifies recurrent driver events and mutational complexity. Nat Genet. 2013;45(5):478-U37.

Duncan R, Richardson SCW. Endocytosis and Intracellular Trafficking as Gateways for Nanomedicine Delivery: Opportunities and Challenges. Mol Pharmaceut. 2012;9(9):2380-402.

Eads CA, Lord RV, Kurumboor SK, Wickramasinghe K, Skinner ML, Long TI, et al. Fields of aberrant CpG island hypermethylation in Barrett's esophagus and associated adenocarcinoma. Cancer research. 2000;60(18):5021-6.

Easton DF, Ford D, Bishop DT. Breast and ovarian cancer incidence in BRCA1-mutation carriers. Breast Cancer Linkage Consortium. American journal of human genetics. 1995;56(1):265-71.

Edwards BK, Ward E, Kohler BA, Eheman C, Zauber AG, Anderson RN, et al. Annual report to the nation on the status of cancer, 1975-2006, featuring colorectal cancer trends and impact of interventions (risk factors, screening, and treatment) to reduce future rates. Cancer. 2010;116(3):544-73.

El-Andaloussi S, Holm T, Langel U. Cell-penetrating peptides: Mechanisms and applications. Curr Pharm Design. 2005;11(28):3597-611.

El-Sayed A, Futaki S, Harashima H. Delivery of macromolecules using arginine-rich cell-penetrating peptides: ways to overcome endosomal entrapment. AAPS J. 2009;11(1):13-22.

Ell C, May A, Pech O, Gossner L, Guenter E, Behrens A, et al. Curative endoscopic resection of early esophageal adenocarcinomas (Barrett's cancer). Gastrointest Endosc. 2007;65(1):3-10.

Enback J, Laakkonen P. Tumour-homing peptides: tools for targeting, imaging and destruction. Biochem Soc T. 2007;35:780-3.

Escher E. A new method of iodine labelling of peptide hormones. Journal of receptor research. 1984;4(1-6):331-6.

Esfahani SA, Heidari P, Kim SA, Ogino S, Mahmood U. Optical Imaging of Mesenchymal Epithelial Transition Factor (MET) for Enhanced Detection and Characterization of Primary and Metastatic Hepatic Tumors. Theranostics. 2016;6(12):2028-38.

Espino A, Cirocco M, Dacosta R, Marcon N. Advanced imaging technologies for the detection of dysplasia and early cancer in barrett esophagus. Clin Endosc. 2014;47(1):47-54.

Euhus DM, Hudd C, LaRegina MC, Johnson FE. Tumor measurement in the nude mouse. J Surg Oncol. 1986;31(4):229-34.

Fadare O, Rodriguez R. The significance of marked nuclear atypia in grade 1 cervical intraepithelial neoplasia. Hum Pathol. 2009;40(10):1487-93.

Fahey F, Zukotynski K, Capala J, Knight N, Organizing Committee C, Participants of NCISJWoTRT. Targeted radionuclide therapy: proceedings of a joint workshop hosted by the National Cancer Institute and the Society of Nuclear Medicine and Molecular Imaging. J Nucl Med. 2014;55(2):337-48.

Falk GW, Rice TW, Goldblum JR, Richter JE. Jumbo biopsy forceps protocol still misses unsuspected cancer in Barrett's esophagus with high-grade dysplasia. Gastrointestinal endoscopy. 1999;49(2):170-6.

Falkenback D, Nilbert M, Oberg S, Johansson J. Prognostic value of cell adhesion in esophageal adenocarcinomas. Dis Esophagus. 2008;21(2):97-102.

Farkona S, Diamandis EP, Blasutig IM. Cancer immunotherapy: the beginning of the end of cancer? BMC Med. 2016;14,73.

Farrow DC, Vaughan TL, Sweeney C, Gammon MD, Chow WH, Risch HA, et al. Gastroesophageal reflux disease, use of H2 receptor antagonists, and risk of esophageal and gastric cancer. Cancer Causes Control. 2000;11(3):231-8.

Fawwaz RA, Wang TS, Estabrook A, Rosen JM, Hardy MA, Alderson PO, et al. Immunoreactivity and biodistribution of indium-111-labeled monoclonal antibody to a human high molecular weight-melanoma associated antigen. J Nucl Med. 1985;26(5):488-92.

Fischer R, Kohler K, Fotin-Mleczek M, Brock R. A stepwise dissection of the intracellular fate of cationic cell-penetrating peptides. The Journal of biological chemistry. 2004;279(13):12625-35.

Fittipaldi A, Ferrari A, Zoppe M, Arcangeli C, Pellegrini V, Beltram F, et al. Cell membrane lipid rafts mediate caveolar endocytosis of HIV-1 Tat fusion proteins. Journal of Biological Chemistry. 2003;278(36):34141-9.

Fitzgerald RC, di Pietro M, Ragunath K, Ang Y, Kang JY, Watson P, et al. British Society of Gastroenterology guidelines on the diagnosis and management of Barrett's oesophagus. Gut. 2014;63(1):7-42.

Fixman ED, Fournier TM, Kamikura DM, Naujokas MA, Park M. Pathways downstream of Shc and Grb2 are required for cell transformation by the Tpr-Met oncoprotein. Journal of Biological Chemistry. 1996;271(22):13116-22.

Fokas E, Rodel C. Definitive, Preoperative, and Palliative Radiation Therapy of Esophageal Cancer. Viszeralmedizin. 2015;31(5):347-53.

Fong CY, Pang L, Holland E, Knox AJ. TGF-beta1 stimulates IL-8 release, COX-2 expression, and PGE(2) release in human airway smooth muscle cells. Am J Physiol Lung Cell Mol Physiol. 2000;279(1):L201-7.

Forde PM, Kelly RJ. Genomic Alterations in Advanced Esophageal Cancer May Lead to Subtype-Specific Therapies. Oncologist. 2013;18(7):823-32.

Forsstrom B, Axnas BB, Rockberg J, Danielsson H, Bohlin A, Uhlen M. Dissecting Antibodies with Regards to Linear and Conformational Epitopes. PloS one. 2015;10(3).

Forster JC, Harriss-Phillips WM, Douglass MJ, Bezak E. A review of the development of tumor vasculature and its effects on the tumor microenvironment. Hypoxia. 2017;5:21-32.

Fouad YA, Aanei C. Revisiting the hallmarks of cancer. Am J Cancer Res. 2017;7(5):1016-36.

Fowler CB, Evers DL, O'Leary TJ, Mason JT. Antigen Retrieval Causes Protein Unfolding: Evidence for a Linear Epitope Model of Recovered Immunoreactivity. J Histochem Cytochem. 2011;59(4):366-81.

Frangioni JV. New technologies for human cancer imaging. J Clin Oncol. 2008;26(24):4012-21.

Frankel AD, Pabo CO. Cellular Uptake of the Tat Protein from Human Immunodeficiency Virus. Cell. 1988;55(6):1189-93.

Freire E, Vanosdol WW, Mayorga OL, Sanchezruiz JM. Calorimetrically Determined Dynamics of Complex Unfolding Transitions in Proteins. Annu Rev Biophys Bio. 1990;19:159-88.

Fretz MM, Penning NA, Al-Taei S, Futaki S, Takeuchi T, Nakase I, et al. Temperature-, concentration- and cholesterol-dependent translocation of L- and D-octa-arginine across the plasma and nuclear membrane of CD34(+) leukaemia cells. Biochemical Journal. 2007;403:335-42.

Fritcher EGB, Brankley SM, Kipp BR, Voss JS, Campion MB, Morrison LE, et al. A comparison of conventional cytology, DNA ploidy analysis, and fluorescence in situ hybridization for the detection of dysplasia and adenocarcinoma in patients with Barrett's esophagus. Human Pathology. 2008;39(8):1128-35.

Galli F, Ruspi L, Marzorati A, Lavazza M, Di Rocco G, Boni L, et al. N staging system: tumor-node-metastasis and future perspectives. Transl Gastroenterol Hepatol. 2017;2:4.

Garcia-Guzman M, Dolfi F, Zeh K, Vuori K. Met-induced JNK activation is mediated by the adapter protein Crk and correlates with the Gab1-Crk signaling complex formation. Oncogene. 1999;18(54):7775-86.

Garofalo A, Chirivi RG, Scanziani E, Mayo JG, Vecchi A, Giavazzi R. Comparative study on the metastatic behavior of human tumors in nude, beige/nude/xid and severe combined immunodeficient mice. Invasion Metastasis. 1993;13(2):82-91.

Gavaghan M. Anatomy and physiology of the esophagus. AORN J. 1999;69(2):372-86; quiz 387-9, 392, 393-4.

Gertler R, Doll D, Maak M, Feith M, Rosenberg R. Telomere length and telomerase subunits as diagnostic and prognostic biomarkers in Barrett carcinoma. Cancer. 2008;112(10):2173-80.

Gherardi E, Stoker M. Hepatocyte Growth-Factor Scatter Factor - Mitogen, Motogen, and Met. Cancer Cell-Mon Rev. 1991;3(6):227-32.

Ghosh R, Gilda JE, Gomes AV. The necessity of and strategies for improving confidence in the accuracy of western blots. Expert Rev Proteomic. 2014;11(5):549-60.

Glasgow RE, Ilson DH, Hayman JA, Gerdes H, Mulcahy MF, Ajani JA. Modern Approaches to Localized Cancer of the Esophagus. J Natl Compr Canc Ne. 2011;9(8):902-11.

Goldenberg DM. Carcinoembryonic Antigen as a Target Cancer Antigen for Radiolabeled Antibodies - Prospects for Cancer Imaging and Therapy. Tumor Biol. 1995;16(1):62-73.

Goldenberg MM. Trastuzumab, a recombinant DNA-derived humanized monoclonal antibody, a novel agent for the treatment of metastatic breast cancer. Clin Ther. 1999;21(2):309-18.

Goodsell DS. The molecular perspective: Cyclooxygenase-2. Stem Cells. 2000;18(3):227-9.

Gora MJ, Suter MJ, Tearney GJ, Li X. Endoscopic optical coherence tomography: technologies and clinical applications [Invited]. Biomed Opt Express. 2017;8(5):2405-44.

Green M, Loewenstein PM. Autonomous Functional Domains of Chemically Synthesized Human Immunodeficiency Virus Tat Trans-Activator Protein. Cell. 1988;55(6):1179-88.

Groff K, Brown J, Clippinger AJ. Modern affinity reagents: Recombinant antibodies and aptamers. Biotechnol Adv. 2015;33(8):1787-98.

Gubler H, Schopfer U, Jacoby E. Theoretical and Experimental Relationships between Percent Inhibition and IC50 Data Observed in High-Throughput Screening. J Biomol Screen. 2013;18(1):1-13.

Guo Z, Peng H, Kang J, Sun D. Cell-penetrating peptides: Possible transduction mechanisms and therapeutic applications. Biomed Rep. 2016;4(5):528-34.

Guterstam P, Madani F, Hirose H, Takeuchi T, Futaki S, El Andaloussi S, et al. Elucidating cell-penetrating peptide mechanisms of action for membrane interaction, cellular uptake, and translocation utilizing the hydrophobic counter-anion pyrenebutyrate. Bba-Biomembranes. 2009;1788(12):2509-17.

Hagan PL, Halpern SE, Dillman RO, Shawler DL, Johnson DE, Chen A, et al. Tumor size: effect on monoclonal antibody uptake in tumor models. J Nucl Med. 1986;27(3):422-7.

Hallbrink M, Floren A, Elmquist A, Pooga M, Bartfai T, Langel U. Cargo delivery kinetics of cell-penetrating peptides. Biochim Biophys Acta. 2001;1515(2):101-9.

Han ZG, Wu YY, Wang K, Xiao YD, Cheng Z, Sun XL, et al. Analysis of progress and challenges for various patterns of c-MET-targeted molecular imaging: a systematic review. EJNMMI research. 2017;7.

Han Z, Xiao Y, Wang K, Yan J, Xiao Z, Fang F, et al. Development of a SPECT Tracer to Image c-Met Expression in a Xenograft Model of Non-Small Cell Lung Cancer. J Nucl Med. 2018;59(11):1686-91.

Hanahan D, Weinberg RA. The hallmarks of cancer. Cell. 2000;100(1):57-70.

Hanahan D, Weinberg RA. Hallmarks of cancer: the next generation. Cell. 2011;144(5):646-74.

Hanna JA, Bordeaux J, Rimm DL, Agarwal S. The Function, Proteolytic Processing, and Histopathology of Met in Cancer. Adv Cancer Res. 2009;103:1-23.

Har-Noy O, Katz L, Avni T, Battat R, Bessissow T, Yung DE, et al. Chromoendoscopy, Narrow-Band Imaging or White Light Endoscopy for Neoplasia Detection in Inflammatory Bowel Diseases. Dig Dis Sci. 2017;62(11):2982-90.

Harris C, Croce B, Munkholm-Larsen S. Esophageal cancer. Ann Cardiothorac Surg. 2017;6(2):190.

Hashimoto N. Expression of COX2 and p53 in Rat Esophageal Cancer Induced by Reflux of Duodenal Contents. ISRN Gastroenterol. 2012;2012:914824.

Hashimoto N. Effects of bile acids on cyclooxygenase-2 expression in a rat model of duodenoesophageal anastomosis. World J Gastroenterol. 2014;20(21):6541-6.

Hassan R, Wu C, Brechbiel MW, Margulies I, Kreitman RJ, Pastan I. 111Indium-labeled monoclonal antibody K1: biodistribution study in nude mice bearing a human carcinoma xenograft expressing mesothelin. Int J Cancer. 1999;80(4):559-63.

Hauser R, Dodds WJ, Patel GK, Dent J, Hogan WJ, Arndorfer RC. Mechanism of Gastroesophageal Reflux (Ger) in Patients with Reflux Esophagitis. Gastroenterology. 1979;76(5):1153-.

Haustein E, Schwille P. Trends in fluorescence imaging and related techniques to unravel biological information. HFSP J. 2007;1(3):169-80.

Hayeck TJ, Kong CY, Spechler SJ, Gazelle GS, Hur C. The prevalence of Barrett's esophagus in the US: estimates from a simulation model confirmed by SEER data. Diseases of the Esophagus. 2010;23(6):451-7.

Hayes DF, Allen J, Compton C, Gustavsen G, Leonard DG, McCormack R, et al. Breaking a vicious cycle. Sci Transl Med. 2013;5(196):196cm6.

Hazin J, Moldenhauer G, Alteyogt P, Brady NR. A novel method for measuring cellular antibody uptake using imaging flow cytometry reveals distinct uptake rates for two different monoclonal antibodies targeting L1. J Immunol Methods. 2015;423:70-7.

Hecht SS. Tobacco smoke carcinogens and lung cancer. J Natl Cancer Inst. 1999;91(14):1194-210.

Hecht M, Papoutsi M, Tran HD, Wilting J, Schweigerer L. Hepatocyte growth factor/c-Met signaling promotes the progression of experimental human neuroblastomas. Cancer research. 2004;64(17):6109-18.

Heidbuchel H, Wittkampf FH, Vano E, Ernst S, Schilling R, Picano E, et al. Practical ways to reduce radiation dose for patients and staff during device implantations and electrophysiological procedures. Europace. 2014;16(7):946-64.

Heitmiller RF, Redmond M, Hamilton SR. Barrett's esophagus with high-grade dysplasia. An indication for prophylactic esophagectomy. Ann Surg. 1996;224(1):66-71.

Heitz F, Morris MC, Divita G. Twenty years of cell-penetrating peptides: from molecular mechanisms to therapeutics. Brit J Pharmacol. 2009;157(2):195-206.

Hellebust A, Richards-Kortum R. Advances in molecular imaging: targeted optical contrast agents for cancer diagnostics. Nanomedicine-Uk. 2012;7(3):429-45.

Heneweer C, Holland JP, Divilov V, Carlin S, Lewis JS. Magnitude of enhanced permeability and retention effect in tumors with different phenotypes: 89Zr-albumin as a model system. J Nucl Med. 2011;52(4):625-33.

Henry NL, Hayes DF. Cancer biomarkers. Mol Oncol. 2012;6(2):140-6.

Herrera LJ, El-Hefnawy T, de Oliveira PEQ, Raja S, Finkelstein S, Gooding W, et al. The HGF receptor c-Met is overexpressed in esophageal adenocarcinoma. Neoplasia. 2005;7(1):75-84.

Herrera M, Sparks MA, Alfonso-Pecchio AR, Harrison-Bernard LM, Coffman TM. Response to Lack of Specificity of Commercial Antibodies Leads to Misidentification of Angiotensin Type-1 Receptor Protein. Hypertension. 2013;61(4):E32-E.

Hillman EM, Amoozegar CB, Wang T, McCaslin AF, Bouchard MB, Mansfield J, et al. In vivo optical imaging and dynamic contrast methods for biomedical research. Philos Trans A Math Phys Eng Sci. 2011;369(1955):4620-43.

Hiom SC. Diagnosing cancer earlier: reviewing the evidence for improving cancer survival. Br J Cancer. 2015;112 Suppl 1:S1-5.

Hischemoller A, Walter C, Weiler V, Hummel H, Thepen T, Huhn M, et al. Labeling of Anti-MUC-1 Binding Single Chain Fv Fragments to Surface Modified Upconversion Nanoparticles for an Initial in Vivo Molecular Imaging Proof of Principle Approach. Int J Mol Sci. 2012;13(4):4153-67.

Histed SN, Lindenberg ML, Mena E, Turkbey B, Choyke PL, Kurdziel KA. Review of functional/anatomical imaging in oncology. Nucl Med Commun. 2012;33(4):349-61.

Holloway RH, Hongo M, Berger K, Mccallum RW. Gastric distention: a mechanism for postprandial gastroesophageal reflux. Gastroenterology. 1985;89(4):779-84.

Holt D, Ma X, Kundu N, Fulton A. Prostaglandin E(2) (PGE (2)) suppresses natural killer cell function primarily through the PGE(2) receptor EP4. Cancer Immunol Immunother. 2011;60(11):1577-86.

Hom C, Vaezi MF. Extraesophageal manifestations of gastroesophageal reflux disease. Gastroenterol Clin North Am. 2013;42(1):71-91.

Hong MK, Laskin WB, Herman BE, Johnston MH, Vargo JJ, Steinberg SM, et al. Expansion of the Ki-67 proliferative compartment correlates with degree of dysplasia in Barrett's esophagus. Cancer. 1995;75(2):423-9.

Hormi-Carver K, Zhang X, Zhang HY, Whitehead RH, Terada LS, Spechler SJ, et al. Unlike esophageal squamous cells, Barrett's epithelial cells resist apoptosis by activating the nuclear factor-kappaB pathway. Cancer Res. 2009;69(2):672-7.

Hu Z, Yang Y, Zhao Y, Huang Y. The prognostic value of cyclooxygenase-2 expression in patients with esophageal cancer: evidence from a meta-analysis. Onco Targets Ther. 2017;10:2893-901.

Huang B, Hu B, Su M, Tian DP, Guo Y, Lian SY, et al. Potential role of minichromosome maintenance protein 2 as a screening biomarker in esophageal cancer high-risk population in China. Human Pathology. 2011;42(6):808-16.

Huang TJ, Wang JY, Lin SR, Lian ST, Hsieh JS. Overexpression of the c-met protooncogene in human gastric carcinoma--correlation to clinical features. Acta oncologica. 2001;40(5):638-43.

Hui SW. Overview of drug delivery and alternative methods to electroporation. Methods Mol Biol. 2008;423:91-107.

Hulme EC, Trevethick MA. Ligand binding assays at equilibrium: validation and interpretation. Brit J Pharmacol. 2010;161(6):1219-37.

Hur C, Miller M, Kong CY, Dowling EC, Nattinger KJ, Dunn M, et al. Trends in esophageal adenocarcinoma incidence and mortality. Cancer. 2013;119(6):1149-58.

Ilson DH. Esophageal cancer chemotherapy: recent advances. Gastrointest Cancer Res. 2008;2(2):85-92.

In H, Palis BE, Merkow RP, Posner MC, Ferguson MK, Winchester DP, et al. Doubling of 30-Day Mortality by 90 Days After Esophagectomy: A Critical Measure of Outcomes for Quality Improvement. Ann Surg. 2016;263(2):286-91.

Inadomi JM, Somsouk MA, Madanick RD, Thomas JP, Shaheen NJ. A Cost-Utility Analysis of Ablative Therapy for Barrett's Esophagus. Gastroenterology. 2009;136(7):2101-14.

Inoue Y, Izawa K, Kiryu S, Tojo A, Ohtomo K. Diet and abdominal autofluorescence detected by in vivo fluorescence imaging of living mice. Mol Imaging. 2008;7(1):21-7.

Imai K, Takaoka A. Comparing antibody and small-molecule therapies for cancer. Nat Rev Cancer. 2006;6(9):714-27.

Jain S, Dhingra S. Pathology of esophageal cancer and Barrett's esophagus. Ann Cardiothorac Surg. 2017;6(2):99-109.

Jalalabadi Y, Shirazi A, Ghavam-Nasiri MR, Aledavood SA, Sardari D, Memar B, et al. Evaluating the expression of cyclooxygenase-2 enzyme by immunohistochemistry in normal and tumoral tissue before and after neoadjuvant chemoradiotherapy in patients with esophageal cancer in Khorasan Province. J Cancer Res Ther. 2018;14(3):509-15.

Janjigian YY, Tang LH, Coit DG, Kelsen DP, Francone TD, Weiser MR, et al. MET expression and amplification in patients with localized gastric cancer. Cancer Epidemiol Biomarkers Prev. 2011;20(5):1021-7.

Jardim DLF, Gagliato DD, Falchook GS, Janku F, Zinner R, Wheler JJ, et al. MET aberrations and c-MET inhibitors in patients with gastric and esophageal cancers in a phase I unit. Oncotarget. 2014;5(7):1837-45.

Jimenez P, Piazuelo E, Sanchez MT, Ortego J, Soteras F, Lanas A. Free radicals and antioxidant systems in reflux esophagitis and Barrett's esophagus. World J Gastroentero. 2005;11(18):2697-703.

Jin Z, Cheng Y, Gu W, Zheng Y, Sato F, Mori Y, et al. A multicenter, double-blinded validation study of methylation biomarkers for progression prediction in Barrett's esophagus. Cancer research. 2009;69(10):4112-5.

Joerger AC, Fersht AR. The tumor suppressor p53: from structures to drug discovery. Cold Spring Harb Perspect Biol. 2010;2(6):a000919.

Jones AT. Macropinocytosis: searching for an endocytic identity and role in the uptake of cell penetrating peptides. J Cell Mol Med. 2007;11(4):670-84.

Joo JY, Lee J, Ko HY, Lee YS, Lim D-H, Kim E-Y, et al. Microinjection free delivery of miRNA inhibitor into zygotes. Scientific Reports. 2014;4:5417.

Kadkhodayan S, Bolhassani A, Sadat SM, Irani S, Fotouhi F. The Efficiency of Tat Cell Penetrating Peptide for Intracellular Uptake of HIV-1 Nef Expressed in E-coli and Mammalian Cell. Curr Drug Deliv. 2017;14(4):536-42.

Kamath AV. Translational pharmacokinetics and pharmacodynamics of monoclonal antibodies. Drug Discov Today Technol, 2016;21-22, 75-83.

Kameoka M, Morgan M, Binette M, Russell RS, Rong LW, Guo XF, et al. The Tat protein of human immunodeficiency virus type 1 (HIV-1) can promote placement of tRNA primer onto viral RNA and suppress later DNA polymerization in HIV-1 reverse transcription. J Virol. 2002;76(8):3637-45.

Kaplon H, Reichert JM. Antibodies to watch in 2018. MAbs. 2018;10(2):183-203.

Karley D, Gupta D, Tiwari A. Biomarker for Cancer: A great Promise for Future. World J Oncol. 2011;2(4):151-7.

Karlikova M, Topolcan O, Wolfe OTJ, Barak V, Zima T. Optimal Use of Biomarkers in Oncology. Biomed Res Int. 2015;2015:423159-.

Katz-Summercorn AC, Frankell AM, Fitzgerald RC. Chapter 4 - Genetics and Biomarkers in Barrett's Esophagus and Esophageal Adenocarcinoma. In: Pleskow DK, Erim T, editors. Barrett's Esophagus. Boston: Academic Press; 2016. p. 37-60.

Kaur S, Venktaraman G, Jain M, Senapati S, Garg PK, Batra SK. Recent trends in antibody-based oncologic imaging. Cancer Lett. 2012;315(2):97-111.

Kawakami K, Brabender J, Lord RV, Groshen S, Greenwald BD, Krasna MJ, et al. Hypermethylated APC DNA in plasma and prognosis of patients with esophageal adenocarcinoma. J Natl Cancer I. 2000;92(22):1805-11.

Keereweer S, Kerrebijn JD, van Driel PB, Xie B, Kaijzel EL, Snoeks TJ, et al. Optical image-guided surgery--where do we stand? Mol Imaging Biol. 2011;13(2):199-207.

Khalil MM, Tremoleda JL, Bayomy TB, Gsell W. Molecular SPECT Imaging: An Overview. Int J Mol Imaging. 2011;2011:796025.

Kim BB, Dikova EB, Sheller U, Dikov MM, Gavrilova EM, Egorov AM. Evaluation of Dissociation-Constants of Antigen-Antibody Complexes by Elisa. J Immunol Methods. 1990;131(2):213-22.

Kircher MF, Hricak H, Larson SM. Molecular imaging for personalized cancer care. Mol Oncol. 2012;6(2):182-95.

Kislinger T, Fu CF, Huber B, Qu W, Taguchi A, Yan SD, et al. N-epsilon-(carboxymethyl)lysine adducts of proteins are ligands for receptor for advanced glycation end products that activate cell signaling pathways and modulate gene expression. J Biol Chem. 1999;274(44):31740-9.

Klauser AG, Schindlbeck NE, Muller-Lissner SA. Symptoms in gastro-oesophageal reflux disease. Lancet. 1990;335(8683):205-8.

Kleinberg L, Knisely JP, Heitmiller R, Zahurak M, Salem R, Burtness B, et al. Mature survival results with preoperative cisplatin, protracted infusion 5-fluorouracil, and 44-Gy radiotherapy for esophageal cancer. Int J Radiat Oncol Biol Phys. 2003;56(2):328-34.

Kobayashi H, Watanabe R, Choyke PL. Improving Conventional Enhanced Permeability and Retention (EPR) Effects; What Is the Appropriate Target? Theranostics. 2014;4(1):81-9.

Kobayashi H, Choyke PL, Ogawa M. Monoclonal antibody-based optical molecular imaging probes; considerations and caveats in chemistry, biology and pharmacology. Curr Opin Chem Biol. 2016;33:32-8.

Koh HK, Geller AC, Miller DR, Grossbart TA, Lew RA. Prevention and early detection strategies for melanoma and skin cancer. Current status. Archives of dermatology. 1996;132(4):436-43.

Konda VJA, Souza RF. Biomarkers of Barrett's Esophagus: From the Laboratory to Clinical Practice. Dig Dis Sci. 2018;63(8):2070-80.

Korb ML, Hartman YE, Kovar J, Zinn KR, Bland KI, Rosenthal EL. Use of monoclonal antibody-IRDye800CW bioconjugates in the resection of breast cancer. J Surg Res. 2014;188(1):119-28.

Kuge Y, Katada Y, Shimonaka S, Temma T, Kimura H, Kiyono Y, et al. Synthesis and evaluation of radioiodinated cyclooxygenase-2 inhibitors as potential SPECT tracers for cyclooxygenase-2 expression. Nucl Med Biol. 2006;33(1):21-7.

Kurumbail RG, Kiefer JR, Marnett LJ. Cyclooxygenase enzymes: catalysis and inhibition. Current opinion in structural biology. 2001;11(6):752-60.

Lagergren J, Bergstrom R, Lindgren A, Nyren O. Symptomatic gastroesophageal reflux as a risk factor for esophageal adenocarcinoma. N Engl J Med. 1999;340(11):825-31.

Lagergren J, Mattson F. Diverging Trends in Recent Population-Based Survival Rates in Oesophageal and Gastric Cancer. Plos One. 2012;7(7).

Lambert R, Hainaut P. The multidisciplinary management of gastrointestinal cancer. Epidemiology of oesophagogastric cancer. Best Pract Res Clin Gastroenterol. 2007;21(6):921-45.

Lammers T, Kiessling F, Hennink WE, Storm G. Drug targeting to tumors: Principles, pitfalls and (pre-) clinical progress. J Control Release. 2012;161(2):175-87.

Lange A, Prenzler A, Frank M, Kirstein M, Vogel A, von der Schulenburg JM. A systematic review of cost-effectiveness of monoclonal antibodies for metastatic colorectal cancer. Eur J Cancer. 2014;50(1):40-9.

Lao-Sirieix P, Lovat L, Fitzgerald RC. Cyclin A immunocytology as a risk stratification tool for Barrett's esophagus surveillance. Clinical Cancer Research. 2007;13(2):659-65.

Laporte JD, Moore PE, Lahiri T, Schwartzman IN, Panettieri RA, Shore SA. p38 MAP kinase regulates IL-1 beta responses in cultured airway smooth muscle cells. Am J Physiol-Lung C. 2000;279(5):L932-L41.

Lau JL, Dunn MK. Therapeutic peptides: Historical perspectives, current development trends, and future directions. Bioorgan Med Chem. 2018;26(10):2700-7.

LeCher JC, Nowak SJ, McMurry JL. Breaking in and busting out: cell-penetrating peptides and the endosomal escape problem. Biomol Concepts. 2017;8(3-4):131-41.

Lee JY, Cho KB, Kim ES, Park KS, Lee YJ, Lee YS, et al. Risk factors for local recurrence after en bloc endoscopic submucosal dissection for early gastric cancer. World J Gastrointest Endosc. 2016;8(7):330-7.

Lee MT, Hung WC, Chen FY, Huang HW. Many-body effect of antimicrobial peptides: On the correlation between lipid's spontaneous curvature and pore formation. Biophysical Journal. 2005;89(6):4006-16.

Lee SJ, Choi YY, Kim C, Chung MS. Correlations between Tumor to Background Ratio on Breast-Specific Gamma Imaging and Prognostic Factors in Breast Cancer. Journal of Korean Medical Science. 2017;32(6):1031-7.

Leelawattanachai J, Kwon KW, Michael P, Ting R, Kim JY, Jin MM. Side-by-Side Comparison of Commonly Used Biomolecules That Differ in Size and Affinity on Tumor Uptake and Internalization. Plos One. 2015;10(4).

Leggett CL, Gorospe EC. Application of confocal laser endomicroscopy in the diagnosis and management of Barrett's esophagus. Ann Gastroenterol. 2014;27(3):193-9.

Lewis CJ, Thrumurthy SG, Pritchard S, Armstrong G, Attwood SE. Comparison of COX-2, Ki-67, and BCL-2 expression in normal esophageal mucosa, Barrett's esophagus, dysplasia, and adenocarcinoma with postablation mucosa and implications for ablative therapies. Surg Endosc. 2011;25(8):2564-9.

Li G, Yang T, Yan J. Cyclooxygenase-2 increased the angiogenic and metastatic potential of tumor cells. Biochem Biophys Res Commun. 2002;299(5):886-90.

Li W, Zheng H, Xu J, Cao S, Xu X, Xiao P. Imaging c-Met expression using 18F-labeled binding peptide in human cancer xenografts. PloS one. 2018;13(6):e0199024-e.

Li X, Zhang XN, Li XD, Chang J. Multimodality imaging in nanomedicine and nanotheranostics. Cancer Biol Med. 2016;13(3):339-48.

Li Y, Wo JM, Ray MB, Jones W, Su RR, Ellis S, et al. Cyclooxygenase-2 and epithelial growth factor receptor up-regulation during progression of Barrett's esophagus to adenocarcinoma. World J Gastroenterol. 2006;12(6):928-34.

Lim YC, Fitzgerald RC. Diagnosis and treatment of Barrett's oesophagus. Brit Med Bull. 2013;107(1):117-32.

Liou GY, Storz P. Reactive oxygen species in cancer. Free Radic Res. 2010;44(5):479-96.

Lipman NS, Jackson LR, Trudel LJ, Weis-Garcia F. Monoclonal versus polyclonal antibodies: distinguishing characteristics, applications, and information resources. ILAR J. 2005;46(3):258-68.

Liu S, Zhang HY, Dai J, Hu SH, Pino I, Eichinger DJ, et al. Characterization of monoclonal antibody's binding kinetics using oblique-incidence reflectivity difference approach. Mabs-Austin. 2015;7(1):110-9.

Liu S, Zheng Y, Volpi D, El-Kasti M, Klotz D, Tullis I, et al. Toward operative in vivo fluorescence imaging of the c-Met proto-oncogene for personalization of therapy in ovarian cancer. Cancer. 2015;121(2):202-13.

Liu XH, Kirschenbaum A, Yao S, Lee R, Holland JF, Levine AC. Inhibition of cyclooxygenase-2 suppresses angiogenesis and the growth of prostate cancer in vivo. J Urology. 2000;164(3):820-5.

Loffeld RJ, Dekkers PE. Experience with oesophageal cancer: a ten-year single centre study reflecting daily practice. ISRN Gastroenterol. 2013;2013:205417.

Long JD, Orlando RC. Anatomy, histology, embryology, and developmental abnormalities of the esophagus. In: Feldman M, Fieldman LS, Sleisenger MH, eds. Gastrointestinal and Liver Diseases. Philadelphia: WB Saunders, 2002:551–560.

Looby E, Abdel-Latif MM, Athie-Morales V, Duggan S, Long A, Kelleher D. Deoxycholate induces COX-2 expression via Erk1/2-, p38-MAPK and AP-1-dependent mechanisms in esophageal cancer cells. BMC Cancer. 2009;9:190.

Lordick F, Mariette C, Haustermans K, Obermannova R, Arnold D. Oesophageal cancer: ESMO Clinical Practice Guidelines for diagnosis, treatment and follow-up. Annals of oncology : official journal of the European Society for Medical Oncology. 2016;27(suppl 5):v50-v7.

Lu RM, Chang YL, Chen MS, Wu HC. Single chain anti-c-Met antibody conjugated nanoparticles for in vivo tumor-targeted imaging and drug delivery. Biomaterials. 2011;32(12):3265-74.

Lu S, Wang TD. In vivo cancer biomarkers of esophageal neoplasia. Cancer Biomark. 2008;4(6):341-50.

Luna RA, Gilbert E, Hunter JG. High-grade dysplasia and intramucosal adenocarcinoma in Barrett's esophagus: the role of esophagectomy in the era of endoscopic eradication therapy. 2012;28(4):362-9.

Lundberg M, Wikstrom S, Johansson M. Cell surface adherence and endocytosis of protein transduction domains. Mol Ther. 2003;8(1):143-50.

Lunedei V, Bazzoli F, Pozzato P, De Luca L, Zagari RM, Fossi S, et al. Endoscopic surveillance in Barrett's esophagus. Minerva Gastroenterol Dietol. 2002;48(2):63-71.

Madani F, Lindberg S, Langel U, Futaki S, Graslund A. Mechanisms of cellular uptake of cell-penetrating peptides. J Biophys. 2011;2011:414729.

Maley CC, Galipeau PC, Finley JC, Wongsurawat VJ, Li XH, Sanchez CA, et al. Genetic clonal diversity predicts progression to esophageal adenocarcinoma. Nat Genet. 2006;38(4):468-73.

Mankoff DA, O'Sullivan F, Barlow WE, Krohn KA. Molecular imaging research in the outcomes era: measuring outcomes for individualized cancer therapy. Acad Radiol. 2007;14(4):398-405.

Mann DA, Frankel AD. Endocytosis and Targeting of Exogenous Hiv-1 Tat Protein. Embo J. 1991;10(7):1733-9.

Mansour NM, El-Serag H B, Anandasabapathy S. Barrett's esophagus: best practices for treatment and post-treatment surveillance. Ann Cardiothorac Surg. 2017;6(2):75-87.

Markl B, Martin B. Pathology of early stage cancer of the gastrointestinal tract. Definition, principles and diagnosis. Chirurg. 2018;89(5):333-8.

Maroun CR, Naujokas MA, Park M. Membrane targeting of Grb2-associated binder-1 (Gab1) scaffolding protein through src myristoylation sequence substitutes for Gab1 pleckstrin homology domain and switches an epidermal growth factor response to an invasive morphogenic program. Mol Biol Cell. 2003;14(4):1691-708.

Marrogi AJ, Travis WD, Welsh JA, Khan MA, Rahim H, Tazelaar H, et al. Nitric oxide synthase, cyclooxygenase 2, and vascular endothelial growth factor in the angiogenesis of non-small cell lung carcinoma. Clinical Cancer Research. 2000;6(12):4739-44.

Marschall ALJ, Frenzel A, Schirrmann T, Schungel M, Dubel S. Targeting antibodies to the cytoplasm. Mabs. 2011;3(1):3-16.

Masclee GMC, Coloma PM, de Wilde M, Kuipers EJ, Sturkenboom MCJM. The incidence of Barrett's oesophagus and oesophageal adenocarcinoma in the United Kingdom and the Netherlands is levelling off. Aliment Pharm Ther. 2014;39(11):1321-30.

Mawhinney MR, Glasgow RE. Current treatment options for the management of esophageal cancer. Cancer Manag Res. 2012;4:367-77.

Megevand E, Denny L, Dehaeck K, Soeters R, Bloch B. Acetic acid visualization of the cervix: An alternative to cytologic screening. Obstet Gynecol. 1996;88(3):383-6.

Melsens E, De Vlieghere E, Descamps B, Vanhove C, De Wever O, Ceelen W, et al. Improved xenograft efficiency of esophageal adenocarcinoma cell lines through in vivo selection. Oncology reports. 2017;38(1):71-81.

Men Z, Wang P, Li C, Chen J, Liu W, Fang Y. High-Temporal-Resolution High-Spatial-Resolution Spaceborne SAR Based on Continuously Varying PRF. Sensors. 2017;17(8).

Mesteri I, Schoppmann SF, Preusser M, Birner P. Overexpression of CMET is associated with signal transducer and activator of transcription 3 activation and diminished prognosis in oesophageal adenocarcinoma but not in squamous cell carcinoma. European journal of cancer. 2014;50(7):1354-60.

Michel MC, Wieland T, Tsujimoto G. How reliable are G-protein-coupled receptor antibodies? Naunyn-Schmiedeberg's Archives of Pharmacology. 2009;379(4):385-8.

Miller CT, Lin L, Casper AM, Lim J, Thomas DG, Orringer MB, et al. Genomic amplification of MET with boundaries within fragile site FRA7G and upregulation of MET pathways in esophageal adenocarcinoma. Oncogene. 2006;25(3):409-18.

Mishra A, Lai GH, Schmidt NW, Sun VZ, Rodriguez AR, Tong R, et al. Translocation of HIV TAT peptide and analogues induced by multiplexed membrane and cytoskeletal interactions. P Natl Acad Sci USA. 2011;108(41):16883-8.

Mittal RK, Chiareli C, Liu JM, Shaker R. Characteristics of lower esophageal sphincter relaxation induced by pharyngeal stimulation with minute amounts of water. Gastroenterology. 1996;111(2):378-84.

Miyawaki A, Sawano A, Kogure T. Lighting up cells: labelling proteins with fluorophores. Nature cell biology. 2003:S1-S7.

Moore KG, Speckmann W, Herzig RP. The use of siRNA to validate immunofluorescence studies. Methods Mol Biol. 2007;356:245-51.

Mourant JR, Freyer JP, Hielscher AH, Eick AA, Shen D, Johnson TM. Mechanisms of light scattering from biological cells relevant to noninvasive optical-tissue diagnostics. Appl Optics. 1998;37(16):3586-93.

Mujumdar RB, Ernst LA, Mujumdar SR, Lewis CJ, Waggoner AS. Cyanine dye labeling reagents: sulfoindocyanine succinimidyl esters. Bioconjug Chem. 1993;4(2):105-11

Mulcahy LA, Pink RC, Carter DR. Routes and mechanisms of extracellular vesicle uptake. Journal of extracellular vesicles. 2014;3.

Muller JM, Erasmi H, Stelzner M, Zieren U, Pichlmaier H. Surgical therapy of oesophageal carcinoma. Br J Surg. 1990;77(8):845-57.

Mullol J, Xaubet A, Lopez E, Rocaferrer J, Picado C. Comparative-Study of the Effects of Different Glucocorticosteroids on Eosinophil Survival Primed by Cultured

Epithelial-Cell Supernatants Obtained from Nasal-Mucosa and Nasal Polyps. Thorax. 1995;50(3):270-4.

Murray L, Sedo A, Scott M, McManus D, Sloan JM, Hardie LJ, et al. TP53 and progression from Barrett's metaplasia to oesophageal adenocarcinoma in a UK population cohort. Gut. 2006;55(10):1390-7.

Nagaraja V, Eslick GD. Forthcoming prognostic markers for esophageal cancer: a systematic review and meta-analysis. Journal of gastrointestinal oncology. 2014;5(1):67-76.

Naini BV, Souza RF, Odze RD. Barrett's Esophagus A Comprehensive and Contemporary Review for Pathologists. Am J Surg Pathol. 2016;40(5):E45-E66.

Nakashima S, Natsugoe S, Matsumoto M, Kijima F, Takebayashi Y, Okumura H, et al. Expression of p53 and p21 is useful for the prediction of preoperative chemotherapeutic effects in esophageal carcinoma. Anticancer Res. 2000;20(3b):1933-7.

Napier KJ, Scheerer M, Misra S. Esophageal cancer: A Review of epidemiology, pathogenesis, staging workup and treatment modalities. World J Gastrointest Oncol. 2014;6(5):112-20.

Narumiya S, FitzGerald GA. Genetic and pharmacological analysis of prostanoid receptor function. J Clin Invest. 2001;108(1):25-30.

Nekarda H, Schlegel P, Schmitt M, Stark M, Mueller JD, Fink U, et al. Strong prognostic impact of tumor-associated urokinase-type plasminogen activator in completely resected adenocarcinoma of the esophagus. Clinical Cancer Research. 1998;4(7):1755-63.

Nelsen EM, Hawes RH, Iyer PG. Diagnosis and management of Barrett's esophagus. Surg Clin North Am. 2012;92(5):1135-54.

Neri D, Montigiani S, Kirkham PM. Biophysical methods for the determination of antibody-antigen affinities. Trends Biotechnol. 1996;14(12):465-70.

Neuner G, Patel A, Suntharalingam M. Chemoradiotherapy for esophageal cancer. Gastrointest Cancer Res. 2009;3(2):57-65.

Newhauser WD, Zhang R. The physics of proton therapy. Phys Med Biol. 2015;60(8):R155-209.

Newsome BW, Ernstoff MS. The clinical pharmacology of therapeutic monoclonal antibodies in the treatment of malignancy; have the magic bullets arrived? Br J Clin Pharmacol. 2008;66(1):6-19.

Nguyen PN, Veschgini M, Tanaka M, Waton G, Vandamme T, Krafft MP. Counteracting the inhibitory effect of proteins towards lung surfactant substitutes: a fluorocarbon gas

helps displace albumin at the air/water interface. Chem Commun (Camb). 2014;50(78):11576-9.

Niesner U, Halin C, Lozzi L, Gunthert M, Neri P, Wunderli-Allenspach H, et al. Quantitation of the tumor-targeting properties of antibody fragments conjugated to cell-permeating HIV-1 TAT peptides. Bioconjug Chem. 2002;13(4):729-36.

Noordzij M, Dekker FW, Zoccali C, Jager KJ. Measures of Disease Frequency: Prevalence and Incidence. Nephron Clin Pract. 2010;115(1):E17-E20.

O'Brien WD, Jr. Ultrasound-biophysics mechanisms. Prog Biophys Mol Biol. 2007;93(1-3):212-55.

O'Connor JP, Aboagye EO, Adams JE, Aerts HJ, Barrington SF, Beer AJ, et al. Imaging biomarker roadmap for cancer studies. Nat Rev Clin Oncol. 2017;14(3):169-86.

Odze RD. Diagnosis and grading of dysplasia in Barrett's oesophagus. J Clin Pathol. 2006;59(10):1029-38.

Ogawa M, Regino CAS, Choyke PL, Kobayashi H. In vivo target-specific activatable near-infrared optical labeling of humanized monoclonal antibodies. Molecular Cancer Therapeutics. 2009;8(1):232-9.

Olafsen T, Wu AM. Antibody vectors for imaging. Seminars in nuclear medicine. 2010;40(3):167-81.

Olds W, Li J. siRNA knockdown validation 101: Incorporating negative controls in antibody research. F1000Res. 2016;5:308.

Olivier M, Hollstein M, Hainaut P. TP53 Mutations in Human Cancers: Origins, Consequences, and Clinical Use. Csh Perspect Biol. 2010;2(1).

Ong CA, Lao-Sirieix P, Fitzgerald RC. Biomarkers in Barrett's esophagus and esophageal adenocarcinoma: predictors of progression and prognosis. World J Gastroenterol. 2010;16(45):5669-81.

Organ SL, Tsao M-S. An overview of the c-MET signaling pathway. Therapeutic advances in medical oncology. 2011;3(1 Suppl):S7-S19.

Oshima H, Oshima M. The role of PGE2-associated inflammatory responses in gastric cancer development. Semin Immunopathol. 2013;35(2):139-50.

Oyama K, Fujimura T, Ninomiya I, Miyashita T, Kinami S, Fushida S, et al. A COX-2 inhibitor prevents the esophageal inflammation-metaplasia-adenocarcinoma sequence in rats. Carcinogenesis. 2005;26(3):565-70.

Pai R, Soreghan B, Szabo IL, Pavelka M, Baatar D, Tarnawski AS. Prostaglandin E2 transactivates EGF receptor: a novel mechanism for promoting colon cancer growth and gastrointestinal hypertrophy. Nat Med. 2002;8(3):289-93.

Palanca-Wessels MC, Barrett MT, Galipeau PC, Rohrer KL, Reid BJ, Rabinovitch PS. Genetic analysis of long-term Barrett's esophagus epithelial cultures exhibiting cytogenetic and ploidy abnormalities. Gastroenterology. 1998;114(2):295-304.

Pansare V, Hejazi S, Faenza W, Prud'homme RK. Review of Long-Wavelength Optical and NIR Imaging Materials: Contrast Agents, Fluorophores and Multifunctional Nano Carriers. Chem Mater. 2012;24(5):812-27.

Pardridge WM, Kang YS, Yang J, Buciak JL. Enhanced Cellular Uptake and in-Vivo Biodistribution of a Monoclonal-Antibody Following Cationization. Journal of pharmaceutical sciences. 1995;84(8):943-8.

Park A, Lee Y, Kim MS, Kang YJ, Park YJ, Jung H, et al. Prostaglandin E2 Secreted by Thyroid Cancer Cells Contributes to Immune Escape Through the Suppression of Natural Killer (NK) Cell Cytotoxicity and NK Cell Differentiation. Frontiers in Immunology. 2018;9

Parkinson DR, Johnson BE, Sledge GW. Making personalized cancer medicine a reality: challenges and opportunities in the development of biomarkers and companion diagnostics. Clin Cancer Res. 2012;18(3):619-24.

Pech O, May A, Gossner L, Rabenstein T, Manner H, Huijsmans J, et al. Curative endoscopic therapy in patients with early esophageal squamous-cell carcinoma or high-grade intraepithelial neoplasia. Endoscopy. 2007;39(1):30-5.

Pelicci G, Giordano S, Zhen Z, Salcini AE, Lanfrancone L, Bardelli A, et al. The Motogenic and Mitogenic Responses to Hgf Are Amplified by the Shc Adapter Protein. Oncogene. 1995;10(8):1631-8.

Peng XJ, Song FL, Lu E, Wang YN, Zhou W, Fan JL, et al. Heptamethine cyanine dyes with a large stokes shift and strong fluorescence: A paradigm for excited-state intramolecular charge transfer. J Am Chem Soc. 2005;127(12):4170-1.

Pennathur A, Farkas A, Krasinskas AM, Ferson PF, Gooding WE, Michael KG, et al. Esophagectomy for T1 Esophageal Cancer: Outcomes in 100 Patients and Implications for Endoscopic Therapy. Ann Thorac Surg. 2009;87(4):1048-55.

Pedersen JB, Lindup WE. Interpretation and analysis of receptor binding experiments which yield non-linear Scatchard plots and binding constants dependent upon receptor concentration. Biochemical pharmacology. 1994;47(2):179-85.

Peterson NC, Wilson GG, Huang Q, Dimasi N, Sachsenmeier KF. Biodistribution Analyses of a Near-Infrared, Fluorescently Labeled, Bispecific Monoclonal Antibody Using Optical Imaging. Comp Med. 2016;66(2):90-9.

Picot D, Loll PJ, Garavito RM. The X-ray crystal structure of the membrane protein prostaglandin H2 synthase-1. Nature. 1994;367(6460):243-9.

Pimentel-Nunes P, Dinis-Ribeiro M. Endoscopic Submucosal Dissection in the Treatment of Gastrointestinal Superficial Lesions: Follow the Guidelines! GE Port J Gastroenterol. 2015;22(5):184-6.

Plewes DB, Kucharczyk W. Physics of MRI: a primer. J Magn Reson Imaging. 2012;35(5):1038-54.

Polee MB, Hop WC, Kok TC, Eskens FA, van der Burg ME, Splinter TA, et al. Prognostic factors for survival in patients with advanced oesophageal cancer treated with cisplatin-based combination chemotherapy. Br J Cancer. 2003;89(11):2045-50.

Ponzetto C, Bardelli A, Zhen Z, Maina F, Dallazonca P, Giordano S, et al. A Multifunctional Docking Site Mediates Signaling and Transformation by the Hepatocyte Growth-Factor Scatter Factor-Receptor Family. Cell. 1994;77(2):261-71.

Pouny Y, Rapaport D, Mor A, Nicolas P, Shai Y. Interaction of Antimicrobial Dermaseptin and Its Fluorescently Labeled Analogs with Phospholipid-Membranes. Biochemistry-Us. 1992;31(49):12416-23.

Powell DW, Pinchuk IV, Saada JI, Chen X, Mifflin RC. Mesenchymal Cells of the Intestinal Lamina Propria. Annu Rev Physiol. 2011;73:213-37.

Pysz MA, Gambhir SS, Willmann JK. Molecular imaging: current status and emerging strategies. Clin Radiol. 2010;65(7):500-16.

Qu XM, Biagi JJ, Hopman WM, Mahmud A. Shifting practice in definitive chemoradiation for localized esophageal cancer. Curr Oncol. 2017;24(5):e379-e87.

Quante M, Bhagat G, Abrams JA, Marache F, Good P, Lee MD, et al. Bile acid and inflammation activate gastric cardia stem cells in a mouse model of Barrett-like metaplasia. Cancer Cell. 2012;21(1):36-51.

Quante M, Graham TA, Jansen M. Insights Into the Pathophysiology of Esophageal Adenocarcinoma. Gastroenterology. 2018;154(2):406-20.

Ramos-Vara JA. Technical aspects of immunohistochemistry. Veterinary pathology. 2005;42(4):405-26.

Rasouli M, Ghadimi MR, Mahmoodi M, Mohammad K, Zeraati H, Hosseini M. Survival Analysis of Patients with Esophageal Cancer using Parametric Cure Model. Asian Pac J Cancer P. 2011;12(9):2359-63.

Ray K, Szmacinski H, Lakowicz JR. Enhanced Fluorescence of Proteins and Label-Free Bioassays Using Aluminum Nanostructures. Anal Chem. 2009;81(15):6049-54.

Reagan-Shaw S, Nihal M, Ahmad N. Dose translation from animal to human studies revisited. FASEB J. 2008;22(3):659-61.

Reichert JM. Antibodies to watch in 2017. MAbs. 2017;9(2):167-81.

Reid BJ, Li X, Galipeau PC, Vaughan TL. Barrett's oesophagus and oesophageal adenocarcinoma: time for a new synthesis. Nat Rev Cancer. 2010;10(2):87-101.

Reubi JC, Maecke HR. Peptide-based probes for cancer imaging. J Nucl Med. 2008;49(11):1735-8.

Rice TW, Patil DT, Blackstone EH. 8th edition AJCC/UICC staging of cancers of the esophagus and esophagogastric junction: application to clinical practice. Ann Cardiothorac Sur. 2017;6(2):119-30.

Riley T, Purssell H, Ang YJJoL, Medicine P. Biomarkers in Barrett's oesophagus. 2018. 2018;3.

Risi MD, Makhlouf H, Rouse AR, Tanbakuchi AA, Gmitro AF. Design and Performance of a Multi-Point Scan Confocal Microendoscope. Photonics. 2014;1(4):421-31.

Rockett JC, Larkin K, Darnton SJ, Morris AG, Matthews HR. Five newly established oesophageal carcinoma cell lines: phenotypic and immunological characterization. Br J Cancer. 1997;75(2):258-63.

Rodrigues GA, Park M. Autophosphorylation Modulates the Kinase-Activity and Oncogenic Potential of the Met Receptor Tyrosine Kinase. Oncogene. 1994;9(7):2019-27.

Rogasch JM, Steffen IG, Hofheinz F, Grosser OS, Furth C, Mohnike K, et al. The association of tumor-to-background ratios and SUVmax deviations related to point spread function and time-of-flight F18-FDG-PET/CT reconstruction in colorectal liver metastases. EJNMMI Res. 2015;5:31.

Romano R, Palamaro L, Fusco A, Iannace L, Maio S, Vigliano I, et al. From Murine to Human Nude/SCID: The Thymus, T-Cell Development and the Missing Link. Clinical & developmental immunology. 2012.

Ross-Innes CS, Becq J, Warren A, Cheetham RK, Northen H, O'Donovan M, et al. Whole-genome sequencing provides new insights into the clonal architecture of Barrett's esophagus and esophageal adenocarcinoma. Nat Genet. 2015;47(9):1038-+.

Ruoslahti E. Tumor penetrating peptides for improved drug delivery. Adv Drug Deliver Rev. 2017;110:3-12.

Rybinski B, Yun K. Addressing intra-tumoral heterogeneity and therapy resistance. Oncotarget. 2016;7(44):72322-42.

Saad RS, El-Gohary Y, Memari E, Liu YL, Silverman JF. Endoglin (CD105) and vascular endothelial growth factor as prognostic markers in esophageal adenocarcinoma. Human Pathology. 2005;36(9):955-61.

Sakkab D, Lewitzky M, Posern G, Schaeper U, Sachs M, Birchmeier W, et al. Signaling of hepatocyte growth factor/scatter factor (HGF) to the small GTPase Rap1 via the

large docking protein Gab1 and the adapter protein CRKL. Journal of Biological Chemistry. 2000;275(15):10772-8.

Salahudeen MS, Nishtala PS. An overview of pharmacodynamic modelling, ligand-binding approach and its application in clinical practice. Saudi Pharm J. 2017;25(2):165-75.

Sampliner RE, Practice Parameters Committee of the American College of G. Updated guidelines for the diagnosis, surveillance, and therapy of Barrett's esophagus. Am J Gastroenterol. 2002;97(8):1888-95.

Sanderson MJ, Smith I, Parker I, Bootman MD. Fluorescence microscopy. Cold Spring Harb Protoc. 2014;2014(10):pdb top071795.

Sandell JL, Zhu TC. A review of in-vivo optical properties of human tissues and its impact on PDT. J Biophotonics. 2011;4(11-12):773-87.

Santander S, Cebrian C, Esquivias P, Conde B, Esteva F, Jimenez P, et al. Cyclooxygenase inhibitors decrease the growth and induce regression of human esophageal adenocarcinoma xenografts in nude mice. Int J Oncol. 2012;40(2):527-34.

Saper CB, Sawchenko PE. Magic peptides, magic antibodies: guidelines for appropriate controls for immunohistochemistry. J Comp Neurol. 2003;465(2):161-3.

Sato K, Gorka AP, Nagaya T, Michie MS, Nani RR, Nakamura Y, et al. Role of Fluorophore Charge on the In Vivo Optical Imaging Properties of Near-Infrared Cyanine Dye/Monoclonal Antibody Conjugates. Bioconjugate chemistry. 2016;27(2):404-13.

Schaeper U, Gehring NH, Fuchs KP, Sachs M, Kempkes B, Birchmeier W. Coupling of Gab1 to c-Met, Grb2, and Shp2 mediates biological responses. J Cell Biol. 2000;149(7):1419-32.

Schiffman JD, Fisher PG, Gibbs P. Early detection of cancer: past, present, and future. Am Soc Clin Oncol Educ Book. 2015:57-65.

Schnell TG, Sontag SJ, Chejfec G, Aranha G, Metz A, O'Connell S, et al. Long-term nonsurgical management of Barrett's esophagus with high-grade dysplasia. Gastroenterology. 2001;120(7):1607-19.

Schoofs N, Bisschops R, Prenen H. Progression of Barrett's esophagus toward esophageal adenocarcinoma: an overview. Ann Gastroenterol. 2017;30(1):1-6.

Schonbrunn A. Editorial: Antibody Can Get It Right: Confronting Problems of Antibody Specificity and Irreproducibility. Mol Endocrinol. 2014;28(9):1403-7.

Schuller HM, Kabalka G, Smith G, Mereddy A, Akula M, Cekanova M. Detection of overexpressed COX-2 in precancerous lesions of hamster pancreas and lungs by molecular imaging: Implications for early diagnosis and prevention. Chemmedchem. 2006;1(6):603-10.

Schulmann K, Sterian A, Berki A, Yin J, Sato F, Xu Y, et al. Inactivation of p16, RUNX3, and HPP1 occurs early in Barrett's-associated neoplastic progression and predicts progression risk. Oncogene. 2005;24(25):4138-48.

Seevinck PR, Seppenwoolde JH, de Wit TC, Nijsen JF, Beekman FJ, van Het Schip AD, et al. Factors affecting the sensitivity and detection limits of MRI, CT, and SPECT for multimodal diagnostic and therapeutic agents. Anti-cancer agents in medicinal chemistry. 2007;7(3):317-34.

Sehdev A, Catenacci DV. Perioperative therapy for locally advanced gastroesophageal cancer: current controversies and consensus of care. J Hematol Oncol. 2013;6:66.

Sekiguchi M, Oda I. High miss rate for gastric superficial cancers at endoscopy: what is necessary for gastric cancer screening and surveillance using endoscopy? Endosc Int Open. 2017;5(8):E727-E8.

Sela M. Antigenicity - Some Molecular Aspects. Science. 1969;166(3911):1365-+.

Selleck MJ, Senthil M, Wall NR. Making Meaningful Clinical Use of Biomarkers. Biomark Insights. 2017;12:1177271917715236-.

Sellers AH. The clinical classification of malignant tumours: the TNM system. Canadian Medical Association journal. 1971;105(8):836-passim.

Shah AK, Saunders NA, Barbour AP, Hill MM. Early diagnostic biomarkers for esophageal adenocarcinoma--the current state of play. Cancer Epidemiol Biomarkers Prev. 2013;22(7):1185-209.

Shah PM, Gerdes H. Endoscopic options for early stage esophageal cancer. J Gastrointest Oncol. 2015;6(1):20-30.

Shaheen N. Ransohoff DF. Gastroesophageal reflux, barrett esophagus, and esophageal cancer: scientific review. JAMA. 2002;287(15):1972-81.

Shaheen NJ. Advances in Barrett's esophagus and esophageal adenocarcinoma. Gastroenterology. 2005;128(6):1554-66.

Shaheen NJ, Falk GW, Iyer PG, Gerson LB. ACG Clinical Guideline: Diagnosis and Management of Barrett's Esophagus. American Journal of Gastroenterology. 2016;111(1):30-50.

Shaikh T, Meyer JE, Horwitz EM. Optimal Use of Combined Modality Therapy in the Treatment of Esophageal Cancer. Surgical oncology clinics of North America. 2017;26(3):405-29.

Sharma N, Srivastava S, Kern F, Xian W, Ming T, McKeon F, et al. Endoscopic modalities for the diagnosis of Barrett's oesophagus. United European Gastroenterol J. 2016;4(6):733-40.

Sharma P. Endoscopic Mucosal Resection as the Primary Treatment for Barrett Esophagus With Dysplasia. Gastroenterology & hepatology. 2015;11(10):703-5.

Sharma P, McQuaid K, Dent J, Fennerty MB, Sampliner R, Spechler S, et al. A critical review of the diagnosis and management of Barrett's esophagus: the AGA Chicago Workshop. Gastroenterology. 2004;127(1):310-30.

Sharma RA, Plummer R, Stock JK, Greenhalgh TA, Ataman O, Kelly S, et al. Clinical development of new drug-radiotherapy combinations. Nat Rev Clin Oncol. 2016;13(10):627-42.

Sharma S, Stolina M, Yang SC, Baratelli F, Lin JF, Atianzar K, et al. Tumor cyclooxygenase 2-dependent suppression of dendritic cell function. Clin Cancer Res. 2003;9(3):961-8.

Shaw PH. The role of p53 in cell cycle regulation. Pathol Res Pract. 1996;192(7):669-75.

Sheng Q, Liu J. The therapeutic potential of targeting the EGFR family in epithelial ovarian cancer. Br J Cancer. 2011;104(8):1241-5.

Sherr CJ, McCormick F. The RB and p53 pathways in cancer. Cancer Cell. 2002;2(2):103-12.

Shi XY, Bhagwandeen B, Leong ASY. p16, cyclin D1, Ki-67, and AMACR as markers for dysplasia in Barrett esophagus. Appl Immunohisto M M. 2008;16(5):447-52.

Shirvani VN, Ouatu-Lascar R, Kaur BS, Omary MB, Triadafilopoulos G. Cyclooxygenase 2 expression in Barrett's esophagus and adenocarcinoma: Ex vivo induction by bile salts and acid exposure. Gastroenterology. 2000;118(3):487-96.

Singh R, Owen V, Shonde A, Kaye P, Hawkey C, Ragunath K. White light endoscopy, narrow band imaging and chromoendoscopy with magnification in diagnosing colorectal neoplasia. World J Gastrointest Endosc. 2009;1(1):45-50.

Sirieix PS, O'Donovan M, Brown J, Save V, Coleman N, Fitzgerald RC. Surface expression of minichromosome maintenance proteins provides a novel method for detecting patients at risk for developing adenocarcinoma in Barrett's esophagus. Clinical Cancer Research. 2003;9(7):2560-6.

Skotland T. Molecular imaging: challenges of bringing imaging of intracellular targets into common clinical use. Contrast Media Mol I. 2012;7(1):1-6.

Smith WL, DeWitt DL, Garavito RM. Cyclooxygenases: structural, cellular, and molecular biology. Annu Rev Biochem. 2000;69:145-82.

Smith WL, Marnett LJ, DeWitt DL. Prostaglandin and thromboxane biosynthesis. Pharmacol Ther. 1991;49(3):153-79.

Smith-Bindman R, Lipson J, Marcus R, Kim KP, Mahesh M, Gould R, et al. Radiation dose associated with common computed tomography examinations and the associated lifetime attributable risk of cancer. Archives of internal medicine. 2009;169(22):2078-86.

Smyth EM, Grosser T, Wang M, Yu Y, FitzGerald GA. Prostanoids in health and disease. J Lipid Res. 2009;50 Suppl:S423-8.

Sobin LH. 7. Chichester, West Sussex, UK, Hoboken NJ: Wiley-Blackwell; 2009. TNM classification of malignant tumours; p. 309.

Sokolov K, Aaron J, Hsu B, Nida D, Gillenwater A, Follen M, et al. Optical systems for In vivo molecular imaging of cancer. Technol Cancer Res T. 2003;2(6):491-504.

Song S, Guha S, Liu K, Buttar NS, Bresalier RS. COX-2 induction by unconjugated bile acids involves reactive oxygen species-mediated signalling pathways in Barrett's oesophagus and oesophageal adenocarcinoma. Gut. 2007;56(11):1512-21.

Sorkin A, Duex JE. Quantitative analysis of endocytosis and turnover of epidermal growth factor (EGF) and EGF receptor. Current protocols in cell biology. 2010;Chapter 15:Unit 15 4.

Souza RF. The role of acid and bile reflux in oesophagitis and Barrett's metaplasia. Biochem Soc Trans. 2010;38(2):348-52.

Spicer SS, Spivey MA, Ito M, Schulte BA. Some ascites monoclonal antibody preparations contain contaminants that bind to selected Golgi zones or mast cells. The journal of histochemistry and cytochemistry : J Histochem Cytochem. 1994;42(2):213-21.

Stachler MD, Taylor-Weiner A, Peng SY, McKenna A, Agoston AT, Odze RD, et al. Paired exome analysis of Barrett's esophagus and adenocarcinoma. Nat Genet. 2015;47(9):1047-+.

Syed ZA, Yin WH, Hughes K, Gill JN, Shi RH, Clifford JL. HGF/c-met/Stat3 signaling during skin tumor cell invasion: indications for a positive feedback loop. Bmc Cancer. 2011;11.

Szabo A, Szendi-Szatmari T, Ujlaky-Nagy L, Radi I, Vereb G, Szollosi J, et al. The Effect of Fluorophore Conjugation on Antibody Affinity and the Photophysical Properties of Dyes. Biophys j. 2018;114(3):688-700.

Tabrizi MA, Tseng CM, Roskos LK. Elimination mechanisms of therapeutic monoclonal antibodies. Drug Discov Today. 2006;11(1-2):81-8.

Tack J. Review article: role of pepsin and bile in gastro-oesophageal reflux disease. Aliment Pharmacol Ther. 2005;22 Suppl 1:48-54.

Tatsugami M, Ito M, Tanaka S, Yoshihara M, Matsui H, Haruma K, et al. Bile acid promotes intestinal metaplasia and gastric carcinogenesis. Cancer Epidemiol Biomarkers Prev. 2012;21(11):2101-7.

Teng Y, Ross JL, Cowell JK. The involvement of JAK-STAT3 in cell motility, invasion, and metastasis. JAKSTAT. 2014;3(1):e28086.

Tham T, Secretary BSG Clinical Services and Standards Committee: 2015. BSG Guidelines: Guidelines on the Diagnosis and Management of Barrett's Oesophagus - An Update.

Thekkek N, Anandasabapathy S, Richards-Kortum R. Optical molecular imaging for detection of Barrett's-associated neoplasia. World J Gastroenterol. 2011;17(1):53-62.

Thrift AP. The epidemic of oesophageal carcinoma: Where are we now? J Cancer epidemiol. 2016;41:88-95.

Thrift AP, Kramer JR, Qureshi Z, Richardson PA, El-Serag HB. Age at onset of GERD symptoms predicts risk of Barrett's esophagus. Am J Gastroenterol. 2013;108(6):915-22.

Tietz O, Marshall A, Wuest M, Wang M, Wuest F. Radiotracers for Molecular Imaging of Cyclooxygenase-2 (COX-2) Enzyme. Curr Med Chem. 2013;20(35):4350-69.

Toseland CP. Fluorescent labeling and modification of proteins. J Chem Biol. 2013;6(3):85-95.

Trenevska I, Li D, Banham AH. Therapeutic Antibodies against Intracellular Tumor Antigens. Front Immunol. 2017;8:1001.

Trivedi PJ. Braden B. Indications, stains and techniques in chromoendoscopy. QJM. 2013;106(2):117-31.

Trusolino L, Bertotti A, Comoglio PM. MET signalling: principles and functions in development, organ regeneration and cancer. Nat Rev Mol Cell Biol. 2010;11(12):834-48.

Tsong TY. Electroporation of cell membranes. Biophys J. 1991;60(2):297-306.

Tsujii M, DuBois RN. Alterations in cellular adhesion and apoptosis in epithelial cells overexpressing prostaglandin endoperoxide synthase 2. Cell. 1995;83(3):493-501.

Tsujii M, Kawano S, DuBois RN. Cyclooxygenase-2 expression in human colon cancer cells increases metastatic potential. Proc Natl Acad Sci U S A. 1997;94(7):3336-40.

Tsujii M, Kawano S, Tsuji S, Sawaoka H, Hori M, DuBois RN. Cyclooxygenase regulates angiogenesis induced by colon cancer cells. Cell. 1998;93(5):705-16.

Tuynman JB, Lagarde SM, ten Kate FJW, Richel DJ, van Lanschot JJB. Met expression is an independent prognostic risk factor in patients with oesophageal adenocarcinoma. Brit J Cancer. 2008;98(6):1102-8.

Uddin MJ, Crews BC, Blobaum AL, Kingsley PJ, Ghebreselasie K, Saleh SS, et al. Synthesis and evaluation of [I-123]-indomethacin derivatives as COX-2 targeted imaging agents. J Labelled Compd Rad. 2009;52(9-10):387-93.

Uddin MJ, Crews BC, Blobaum AL, Kingsley PJ, Gorden DL, McIntyre JO, et al. Selective Visualization of Cyclooxygenase-2 in Inflammation and Cancer by Targeted Fluorescent Imaging Agents. Cancer research. 2010;70(9):3618-27.

Uddin MJ, Crews BC, Ghebreselasie K, Tantawy MN, Marnett LJ. [I-123]-Celecoxib Analogues as SPECT Tracers of Cyclooxygenase-2 in Inflammation. Acs Med Chem Lett. 2011;2(2):160-4.

Uddin MJ, Marnett LJ. Synthesis of 5-and 6-Carboxy-X-rhodamines. Org Lett. 2008;10(21):4799-801.

Underwood TJ, Hayden AL, Derouet M, Garcia E, Noble F, White MJ, et al. Cancer-associated fibroblasts predict poor outcome and promote periostin-dependent invasion in oesophageal adenocarcinoma. J Pathol. 2015;235(3):466-77.

Vaezi MF, Richter JE. Role of acid and duodenogastroesophageal reflux in gastroesophageal reflux disease. Gastroenterology. 1996;111(5):1192-9.

van Dam GM, Themelis G, Crane LM, Harlaar NJ, Pleijhuis RG, Kelder W, et al. Intraoperative tumor-specific fluorescence imaging in ovarian cancer by folate receptor-alpha targeting: first in-human results. Nat Med. 2011;17(10):1315-9.

Vandamme TF, Anton N, Torchilin V. Targeted imaging. Adv Drug Deliv Rev. 2014;76:1.

van der Poel HG, Buckle T, Brouwer OR, Olmos RAV, van Leeuwen FWB. Intraoperative Laparoscopic Fluorescence Guidance to the Sentinel Lymph Node in Prostate Cancer Patients: Clinical Proof of Concept of an Integrated Functional Imaging Approach Using a Multimodal Tracer. Eur Urol. 2011;60(4):826-33.

van Leeuwen FWB, Cornelissen B, Caobelli F, Evangelista L, Rbah-Vidal L, Del Vecchio S, et al. Generation of fluorescently labeled tracers - which features influence the translational potential? EJNMMI Radiopharm Chem. 2017;2(1):15-.

van Putten M, Johnston BT, Murray LJ, Gavin AT, McManus DT, Bhat S, et al. "Missed' oesophageal adenocarcinoma and high-grade dysplasia in Barrett's oesophagus patients: A large population-based study. United Eur Gastroent. 2018;6(4):519-28.

Varkouhi AK, Scholte M, Storm G, Haisma HJ. Endosomal escape pathways for delivery of biologicals. J Control Release. 2011;151(3):220-8.

Vasquez KO, Casavant C, Peterson JD. Quantitative whole body biodistribution of fluorescent-labeled agents by non-invasive tomographic imaging. PLoS One. 2011;6(6):e20594.

Webb NE, Montefiori DC, Lee B. Dose-response curve slope helps predict therapeutic potency and breadth of HIV broadly neutralizing antibodies. Nat Commun. 2015;6.

Vira S, Mekhedov E, Humphrey G, Blank PS. Fluorescent-labeled antibodies: Balancing functionality and degree of labeling. Anal Biochem. 2010;402(2):146-50.

Visrodia K, Singh S, Krishnamoorthi R, Ahlquist DA, Wang KK, Iyer PG, et al. Magnitude of Missed Esophageal Adenocarcinoma After Barrett's Esophagus Diagnosis: A Systematic Review and Meta-analysis. Gastroenterol. 2016;150(3):599-607 e7; quiz e14-5.

Viticchie G, Muller PAJ. c-Met and Other Cell Surface Molecules: Interaction, Activation and Functional Consequences. Biomedicines. 2015;3(1):46-70.

Vives E, Brodin P, Lebleu B. A truncated HIV-1 Tat protein basic domain rapidly translocates through the plasma membrane and accumulates in the cell nucleus. J Biol Chem. 1997;272(25):16010-7.

von Rahden BHA, Stein HJ, Feith M, Puhringer F, Theisen J, Siewert JR, et al. Overexpression of TGF-beta 1 in esophageal adenocarcinoma is associated with advanced stage of disease and poor prognosis. Mol Carcinogen. 2006;45(10):786-94.

Volpi D. Tissue autofluorescence: watch out what's on the menu. 2012. [10 Nov 2018]. Available from: http://users.ox.ac.uk/~atdgroup/technicalnotes/Tissue%20autofluorescence_watch%20out%20what%27s%20on%20the%20menu.pdf

Volpi D, Tullis IDC, Laios A, Pathiraja PNJ, Haldar K, Ahmed AA, et al. A novel multiwavelength fluorescence image-guided surgery imaging system: SPIE; 2014.

Voskuil J. Commercial antibodies and their validation. F1000Research. 2014;3:232.

Wang CS, Wang ZH, Zhao T, Li Y, Huang G, Sumer BD, et al. Optical molecular imaging for tumor detection and image-guided surgery. Biomaterials. 2018;157:62-75.

Wang GQ, Abnet CC, Shen Q, Lewin KI, Sun XD, Roth MJ, et al. Histological precursors of oesophageal squamous cell carcinoma: results from a 13-year prospective follow up study in a high-risk population. Gut. 2005;54(2):187-92.

Wang JS, Guo MZ, Montgomery EA, Thompson RE, Cosby H, Hicks L, et al. DNA Promoter Hypermethylation of p16 and APC Predicts Neoplastic Progression in Barrett's Esophagus. Am J Gastroenterol. 2009;104(9):2153-60.

Wang K, Chi C, Hu Z, Liu M, Hui H, Shang W, et al. Optical Molecular Imaging Frontiers in Oncology: The Pursuit of Accuracy and Sensitivity. Engineering. 2015;1(3):309-23.

Wang RH. From reflux esophagitis to Barrett's esophagus and esophageal adenocarcinoma. World J Gastroenterol. 2015;21(17):5210-9.

Wang TD, Van Dam J. Optical biopsy: a new frontier in endoscopic detection and diagnosis. Clin Gastroenterol Hepatol. 2004;2(9):744-53.

Wang VS, Hornick JL, Sepulveda JA, Mauer R, Poneros JM. Low prevalence of submucosal invasive carcinoma at esophagectomy for high-grade dysplasia or intramucosal adenocarcinoma in Barrett's esophagus: a 20-year experience. Gastrointest. Endosc. 2009;69(4):777-83.

Wang YG, Hassan MD, Shariff M, Zamri SM, Chen X. Histopathology and cytopathology of white spot syndrome virus (WSSV) in cultured Penaeus monodon from peninsular Malaysia with emphasis on pathogenesis and the mechanism of white spot formation. Dis Aquat Organ. 1999;39(1):1-11.

Wani S, Puli SR, Shaheen NJ, Westhoff B, Slehria S, Bansal A, et al. Esophageal adenocarcinoma in Barrett's esophagus after endoscopic ablative therapy: a meta-analysis and systematic review. Am J Gastroenterol. 2009;104(2):502-13.

Wani S, Sharma P. Narrow band imaging in Barrett's esophagus. Expert Rev Gastroenterol Hepatol. 2007;1(1):53-60.

Warram JM, de Boer E, Sorace AG, Chung TK, Kim H, Pleijhuis RG, et al. Antibody-based imaging strategies for cancer. Cancer metastasis rev. 2014;33(2-3):809-22.

Waterton JC, Pylkkanen L. Qualification of imaging biomarkers for oncology drug development. Eur J Cancer. 2012;48(4):409-15.

Watson GA, Zhang X, Stang MT, Levy RM, Queiroz de Oliveira PE, Gooding WE, et al. Inhibition of c-Met as a therapeutic strategy for esophageal adenocarcinoma. Neoplasia. 2006;8(11):949-55.

Weaver JMJ, Ross-Innes CS, Shannon N, Lynch AG, Forshew T, Barbera M, et al. Ordering of mutations in preinvasive disease stages of esophageal carcinogenesis. Nat Genet. 2014;46(8):837-43.

Weidner KM, Behrens J, Vandekerckhove J, Birchmeier W. Scatter Factor - Molecular Characteristics and Effect on the Invasiveness of Epithelial-Cells. J Cell Biol. 1990;111(5):2097-108.

Weisbart RH, Gera JF, Chan G, Hansen JE, Li E, Cloninger C, et al. A cell-penetrating bispecific antibody for therapeutic regulation of intracellular targets. Mol Cancer Ther. 2012;11(10):2169-73.

Weissleder R, Ntziachristos V. Shedding light onto live molecular targets. Nature medicine. 2003;9(1):123-8.

Weller MG. Quality Issues of Research Antibodies. Anal Chem Insights. 2016;11:21-7.

Westhoff MA, Serrels B, Fincham VJ, Frame MC, Carragher NO. SRC-mediated phosphorylation of focal adhesion kinase couples actin and adhesion dynamics to survival signaling. Mol Cell Biol. 2004;24(18):8113-33.

Weston AP, Banerjee SK, Sharma P, Tran TM, Richards R, Cherian R. p53 protein overexpression in low grade dysplasia (LGD) in Barrett's esophagus: Immunohistochemical marker predictive of progression. Am J Gastroenterol. 2001;96(5):1355-62.

Wheeler JB, Reed CE. Epidemiology of esophageal cancer. Surg Clin North Am. 2012;92(5):1077-87.

Wiedmann MW, Mossner J. New and emerging combination therapies for esophageal cancer. Cancer Manag Res. 2013;5:133-46.

Willner V, Bandes J, Hollander F. The normal anatomy and physiology of the esophagus. J Mt Sinai Hosp N Y. 1956; 23(1):3-13.

Wilson BC, Jermyn M, Leblond F. Challenges and opportunities in clinical translation of biomedical optical spectroscopy and imaging. J Biomed Opt. 2018;23(3).

Wisniewski JR, Hein MY, Cox J, Mann M. A "proteomic ruler" for protein copy number and concentration estimation without spike-in standards. Molecular & cellular proteomics : MCP. 2014;13(12):3497-506.

Wong JS, Warbrick E, Vojtesk B, Hill J, Lane DP. Anti-c-Met antibodies recognising a temperature sensitive epitope, inhibit cell growth. Oncotarget. 2013;4(7):1019-36.

Wong MCS, Hamilton W, Whiteman DC, Jiang JY, Qiao Y, Fung FDH, et al. Global Incidence and mortality of oesophageal cancer and their correlation with socioeconomic indicators temporal patterns and trends in 41 countries. Sci Rep. 2018;18(1):4522.

World Health Organisation, WHO. 2018. Latest global cancer data. [10 Nov 2018]. Available from: https://www.who.int/cancer/PRGlobocanFinal.pdf

Wu AM, Yazaki PJ. Designer genes: recombinant antibody fragments for biological imaging. The quarterly journal of nuclear medicine : official publication of the Italian Association of Nuclear Medicine (AIMN) [and] the International Association of Radiopharmacology (IAR). 2000;44(3):268-83.

Wu H, Shi H, Zhang H, Wang X, Yang Y, Yu C, et al. Prostate stem cell antigen antibody-conjugated multiwalled carbon nanotubes for targeted ultrasound imaging and drug delivery. Biomaterials. 2014;35(20):5369-80.

Xian CJ, Couper R, Howarth GS, Read LC, Kallincos NC. Increased expression of HGF and c-met in rat small intestine during recovery from methotrexate-induced mucositis. Br J Cancer. 2000;82(4):945-52.

Xiao GH, Jeffers M, Bellacosa A, Mitsuuchi Y, Vande Woude GF, Testa JR. Anti-apoptotic signaling by hepatocyte growth factor/Met via the phosphatidylinositol 3-kinase/Akt and mitogen-activated protein kinase pathways. P Natl Acad Sci USA. 2001;98(1):247-52.

Xie SH, Lagergren J. Risk factors for oesophageal cancer. Best Pract Res Clin Gastroenterol. 2018;36-37:3-8.

Xu YP, Lin G, Sun XJ, Yan MH, Zhang G, Hu JL, et al. C-Met as a Molecular Marker for Esophageal Squamous Cell Carcinoma and Its Association with Clinical Outcome. J Cancer. 2016;7(5):587-94.

Yam CH, Fung TK, Poon RYC. Cyclin A in cell cycle control and cancer. Cell Mol Life Sci. 2002;59(8):1317-26.

Yang NJ, Hinner MJ. Getting across the cell membrane: an overview for small molecules, peptides, and proteins. Methods Mol Biol. 2015;1266:29-53.

Yantiss RK. Diagnostic challenges in the pathologic evaluation of Barrett esophagus. Arch Pathol Lab Med. 2010;134(11):1589-600.

Yazaki E. Sifrim D. Anatomy and physiology of the esophageal body. Dis Esophagus. 2012;25(4):292-8.

Zarnegar R, Michalopoulos G. Purification and Biological Characterization of Human Hepatopoietin-a, a Polypeptide Growth-Factor for Hepatocytes. Cancer res. 1989;49(12):3314-20.

Zhang HR, Salo D, Kim DM, Komarov S, Tai YC, Berezin MY. Penetration depth of photons in biological tissues from hyperspectral imaging in shortwave infrared in transmission and reflection geometries. J Biomed Opt. 2016;21(12).

Zhang YW. Epidemiology of esophageal cancer. World journal of gastroenterology. 2013;19(34):5598-606.

Zorko M, Langel U. Cell-penetrating peptides: mechanism and kinetics of cargo delivery. Adv Drug Deliver Rev. 2005;57(4):529-45.